

**Influence of defect chemistry on heterogeneous catalysis:
Two examples using $\text{Sr}(\text{Fe}_x\text{Ti}_{1-x})\text{O}_{3-\delta}$ and Li_3N**

Von der Fakultät Chemie der Universität Stuttgart
zur Erlangung der Würde eines
Doktors der Naturwissenschaften (Dr. rer. nat.)
genehmigte Abhandlung

Vorgelegt von

Miloš Vračar

aus Belgrad (Serbien)

Hauptberichter:	Prof. Dr. Joachim Maier
Mitberichter:	Prof. Dr. Helmut Bertagnoli
Weiterer Prüfer:	Prof. Dr. Fritz Aldinger
Prüfungsvorsitzender:	Prof. Dr. Thomas Schleid
Tag der Einreichung:	3. März 2008
Tag der mündlichen Prüfung:	28. April 2008

MAX-PLANCK-INSTITUT FÜR FESTKÖRPERFORSCHUNG
Stuttgart
2008

... to the dearest memory of my mother Dr. Živojinka Vračar

and to my father Dr. Mile Vračar

... najdražem sećanju na moju majku Dr. Živojinku Vračar

i mom ocu Dr. Miletu Vračar

Contents

Zusammenfassung	9
Abstract	13
Acronyms and Symbols	17
1 Introduction and Motivation	21
2 Sr(Fe_xTi_{1-x})O_{3-δ} solid solutions: characteristic properties and their variation	25
2.1 Atomic structure	25
2.1.1 Bulk structure	25
2.1.2 Surface structure	28
2.2 Oxygen nonstoichiometry	29
2.3 UV-Visible spectra	30
2.4 Electrical conductivity and Diffusion	32
2.5 Applications	35
2.6 Short summary	36
3 Local structure investigation around Fe and Ti in Sr(Fe_xTi_{1-x})O_{3-δ}	39
3.1 Introduction	39
3.1.1 Jahn-Teller effect and its implications	39
3.1.2 Jahn-Teller distortion in Sr(Fe _x Ti _{1-x})O _{3-δ}	40
3.2 Basic principles of XAS	41
3.3 Experimental details	46
3.3.1 Principle of XAS measurement and details	46
3.3.2 XAS data analysis	47
3.3.3 Raman and IR measurements	48
3.4 Results	48
3.4.1 XANES	48
3.4.2 EXAFS	50
3.4.3 Vibrational spectroscopy	56
3.5 Discussion	58

3.6	Summary and conclusions	63
4	Catalytic activity of $\text{Sr}(\text{Fe}_x\text{Ti}_{1-x})\text{O}_{3-\delta}$: CH_4 and CO oxidation	67
4.1	Introduction	67
4.1.1	Importance of point defects in heterogeneous catalysis	68
4.1.2	Two test reactions	70
4.2	Chemical kinetics details	71
4.2.1	Adsorption isotherms	71
4.2.2	Chemical kinetics	72
4.3	Experimental details	76
4.3.1	Sample preparation	76
4.3.2	Experimental setup	80
4.3.3	Thermogravimetry	85
4.4	Reactions and Results	87
4.4.1	Reaction conditions	87
4.4.2	Reaction results: methane oxidation	89
4.4.3	Reaction results: carbon monoxide oxidation	93
4.4.4	Short summary of the results	95
4.5	Discussion	97
4.5.1	Literature review	97
4.5.2	Kinetic models	101
4.5.3	Interpretation	113
4.6	Conclusions	117
5	Electrocatalytic ammonia synthesis using Lithium nitride solid electrolyte	123
5.1	Introduction	124
5.1.1	Properties of lithium nitride	125
5.1.2	Ammonia synthesis	129
5.2	Experimental details	130
5.2.1	Sample preparation	132
5.2.2	Sample characterization	134
5.2.3	Electrodes for IS and electrocatalysis	135
5.2.4	Impedance spectroscopy	135
5.2.5	Cyclic voltammetry	135
5.2.6	Scanning electron microscopy and optical micrographs	136
5.2.7	Experimental setup	136
5.2.8	Detection of ammonia	138
5.2.9	Reaction conditions	140
5.3	Results and Discussion	141
5.3.1	XPS results	141

5.3.2	XRD analysis of single crystals	142
5.3.3	Impedance spectroscopy	143
5.3.4	Electrocatalytic reactions in the SC and QDC reactors	144
5.3.5	XRD analysis after reactions	153
5.4	Conclusions	155
	Bibliography	157
	Acknowledgments	171
	Curriculum Vitae	175

Zusammenfassung

Ausgangspunkt der vorliegenden Arbeit war es, die Rolle der Defektchemie in der heterogenen Katalyse, besonders im Bezug auf Punktfehler, hervorzuheben. Diese wirken als aktive Zentren und sind Grundvoraussetzung für die ionische Leitfähigkeit, die in der Elektrokatalyse wesentlich ist. Die elementarsten aktiven Zentren in der heterogenen Katalyse sind elektronische und ionische Punktdefekte. Bei Temperaturen oberhalb des absoluten Nullpunkts weist jeder Feststoff Defekte auf, selbst reine Feststoffe enthalten intrinsische Defekte wie z.B. Leitungsband-Elektronen oder Valenzband-Löcher, oder Defekte von Schottky- oder Frenkel-Typ. Die Defektkonzentrationen lassen sich mittels Dotierung wie auch durch Bestrahlung mit UV-Licht, γ -Strahlen, Neutronen oder Ionen erhöhen. In der Literatur wurde die Rolle ionischer Defekten in der heterogenen Katalyse oft unterschätzt.

In dieser Arbeit werden an zwei Systeme zwei verschiedene Aspekte betrachtet. In beiden Systemen spielen die ionische Ladungsträger eine wichtige Rolle. Als erstes Beispiel werden die katalytischen Eigenschaften gemischleitender Proben der $\text{Sr}(\text{Fe}_x\text{Ti}_{1-x})\text{O}_{3-\delta}$ -Mischungsreihe in CO-Oxidation und CH_4 -Oxidation untersucht. Zusätzlich wird die lokale Umgebung des Fe mittels EXAFS und Schwingungsspektroskopie untersucht. Der Eisengehalt wirkt dabei als Kontrollparameter, der sowohl die elektronische und ionische Leitfähigkeit bestimmt als auch die lokale Struktur des Materials beeinflusst. Die experimentellen Ergebnisse weisen darauf hin, dass es in oxidierten Proben mit niedrigen Eisengehalt an isolierten Fe^{4+} -Zentren eine Jahn-Teller-Verzerrung gibt, die bei stark eisenhaltigen Proben nicht zu erwarten ist. Zum Vergleich der katalytischen Aktivität werden die CH_4 - und CO-Oxidation jeweils in Sauerstoffüberschuss und mit einem Temperaturprogramm durchgeführt. In den beiden Reaktionen steigen die Aktivitäten mit dem Eisengehalt an und erreichen ein Plateau bei $x \approx 0.1$. Um kinetische Parameter wie partielle Reaktionsordnungen zu bestimmen, werden partialdruckabhängige Messungen durchgeführt. Über die ganze Mischungsreihe wird für beide Reaktionen eine niedrige Sauerstoff-Reaktionsordnung von $n \approx 0.1$ bis 0.2 gefunden. In der CO-Oxidation bleibt die CO-Reaktionsordnung hoch bei etwa $m = 0.8$. In der CH_4 -Oxidation zeigt sich mit steigendem x parallel zur Änderung der Umsätze ein Übergang von $m \approx 0.6$ für $x < 0.01$ zu $m \approx 0.8$ für $x \geq 0.01$. Die thermogravimetrische *in situ* Messung unter Reaktionsbedingungen mit einer hoch eisenhaltigen Proben hat gezeigt, dass bei CO-Oxidation trotz Sauerstoffüberschuss eine Reduktion (Erniedrigung des Sauerstoffgehalts) der Probe stattfindet. Dieser Befund weist darauf hin, dass detaillierte kinetische Modelle für das Verständnis der gemessenen partiellen Reaktionsordnungen notwendig sind. Die Hauptrolle in den kinetischen

Modellen spielt die jeweilige reaktive Sauerstoffspezies, entweder eine adsorbierte atomare Sauerstoffspezies O_{ad}^* oder eine Gittersauerstoffspezies O_O^* (* bezeichnet die Ladung, entweder 1- oder 2-). Die kinetischen Modellen sind in zwei Gruppen unterteilt: Gruppe **A**, in der die Konzentration der reaktiven Spezies im Gleichgewicht mit der Gasphase ist; und Gruppe **B**, in der der CO/CH₄-Reaktionszweig am schnellsten ist, wobei die Konzentration der reaktiven Sauerstoffspezies durch den ratenbestimmenden Schritt des Sauerstoff-Reaktionszweigs bestimmt wird. In den **B**-Fällen wird ein empirischer f -Faktor eingeführt, der beschreibt, wieviel der effektive O₂-Partialdruck in der Probe vom Partialdruck in der Gasphase abweicht. Der f -Faktor verbindet die Defektchemie der Proben mit den kinetischen Modellen, was insgesamt zu einer konsistenten Erklärung der experimentellen Ergebnisse führten. Für die CO-Oxidation an hoch eisenhaltigen Proben wird gezeigt, dass die **B**-Modelle die experimentellen Ergebnissen am besten beschreiben können. Es kann jedoch nicht entschieden werden, ob O_{ad}^* oder O_O^* die reaktive Spezies ist. Für die CH₄-Oxidation an hoch eisenhaltigen Proben wird gezeigt, dass ein **A**-Modell mit O_O^* als reaktiver Spezies die experimentellen Ergebnissen am besten erklärt. Für die Reaktionen an niedrig eisenhaltigen Proben kann aufgrund der beschränkten thermogravimetrischen Messgenauigkeit nicht bestimmt werden, ob sich die Sauerstoffstöchiometrie während der Katalyse ändert (**A**- oder **B**-Modell). Die Ergebnisse zeigen, dass man in Systemen wie gemischtleitenden Perowskiten, in denen es zur Stöchiometrieabweichung während einer heterogenen Reaktion kommen kann, die gemessenen (scheinbaren) partiellen Reaktionsordnungen nicht direkt mit einem vereinfachten kinetischen Modell vergleichen darf. Für solche Systeme wird gezeigt, dass die Defektchemie eine entscheidende Rolle spielt. Es wird auch gezeigt, dass rein kinetische Untersuchungen nicht ausreichend sind, um zu bestimmen, ob adsorbierte oder Gitter-Sauerstoffspezies an der Reaktion teilnehmen.

Die Möglichkeit zur elektrokatalytischen Synthese von Ammoniak unter Verwendung von Lithiumnitrid wurde als zweites Beispiel untersucht. Li₃N weist zum einen eine erhebliche Li⁺-Ionenleitfähigkeit und eine niedrige thermodynamische Zersetzungsspannung auf. Durch die besondere Reaktivität von Lithium mit N₂ kann außerdem an der Kathode Li₃N zürückgebildet werden. Mit einem Wechsel der Polarität im richtigen Takt in H₂/N₂-Atmosphäre sollte ein Dauerbetrieb möglich sein, ohne der Kontakt zu den Elektroden zu verlieren. Diese Sichtweise ist recht vereinfacht. Beim realen Experiment treten mehrere praktische Probleme auf. Die enorme chemische Reaktivität des Materials und die strukturelle Veränderungen der Proben unter Stromfluss verhindern eine genaue Reproduzierbarkeit der Messungen. Drei verschiedene Arten von Li₃N-Proben wurden untersucht: "alte" einkristalline Proben (gezogen im Czochralskiprozess), "neue" einkristalline Proben (hergestellt mit der Floating-Zone-Methode), und gesinterte Proben. Als erstes wurden elektrokatalytische Experimente in einem Einzelkammerreaktor mit Platin-Netz-Elektroden in einer Atmosphäre von 8 % H₂ in N₂ durchgeführt. In einem Experiment bei 145 °C mit einer der "alten" einkristallinen Proben wurde unter einem Spannungsimpuls von 200 V Ammoniak erzeugt. Überdies wurden auch Messungen unter gleichen Bedingungen, allerdings in 5 % H₂ in Ar durchgeführt. Das Ergebnis war erneut Ammoniaksynthese. Das zeigte die Beteiligung des Stickstoffs aus der Probe in der

Ammoniakbildung. In Bezug auf die Strommenge, die durch die Probe geflossen ist, liegt die geschätzte Effizienz zwischen 2 und 7 %. Die niedrige Effizienz könnte durch eine kleine ionische Überführungszahl der Probe verursacht sein. Ein Massetransport von Lithium wurde jedoch eindeutig beobachtet. Die quantitative Röntgen-Pulveranalyse hat weder Bildung von Li_2NH noch LiNH_2 ergeben, obwohl diese Verbindungen thermodynamisch günstig wären. Die Ergebnisse weisen darauf hin, dass die elektrokatalytische Ammoniaksynthese unter Anwendung von Lithiumnitrid bei moderaten Temperaturen und Umgebungsdruck möglich ist. Um zu beweisen, dass Ammoniak nicht durch einen Plasmaprozess entstanden ist, sind weitere Untersuchungen nötig. Um eine höhere Effizienz zu erreichen, sind Lithiumnitrid-Proben von hoher Qualität erforderlich; z.B. Einkristalle ohne Korngrenzen und mit einer ionischen Überführungszahl nahe eins. Wäre es möglich, einen reversiblen Dauerbetrieb zu erreichen, könnte die beschriebene elektrokatalytische Zelle als elektrogesteuerte Micro/nano-Ammoniakpumpe zur Anwendung kommen.

Abstract

Starting point for this work was to emphasize the role of defect chemistry in heterogeneous catalysis, particularly in respect of point defects. These act as active centers and are basic requirement for ionic conductivity which is important for electrocatalysis. The most elementary active centers in heterogeneous catalysis are electronic and ionic point defects. Each solid, including pure solids, has intrinsic defects above absolute zero temperature, e.g., conduction band electrons, valence band holes, Schottky- or Frenkel-type defects. Defect concentration can be enhanced by doping, as well as by irradiation with UV light, γ -rays, neutrons, or ions. The role of ionic defects in heterogeneous catalysis is often undervalued in the literature.

Two systems will be considered from two different aspects. In both systems ionic charge carriers play an important role. As first example, catalytic properties of the mixed-conducting $\text{Sr}(\text{Fe}_x\text{Ti}_{1-x})\text{O}_{3-\delta}$ solid solution series will be investigated in CO and CH_4 oxidation. Additionally, the local structure around Fe will be investigated by EXAFS and vibrational spectroscopy. The iron content acts as a control parameter, which determines the electronic and ionic conductivity, and influences the local structure of the material as well. Experimental results suggest that in oxidized samples with low iron content there is a Jahn-Teller distortion around Fe^{4+} centers, which is not expected in samples with high iron content. For the comparison of catalytic activity, CO and CH_4 oxidation in oxygen excess were performed with a temperature program. In both reactions, the catalytic activity increases with increasing iron content and reaches a plateau at $x = 0.1$. To determine kinetic parameters such as partial reaction orders, partial pressure dependent measurements were performed. In both reactions, a low oxygen partial reaction order of $n \approx 0.1$ to 0.2 was found over the whole solid solution series. In CO oxidation the CO partial reaction order is higher and is approximately constant of $m = 0.8$. In CH_4 oxidation, there is a transition in CH_4 partial reaction order from $m \approx 0.6$ for $x < 0.01$ to $n \approx 0.8$ for $x \geq 0.01$, similar to the variation found in the activity. The *in situ* thermogravimetry under reaction conditions showed that for CO oxidation on a high- x sample, in spite of oxygen excess, a reduction of the sample occurs. This finding suggests that for the understanding of the measured partial reaction orders more detailed kinetic models are needed. The main role in the kinetic models plays an oxygen reactive species, either an adsorbed atomic oxygen species O_{ad}^* or a lattice oxygen species O_O^* (* stands for the charge, 1- or 2-). Kinetic models are divided into two groups: group **A**, in which the concentration of the reactive species is in equilibrium with the gas phase; and group **B**, in which the CO/ CH_4 reaction branch is the fastest, whereby the concentration of the reactive oxygen species is

determined by the rate determining step of the oxygen branch. For **B** cases, an empirical f factor was introduced, which describes how much the oxygen partial pressure within the sample differs from the gas phase. The f factor connects the defect chemistry of the sample with the kinetic models, which altogether lead to a consistent explanation of the experimental results. For CO oxidation on high- x samples it was shown that **B** models explain best the experimental results. Nevertheless the final proof whether O_{ad}^* or O_O^* is the reactive species cannot be given. For CH_4 oxidation on high- x samples it is shown that an **A** model with O_O^* as the reactive species explains best the experimental results. For the reactions on low- x samples it is not possible to decide whether or not there is a change in sample stoichiometry (**A** or **B** model) during the catalysis due to a limited accuracy of thermogravimetric measurements. The results show that in systems such as mixed-conducting perovskites, in which a stoichiometry change during a heterogeneous catalytic reaction can occur, the apparent partial reaction orders must not be directly compared to the simplified kinetic models. For such systems it was shown that defect chemistry does play an essential role. It was also shown that kinetic investigations alone can not judge on the participation of O_{ad}^* or O_O^* species in the reaction.

As second example, the possibility of electrocatalytic ammonia synthesis using lithium nitride is studied. Here lithium nitride acts as electrolyte in an electrolytic cell. On electrolysis of the Li_3N electrolyte, reactive nitrogen species should form at the anode three-phase boundaries, which ought to be reactive enough to convert hydrogen molecules from the gas phase to ammonia. Li_3N exhibits a considerable Li^+ ionic conductivity and a low thermodynamic decomposition voltage. Because of the high reactivity of Li towards N_2 , a new layer of Li_3N can be formed at the cathode. In H_2/N_2 atmosphere and with a proper change of voltage polarity at electrodes, a steady state of ammonia production should be possible without losing the contact to the electrolyte. This is a simplified picture. Many practical problems appear in real experiments. The very high chemical reactivity of Li_3N and structural changes of the samples under current flow inhibit reproducibility of measurements. Three different kinds of the samples were investigated: "old" single crystalline samples (grown in Czochralsky process), "new" single crystalline samples (obtained by floating zone technique), and sintered samples. First, electrocatalytic experiments in a single chamber reactor with Pt-net electrodes in 8 % H_2 in N_2 atmosphere were performed. In an experiment at 145 °C on an "old" single crystalline sample, ammonia was produced under a voltage pulse of 200 V. Moreover, the measurement was repeated under the same conditions but in 5 % H_2 in Ar. The result was again ammonia synthesis. This showed clearly the nitrogen which formed ammonia was coming from the sample. In respect of the amount of charge transported through the sample, the estimated efficiency is between 2 and 7 %. The low efficiency is probably due to a low ionic transference number. Lithium mass transport was clearly observed. Quantitative x-ray powder diffraction analysis showed that neither Li_2NH nor $LiNH_2$ was generated although the formation of those compounds is thermodynamically allowed. The results suggest that the electrocatalytic ammonia synthesis can be possible at moderate temperatures and at ambient pressure using Li_3N . Further investigations are needed to confirm that the ammonia is not produced via a

plasma process. To achieve higher efficiency, high-quality Li_3N samples e.g., single crystals without grain boundaries and with a higher ionic transference number are needed. If the optimized electrocatalytic cell for ammonia synthesis can be achieved, it could find its application as an NH_3 micro/nano pump. Such a device could deliver a desired amount of NH_3 in an electronically controlled way.

Acronyms and Symbols

List of Acronyms

ac	alternating current
BET	Brunauer-Emmett-Teller method
BFT	back-Fourier transformation
CB	conduction band
CF	crystal field
CFSE	crystal field stabilization energy
CN	coordination number
cus	coordinative unsaturation
CV	cyclic voltammetry
dc	direct current
EDX	energy dispersive x-ray spectroscopy
ER	Eley-Rideal mechanism
ESR	electron spin resonance
EXAFS	extended x-ray absorption fine structure
FT	Fourier transformation
FTIR	Fourier transform infrared (spectroscopy, spectrometer)
FZ	floating zone
gb	grain boundary
HRTEM	high resolution transmission electron microscope
IR	infra-red
IS	impedance spectroscopy
JTE	Jahn-Teller effect
JTD	Jahn-Teller distortion
LH	Langmuir-Hinshelwood mechanism
MFC	mass flow controller
MIEC	mixed ionic electronic conductor
MS	mass spectrometer/spectrum
MSRD	mean square radial displacement
MvK	Mars-van Krevelen mechanism
NEMCA	non-Faradaic electrochemical modification of catalytic activity

NSC	‘new’ single crystal
OSC	‘old’ single crystal
QDC	quasi-double chamber (reactor)
RDS	rate determining step
SC	single chamber (reactor)
SEM	scanning electron microscope
SOFC	solid oxide fuel cell
SPC	sintered poly-crystalline (sample)
STO	strontium titanate
TG	thermogravimetry
TM	transition metal
TMO	transition metal oxide
TOF	turnover frequency
VB	valence band
XAS	x-ray absorption spectroscopy
XANES	x-ray absorption near-edge structure
XPS	x-ray photoelectron spectroscopy
XRD	x-ray diffraction

List of Symbols

A	group kinetic cases where no stoichiometry change occurs
B	group kinetic cases where a stoichiometry change does occur
c_i	concentration of species i
δ	oxygen deficiency
D_{V_O}	oxygen vacancy diffusion coefficient
D_O^δ	oxygen chemical diffusion coefficient
E_a	activation energy
E_g	energy band gap
E_0	x-ray absorption edge
$\Phi_i(k, R_i)$	phase shift in the wave function
F	Faraday constant
$F_i(k, R_i)$	backscattering amplitude
h	electron hole
I	x-ray beam intensity, or electric current
k	photoelectron wave vector
$\mu(E)$	x-ray absorption coefficient
μ_O	oxygen chemical potential
m	CO/CH ₄ partial reaction order

n	oxygen partial reaction order
N_i	number of atoms in a coordination shell
O_{ad}^-	adsorbed oxygen (reactive) species
O_O^*	lattice oxygen (reactive) species
P_{O_2}	oxygen partial pressure
R	universal gas constant
R_i	average distance between adsorbing atom and its neighbors
R_A	reaction rate of species A
σ_i^2	mean square radial displacement
σ_i	conductivity of species i
S_0^2	the scale factor of scattering amplitude damping
t	Goldschmidt tolerance factor
T	temperature
V_O	oxygen vacancy
w_O	oxygen thermodynamic factor
x	iron content or content of a dopant
X	conversion
$\chi(k)$	EXAFS signal

Chapter 1

Introduction and Motivation

The surface of a solid is a two-dimensional extended defect, therefore, its physicochemical properties can greatly differ from those of the bulk. For example, even in a pure ionic solid, terminal ions which form the ideally flat surface have a reduced coordination, and in a crude approximation¹ experience a different Madelung potential as compared to bulk atoms (i.e., they are less strongly bound and have higher energies). This can lead to an enhanced reactivity and catalytic activity. Perfect surfaces often do not contribute much to the catalytic activity but rather the so-called *active centers*² present. Imperfections of the surface such as kinks, steps, or dislocations, further decrease the coordination of surface atoms which form the imperfections and are said to be coordinatively unsaturated. Such species at the surface can facilitate adsorption and can act as active centers in catalysis.

The most elementary active centers for catalysis are electronic and ionic point defects. Each solid has defects at temperatures higher than absolute zero. This holds not only for extrinsic (i.e., doped) solids but even intrinsic (pure) solids exhibit intrinsic defects such as electrons, holes, Schottky- and Frenkel-type defects. The defect concentration in a solid is not only enhanced by doping procedures, but also by irradiation with UV light, γ -rays, neutrons or ions. Therefore increased oxygen vacancy concentrations are present, for example, not only in Fe doped SrTiO₃ or Li doped MgO but also in γ -ray irradiated MgO.

The role of electronic defects (electrons and holes) in heterogeneous catalysis on semiconductors was acknowledged very early, and one of the first theories involving the charge transfer was proposed by C. Wagner and K. Hauffe in 1938 [1]. Electronic defects in catalysis have been broadly investigated ever since. Electronic defects readily act as active redox centers through which the charge transfer needed for the reaction may find its energetically most optimal path.

However, the role of ionic point defects in heterogeneous catalysis is not much appreciated in research and literature. Most naturally, ionic defects in solids act as acid-base active centers. This point was clearly stressed in Ref. [2]. One of the first examples of catalysis involving ionic point defects was reported by Simkovich and Wagner [3]. The authors showed that

¹discarding here more subtle quantum mechanical aspects of chemical binding

²the term introduced by H. S. Taylor, Proc. Roy. Soc. [London] A108, 105 (1925)

the rate of dehydrohalogenation of alkyl halides on the surface of AgCl may be enhanced by homogeneous CdCl₂ doping which increases the silver vacancy concentration. The insulating nature of AgCl assures that the influence of electronic defects is minimized. In this case ionic defects act purely as acid-base centers. Also, the role of ionic point defects in AgCl heterogeneously doped with γ -Al₂O₃ in dehydrohalogenation of tertiary butyl chloride was elucidated [4]. The authors of Ref. [4] also argued that the reaction rate increased due to an enhanced silver vacancy concentration.

Catalysis may also be enabled in systems through which a current flows. This is possible in permeation membrane reactors; where a flux (e.g., an oxygen flux) is caused by an outer gradient in the chemical potential (e.g., a gradient in the oxygen partial pressure). In ionic systems this presupposes mixed conductivity (electronic and ionic conductivity). The oxygen being released at one surface may be particularly reactive as being *in statu nascendi*. The same may happen in electrolytic systems where oxygen release is caused by an internal O²⁻ flux compensated by an outer electric current. Besides these Faradaic effects there might also be a favorable polarization occurring at the electrodes if the electrode reactions are not really reversible. Then a locally increased oxygen activity (a_{O}) or even an additionally increased ion activity ($a_{\text{O}^{2-}}$) owing to spill-over (such effects have been described in literature, e.g., Refs. [5] and [6]) may result.

In this work two systems that emphasize different aspects are considered. In both examples defect chemistry and the presence of ionic charge carriers play an important role. First, catalytic properties of a mixed-conducting Sr(Fe_xTi_{1-x})O_{3- δ} solid solution series is studied with respect to its role of a ‘classical’ heterogeneous catalyst in carbon monoxide oxidation and methane oxidation. This solid solution series is a very interesting system with a rich electronic and ionic defect chemistry. The iron content³ in Sr(Fe_xTi_{1-x})O_{3- δ} can be understood as a control parameter: (i) it determines, as summarized in Chapter 1, among other properties its ionic and electronic conductivity; (ii) it influences the local structure of the material, through the presence of a Jahn-Teller distortion around Fe⁴⁺ centers, as discussed in Chapter 2; and finally, as discussed in Chapter 3, (iii) it is essential to the catalytic activity in CO oxidation and CH₄ oxidation.

Second, the possibility of electrocatalytic ammonia synthesis using lithium nitride is studied, as described in Chapter 4. Here lithium nitride acts as electrolyte in an electrolytic cell. On electrolysis of the Li₃N electrolyte, reactive nitrogen species should form at the anode three-phase boundaries, which ought to be reactive enough to convert hydrogen molecules from the gas phase to ammonia.

³considering the iron as a dopant is justifiable for low iron concentration, but at iron contents higher than few percent, Sr(Fe_xTi_{1-x})O_{3- δ} should be understood as a material of its own.

Chapter 2

Sr(Fe_xTi_{1-x})O_{3-δ} solid solutions: characteristic properties and their variation

In this chapter the properties of the Sr(Fe_xTi_{1-x})O_{3-δ} solid solution series which are relevant for the discussion of the work presented in Chapters 3 and 4 are summarized. The samples were prepared by solid state reactions as described in Section 4.3.1.

2.1 Atomic structure

2.1.1 Bulk structure

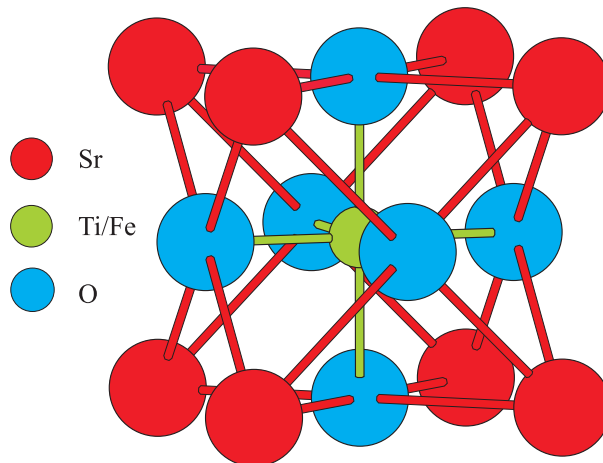


Figure 2.1: SrTiO₃, perovskite structure.

Strontium titanate, SrTiO₃, belongs to the perovskite family with a cubic structure and the general formula ABO₃, and is an example of a predominantly ionic compound. As in every cubic perovskite-type oxide, the structure is built from corner-shared rigid BO₆ (TiO₆) octahedra, where B is a transition metal (TM) ion which has a preference for octahedral

Table 2.1: Shannon ionic radii of the ions [8]. Indices l and h stand for the low and high spin configurations, respectively; u stands for unspecified spin configuration. †Coordination number (CN).

Site in ABO_3	A		B								
CN†	12		6								
Element	Sr	Ti	Fe		Sc	Mn			Co		
Oxidation state	2+	4+	3+	4+	3+	2+	3+	4+	2+	3+	4+
Ionic radius (Å)	1.44	0.605	0.645 ^h	0.585 ^h	0.745	0.83 ^h	0.645 ^h	0.53 ^u	0.65 ^l	0.545 ^l	0.53 ^u

coordination (the coordination number of A is 12). In stoichiometric ABO_3 compounds, the valence states of A^{m+} and B^{n+} must satisfy the electroneutrality condition $m + n = 6$ (no ABO_3 compound has been found in which $m > n$). Simultaneously, the sizes (radii, r_{ion}) of the A, B and O ions satisfy the relation

$$0.75 < \frac{r_{\text{A}} + r_{\text{O}}}{\sqrt{2}(r_{\text{B}} + r_{\text{O}})} < 1.1 \quad (2.1)$$

which describes the optimum ratio of A–O and B–O lengths of a stable perovskite structure. This relation uses the (Goldschmidt) tolerance factor [7]:

$$t = \frac{(r_{\text{A}} + r_{\text{O}})}{\sqrt{2}(r_{\text{B}} + r_{\text{O}})}. \quad (2.2)$$

The Shannon ionic radii of all relevant ions are given in Table 2.1 [8].

The spatial arrangement of atoms in strontium titanate for $T > 105$ K is shown in Figure 2.1; Sr cations form a cubic cell with face centered O anions, the smaller Ti cation is in the center of the cubic cell. By cooling down SrTiO_3 undergoes a phase transition from cubic to tetragonal phase at about $T = 105$ K [9, 10, 11]. Since the structure can be regarded as a cubic close packing of Sr^{2+} and O^{2-} with 1/4 of octahedron voids occupied by the B cations, this structure is tolerant to substitution of Ti cations by other cations of similar size – this is a general property of the perovskite structure which makes it very interesting for tailoring material properties. Although numerous oxides belong to this family, SrTiO_3 is one of the few oxide systems which naturally at high preparation temperatures allows for complete gradual aliovalent substitution on the B site, particularly by Fe atoms as dopant, from zero iron content to complete substitution corresponding to SrFeO_3 . This feature is rather exceptional and already for different types of substituent atoms such as scandium or manganese it is not possible to attain a complete single phase solid solution series. In its octahedral environment the iron atom can have the valence states 3+ (Fe^{3+}) or 4+ (Fe^{4+}), the relative amounts of each depending on the external conditions¹: oxygen partial pressure (P_{O_2}) and temperature (T). Titanium exhibits only the valence state of 4+ (Ti^{4+}) under the applied conditions. When the iron is in the valence state of 3+ the necessary charge compensation

¹if the oxygen in the lattice is in thermodynamical equilibrium with environment.

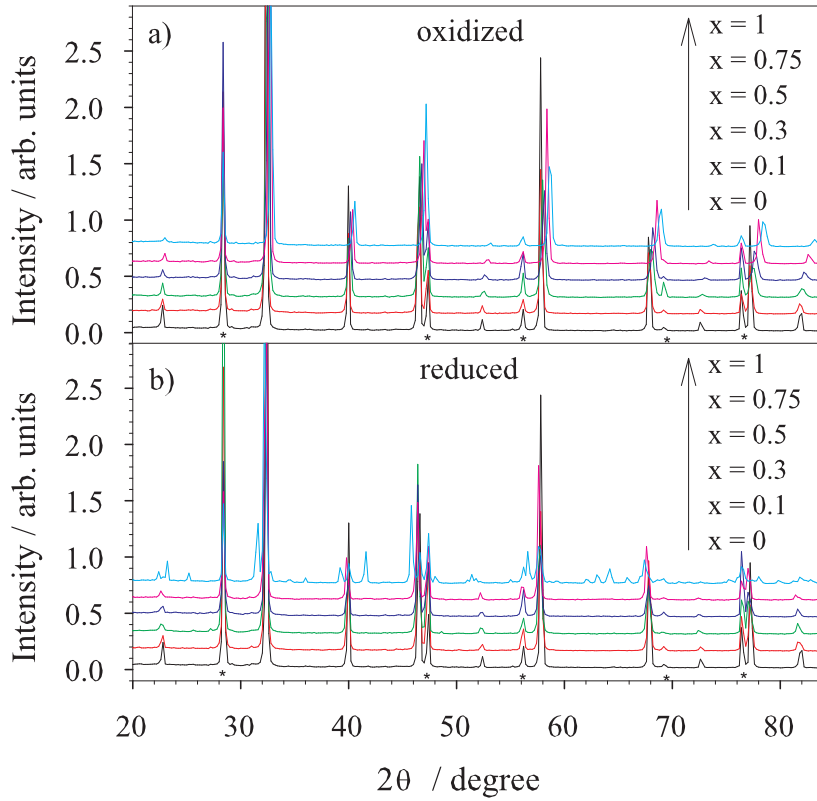
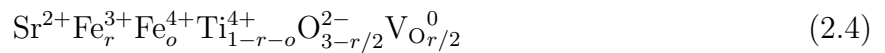


Figure 2.2: X-ray diffractograms of $\text{Sr}(\text{Fe}_x\text{Ti}_{1-x})\text{O}_{3-\delta}$ for various iron content x . The asterisk * designates the internal silicon reference.

occurs predominantly through the formation of oxygen vacancies in the lattice, more precisely two Fe^{3+} are compensated by one oxygen vacancy V_{O} (in Kröger-Vink notation [12] if relative charges are used V_{O}^{\cdot} is the correct notation). The chemical formula which describes such a case, under the assumption that the O^- concentration is negligible in the electroneutrality condition (this does not hold for very low Fe doping), would be



or more precisely



where $r + o (= x)$ is the total iron content in the compound. This formula can be further generalized for other TM ions in SrTiO_3 (like Sc, Mn, Co), where oxidation states of TM different from 4+ lead to modifications in the oxygen nonstoichiometry.

The x-ray diffractograms of oxidized and reduced samples (all iron present as 4+ or 3+, respectively, for details see Section 2.2) throughout the $\text{Sr}(\text{Fe}_x\text{Ti}_{1-x})\text{O}_{3-\delta}$ series are shown in Figure 2.2. X-ray diffraction (XRD) patterns were measured at room temperature using $\text{Cu } K\alpha$ radiation in Bragg-Brentano geometry with internal Si standard in the range $2\theta=10-120^\circ$ (Fig. 2.2). All oxidized samples and the reduced samples with $x < 0.9$ were found to be single phase cubic ABO_3 perovskites (space group $Pm\bar{3}m$), while the reduced ones with $x = 0.9$ and

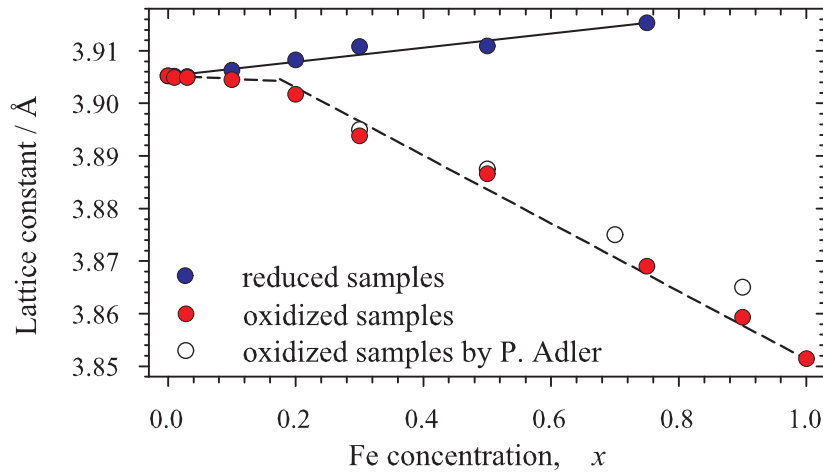


Figure 2.3: Lattice constant of $\text{Sr}(\text{Fe}_x\text{Ti}_{1-x})\text{O}_{3-\delta}$ for various iron content x . Open circles represent the data from Ref. [13].

$x = 1$ were predominantly or purely of brownmillerite structure [14, 15] (space group $Ibm2$). Lattice parameters were refined by least squares minimization using the program LCLSQ [16] after indexing with the program DICVOL91 [17].

In the case of oxidized samples the pattern of reflections does not change and there is only a decrease of the lattice constant with increasing iron content. This can be seen more clearly in Figure 2.3 where the refined lattice constants are given as a function of iron content. Since Ti^{4+} cations are bigger than Fe^{4+} , a linear variation of lattice constant with composition at constant temperature (Vegard's law) is to be expected. However, for the oxidized samples Vegard's law is not obeyed: there are two segments with different slopes changing at about $x = 0.2$ in Figure 2.3. The first segment is intimately related with a larger tolerance factor (influenced by the smaller size of Fe^{4+}). In the second segment, the decrease of the lattice constant due to the difference in ion sizes with the increase of iron content is observed. This will be discussed in more detail in Chapter 3. In the case of reduced samples there is only a very slight increase in lattice constant with increasing iron content. The increase of the lattice constant with the increase of iron content is to be expected since Ti^{4+} cations are smaller than Fe^{3+} .

2.1.2 Surface structure

If the surface of an ionic crystal has a dipole moment perpendicular to it, it is unstable and it will undergo a substantial reconstruction [18]. For SrTiO_3 there are two possible (100) non-polar surface terminations with similar surface energies: a TiO_2 -terminated surface, and SrO -terminated surface. Due to its polarity the unperturbed (111) surface is considered to be much less stable, and a heavy reconstruction is expected. In the case of the polar (110) surface the different terminations show large differences in surface energy, and the most stable surface is the reconstructed O-terminated surface with oxygen vacancies which has surface

energy close to that of (100) [19]. This is an indication that both (100) and (110) surfaces can coexist in polycrystalline materials. A similar conclusion would apply for $\text{Sr}(\text{Fe}_x\text{Ti}_{1-x})\text{O}_{3-\delta}$ keeping in mind that Fe^{3+} is compensated by additional vacancies.

2.2 Oxygen nonstoichiometry

As already described by Eq. (2.4), in $\text{Sr}(\text{Fe}_x\text{Ti}_{1-x})\text{O}_{3-\delta}$ the charge compensation for Fe^{3+} at the B site occurs predominantly by formation of oxygen vacancies. This is expected also for other transition metal ions with oxidation state lower than 4+ present in SrTiO_3 at the B site. At $T \geq 300$ °C the oxygen vacancies in $\text{Sr}(\text{Fe}_x\text{Ti}_{1-x})\text{O}_{3-\delta}$ become sufficiently mobile and powder samples can equilibrate with the gas phase within minutes. As a typical example of oxygen nonstoichiometry in $\text{Sr}(\text{Fe}_x\text{Ti}_{1-x})\text{O}_{3-\delta}$ solid solutions, the oxygen nonstoichiometry of $\text{Sr}(\text{Fe}_{0.5}\text{Ti}_{0.5})\text{O}_{3-\delta}$ determined by thermogravimetric measurements (TG) is shown in Figure 2.4. It can be seen that the oxygen deficiency δ increases with increasing temperature at con-

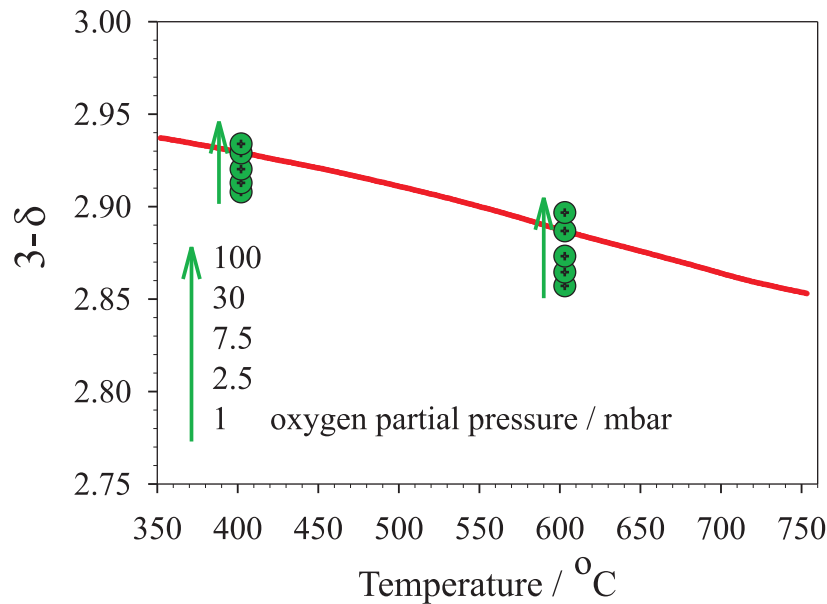


Figure 2.4: Oxygen nonstoichiometry of $\text{Sr}(\text{Fe}_{0.5}\text{Ti}_{0.5})\text{O}_{3-\delta}$ determined by thermogravimetry. The temperature dependency of the oxygen nonstoichiometry for a fixed $P_{\text{O}_2} = 30$ mbar is given by the red curve. The P_{O_2} -dependencies of the oxygen nonstoichiometry at two fixed temperatures for the indicated P_{O_2} s are given by green points.

stant P_{O_2} . Also, a decrease of P_{O_2} at constant temperature increases the oxygen deficiency δ , as shown by green points in Figure 2.4.

The highest oxygen deficiency of $\text{Sr}(\text{Fe}_x\text{Ti}_{1-x})\text{O}_{3-\delta}$ could be obtained after equilibration under reducing conditions (e.g. 8 % H_2 in N_2 at 700 °C) which is in the following called *reduction*. Under these conditions all iron ions can be assumed to be in the valence state of 3+ [20]. Therefore absolute oxygen deficiencies can be determined taking into account also the weight change occurring after gas switching from a given P_{O_2} to 8 % H_2 at 700 °C.

Table 2.2: Degree of oxidation of oxidized $\text{Sr}(\text{Fe}_x\text{Ti}_{1-x})\text{O}_3$ samples determined by TG and iodometric titration [21].

Fe content x	thermogravimetry %	titration %
0.03	100±10	
0.1	100±5	
0.2	96±5	
0.3	95±2	95±3
0.5	93±2	96±3
0.75	98±2	102±3
0.9	96±2	102±3
1.0	98±2	101±3

In contrast to reduction, oxidizing all Fe ions to the Fe^{4+} state (which in the following is called *oxidation*) is much harder. After exposing powder samples to a high oxygen pressure (about 500 bar) and a temperature as low as possible but still allowing slow equilibration ($T \approx 200$ °C), it is assumed that the great majority of Fe ions are in Fe^{4+} state. Thermogravimetric measurements showed that all samples are more than 95 % oxidized, with only the $x = 0.5$ sample exhibiting a slightly lower value of 93 %. For samples with $x \geq 0.3$ iodometric titrations yielded degrees of oxidation ≥ 95 %. The results are summarized in Table 2.2 [21].

The maximal (possible) oxygen deficiency is limited by the iron content x (Eq. 2.4), and it increases with increasing x under reducing conditions. If the samples are submitted to intermediate P_{O_2} (0.001–0.1 bar) and temperature (400–600 °C), $\text{Sr}(\text{Fe}_x\text{Ti}_{1-x})\text{O}_{3-\delta}$ contains a mixture of Fe^{3+} and Fe^{4+} . There is a tendency of the ratio $[\text{Fe}^{3+}]/[\text{Fe}^{4+}]$ to decrease with increasing iron content x at given P_{O_2} and temperature [22]. The presence of mixed valence states can have an impact on catalytic activity of the material (discussed in Chapter 4).

2.3 UV-Visible spectra

The UV-Visible diffuse reflectance spectra of $\text{Sr}(\text{Fe}_x\text{Ti}_{1-x})\text{O}_{3-\delta}$ powder samples (diluted with Al_2O_3) were measured separately after two different pre-treatments: after oxidation and after reduction. Photographs of the samples are shown in Figure 2.5. Pure SrTiO_3 is white, as expected for wide bandgap oxides, independently of the reducing or oxidizing pretreatment. Oxidized samples have colors ranging gradually from pale brown already for $x = 0.003$, dark brown for $x = 0.1$ and to black color for $x \geq 0.2$. Reduced samples have colors ranging gradually from "dirty" white for the lowest iron content (not shown), pale brown for $x = 0.1$, orange-brown for $x = 0.3$, and to dark brown-red for $x = 1$. The diffuse reflectance spectra were calculated from the reflectivity R using the Kubelka-Munk function: $f(R) = (1 - R)^2/2R = 2\alpha/S$, which is proportional to the absorption coefficient $\alpha(E)$ when the scattering modulus S is assumed to be constant. The results are shown in Figure 2.6 for (a) oxidized samples and



Figure 2.5: Sample photographs. The leftmost sample is the undoped SrTiO_3 ; upper row: oxidized samples, lower row: reduced samples. In both rows iron content increases from left to right: $x = 0.01$, 0.1, 0.3 and 1.

(b) reduced samples. In both cases the main absorption edge is present at ≈ 3.2 eV, which corresponds to the excitation of electrons from the valence to the conduction band. From quantum mechanical calculations it is known that the valence (VB) band is formed from O $2p$ orbitals and that Ti $3d$ orbitals build up the conduction band [23, 24]. Since these Ti $3d$ orbitals are empty, SrTiO_3 belongs to the d^0 group of transition-metal oxides. The oxidized

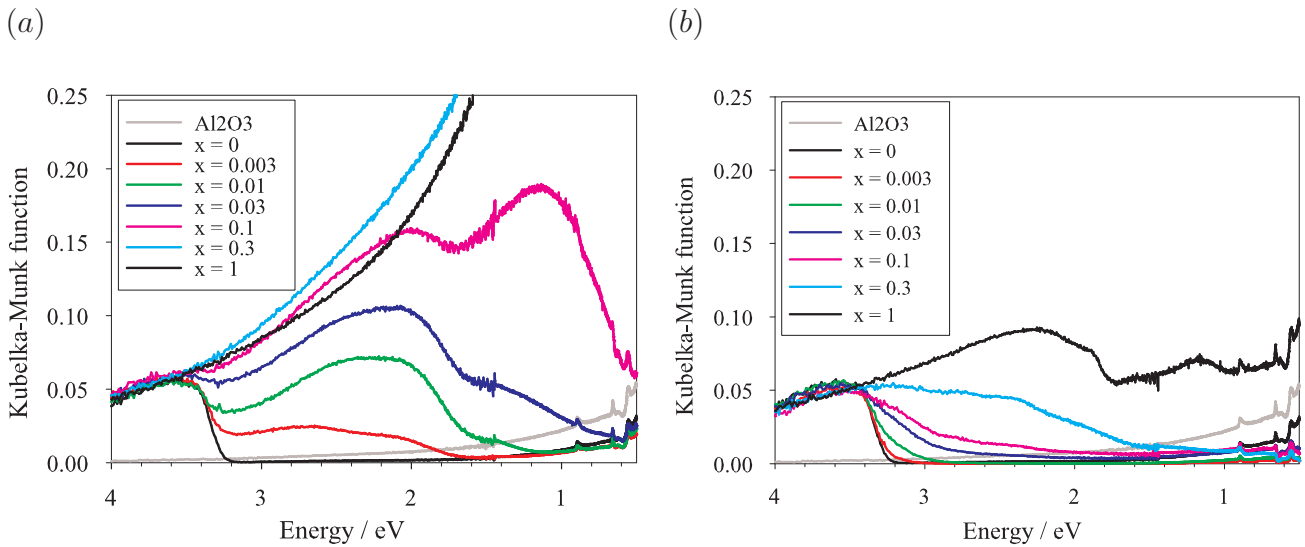


Figure 2.6: UV-Visible spectra of $\text{Sr}(\text{Fe}_x\text{Ti}_{1-x})\text{O}_{3-\delta}$ for two different pre-treatments: (a) oxidized samples and (b) reduced samples.

samples (almost all iron being Fe^{4+}) show strong absorption bands. For high iron contents, $x \geq 0.2$, the bands cannot be resolved, which is to be expected when the conduction band is formed by the overlap of partially occupied iron d orbitals. For lower iron contents three absorption bands can be observed: at ≈ 2.75 eV (≈ 450 nm), ≈ 2.1 eV (≈ 590 nm) and ≈ 1.1 eV (≈ 1130 nm). It can be seen that these absorption bands are strongly dependent on the iron content. Integrated intensities of the first two peaks are proportional to the iron content

[25]. The intensity of the third peak increases overproportionally with increasing iron content starting from $x = 0.03$. The first two peaks are attributed to charge transfer transitions of valence band electrons (VB: O $2p$) into ligand field $3d$ states of Fe^{4+} lying within the band gap, $VB \rightarrow e_g$ and $VB \rightarrow t_{2g}$, respectively [26, 27]. According to conductivity measurements, the $\text{Fe}^{3+/4+}$ level is estimated to lie ≈ 0.8 eV above the VB [28]. The difference to the optical excitation energy can be explained by the Frank-Condon principle: the change of the valence state of an Fe impurity center makes a drastic change in the structure of such ionic materials. Because of the symmetry selection rules, charge transfer absorption bands are more intense than $d-d$ transitions [29]. The origin of the third peak at 1.1 eV is not quite clear. At least two explanations can be offered. First, if a small-polaron conduction mechanism is supposed (which is supported by the findings given in Section 2.4) the absorption is related to these polarons. The energy of the excitation is expected to be $E_{opt} = 4E_a \approx 1.2$ eV, where E_a is the thermal activation energy for polaron hopping conduction (see Section 2.4). The second possible peak origin is an absorption by exciton formation, which is to be expected in materials with wide bands and high dielectric constants [29]. The energy of exciton formation can be estimated using a quasi-hydrogenic approximation: $E_n = -R_y\mu/(\epsilon_r^2n^2)$, where R_y is the Rydberg constant (13.6 eV), n is the principal quantum number (here assumed to be unity), $\epsilon_{r,opt}$ the dielectric constant at high frequencies (of about 5.8 for SrTiO_3 [30]) and μ is the reduced mass calculated from electron and hole effective masses in electron mass units (estimated to be ≈ 2.5 [31]). The resulting energy for exciton formation is $E_1 \approx 0.94$ eV, which for this crude model is sufficiently close to be a possible explanation.

For the reduced samples in Figure 2.6 (b) only very weak absorption bands are present. For low iron content there are no peaks characteristic of charge-transfer absorption. Also, there is no peak at 1.1 eV. Of course, the band gap absorption edge is present at the same energy as in oxidized samples (visible at low iron contents).

2.4 Electrical conductivity and Diffusion

Strontium titanate is a representative example of a mixed ionic electronic conductor (MIEC) with mobile V_{O} , and n - or p -type electronic conductivity depending on the ambient P_{O_2} . Pure SrTiO_3 is a large bandgap semiconductor with a bandgap of 3.2 eV, which under strongly reducing conditions at high T becomes an n -type semiconductor [32]. For iron content $x \leq 0.01$, the distribution of defects ($\text{Fe}^{3+/4+}$ and V_{O}) can be taken as random and the interaction between them is mainly electrostatic. In this case a dilute point defect model can be applied [28]. The impurity energy level of $\text{Fe}^{3+/4+}$ lies about 0.8 eV above the valence band [28]. The material is still a large-band semiconductor, with isolated and localized impurity levels, and can be considered as an "electron poor" material. Since the Fe^{3+} is a negatively charged defect (relative to the ideal lattice), concentrations of all other negative defects decrease upon Fe doping and the electronic conductivity is of p -type. Iron impurity bands start to form for iron contents $x \geq 0.03$. In an attempt to describe the whole range of the iron content it has

been suggested that for higher iron concentrations the Fe ions can not be taken solely as a dopant-defect in the structure, but rather they must be considered as a major constituent that contributes to the energy-band structure [33]. With the increasing iron concentration the impurity band starts gradually to form from partially occupied Fe $3d$ states within the bandgap which is reflected in the conductivity. The electronic conductivities of oxidized samples are shown in Figure 2.7 [34]. They are obtained from the total conductivity measurements under conditions where the oxygen stoichiometry is frozen. For samples equilibrated at intermediate P_{O_2} (between 10^{-11} and 10^{-5} bar) and quenched, the total conductivity is of ionic type and exhibits a P_{O_2} -independent plateau [35]. Compared to these plateau values, the ionic conductivity does not significantly contribute to the total conductivity in the measurements of the oxidized samples with frozen-in stoichiometry, which then directly corresponds to the p -type electronic conductivity. In Figure 2.7 it can be seen clearly that the conductivity is thermally activated and dependent on the iron content. For low iron content, the activation energy is about 0.9 eV and mainly corresponds to the hole formation enthalpy for the reaction



However, the ratio $[Fe^{3+}]/[Fe^{4+}]$ is almost constant with temperature, because $[h^{\cdot}] \ll \min([Fe_{Ti}^{\times}], [Fe'_{Ti}])$. In this regime the hole mobility is a weak function of T and decreases with increasing temperature which are characteristics of the valence band conduction mechanism [36]. The temperature dependence of σ is dominated by the carrier (hole) formation process. For higher iron content, E_a does not change much with increasing iron content and has a value of $E_a \approx 0.3$ eV for $0.1 \leq x \leq 0.3$. In agreement with Ref. [37], the conduction is assigned to the small polaron hopping mechanism. Since the charge carrier concentration is constant (a frozen stoichiometry implies a frozen $[Fe^{3+}]/[Fe^{4+}]$ ratio), the temperature dependence of the electronic conductivity is dominated by the temperature dependence of the electronic mobility.

Apart from the electronic conductivity, the presence of ionic conductivity in pure and acceptor doped $SrTiO_3$ was confirmed in many investigations under various conditions (P_{O_2} , T and doping levels), e.g. Refs. [38, 39]. The mechanism of ionic conduction is an oxygen vacancy hopping mechanism. Having measured the ionic conductivity, one can in principle calculate the self-diffusion coefficient of the oxygen ions, D_O^Q . Yet another kind of experiment, a chemical diffusion experiment, gives a different diffusion coefficient, i.e., the chemical diffusion coefficient of oxygen, D_O^δ [40]. This is an important parameter for sample equilibration with the oxygen-containing gas phase (as in results presented in Section 4.5). D_O^δ describes the oxygen diffusion driven by a chemical potential gradient of oxygen. As discussed in Ref. [40], D_O^δ incorporates contributions from both electronic carriers and oxygen vacancies, therefore it has a more complex nature. Generally, it can be expressed in terms of the oxygen vacancy ($D_{V_{\ddot{O}}}$) and the electron holes (D_h) diffusion coefficients

$$D_O^\delta = \frac{\sigma_h}{\sigma} D_{V_{\ddot{O}}} + \frac{\sigma_{V_{\ddot{O}}}}{\sigma} D_h, \quad (2.6)$$

where σ is the total conductivity; $\sigma_{V_{\ddot{O}}}$ and σ_h are conductivities of oxygen vacancies and holes, respectively. More generally, in a view of component flow, the chemical diffusion coefficient is

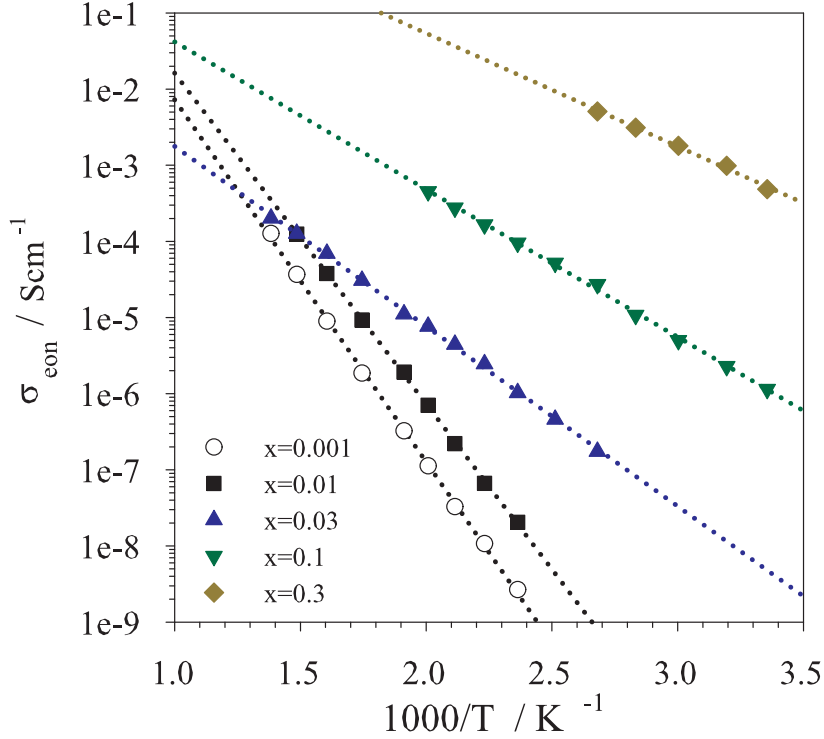


Figure 2.7: Electronic conductivity of $\text{Sr}(\text{Fe}_x\text{Ti}_{1-x})\text{O}_3$, oxidized samples, frozen stoichiometry [34].

given by

$$D_{\text{O}}^{\delta} = \frac{1}{4F^2} \sigma_{\text{O}}^{\delta} \frac{\partial \mu_{\text{O}}}{\partial c_{\text{O}}} = \frac{RT}{4F^2} \sigma_{\text{O}}^{\delta} \frac{w_{\text{O}}}{c_{\text{O}}} \quad (2.7)$$

where μ_{O} is the oxygen chemical potential, $\sigma_{\text{O}}^{\delta} = \sigma_{\text{h}} \sigma_{\text{V}_{\text{O}}^{\cdot\cdot}} / (\sigma_{\text{h}} + \sigma_{\text{V}_{\text{O}}^{\cdot\cdot}})$ is the ambipolar conductance, w_{O} is the thermodynamic factor, and c_{O} is the concentration of oxygen. In the case of slightly Fe-doped SrTiO_3 in which the internal iron redox reaction [Eq. (2.5)] takes place, as shown in Ref. [41, 42], the thermodynamic factor becomes

$$w_{\text{O}} = \left(\frac{1}{c_{\text{V}_{\text{O}}^{\cdot\cdot}}} + 4 \frac{\chi_{\text{h}}}{c_{\text{h}}} \right) c_{\text{O}} \quad \text{with} \quad \chi_{\text{h}} = \left(1 + \frac{xK}{(K + c_{\text{h}})^2} \right)^{-1}, \quad (2.8)$$

where $c_{\text{V}_{\text{O}}^{\cdot\cdot}}$ is oxygen vacancy concentration, c_{h} is hole concentration, x is the iron content, and K is the equilibrium constant of the iron redox reaction. The additional factor χ_{h} measures the increase in free holes compared to the increase in the total number of holes: $\partial[\text{h}^{\cdot}] / \partial([\text{h}^{\cdot}] + [\text{Fe}^{\times}])$. Since $[\text{h}^{\cdot}] \ll [\text{Fe}'_{\text{Ti}}] \sim [\text{Fe}^{\times}_{\text{Ti}}]$, the thermodynamic factor can be further simplified [42] to

$$w_{\text{O}} = \left(\frac{1}{[\text{V}_{\text{O}}^{\cdot\cdot}]} + 4 \frac{1}{[\text{Fe}^{\cdot}]} + 4 \frac{1}{[\text{Fe}^{\times}]} \right) c_{\text{O}}. \quad (2.9)$$

According to TG analysis, under conditions relevant for catalytical studies presented in Chapter 4, the $[\text{Fe}^{3+}] / [\text{Fe}^{4+}]$ ratio in samples is about unity, i.e., $[\text{Fe}^{3+}] \approx [\text{Fe}^{4+}]$; and since $[\text{Fe}^{3+}] = 2[\text{V}_{\text{O}}^{\cdot\cdot}]$, the thermodynamic factor is finally given by

$$w_{\text{O}} \approx \frac{5}{[\text{V}_{\text{O}}^{\cdot\cdot}]} c_{\text{O}}. \quad (2.10)$$

Inclusion of this result for w_{O} into Eq. (2.7), which with $\sigma_{\text{O}}^{\delta} \approx \sigma_{\text{V}_{\text{O}}}$ (since the electronic conductivity dominates under relevant conditions) brings about the final estimation of D_{O}^{δ} for slightly Fe-doped SrTiO_3

$$D_{\text{O}}^{\delta} \approx 5D_{\text{V}_{\text{O}}}, \quad \text{low } x \quad (2.11)$$

For high iron content, the defect chemistry is more complicated (e.g. appearance of defect associates) and not neatly analytically tractable. However, the empirically obtained relation showed that the oxygen chemical diffusion coefficient stays in the same order of magnitude for highly doped samples

$$D_{\text{O}}^{\delta} = \alpha D_{\text{V}_{\text{O}}}, \quad \text{high } x \quad (2.12)$$

where α is a weak function of iron concentration and is between 1 and 10, depending on the particular case [20]. With typical values of $D_{\text{V}_{\text{O}}}$ for similar perovskite systems (e.g. taken from Ref. [43]), and with the help of Eqs. (2.11) and (2.12), a time interval needed to equilibrate a 1 μm particle to external P_{O_2} can be estimated: $\tau < 1$ s at 300 °C, and $\tau \sim 1$ ms at 600 °C. These estimated values show that samples in experiments, described in Chapter 4, were indeed equilibrated with externally given P_{O_2} during the reactions.

2.5 Applications

Owing to their electrical and dielectric properties the alkaline earth titanate perovskites are generally used for construction of resistors, capacitors, actuators and sensors. SrTiO_3 is a material with high relative dielectric constant which makes it suitable for use in capacitors. Upon doping with iron, SrTiO_3 starts to show spin-glass behavior as a consequence of a competition between ferro- and antiferromagnetic exchange interactions [13]. At the same time this material becomes interesting for oxygen sensor applications, e.g. $\text{SrFe}_{0.3}\text{Ti}_{0.7}\text{O}_{3-\delta}$ has a negligible temperature dependence of the electrical resistivity in the temperature range of 700 °C to 1000 °C and in the P_{O_2} range between 10^{-4} and 1 bar [44]. Its oxygen sensing characteristic can be further improved by acceptor (Ga at B site) and donor (La at A site) doping [44]. A potential use of these materials for hydrocarbon sensing was investigated in the case of propane sensing [45]. The $\text{Sr}(\text{Fe}_x\text{Ti}_{1-x})\text{O}_{3-\delta}$ solid solutions are mixed conducting perovskites; they belong to the transition metal oxide class of materials which can serve as key materials in solid state fuel cells [46, 47], permeation membranes/reactors [48] and combustion catalysts [49, 50, 51, 52]. Solid oxide fuel cells (SOFC), permeation reactors and gas turbines have typically high working temperatures and therefore the use of noble metal catalysts in these devices/applications is not appropriate due to their high vapor pressures, the tendency to sinter at these temperatures and the price. One possible approach is the use of oxide-based catalysts such as the well known perovskites because they allow substitution on A and B sites, often to a very high degree, and therefore allow ‘tailoring’ of the defect chemistry, conductivity and other properties such as thermal expansion or chemical compatibility.

2.6 Short summary

From the previous discussion it can be seen that essentially all relevant physical properties of the $\text{Sr}(\text{Fe}_x\text{Ti}_{1-x})\text{O}_{3-\delta}$ solid solution series change continuously from those for SrTiO_3 towards the ones for SrFeO_3 with increasing iron content x . It is important to emphasize the change of the electronic structure: the energy bandgap monotonically decreases (almost linearly) from $E_g(x = 0) = 3.2$ eV to $E_g(x = 1) \approx 2$ eV [33]. The top of the valence band is gradually formed by covalent admixture of Fe $3d$ and O $2p$ with increasing x (since $\text{Fe}^{3+/4+}$ level lies close to the top of the O $2p$ band) and shifts closer to the bottom of the conduction band. In other words, the "electron poor" $\text{Sr}(\text{Fe}_x\text{Ti}_{1-x})\text{O}_{3-\delta}$ for low $x \leq 0.01$, becomes an "electron rich" material for higher iron contents x . In Chapters 3 and 4, the effect of the change of the electronic structure on the local structure around the Fe ions, as well as on catalytic activity, will be studied in detail. Also, with increasing iron content the concentration of ionic defects changes correspondingly; in particular, the concentration of oxygen vacancies increases with increasing x for a chosen degree of oxidation of $\text{Sr}(\text{Fe}_x\text{Ti}_{1-x})\text{O}_{3-\delta}$. The comparison of the catalytic activity of $\text{Sr}(\text{Sc}_x\text{Ti}_{1-x})\text{O}_3$ will allow one to separate the different effects of electronic structure and ionic defect concentration.

Chapter 3

Local structure investigation around Fe and Ti in $\text{Sr}(\text{Fe}_x\text{Ti}_{1-x})\text{O}_{3-\delta}$

In this chapter the general properties of the $\text{Sr}(\text{Fe}_x\text{Ti}_{1-x})\text{O}_{3-\delta}$ solid solution series, summarized in the previous chapter, will be specified (further broadened) by the results of the local structure investigations obtained from x-ray absorption spectroscopy (XAS) and vibrational (Raman and infrared) spectroscopy [21].

3.1 Introduction

Motivation for the investigation of the local structure of these materials was found in the facts (*i*) that their electronic properties, as discussed in Chapter 2, change drastically from isolated iron impurities hosted in a large band gap semiconductor (SrTiO_3) to the metallic but strongly correlated SrFeO_3 [53], and (*ii*) that a Jahn-Teller distortion around the dilute Fe^{4+} centers in $\text{Sr}(\text{Fe}_x\text{Ti}_{1-x})\text{O}_{3-\delta}$ ($x \approx 0.03$) was predicted by quantum chemical calculations [54], while it is known that the iron in SrFeO_3 has an undistorted octahedral coordination [53]. The transition between these limiting cases, as seen from XAS and vibrational spectroscopy, will be discussed in this chapter. Before delving into details, general notions and implications of the Jahn-Teller effect will be given briefly.

3.1.1 Jahn-Teller effect and its implications

According to the Jahn-Teller theorem [55], any non-linear molecule with a degenerate electronic ground state will undergo a distortion of its nuclear configuration to remove the degeneracy. Such a distortion is therefore called a Jahn-Teller distortion (JTD). This apparently simple statement has numerous important implications in the fields of solid-state physics and chemistry. For example, it influenced the discovery of high-temperature superconductivity through the Jahn-Teller polaron model (J. G. Bednorz and K. A. Müller, *The Nobel lecture*), and also colossal magnetoresistance¹ is explained by essential involvement of the JT effect

¹for its discovery the Nobel prize has been recently awarded to A. Fert and P. Grünberg

[56]. The JT effect exists in systems for which the Born-Oppenheimer approximation² is not valid, i.e., where a significant *vibronic* (vibrational-electronic) coupling between the ions and the trajectory of electrons occurs. For a particular system, the coupling of this kind is usually specified in more detail by indicating which representation of electronic states interacts with which vibrational modes, e.g. $E \otimes e$ means that a twofold orbital degenerate electronic state E interacts with doubly degenerate vibrational e modes³. In addition to the already mentioned examples, JT effects are suggested to be important for the prediction of specific reactivity, first reported for octahedral complexes of Cu(II) and other similar MX_6 systems with a JT $E \otimes e$ problem [56]⁴. The importance of these kind of couplings for the reactivity is illustrated by the quotation [56]

The occurrence of distorting forces and changes in the force constants and anharmonicity induced by electronic rearrangements via vibronic coupling directly explain the change in the reactivity of the molecule – its chemical activation.

3.1.2 Jahn-Teller distortion in $\text{Sr}(\text{Fe}_x\text{Ti}_{1-x})\text{O}_{3-\delta}$

In the quantum chemical calculations done by Evarestov *et al.*, [54] a JTD has been confirmed for dilute Fe^{4+} centers in SrTiO_3 . For dilute Fe^{4+} centers, this effect was not hard to anticipate on the grounds of a JT argument. As previously discussed, the Fe ions in $\text{Sr}(\text{Fe}_x\text{Ti}_{1-x})\text{O}_{3-\delta}$ (when not fully reduced) are, at least partly, in Fe^{4+} state. Their electronic configuration is therefore d^4 (high spin), which is further split into $t_{2g}^3 e_g^1$ configuration due to a crystal field imposed by octahedral coordination of iron in the host material, as shown on the left-hand side of Figure 3.1 (a). The e_g^1 is a doubly degenerate electronic state and, according to JT theorem, a JTD is expected in this case. A JTD due to a degeneracy in the e_g states of an impurity center (at the octahedral site) in transition metal oxides (TMO) is expected to be larger than those stemming from t_{2g} degeneracies [29]. However, the magnitude of the anticipated JTD in $\text{Sr}(\text{Fe}_x\text{Ti}_{1-x})\text{O}_{3-\delta}$ remained unknown and quantum chemical calculations were therefore needed. The Fe^{3+} ions present in $\text{Sr}(\text{Fe}_x\text{Ti}_{1-x})\text{O}_{3-\delta}$ have a high spin d^5 -electronic configuration which in octahedral coordination splits into an orbitally non-degenerate $t_{2g}^3 e_g^2$ configuration. No JTD is expected for these impurity centers.

Some details of the calculations by Evarestov *et al.* [54] shall be briefly mentioned. The JT effect in these systems belongs to the class of $E \otimes e$ problems. The resulting structure in this study was calculated for the initially imposed cubic structure at 0 K temperature⁵ in spite of the fact that SrTiO_3 has a tetragonal structure below 105 K, with slightly tilted TiO_6 octahedra. Nevertheless, the tetragonal structure is very close to a cubic structure [9, 10, 11].

²the Born-Oppenheimer (and the more sophisticated adiabatic) approximation assumes that motions of nuclei and electrons are separable [57].

³for more details the reader is referred to an in-depth study of provided by Ref. [56]

⁴and the reference therein

⁵as usual for various quantum chemical approaches, temperatures higher than 0 K are not (or hardly) accessible

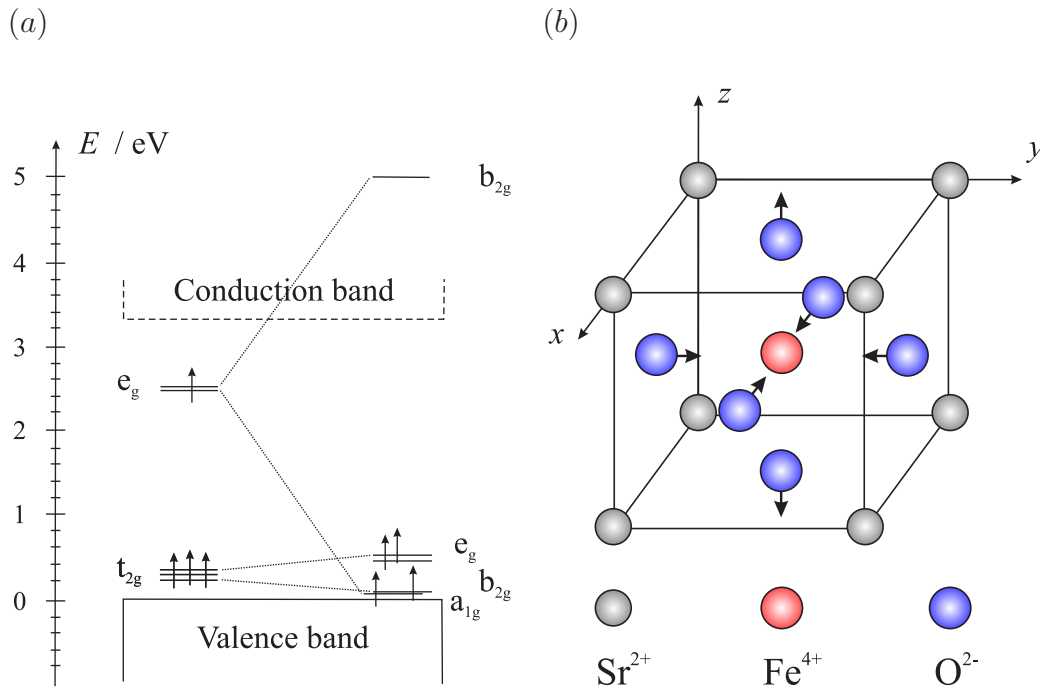


Figure 3.1: A JTD around dilute Fe^{4+} centers in $\text{Sr}(\text{Fe}_x\text{Ti}_{1-x})\text{O}_{3-\delta}$ predicted by quantum chemical calculations [54].

Although the c in tetragonal phase appears to be $c_{tetrag} \approx 2c_{cubic}$, no relative atom position was changed more than 10^{-4} . Since the calculated JTD is in a range of 10^{-2} this approach is fully acceptable. The predicted JTD is illustrated in Figure 3.1 (b): the four oxygen ions in $x - y$ plane are displaced towards the Fe^{4+} center by 0.028 \AA and the other two oxygen ions are displaced outwards by 0.052 \AA . The energy diagram of the stabilized structure is shown on the right-hand side of Figure 3.1 (a).

Another question still remained: at which iron content x (starting from low $x \approx 0$ and going to the limiting $x = 1$) does the JTD disappear? The answer to this question and the experimental confirmation of the calculated JTD were the motivation to perform XAS, Raman and infrared (IR) spectroscopy experiments on representative samples of the whole $\text{Sr}(\text{Fe}_x\text{Ti}_{1-x})\text{O}_{3-\delta}$ solid solution series. The predicted magnitude of the JTD was considered to be detectable by XAS which can be regarded as complementary to the XRD analysis. Electron spin resonance (ESR), although usually very useful for studying JT distortions, could not be applied in this case since the Fe^{4+} centers are not ‘visible’ for ESR.

3.2 Basic principles of XAS

Advances in the development of high-quality x-ray (synchrotron) sources in the last several decades has enabled the emergence of various experimental techniques based on the interaction of x-rays with matter⁶. The XAS technique is based on the x-ray absorption by a material,

⁶a review of these techniques can be found in Ref. [58]

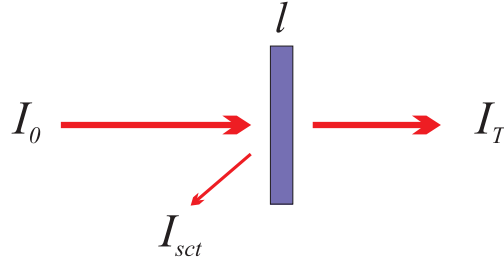


Figure 3.2: Basic principle of x-ray absorption: I_0 is the incident beam intensity

which is manifested in the attenuation of an incident beam intensity I_0 . This is shown schematically in Figure 3.2. After passing through a sample of thickness l , the resulting transmitted (detected) intensity I_T behind the sample is given by the equation

$$I_T(E) = I_0(E) e^{-\mu_{app}(E)l} \quad (3.1)$$

where $\mu_{app}(E)$ is the absorption coefficient of the sample dependent on the incident x-ray photon energy E . Due to (elastic and inelastic) scattering effects on the atoms in the sample, the true absorption coefficient $\mu(E)$ differs from the apparent $\mu_{app}(E)$, as the latter includes also a scattering part $\mu_{sct}(E)$. However, $\mu_{sct}(E)$ is only a weak function of E and is very small for thin samples, and can therefore be neglected in the following discussion. On the other hand, $\mu(E)$ depends strongly on energy⁷ and this dependency contains comprehensive information about the local environment of the absorbing atom. In order to approach the absorption process on the atomic level, the measured (macroscopic) $\mu(E)$ can be written as

$$\mu(E) = \left(\frac{\rho_m N_A}{A}\right) \sigma_a(E) \quad (3.2)$$

where ρ_m , N_A and A are the mass density, the Avogadro number and the atomic mass number, respectively, and $\sigma_a(E)$ is the absorption cross-section per atom. For samples containing different elements, the overall $\mu(E)$ can be decomposed into distinct contributions from each element σ_a^i . However, since different features in $\sigma_a^i(E)$ are usually well-separated in energies, one the σ_a^i dominates the others in the overall $\sigma_a(E)$ in a limited range of E . By choosing an energy window, a particular element whose σ_a^i dominates in this window can be selected for the absorption experiment, whereby its local structure can be selectively investigated⁸. Note that the pre-factor of $\sigma_a(E)$ in Eq. (3.2) explains how the overall absorption depends on the concentration of a particular element in the sample, e.g. on iron content x in the case of $\text{Sr}(\text{Fe}_x\text{Ti}_{1-x})\text{O}_{3-\delta}$.

In the case of absorption by an atomic gas, the atomic $\sigma_a(E)$ decreases slowly with increasing E , containing a set of abrupt jumps at the characteristic energies of the elements. These energies correspond to the energies of the atomic levels (with increasing energies, in the

⁷hence, there is a need for a stable and intense broad energy range x-ray source

⁸therefore XAS belongs to the group element selective measurement techniques

reverse order, K, L, M, \dots). This process can also be viewed as a kind of photoelectric effect, and the released electron is called the photoelectron.

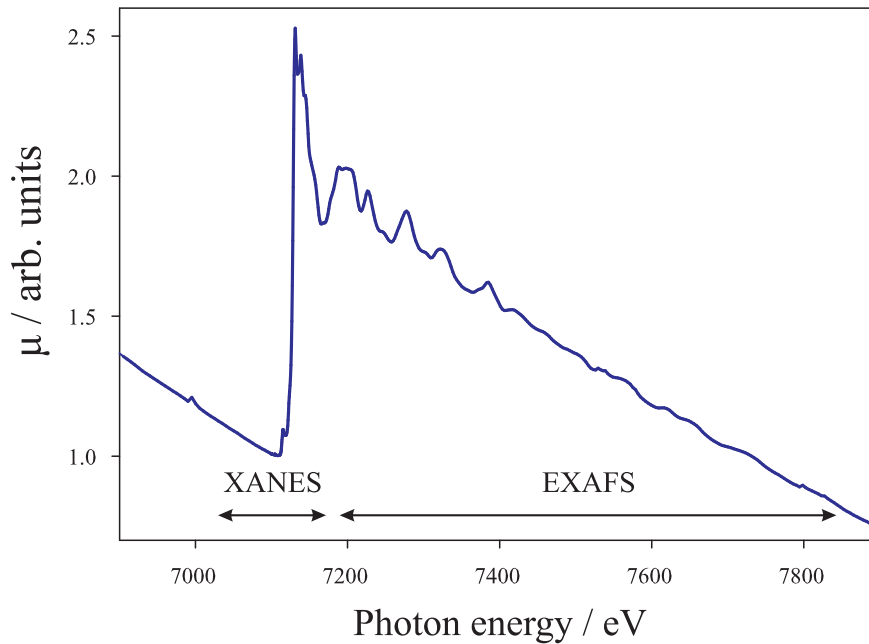


Figure 3.3: XANES and EXAFS regions

When the absorption occurs on an atom in a material (crystalline or amorphous), the photoelectron is being scattered in various ways by the neighboring atoms. The $\sigma_a(E)$ therefore contains additional information on the local environment of the absorbing atom in the form of fine oscillations which modulate the atomic-like $\sigma_a(E)$, Figure 3.3, usually starting from about 30 eV before the energy of the edge E_0 and extending up to 1 keV above the E_0 . The energy range around E_0 , approximately from $E_0 - 30$ eV to $E_0 + 40$ eV, belongs to the so-called x-ray absorption near edge structure (XANES) and the range above $\approx E_0 + 40$ eV is called extended x-ray absorption fine structure (EXAFS), Figure 3.3. This division is justified only by the different methods used to describe these two energy regions where absorption phenomena occur. The origin of these subtle features (and also of the pure atomic $\sigma_a(E)$) can theoretically be understood and described by quantum mechanical treatment of the interaction of the incident radiation with the atoms in the sample. Using time-dependent perturbation theory, the interaction is specified by a perturbation Hamiltonian \hat{H}_I which induces transitions between the initial state $|i\rangle$ (photon, core electron, no photoelectron) and the final state $\langle f|$ (no photon, core hole, photoelectron). In first-order perturbation theory, the transition⁹ probability (or frequency) is given by Fermi's golden rule as

$$P(E) = \frac{2\pi}{\hbar} |M_{if}|^2 \rho(E_f) \quad (3.3)$$

⁹each transition is one successful absorption

where the matrix element is given by $M_{if} = \langle f | \hat{H}_I | i \rangle$ and $\rho(E_f)$ is the density of the final states. Thus, $\sigma_a(E)$ is proportional to $P(E)$. Neglecting magnetic interactions and taking only the part of \hat{H}_I responsible for absorption, the matrix element becomes

$$M_{if} = \langle f | \frac{e}{m_e} \mathbf{p} \cdot \mathbf{A} | i \rangle \quad (3.4)$$

where \mathbf{p} is the momentum operator and $\mathbf{A}(\mathbf{r})$ is the vector potential of the incident electromagnetic field. Usually the spatial dependence of \mathbf{A} can be neglected for deep-core excitations, and the final form of the interaction Hamiltonian becomes $\hat{H}_I = (e/q_e) \mathbf{p} \hat{\epsilon}$ where $\hat{\epsilon}$ is the polarization vector of the incident radiation. This form is the so-called *dipole approximation*. In view of Eq. (3.3) the XANES region starts, with increasing E , with the appearance of electronic transitions from a core atomic orbital to unoccupied bound (final) states. The energy and density of the unoccupied states are determined by the material's electronic band structure, which is generally unknown and is a solid-state problem on its own. Apart from multiple scattering effects, these transitions are also very sensitive to the nature of chemical bonding of the absorbing atom. The theoretical treatment of these transitions involves complicated many-body interactions; indeed, the complete theory for absorption in the XANES range has not yet been fully developed, and one is usually limited to qualitative discussions of the phenomenon.

The EXAFS part of the spectrum is more readily theoretically tractable. In practice, the oscillating part $\chi(k)$ is extracted from the recorded $\mu_{\text{expt}}(E) \propto \sigma_a(E)$ using the following equation

$$\chi(k) = \frac{\mu_{\text{expt}}(E) - \mu_0(E) - \mu_b(E)}{\mu_0(E)} \quad (3.5)$$

where $\mu_b(E)$ is the pre-edge background extrapolated beyond the absorption edge, $\mu_0(E)$ is the atomic-like contribution, and $k = [(2m_e/\hbar^2)(E - E_0)]^{1/2}$ is the wave vector of the photoelectron, with E_0 being the photoelectron energy origin. It can be shown that $\chi(k)$ arises from the modification of the free atom final state $\langle f_0 |$ due to neighboring atoms which is then described by $\langle f_0 + \Delta f |$, (i.e., due to *back scattering* of the photoelectron off the neighboring atoms) [58]

$$\chi(k) \propto \langle \Delta f | \hat{H}_I | i \rangle \quad (3.6)$$

Further, it can be shown that the EXAFS $\chi(k)$ signal resulting from absorption by a system comprising an absorbing atom and a set of nearest neighbors (first coordination shell) can be accurately described in the single-scattering curved-wave cumulant approximation as [59]

$$\chi(k) = S_0^2 \frac{N_i}{k R_i^2} F_i(k, R_i) e^{-2\sigma_i^2 k^2 + \frac{2}{3} C_{4i} k^4} \sin[2k R_i - \frac{4}{3} C_{3i} k^3 + \Phi_i(k, R_i)] \quad (3.7)$$

where the index i denotes the coordination shell (e.g. $i = 1$ for the first coordination shell), N_i is the number of atoms inside the shell i.e., $N_1 = \text{CN}$, R_i is the average distance between the absorbing atom and its neighbors, S_0^2 is the scale factor which accounts for amplitude damping due to multi-electron processes (depends mainly on the absorbing atom), $F_i(k, R_i)$

is the backscattering amplitude, $\Phi_i(k, R_i)$ is the phase shift, σ_i^2 is the mean square relative displacement (MSRD) corresponding to the thermal Debye-Waller factor in the absence of static distortions, and C_{3i} and C_{4i} are the higher order cumulants of the distance distribution. $F_i(k, R_i)$ describes the probability that the photoelectron will be backscattered from a neighboring atom to the absorbing atom, and $\Phi_i(k, R_i)$ is the phase shift experienced by the photoelectron. $F_i(k, R_i)$ and $\Phi_i(k, R_i)$ are generally unknown functions of atom pairs (e.g. Fe–O and Ti–O), and must therefore be calculated. If they are calculated using a complex exchange and correlation potential (e.g. of a Hedin-Lundquist type), a factor describing the photoelectron mean free path is included in the backscattering amplitude, and is therefore omitted in Eq. (3.7). Thus, it can be seen that $\chi(k)$ is determined by the local structure through Eq. (3.7). Similarly, contributions of higher coordination shells can be included, and the summation over all considered shells will appear in Eq. (3.7).

Examples of Fe K -edge $\chi(k)$ measured on $\text{SrFe}_x^{4+}\text{Ti}_{1-x}\text{O}_3$ samples are given in Figure 3.4 (a), where as the standard procedure, the extracted $\chi(k)$ were weighted by k^2 in order to compensate for amplitude attenuation at high k values. A measured $\chi(k)$ naturally contains

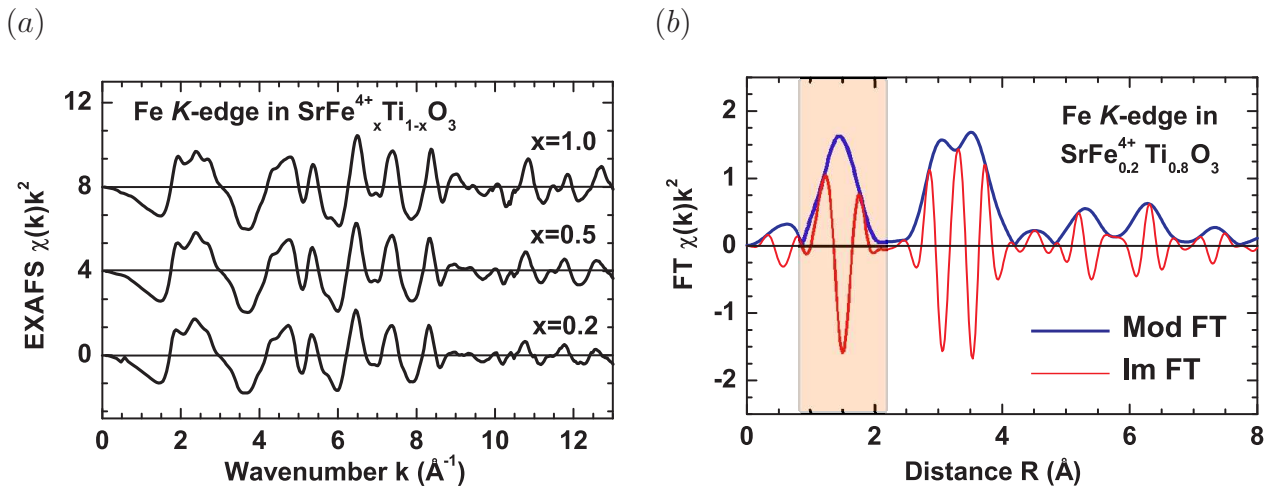


Figure 3.4:

contributions of all shells (as well as contributions from multiple scattering processes) which can be seen in Fourier transform (FT) of $\chi(k)k^2$, Figure 3.4 (b). Visually, the FT only gives an approximate idea about the distribution of neighboring atoms in real space, and so the observed features must not be taken as true distances. The part which corresponds to the first coordination shell (shaded region) has no contribution from multiple-scattering effects, which is not the case at higher R values. In order to extract the information about the first coordination shell, the FT $\chi(k)k^2$ is multiplied by a window function, and Back-Fourier transformed (BFT) to get the filtered first shell $\chi^{1sh}(k)$. The procedure is called a Fourier filtering. By a fitting procedure (e.g. a non-linear least-squares fitting procedure) of Eq. (3.7) to $\chi^{1sh}(k)$, all featuring parameters of the equation can be estimated. In depth details about XAS theory and practice can be found in Refs. [58, 59, 60] (and in the references therein).

3.3 Experimental details

The powder samples for XAS, Raman and IR measurements were prepared by the procedure described in Section 4.3.1. The results from XRD are given in Chapter 2.

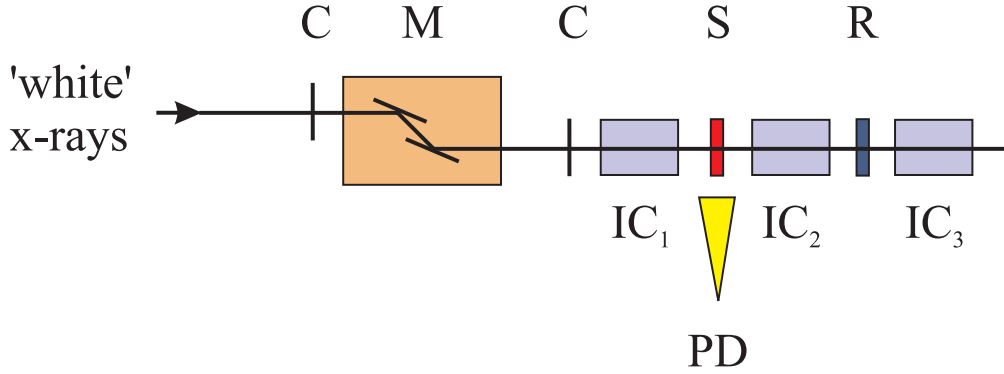


Figure 3.5: A simplified XAS setup.

3.3.1 Principle of XAS measurement and details

The XAS spectra were recorded at the ESRF BM29 beam line (Grenoble, France): oxidized $\text{SrFe}^{4+}\text{Ti}_{1-x}\text{O}_3$ samples were measured both at Fe and Ti K edges, and reduced $\text{SrFe}^{3+}\text{Ti}_{1-x}\text{O}_{3-x/2}$ samples only at Fe K edge.

A simplified sketch of the experimental setup is given in Figure 3.5, more details about the setup can be found in Ref. [61]. In a synchrotron *white*¹⁰ x-rays are generated by electrons cycling in a storage ring. For the XAS performed at ESRF the storage ring energy and average current were 6.0 GeV and 200 mA, respectively. The generated x-rays enter the beam line, and pass through the first slit C (for beam collimation) into a double crystal monochromator M. The harmonic rejection, with rejection level better than 10^{-5} , is achieved using a double reflection on a pair of Si mirrors with grazing incidence of 3 mrad and 5 mrad for Fe and Ti K edge, respectively. The energy resolution $\Delta E/E$ was about $2 \cdot 10^{-4}$. The beam intensity can be measured at three different positions by ionization chambers filled with nitrogen: IC₁ measures I_0 before the sample S, IC₂ measures I_T after S, and IC₃ measures intensity I_R after the reference sample. I_R is used for energy calibration. I_0 and I_T were measured with a rate of 1-4 s per point, and $\mu(E)$ was directly recorded as $\mu(E) = \ln(I_0/I_T)/l$, [see Eq. (3.1)]. This configuration of measurement is called a *transmission mode* experiment. For measurement in transmission mode it is important that powder samples are carefully prepared in the form of a uniform thin layer but without any pin holes. The powder samples were deposited on Milipore filters and fixed by Kapton tape. The obtained sample thickness corresponded to an absorption jump $\Delta\mu_x = 0.12 - 0.72$ at the Fe K -edge and $0.31 - 1.0$ at the Ti K -edge,

¹⁰polychromatic

depending on the composition. For poorly absorbing samples the *fluorescence mode*¹¹ is better suited, the difference being in the signal acquisition by a photo-detector PD (a 13-element Ge solid state detector). In this case the fluorescence I_F intensity was measured a rate of 4 s per point. For fluorescence mode, the absorption coefficient is obtained as $\mu(E) \sim I_F/I_0$. The setup is also equipped for low temperature measurements with a closed-loop liquid helium cryostat with a heating resistor. The temperature during each measurement was stabilized within 2 K. Low temperature XAS measurements were performed in the range from 20 to 350 K.

3.3.2 XAS data analysis

Data analysis was based on the EDA software package [62]. Some of the results were checked with the FEFFIT 2.55 code [63], and a good agreement was found.

XANES

The XANES region at the Fe(Ti) K edge was separated from the total x-ray absorption coefficient by subtracting the pre-edge background and normalizing the absorption coefficient around 100 eV above the edge (Figures 3.7 and 3.8). The XANES signals at both edges consist of the clearly visible pre-edge peak(s), the main absorption edge, and the fine structure above it. No calculations were done, and XANES features were only qualitatively analyzed.

EXAFS

The required backscattering amplitude $F_i(k, R_i)$ and phase shift $\Phi_i(k, R_i)$ functions for the Fe–O and Ti–O atom pairs were calculated with the FEFF8 code using the complex exchange-correlation Hedin-Lundqvist potential [64, 65]. The calculations were performed for a cluster with radius of 8 Å having the structure of cubic $\text{SrFeO}_3(\text{SrTiO}_3)$ and centered at the Fe(Ti) atom, respectively. Calculations of the cluster potentials were done in the *muffin-tin* (MT) self-consistent-field approximation using default values of MT radii as provided within the FEFF8 code [64]. The Fe(Ti) K -edge EXAFS signals $\chi(k)$ were extracted according Eq. (3.5). The choice of correct E_0 value is important, since it affects the amplitude and the phase of the EXAFS signal, especially at low k values, and therefore restricts the accuracy of interatomic distance determination. The best results were achieved when the E_0 position in the experimental signal under study was set in the same way as for the reference signal, which can be either another experimental signal, measured for the reference compound with known crystallographic structure, or a theoretically calculated signal by one of the available *ab initio* codes [64, 66, 67]. In this work, the FEFF8 code [64] was used for generating the reference signal, and the E_0 position was set at 7117.0 eV for Fe^{4+} , 7116.5 eV for Fe^{3+} and 4971.0 eV for Ti^{4+} . The FEFF8 code was also used for the interpretation of peaks in Fourier transforms as in previous works [68, 69]. The FT were calculated in the k -space range from

¹¹which accompanies successful absorption due to relaxation processes of the core hole

0.5 to 15 \AA^{-1} (or less when limited by the signal quality) using the Kaiser-Bessel window function with parameter $A = 2$ as implemented in Ref. [62]. Note that due to the presence of the scattering phase shifts, the positions of peaks in the FTs generally differ from the true values. The first coordination shell around the iron and titanium atoms was isolated by BFT (typically in the range from 0.8 to 2.1 \AA) and analyzed by the best-fit procedure using the model described below. The fit procedure was performed in k -space using, typically, the range from 2 to 12 \AA^{-1} . However, for a few reduced samples the range was shortened to $k=2-8 \text{\AA}^{-1}$ due to poor signal quality at high k -values. The value of the amplitude reduction factor S_0^2 due to many-body effects was estimated to be 0.67 for both Fe and Ti K edges, based on the known coordination numbers of end members SrTiO_3 and SrFeO_3 . This value of S_0^2 is close to 0.69 found for $\text{SrFe}_x\text{Sn}_{1-x}\text{O}_{3-y}$ in Ref. [70] and which is also given in Ref. [59] for Fe as the absorbing atom. The distances determined in the fitting procedure were brought in accord with the distances known from XRD data for SrTiO_3 and SrFeO_3 (Ti and Fe K edges, respectively) by a constant shift of 0.02 \AA (see Figure 3.13). The error bars were estimated based on the largest data scatter appearing in the course of the analysis.

3.3.3 Raman and IR measurements

Raman spectra were recorded on powder samples at room temperature with a Jobin-Yvon LABRAM V010 spectrometer (single monochromator equipped with a Notch filter and charge coupled device camera) in backscattering geometry with excitation wavelengths of 632.8 and 784.7 nm and a power of 4 mW. Low temperature Raman spectra were recorded on slightly compacted powder samples with a Dilor-XY triple monochromator spectrometer using a CCD camera in backscattering geometry at an excitation wavelength of 514.5 nm and a power of 10 mW. Infrared spectra (IR) were measured at room temperature in diffuse reflection mode on KBr diluted powder samples (3 mg in 400 mg KBr) with a Bruker IFS 66 spectrometer. The measured reflectivity R was transformed into the Kubelka-Munk function $KM = (1 - R)^2/2R$ which is proportional to the absorption coefficient.

3.4 Results

3.4.1 XANES

The XANES signals at the Fe and Ti K -edges in $\text{Sr}(\text{Fe}_x\text{Ti}_{1-x})\text{O}_{3-\delta}$ samples reveal qualitative similarity, but although iron and titanium occupy the same crystallographic site and have similar scattering amplitudes they differ in details. In Figure 3.6, Fe and Ti K -edge XANES of oxidized $\text{Sr}(\text{Fe}_{0.75}\text{Ti}_{0.25})\text{O}_3$ are given for illustration. The spectra were aligned relative to the absorption threshold, and as seen in the figure, a good correspondence between the main absorption maxima located at 18 eV is observed. The main features at higher energies, determined by the frequency of the EXAFS oscillations, are in close correspondence indicating the expected similarity of the local structure around Ti and Fe. However, in contrast to the Ti

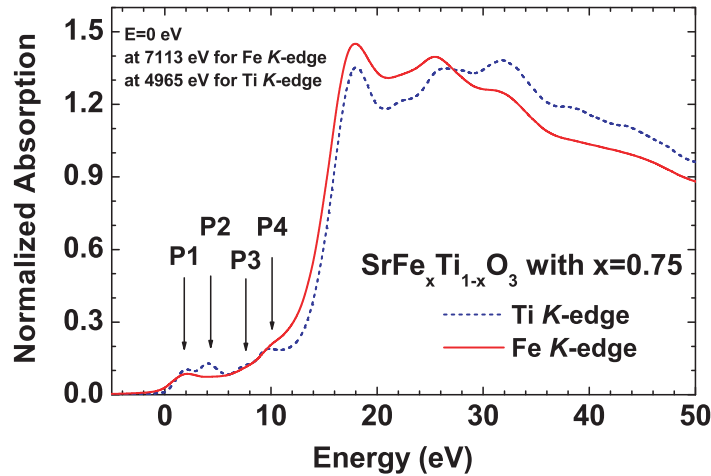


Figure 3.6: Comparison of the Ti and Fe K -edge XANES signals in the oxidized $\text{Sr}(\text{Fe}_x\text{Ti}_{1-x})\text{O}_3$ ($x = 0.75$) sample. The energy scale of two spectra was aligned relative to the absorption threshold.

K edge, the pre-edge structures at the Fe K edge are less resolved. A group of four pre-edge

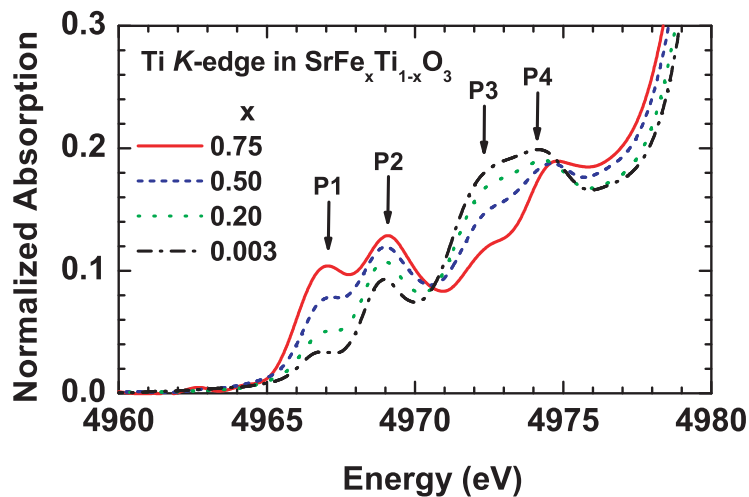


Figure 3.7: Ti K -edge XANES signals in oxidized $\text{Sr}(\text{Fe}_x\text{Ti}_{1-x})\text{O}_3$ samples at room temperature (enlarged pre-edge Ti K -edge XANES region).

peaks is observed at the Ti K edge (Figure 3.7), whereas a single broad peak is visible at the Fe K edge (Figure 3.8; the edge region of Fe_2O_3 is shown for comparison). Two effects should be noted: (i) the intensity of the pre-edge peaks varies with composition, see section 3.5; (ii) for the Fe K -edge, the pre-edge peak intensity is slightly higher in reduced samples for the same composition, and there is an energy difference of about 0.5 eV between the edges of the first pre-edge peaks in oxidized and reduced samples. The reason for this small shift is the large covalency of the $\text{Fe}^{4+}-\text{O}^{2-}$ bonds (corresponding to a heavy admixture of the $d^5\bar{L}$ states; \bar{L} means a hole in oxygen $2p$ orbitals) which reduces the charge on Fe^{4+} [71, 72]. Note also that the edge energy position (7113 eV) of the first pre-edge peak for reduced samples is in

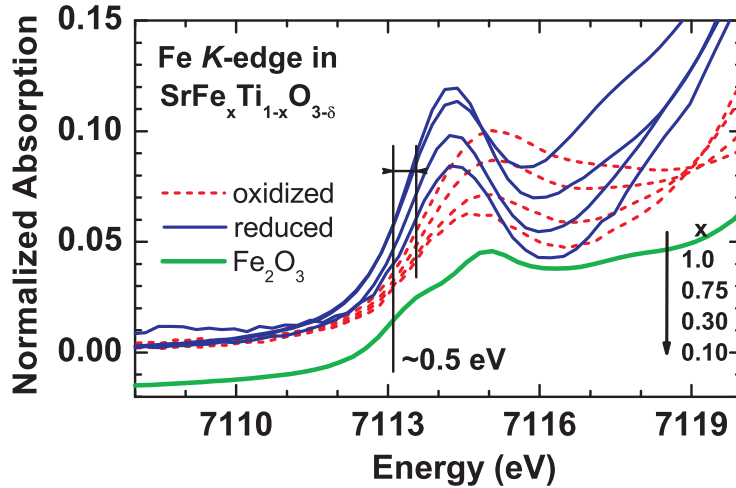


Figure 3.8: Fe K -edge XANES signals in oxidized (dashed curves) and reduced (solid curves) $\text{Sr}(\text{Fe}_x\text{Ti}_{1-x})\text{O}_{3-\delta}$ ($\delta = x/2$) samples at room temperature (enlarged pre-edge Fe K -edge XANES region). The curve for $\alpha\text{-Fe}_2\text{O}_3$ is shifted downwards by -0.02 for clarity.

good agreement with that for Fe_2O_3 , having all iron ions in 3+ valence state. A correlation between the variations of the pre-peaks and the local environment around Fe/Ti ions will be discussed to some extent in Section 3.5.

3.4.2 EXAFS

The experimental Fe and Ti K -edge EXAFS signals $\chi(k)k^2$ and their FTs of oxidized and reduced $\text{Sr}(\text{Fe}_x\text{Ti}_{1-x})\text{O}_{3-\delta}$ samples are shown in Figures 3.9-3.11. Note that all obtained EXAFS $\chi(k)k^2$ signals have a very good signal-to-noise ratio up to 12 \AA^{-1} . The FTs of the EXAFS signals are typical for the perovskite-type structure [68] and exhibit a number of well resolved peaks up to 8 \AA . In this work, the emphasis is laid mainly on the analysis of the first peak at about 1.5 \AA , which is clearly isolated and corresponds to the first coordination shell of Fe(Ti) atoms. In ‘stoichiometric’ i.e., fully oxidized $\text{Sr}(\text{Fe}_x^{4+}\text{Ti}_{1-x})\text{O}_3$, the first shell is composed of six oxygen atoms, whereas some decrease of the coordination number can be expected in reduced samples due to the presence of oxygen vacancies.

The analysis of peaks beyond the first one is a more demanding task due to the overlap of contributions from outer coordination shells and additional complications caused by strong multiple-scattering effects, mainly in linear atomic chains such as B–O–B and O–B–O (B = Fe or Ti) [68]. However, based on qualitative comparison of FTs one can draw some conclusions. In cubic perovskite-type compounds the amplitude of the peak corresponding to the second coordination shell (the peak at 3.5 \AA in Figures 3.9 and 3.11) depends strongly on the bond angle B–O–B between two BO_6 octahedra [68, 73]. In oxidized cubic $\text{Sr}(\text{Fe}_x^{4+}\text{Ti}_{1-x})\text{O}_3$ this peak is strong at both Fe and Ti K -edges, being comparable in amplitude with the first shell peak at 1.5 \AA , and varies slightly with composition due to the lattice parameter variation. At

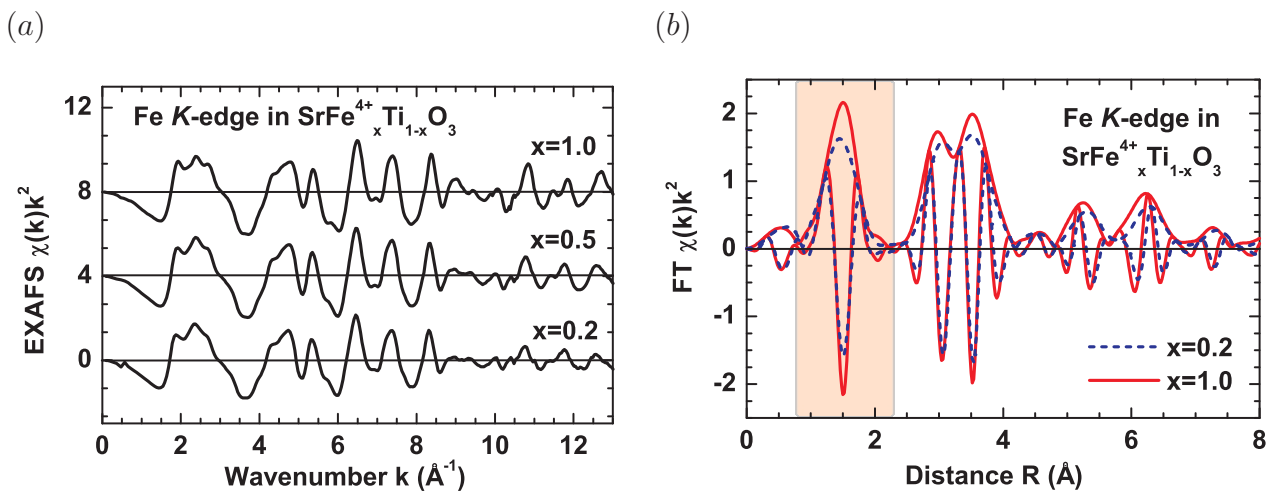


Figure 3.9: (a) Iron concentration dependence of experimental Fe K -edge EXAFS signals $\chi(k)k^2$, and (b) their Fourier transforms in fully oxidized $\text{Sr}(\text{Fe}_x^{4+}\text{Ti}_{1-x})\text{O}_3$ samples at room temperature. Only a representative selection of spectra are shown for clarity.

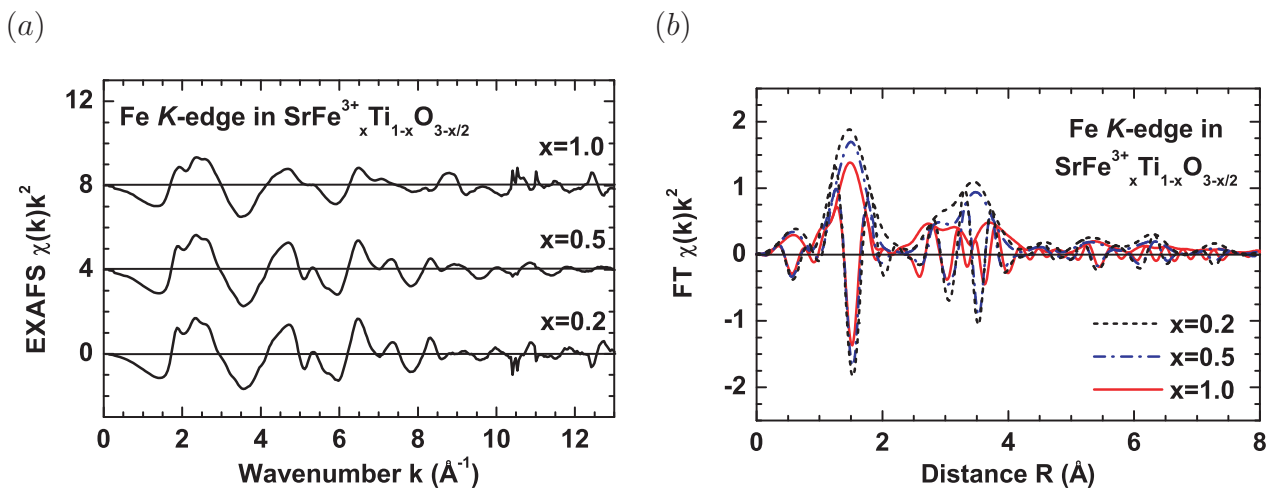


Figure 3.10: (a) Concentration dependence of experimental Fe K -edge EXAFS signals $\chi(k)k^2$, and (b) their Fourier transforms in fully reduced $\text{Sr}(\text{Fe}_x^{3+}\text{Ti}_{1-x})\text{O}_{3-x/2}$ samples at room temperature. Only a representative selection of spectra are shown for clarity. Note that the sample with $x=1$ has brownmillerite structure.

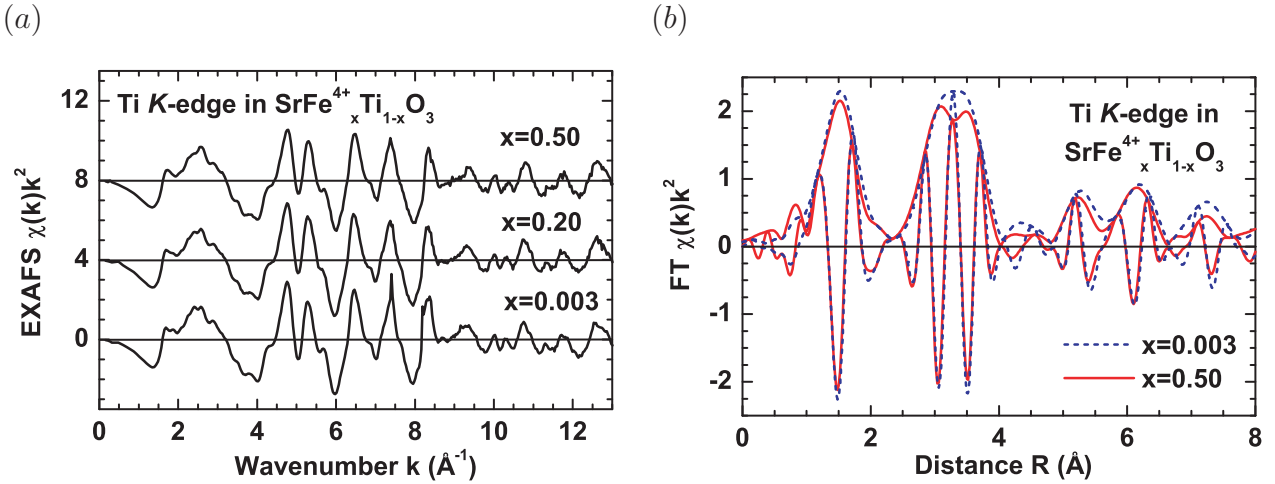


Figure 3.11: (a) Concentration dependence of experimental Ti K -edge EXAFS signals $\chi(k)k^2$, and (b) their Fourier transforms in fully oxidized $\text{Sr}(\text{Fe}_x^{4+}\text{Ti}_{1-x})\text{O}_3$ samples at room temperature. Only a representative selection of spectra are shown for clarity.

the same time, the amplitude of the peak at 3.5 \AA in reduced $\text{Sr}(\text{Fe}_x^{3+}\text{Ti}_{1-x})\text{O}_{3-x/2}$ is smaller than that for the first shell by nearly a factor of $1/2$. Such a behavior usually indicates a deviation of the B–O–B angles from linear configuration due to rotations of BO_6 octahedra or off-center displacement of metal ions. Similar effects have been observed in many perovskite-type compounds, e.g. in tungsten oxides [74] upon a change of stoichiometry or in ReO_3 [75] upon pressure variation. Another possible explanation can be a strong increase of the static or thermal disorder, as has been observed in ReO_3 upon heating [69]. Note that the peaks due to outer shells in reduced $\text{Sr}(\text{Fe}_x^{3+}\text{Ti}_{1-x})\text{O}_{3-x/2}$, located at distances above 4 \AA in Figure 3.10, have also much smaller amplitudes than analogous peaks in oxidized $\text{Sr}(\text{Fe}_x^{4+}\text{Ti}_{1-x})\text{O}_3$ (Figures 3.9 and 3.11). This suggests the presence of long non-linear chains B–O–B–O–B in reduced samples, and thus a possible deviation of their local structure from cubic symmetry due to the presence of oxygen vacancies.

The results of the fitting of the first B–O coordination shell are shown in Figures 3.12-3.14. In the stoichiometric perovskite structure, the coordination number of oxygen (Figure 3.12) around the Fe as well as the Ti cation is 6 for the fully oxidized samples. This fact was used as the reference point to determine the values of S_0^2 mentioned in Section 3.3.2. Using these values, a decrease of the coordination number around Fe^{3+} is observed for the completely reduced samples having large iron concentrations, while the large error bars at low x (due to the increased noise in the spectra) do not allow an unambiguous conclusion for the low doped samples. The electroneutrality condition requires the oxygen vacancy concentration to be equal to half of the Fe^{3+} concentration. In dilute systems with isolated Fe ions, this means that even if the electrostatic attraction of the oppositely charged defects is strong, only half of the Fe^{3+} can have a V_O in the first coordination shell. For $x \leq 0.003$, electron paramagnetic resonance measurements show that the tendency for a V_O to be located in the first coordination shell of Fe^{3+} (Fe'_{Ti}) [12] decreases with increasing iron content [76]. For large

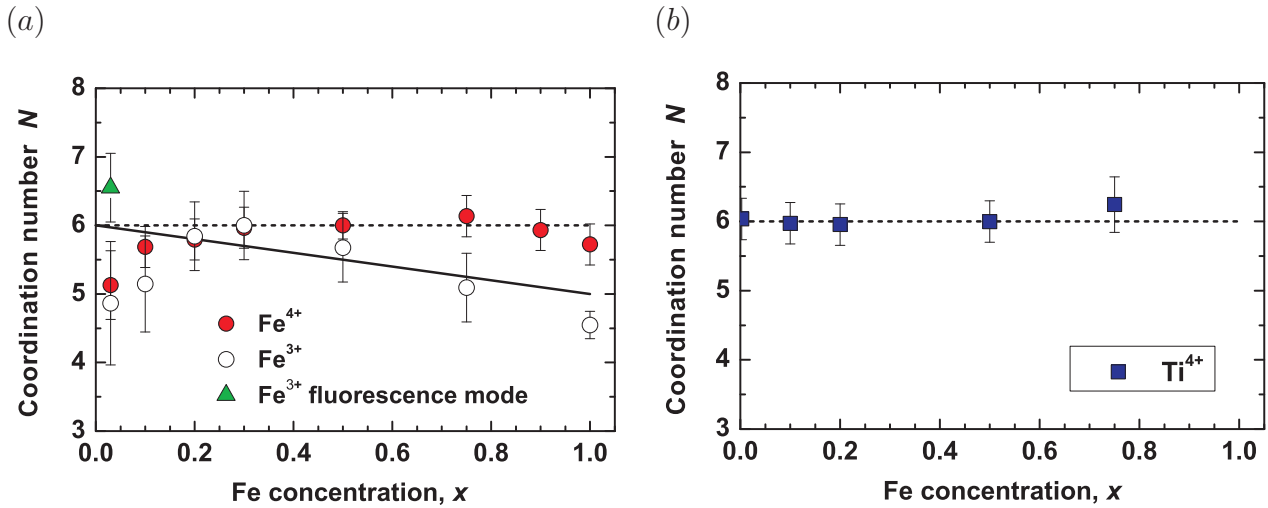


Figure 3.12: Concentration dependence of the first coordination shell CNs around: (a) Fe^{4+} ($\text{Sr}(\text{Fe}_x^{4+}\text{Ti}_{1-x})\text{O}_3$ oxidized samples) and Fe^{3+} ($\text{Sr}(\text{Fe}_x^{3+}\text{Ti}_{1-x})\text{O}_{3-x/2}$ reduced samples), and (b) Ti^{4+} ($\text{Sr}(\text{Fe}_x^{4+}\text{Ti}_{1-x})\text{O}_3$ oxidized samples); all at room temperature. Dashed lines correspond to the octahedral coordination of the $\text{Fe}^{4+}(\text{Ti}^{4+})$ ions in the stoichiometric perovskite. Solid line indicates the expected coordination for Fe^{3+} ions in the presence of oxygen vacancies.

x , $\text{Fe}'_{\text{Ti}}-\text{V}_{\text{O}}$ pairs are unavoidable if Fe and Ti are randomly distributed (there is no evidence for an Fe/Ti ordering): for $x = 0.5$, 0.25 oxygens per B cation are missing, and since each belongs to two octahedra, in every second octahedron an oxide ion is absent. This leads to expected coordination numbers for Fe^{3+} of 5.5 ($x = 0.5$) and 5.25 ($x = 0.75$) which agree with the experimental findings within the error bars (a distribution of the V_{O} between octahedrally and fourfold coordinated Fe^{3+} as concluded from Mössbauer spectra would result in the same averaged coordination numbers, e.g., see Refs. [77, 78]). The deviation observed for $x=1$ from the value of 5 expected for the brownmillerite structure is likely due to experimental errors. The coordination number of O around Ti is also expected to fall below 6 for the reduced samples with large x ; unfortunately these measurements are missing because of limited beam time.

Figure 3.13 shows the average (Fe,Ti)–O distances determined from XRD (half value of the lattice constant) and EXAFS (local Fe–O and Ti–O distances). From the Shannon ionic radii (Table 2.1) the substitution of Ti^{4+} ($r = 0.605 \text{ \AA}$ in octahedral coordination) by Fe^{3+} ($r = 0.645 \text{ \AA}$) is expected to increase the lattice constant, whereas Fe^{4+} ($r = 0.585 \text{ \AA}$) should decrease it. As Figure 3.13 shows, these general trends are indeed observed in the XRD data. The lattice parameter remains constant for $x \leq 0.15$ and then decreases linearly with increasing x . This deviation from Vegard's law can be rationalized as follows: The Ti^{4+} in SrTiO_3 is slightly too small for its octahedral site (the Goldschmidt tolerance factor $t = (r_{\text{A}} + r_{\text{O}})/[\sqrt{2} \cdot (r_{\text{B}} + r_{\text{O}})] = 1.002$ is larger than unity; the facile displacement of Ti^{4+} inside the O_6 octahedron gives rise to the high relative dielectric constant $\epsilon_r \approx 300$ at room temperature). Therefore, the lattice parameter is determined essentially by close packing of the Sr^{2+} and O^{2-} ions. Substituting Ti^{4+} by the smaller Fe^{4+} can decrease the lattice parameter

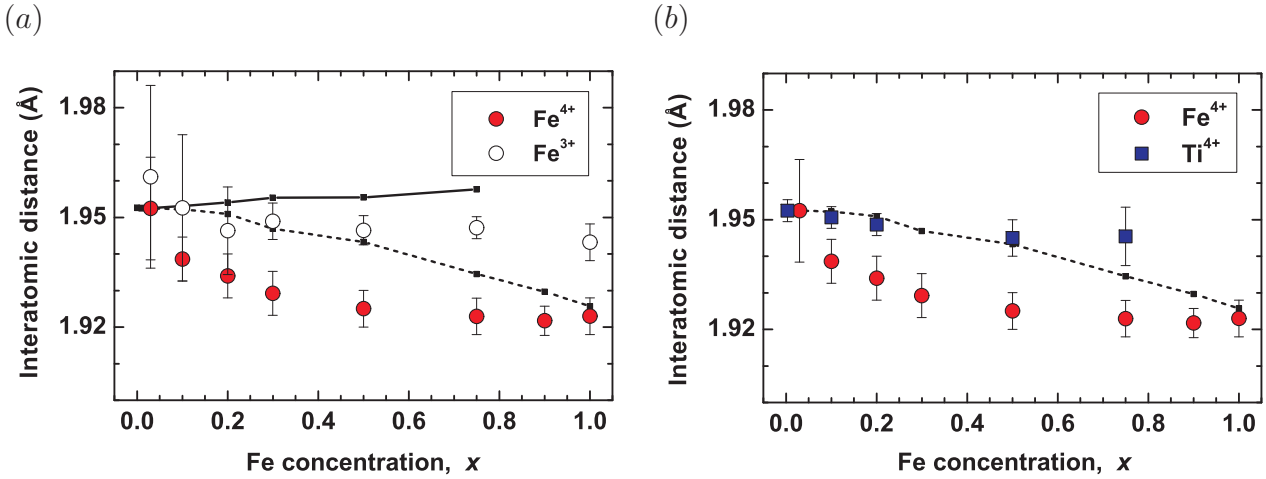


Figure 3.13: (a) Concentration dependence of the $\text{Fe}^{4+}\text{-O}^{2-}$ [$\text{Sr}(\text{Fe}_x^{4+}\text{Ti}_{1-x})\text{O}_3$ oxidized samples] and $\text{Fe}^{3+}\text{-O}^{2-}$ [$\text{Sr}(\text{Fe}_x^{3+}\text{Ti}_{1-x})\text{O}_{3-x/2}$ reduced samples]; and (b) $\text{Fe}^{4+}\text{-O}^{2-}$ and $\text{Ti}^{4+}\text{-O}^{2-}$ [$\text{Sr}(\text{Fe}_x^{4+}\text{Ti}_{1-x})\text{O}_3$ oxidized samples]. Distances correspond to the first coordination shell, all at room temperature. The half values of the lattice constants obtained by XRD are shown for comparison: dashed curve for oxidized and solid curve for reduced samples.

only indirectly, i.e., by withdrawing electron density from the O^{2-} ions which reduces their size. Obviously this occurs only for $x \geq 0.15$.

The local distances determined by EXAFS analysis exhibit a more detailed picture with different Ti–O and Fe–O distances for the same sample. For the oxidized samples, the Ti–O distance remains essentially constant, at about 1.95 Å (the same as in SrTiO_3), while the Fe–O distances stay close to that in SrFeO_3 (1.92 Å) for large x and increase only for $x \leq 0.3$. The composition variation of the Fe(Ti)–O distances, determined by EXAFS, deviates from the half values of the lattice constants obtained by XRD (Figure 3.13). Although the ‘fully oxidized’ samples still contain a minor oxygen deficiency (see Table 2.2), the small fraction of Fe^{3+} is not sufficient to explain the increasing Fe–O distances just by averaging constant contributions from $\text{Fe}^{4+}\text{-O}$ and $\text{Fe}^{3+}\text{-O}$ (e.g., for $x = 0.1$, about half of the Fe would have to be Fe^{3+} to yield the observed Fe–O distance). For the reduced samples, we found nearly constant Fe–O distances of about 1.95 Å, which is slightly shorter at high iron content than the half values of the lattice constants obtained by XRD (Figure 3.13) (no Ti EXAFS data are available for these samples). Individual local EXAFS distances different from the averaged XRD value were also observed in other solid solution series, e.g. in $\text{Ca}(\text{Zr}_x\text{Ti}_{1-x})\text{O}_3$ ($0 \leq x \leq 1$, samples calcined at 1200 °C) [79] or $(\text{Fe}_x\text{Mn}_{1-x})\text{Nb}_2\text{O}_6$ ($0 \leq x \leq 1$) [80].

Figure 3.14 shows MSRDS at room temperature for $\text{Fe}^{4+}\text{-O}^{2-}$, $\text{Fe}^{3+}\text{-O}^{2-}$ and $\text{Ti}^{4+}\text{-O}^{2-}$ bonds (note that the EXAFS MSRDS models the disorder in the B–O bond length, while the Debye-Waller factor used in XRD describes the disorder of an atom around its equilibrium lattice position). The MSRDS of $\text{Fe}^{3+}\text{-O}^{2-}$ (reduced samples) is to good approximation independent of the iron concentration. The same behavior is observed for the MSRDS of $\text{Ti}^{4+}\text{-O}^{2-}$ (oxidized samples). Most interestingly, the MSRDS of $\text{Fe}^{4+}\text{-O}^{2-}$ exhibits a strong decrease with an increase of iron concentration, such that it is larger than the $\text{Fe}^{3+}\text{-O}^{2-}$ MSRDS for small

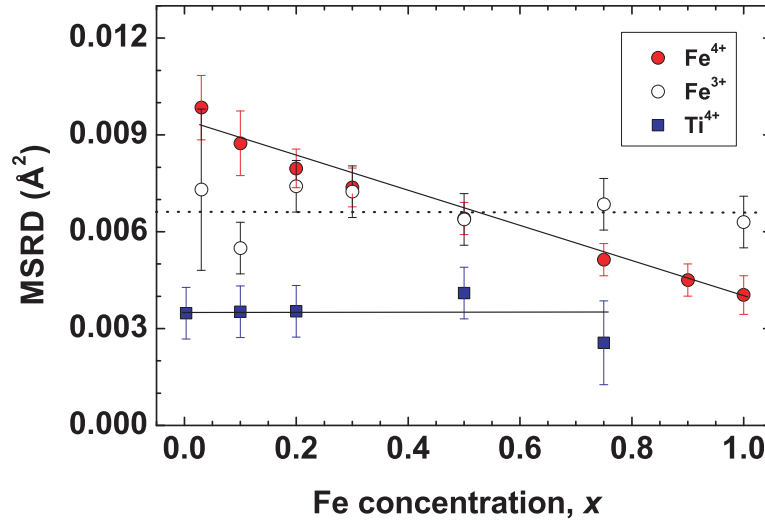


Figure 3.14: Concentration dependence of the mean square relative displacement (MSRD) for Fe^{4+} -O and Ti^{4+} -O bonds [$\text{Sr}(\text{Fe}_x^{4+}\text{Ti}_{1-x})\text{O}_3$ oxidized samples], and Fe^{3+} -O bonds [$\text{Sr}(\text{Fe}_x^{3+}\text{Ti}_{1-x})\text{O}_{3-x/2}$ reduced samples] in the first coordination shell, all at room temperature. Dotted lines are guides for the eye.

x , lower than that for large x , and finally in SrFeO_3 achieving about the same value as the Ti^{4+} - O^{2-} MSRD in all samples. A $x = 0.75$ sample prepared with deliberately incomplete oxidation ($\text{SrFe}_{0.75}\text{Ti}_{0.25}\text{O}_{2.906}$ instead of $\text{SrFe}_{0.75}\text{Ti}_{0.25}\text{O}_3$) has a MSRD slightly below that of the reduced sample. This demonstrates that the mixed valence of the Fe does not increase the Fe-O MSRD above the value of the reduced samples. In the above mentioned EXAFS studies of $\text{Ca}(\text{Zr}_x\text{Ti}_{1-x})\text{O}_3$ [79] and $(\text{Fe}_x\text{Mn}_{1-x})\text{Nb}_2\text{O}_6$ [80], the Ti-O and Zr-O MSRDs [79] and the Fe-O and Mn-O MSRDs remain essentially constant throughout the whole solid solution series [80].

The temperature dependence of the Fe-O MSRD of some samples is shown in Figure 3.15. As expected, the MSRD decreases as temperature decreases and remains approximately constant below 100 K. Even for SrFeO_3 where disorder due to Fe/Ti substitution, JT distortion and oxygen vacancies are not expected, the temperature dependence cannot be quantitatively described by correlated Einstein [81] or correlated Debye [82] models. The failure of these simple models is not surprising since lattice dynamics calculations for SrTiO_3 [83] yield phonon spectra that can be described neither by a single frequency nor by a Debye-type frequency distribution. The slope of the Fe^{4+} - O^{2-} MSRD versus temperature curve observed for SrFeO_3 ($1.3 \times 10^{-5} \text{ \AA}^2/\text{K}$ in the range of 200-350 K) is comparable to the Ti^{4+} - O^{2-} MSRD value determined for SrTiO_3 in the high temperature region ($1.2 \times 10^{-5} \text{ \AA}^2/\text{K}$ in the range of 200-1000 K) [84]. Although a quantitative model for the temperature dependence of MSRD is not available yet, Figure 3.15 shows that there is a strong static disorder contribution, increasing with decreasing iron content. The temperature-dependent vibrational contribution is of comparable magnitude for different compositions, being only slightly higher for SrFeO_3 .

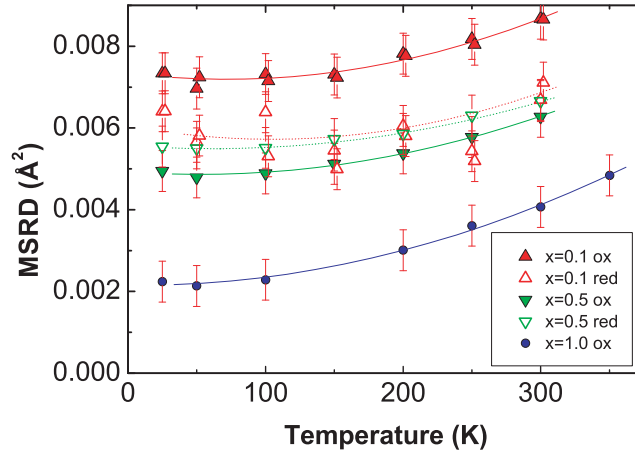


Figure 3.15: Temperature dependence of the mean square relative displacement (MSRD) for $\text{Fe}^{4+}-\text{O}^{2-}$ bonds ($\text{Sr}(\text{Fe}_x\text{Ti}_{1-x})\text{O}_3$ oxidized samples, solid symbols); and $\text{Fe}^{3+}-\text{O}^{2-}$ bonds ($\text{Sr}(\text{Fe}_x\text{Ti}_{1-x})\text{O}_{3-x/2}$ reduced samples, open symbols) in the first coordination shell. Lines are guides for the eye.

3.4.3 Vibrational spectroscopy

The peak positions in the IR spectra of the oxidized $\text{Sr}(\text{Fe}_x\text{Ti}_{1-x})\text{O}_3$ samples (Figure 3.16) hardly change with increasing iron concentration. This finding is not unexpected since substitution of Fe^{4+} for Ti^{4+} should not drastically alter the force constant and the reduced mass (the observed peaks involve mainly B–O motions with the reduced mass being close to that of oxygen). However, for the reduced $\text{Sr}(\text{Fe}_x\text{Ti}_{1-x})\text{O}_{3-x/2}$ samples a splitting of the peak centered at 645 cm^{-1} into three components is found. The relative contribution of the 645 cm^{-1} peak ($\text{Ti}^{4+}-\text{O}^{2-}$ vibration) decreases with increasing iron concentration, while the component at 590 cm^{-1} and the weaker shoulder at 710 cm^{-1} gain weight ($\text{Fe}^{3+}-\text{O}^{2-}$ vibrations).

In cubic perovskites, all first-order Raman lines are symmetry-forbidden. Raman spectra for the oxidized and reduced samples are shown in Figure 3.17. The broad structures at $250\text{--}400\text{ cm}^{-1}$ and at $600\text{--}800\text{ cm}^{-1}$ in pure SrTiO_3 ($x = 0$) are due to second-order Raman scattering [86, 88]. The SrTiO_3 phonon modes [85, 86, 87, 88], determined, e.g., from Hyper-Raman measurements, are indicated by vertical lines (LO4 and TO4 correspond to B–O stretching, and LO3 and TO3 to O–B–O bending modes). For the reduced $\text{Sr}(\text{Fe}_x\text{Ti}_{1-x})\text{O}_{3-x/2}$ samples the spectra become less structured with increasing iron concentration. The substitution of Fe^{3+} for Ti^{4+} (which leads also to the appearance of oxygen vacancies located more or less close to the Fe^{3+} centers) represents a local symmetry lowering and could in principle lead to the appearance of Raman lines. For SrTiO_3 it is known that symmetry breaking by an applied electrical field [85] or the preparation of thin films [89] leads to the observation of first-order Raman peaks. The effect of B-site cation substitution was studied, e.g., for cubic $\text{Sr}(\text{Mg}_{0.05}\text{Ti}_{0.95})\text{O}_{3-\delta}$ where a weak new peak at 762 cm^{-1} was observed [90], and for orthorhombic $\text{Ca}(\text{Zr}_x\text{Ti}_{1-x})\text{O}_3$ where a strong additional peak in the range of $750\text{--}800\text{ cm}^{-1}$ was found for $0.25 \leq x \leq 0.75$ [91]. In the spectra of the reduced samples $\text{Sr}(\text{Fe}_x\text{Ti}_{1-x})\text{O}_{3-x/2}$ even

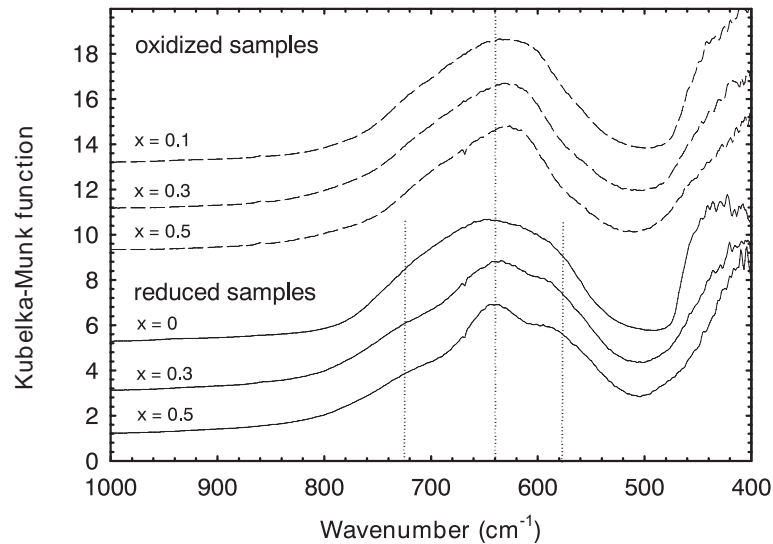


Figure 3.16: Diffuse reflection infrared spectra for fully oxidized (top panel) and fully reduced (lower panel) $\text{Sr}(\text{Fe}_x\text{Ti}_{1-x})\text{O}_{3-\delta}$ samples (for $x = 0$ the spectra of oxidized and reduced samples are identical). The spectra are scaled to comparable intensity at 645 cm^{-1} and shifted upward for clarity. For oxidized samples with $x > 0.5$ the high electronic conductivity of the samples impedes spectra acquisition.

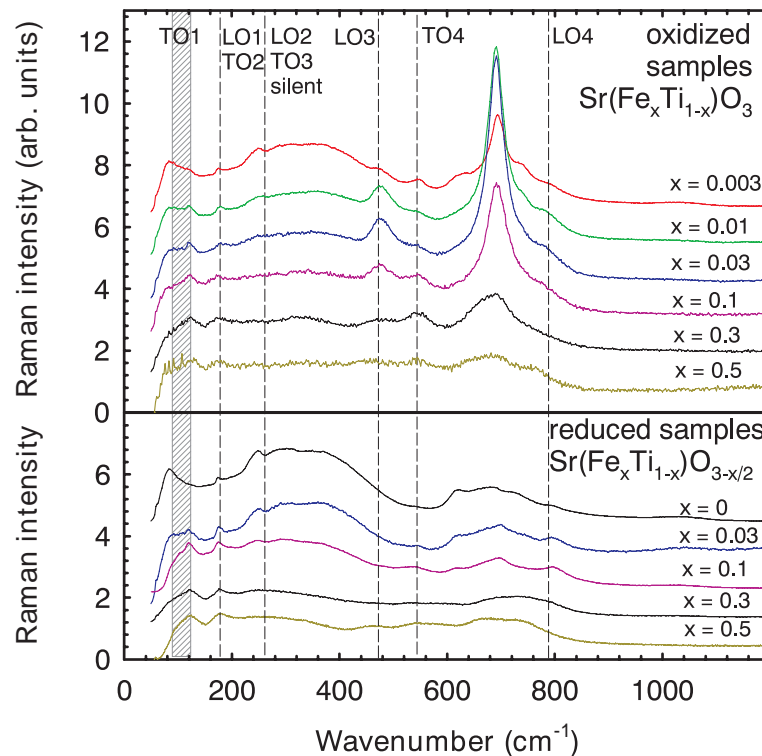


Figure 3.17: Raman spectra for fully oxidized (top panel) and fully reduced (lower panel) $\text{Sr}(\text{Fe}_x\text{Ti}_{1-x})\text{O}_{3-\delta}$ samples (for $x = 0$ the spectra of oxidized and reduced samples are identical). The spectra are scaled to comparable intensity in the $200\text{-}400 \text{ cm}^{-1}$ range and shifted upward for clarity. For samples with $x > 0.5$ the high electronic conductivity of the samples impedes spectra acquisition. The positions of the SrTiO_3 phonon modes classified following Refs. [85, 86, 87] and [88] are indicated by vertical lines.

for large x , the presence of Fe^{3+} and oxygen vacancies obviously does not create a sufficient symmetry distortion for inducing pronounced Raman peaks. Spectra measured on oxygen vacancy-containing $\text{Sr}(\text{Sc}_{0.03}\text{Ti}_{0.97})\text{O}_{2.985}$ also do not show first-order Raman peaks.

For the oxidized $\text{Sr}(\text{Fe}_x\text{Ti}_{1-x})\text{O}_3$ samples, a pronounced line at 690 cm^{-1} appears at an iron concentration as low as $x = 0.003$. Its intensity increases up to $x = 0.03$ and then decreases (Figure 3.19). The full width at half maximum (FWHM) of the peak increases almost linearly from 30 cm^{-1} ($x = 0.003$) to 70 cm^{-1} ($x = 0.3$), while the peak position shifts only slightly to 695 cm^{-1} for large x . For $x = 0.03$, a systematic decrease of the 690 cm^{-1} peak was observed for samples with a smaller degree of oxidation (prepared by heating to $500\text{ }^\circ\text{C}$ in air or $700\text{ }^\circ\text{C}$ in N_2 ; spectra not shown). Since all these peaks are observed with the same frequencies and intensities for all applied excitation wavelengths (784.7, 632.8 and 514.5 nm), luminescence effects are not the origin of these lines. The fact that the frequency of 690 cm^{-1} does not split into TO and LO modes and does not correspond to any of the SrTiO_3 first-order phonons can be seen as an indication that this peak is caused by a vibration with local character. For such a local vibration, modes with inversion symmetry at the Fe^{4+} center would also become Raman active. On the other hand, the symmetry reduction at the Fe^{4+} center also makes the LO3, TO4, and LO4 modes weakly allowed. The intensity at the 475 cm^{-1} SrTiO_3 phonon frequency (and also of the shoulder at 795 cm^{-1} which is difficult to quantify) increases in parallel to the 690 cm^{-1} peak, while the intensity at 545 cm^{-1} exhibits a broad maximum centered around $x = 0.2$.

In Figure 3.19 (b) low temperature measurements are shown. The measurements were performed on the oxidized $\text{Sr}(\text{Fe}_{0.01}\text{Ti}_{0.99})\text{O}_3$ sample from room temperature down to 120 K in steps of 20 K and an additional spectrum at 80 K was recorded bearing in mind the phase transition of SrTiO_3 into the tetragonal phase at 105 K (in first approximation, this does not change the character of the spectrum). The amplitude of the most pronounced peak at 690 cm^{-1} increased by about 120 % upon cooling, whereas the FWHM decreased by about 50 % resulting in an overall peak intensity increase by about 20 %.

3.5 Discussion

In the case of Fe^{3+} ions, the high-spin ground state $d^5(t_{2g}^3e_g^2)$ configuration[92] does not suppose any local structural distortion. Pure SrFeO_3 has $\text{Fe}^{4+}(d^4)$ ions in a high-spin configuration, but has no JT distortion and exhibits metallic conductivity. These facts are explained by strong mixing of $d^4(t_{2g}^3e_g)$ and $d^5\bar{L}(t_{2g}^3e_g^2)$ configurations in the ground state that stabilizes the undistorted cubic perovskite structure and indicates a strong degree of covalency in the Fe–O bonds [71, 72]. A local JT distortion can therefore be expected only for low iron concentrations where delocalization of the iron d electrons is not yet of influence. In this context, it is worth mentioning that $x \approx 0.03$ marks the border between the low concentration regime with essentially independent Fe centers, and the higher concentration regime where the formation of an iron impurity band begins [54] and the electronic conductivity significantly increases

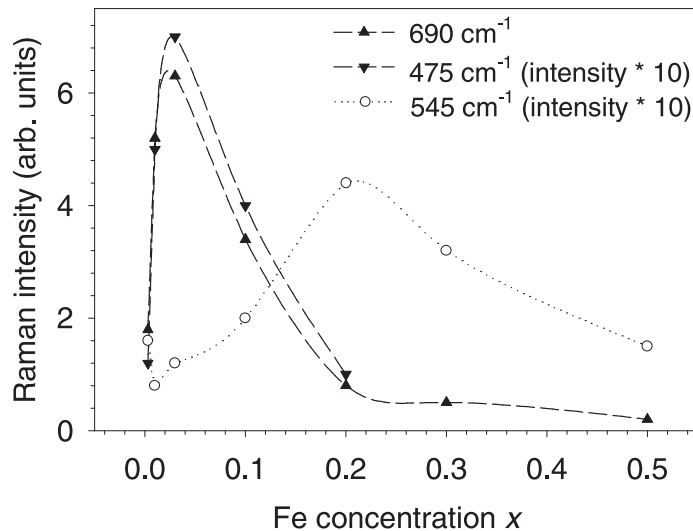


Figure 3.18: Intensity of selected Raman peaks for fully oxidized $\text{Sr}(\text{Fe}_x\text{Ti}_{1-x})\text{O}_3$ samples. For clarity the values for the peaks at 475 cm^{-1} and 545 cm^{-1} are multiplied by a factor of 10.

(together with the decrease in the activation energy for conductivity) [20], see Section 2.4.

While the origin of the XANES pre-edge peaks has been given above, we discuss here their composition dependence and their relationship with the EXAFS findings. The Ti–O MSRD (Figure 3.14) and bond length (Figure 3.13) are almost constant for all x in oxidized $\text{Sr}(\text{Fe}_x\text{Ti}_{1-x})\text{O}_3$, indicating similar degree of distortion around Ti^{4+} ions. Therefore, one could expect that the intensity of the peak P2 in Figure 3.7 should not change with composition, and its variation to be mostly connected with a variation of the background contribution from the neighboring peak P1 [93]. The P1 peak (quadrupole transition to $3d$ states) decreases for lower iron content, and its intensity variation is larger at the Ti K edge (Figure 3.7) than at the Fe K edge (Figure 3.8). The change of the P1 intensity is determined by a variation of the squared transition matrix element and of the occupation number of $3d$ metal states. Since the Ti environment does not change significantly, we do not expect the overlap integral to change. On the other hand, for large x , the stronger electron withdrawal from O^{2-} to Fe^{4+} can result in a decreased Ti $3d$ occupation number. Note that the quadrupole transition at the Ti K edge is extremely sensitive to the occupation number [94].

In the case of the P1 peak for Fe^{4+} , the decrease of the $\text{Fe}^{4+}\text{--O}^{2-}$ distances with increasing x might be viewed as an indication for ‘more compact’ $3d$ orbitals which leads to an increase of the overlap integrals and, thus, to the P1 peak intensity increase with increasing x . However, in the case of Fe^{3+} ions, the $\text{Fe}^{3+}\text{--O}^{2-}$ distance hardly varies with composition. Taking into account the difference between peaks at 3.5 \AA in the FTs (Figures 3.9 and 3.10, as discussed above in Section 3.4.2), one can correlate the change in the Fe^{3+} $3d$ states with the variation of B–O–B bond angles and the presence of oxygen vacancies. Both effects are expected to result in $3d$ band narrowing, and thus in more localized $3d$ wave functions, increasing the pre-edge intensity for high Fe^{3+} content (Figure 3.8).

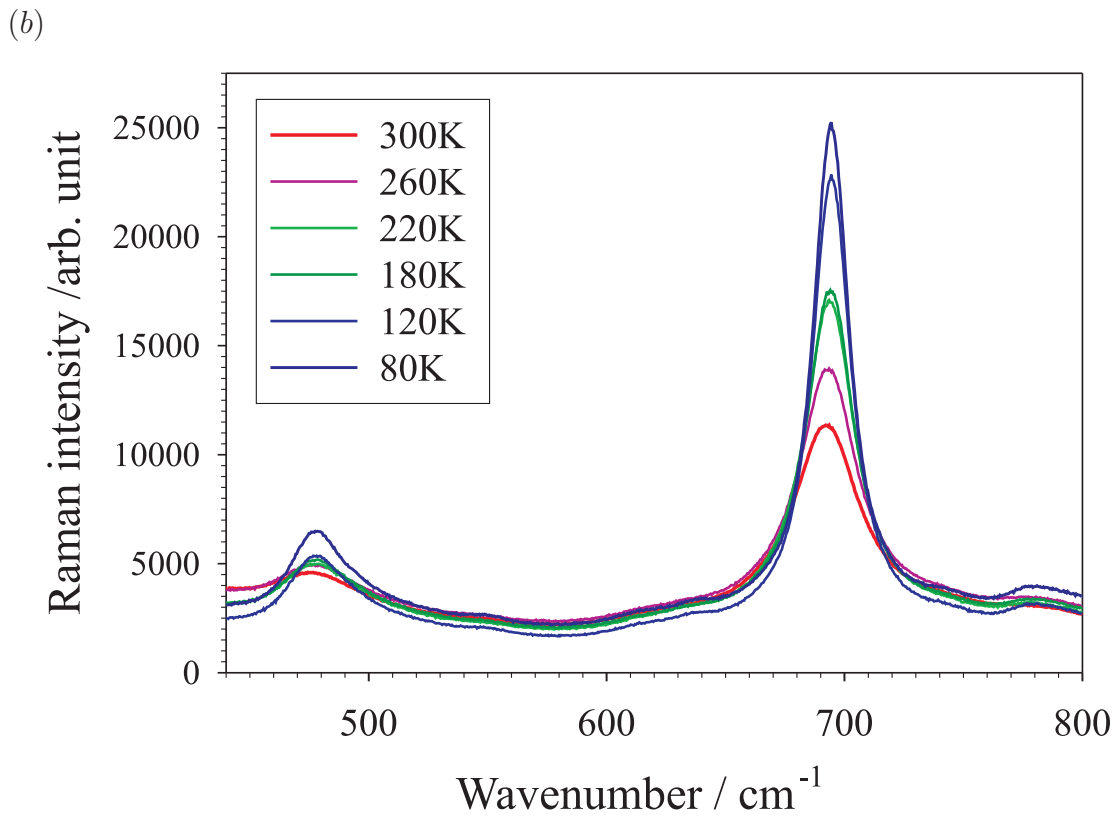
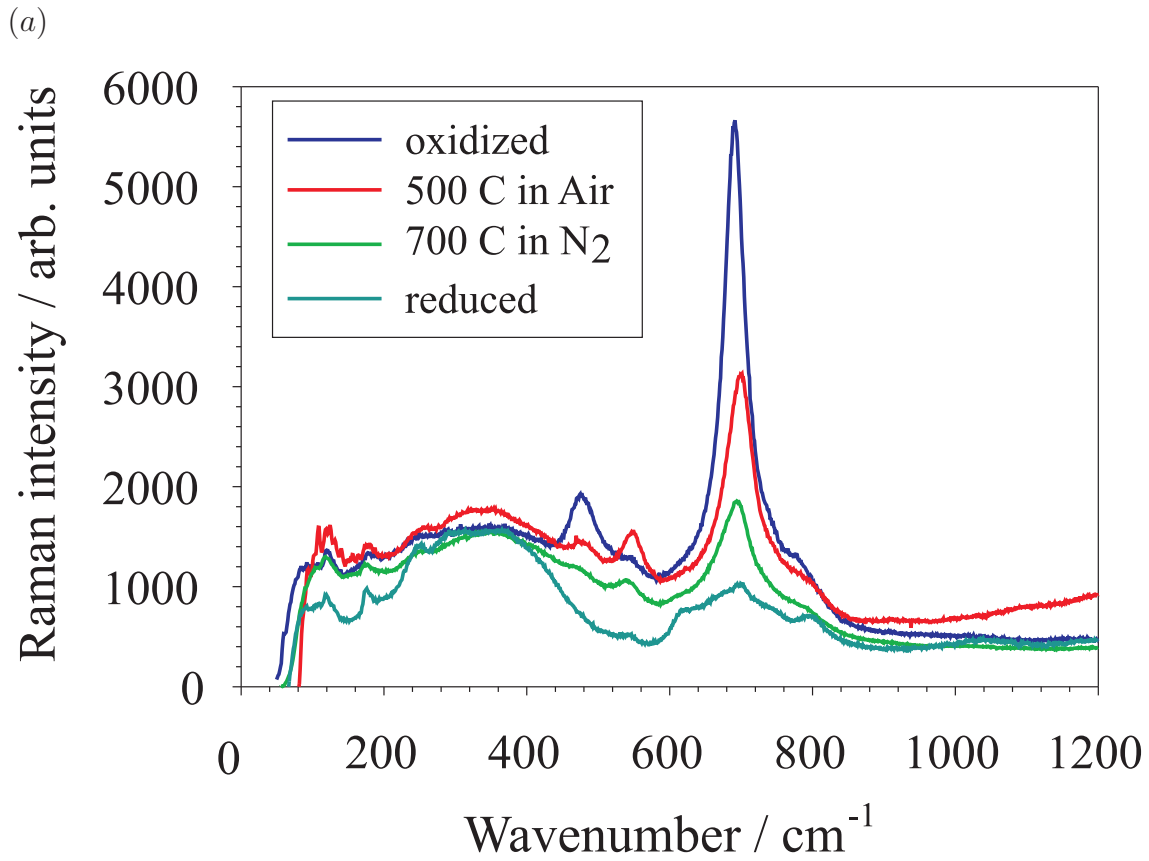


Figure 3.19: (a) Raman spectra of $\text{Sr}(\text{Fe}_{0.03}\text{Ti}_{0.97})\text{O}_{3-\delta}$ sample for different overall oxidation states; (b) Low temperature Raman spectra of $\text{Sr}(\text{Fe}_{0.01}\text{Ti}_{0.99})\text{O}_3$ sample.

One should also note that the pre-edge peak intensity at the Fe K edge (Figure 3.8) is slightly higher in reduced samples than in oxidized ones for the same composition. This difference can be partially attributed to a decrease of the Fe^{3+} coordination number found in EXAFS analysis [Figure 3.12 (a)]. Such a phenomenon has been previously discussed for ferric complexes [95] and iron coordination in silicate glasses [96].

The independence of the $\text{Ti}^{4+}\text{-O}^{2-}$ MSRD (oxidized samples) from the iron concentration (Figure 3.14) is consistent with the fact that these samples exhibit no x -dependent disorder due to oxygen vacancies, and also with the observation of almost x -independent IR frequencies (Figure 3.16). The finding of an almost constant $\text{Fe}^{3+}\text{-O}^{2-}$ MSRD (reduced samples) over an extended concentration range from $x \approx 0$ up to $x = 0.75$ is not self-evident, since the concentration of oxygen vacancies which potentially induce disorder increases linearly with x . On the other hand, the $\text{Fe}^{3+}\text{-O}^{2-}$ vibration frequencies observed in the IR spectra are found to be x -independent. Moreover, an oxygen vacancy next to a B cation tends to displace the cation closer to the remaining oxide ions (the attractive force of the missing O^{2-} is absent). Since Fe^{3+} is larger than Ti^{4+} , it is difficult for the Fe^{3+} to approach closer to the remaining O^{2-} anions. A tendency for the B cations to shift away from the V_{O} was confirmed, e.g., for $\text{Fe}'_{\text{Ti}}\text{-V}_{\text{O}}$ in PbTiO_3 by density functional theory (DFT) calculations but the displacement is significantly more pronounced for the smaller Ti^{4+} than for the Fe^{3+} ion [97].

The variation of the $\text{Fe}^{4+}\text{-O}^{2-}$ MSRD (oxidized samples) with iron concentration is non-trivial. For x close to 1, its value approaches that of the $\text{Ti}^{4+}\text{-O}^{2-}$ MSRD, which seems to be reasonable since the vibrational characteristics of $\text{Fe}^{4+}\text{-O}^{2-}$ and $\text{Ti}^{4+}\text{-O}^{2-}$ are similar. The increase of the $\text{Fe}^{4+}\text{-O}^{2-}$ MSRD with decreasing x is more remarkable. For $x \rightarrow 0$ it increases by a factor of about 3 and is significantly larger than the $\text{Fe}^{3+}\text{-O}^{2-}$ MSRD. If one takes the MSRD of SrFeO_3 as a reference point for the vibrational disorder, the excess contribution is 0.006 \AA^2 for $x = 0$. Since the vibrational characteristics can be assumed to be similar for all $\text{Fe}^{4+}\text{-O}^{2-}$ bonds in the oxidized samples and the remaining minor oxygen vacancy concentration was shown to not increase the MSRD, this excess $\text{Fe}^{4+}\text{-O}^{2-}$ MSRD contribution strongly implies a bond length distribution. In first-order approximation, the MSRD is the sum of a static and a vibrational disorder component [59]

$$\text{MSRD} = \text{MSRD}_{\text{stat}} + \text{MSRD}_{\text{vib}} \quad (3.8)$$

and from $\text{MSRD}_{\text{stat}} = 0.006 \text{ \AA}^2$ ($x = 0$) the bond length distribution is calculated from [59]

$$\Delta r = \frac{m+n}{\sqrt{mn}} \sqrt{\text{MSRD}_{\text{stat}}} \quad (3.9)$$

resulting in $\Delta r \approx 0.16 \text{ \AA}$ (here we inserted $m = 4$ and $n = 2$ corresponding to a JT distortion, but setting $m = n$ hardly changes the numerical result). A plausible explanation for such a distribution occurring only for Fe^{4+} and not for Ti^{4+} or Fe^{3+} could be a JT distortion. This broadening of the bond length distribution is significantly larger than the Fe–O distance increase of 0.03 \AA between $x = 1$ and $x \rightarrow 0$. The magnitude of the total distortion of 0.16 \AA

is larger than the sum of the contraction of 0.028 Å along the x and y axes and the elongation of 0.052 Å along z -direction found in quantum chemical calculations of an isolated Fe^{4+} in SrTiO_3 [54].

Since the respective transitions are allowed in cubic perovskites, the IR peaks observed in Figure 3.16 represent an average over the contributions from Ti–O and Fe–O bond vibrations. For the oxidized samples, the IR frequencies are almost independent of the iron concentration x , therefore we expect that (independent of the exact model) the vibrational contribution to the MSRD of $\text{Fe}^{4+}\text{--O}^{2-}$ is also independent of x . A splitting of IR peaks due to a JT distortion around Fe^{4+} would not show up in the IR spectra because for small $x \leq 0.03$ (where the strongest JT effect is expected) their statistical weight is too small, while for large x , the JT distortion is expected to vanish.

In contrast to the IR measurements, the Raman spectra are sensitive to local symmetry reduction since the undistorted cubic perovskites exhibit no allowed first-order peaks at all. The pronounced new peak at 690 cm^{-1} appears for the oxidized samples with low to moderate iron content. The spectra of the reduced samples remain essentially unchanged, however, although at first glance the incorporation of Fe^{3+} and oxygen vacancies should induce an even stronger symmetry reduction. This could be interpreted as an indication for the local symmetry reduction being inseparably related to the 4+ oxidation state of iron. While such a local symmetry breaking could be caused by an anisotropic JT-type distortion or alternatively by an isotropic bond length change around Fe^{4+} , the observed broadening of the $\text{Fe}^{4+}\text{--O}^{2-}$ distance distribution with only a slight increase of the bond length (see discussion above) and the concentration dependence of this Raman line (see below) clearly favor the first interpretation. The absence of an intensity decrease (and even a peak intensity increase observed) upon cooling shows that the peak does not arise from anharmonicity effects.

For the lowest iron concentrations $x < 0.03$, the 690 cm^{-1} Raman peak area is approximately proportional to the Fe concentration, while already for $x \geq 0.03$, the peak area decreases with the increase in x . Obviously a continuous decrease of the JT distortion with increasing iron concentration occurs which shows up in the decreasing excess contribution to the $\text{Fe}^{4+}\text{--O}^{2-}$ MSRD as well as in the decreasing Raman peak area (note that these two quantities are not necessarily proportional). The decrease of the line intensity already at $x > 0.03$ is difficult to rationalize for the symmetry breaking being caused by an isotropic local bond length change. On the other hand, the fact that in this Fe concentration range also the electronic conductivity changes drastically [20] points towards the importance of the electronic structure. That supports the hypothesis that Raman line is related to the presence of a JT distortion. In parallel to the decrease in Raman peak area, the FWHM of the 690 cm^{-1} peak increases. A similar observation was done for rhombohedral $\text{La}_{0.93}\text{Mn}_{0.98}\text{O}_3$ [98] where a temperature decrease leads to a transition into a ferromagnetic phase with decreased deformation in the MnO_6 octahedra. The intensity of the Raman peaks at 499 and 517 cm^{-1} assigned to local JT distortions decreases with decreasing temperature while the FWHM increases, which was interpreted by a reduced phonon lifetime related to the decreasing local distortions.

In principle, an off-center position of the Fe^{4+} , e.g., along the z axis cannot be ruled out. Such a displacement would also remove the degeneracy of the singly occupied e_g orbitals. For Ni^+ and Cu^{2+} in SrO , such a combined distortion ("pseudo-JT effect") was observed [99, 100]. Nevertheless, it has to be emphasized that in these cases the substituting cation is about 0.2 Å smaller than the Sr^{2+} ion [100], while the size difference between Fe^{4+} and Ti^{4+} amounts to only 0.02 Å.

The fact that we do not observe a splitting of the first shell due to the JT effect around Fe^{4+} ions at low concentrations directly in EXAFS spectra or in their FTs can be attributed to the type of local distortion, resulting in several groups of strongly overlapping $\text{Fe}^{4+}\text{-O}^{2-}$ distances. As a result, the existing JT distortion expresses itself in large increase of the first shell MSRD (Figure 3.15). Such an effect was observed previously in LaMnO_3 (Mn, high spin d^4 , coherent JT effect, monoclinic unit cell) [101], where the distribution of Mn–O bond lengths ranging from 1.91–2.15 Å was also not resolved into individual peaks (although spectra were measured to high k values of 15 Å⁻¹), but large MSRD values were found (0.0095 Å² at 300 K, being comparable to our oxidized samples with $x \leq 0.1$). Also, only an anomalous MSRD increase with temperature was observed for $(\text{Sr}_x\text{La}_{1-x})\text{MnO}_3$ samples in the temperature range where the transition from the ferromagnetic phase (no JT effect) to the paramagnetic state (JT distortion for Mn^{4+}) occurs [102]. This seems to be a comparable case to our findings. For $\text{Sr}_{0.5}\text{La}_{1.5}\text{Li}_{0.5}\text{Fe}_{0.5}^{4+}\text{O}_4$ which crystallizes in the K_2NiF_4 structure with Fe^{4+} in a tetragonally distorted octahedron, a splitting of the Fe K -absorption edge by ≈ 3 eV was observed [103, 104]. The absence of such a splitting in our case can be understood from the fact that the difference in Fe–O distances is only 0.16 Å as compared to 0.5 Å reported for $\text{Sr}_{0.5}\text{La}_{1.5}\text{Li}_{0.5}\text{Fe}_{0.5}^{4+}\text{O}_4$ in Refs. [103, 104].

3.6 Summary and conclusions

Structural studies of $\text{Sr}(\text{Fe}_x\text{Ti}_{1-x})\text{O}_{3-\delta}$ perovskites as a function of composition and iron oxidation state have been performed by means of XRD, Fe and Ti K -edge XAS, and vibrational (Raman and infrared) spectroscopy with the emphasis on the possible Jahn-Teller distortion around Fe^{4+} ions.

The local electronic structure probed by XANES, as well as the long range order probed by XRD (Chapter 2), and the short range order reflected in EXAFS, showed a dependence on composition as well as on iron oxidation state.

The variation of the pre-edge peak intensity in the XANES signals is attributed to the modification of the Fe(Ti)–O bond lengths and B–O–B bonding angles, resulting in a change of localization of $3d$ -metal states and their occupation numbers n_d .

Although none of the individual observations alone gives a final proof of a JT distortion around Fe^{4+} ions, the combination of results obtained by XAS (especially the iron concentration dependence of the $\text{Fe}^{4+}\text{-O}^{2-}$ MSRD) and vibrational spectroscopies strongly supports its presence, most pronounced for $x \approx 0.03$ and decreasing for higher iron concentrations. The

decrease of the JT effect with increasing x can be understood qualitatively by the change in the electronic structure of the materials from insulator to metal. A quantitative modeling of the variation of the $\text{Fe}^{4+}\text{-O}^{2-}$ MSRD and the intensities of the Raman lines remains a challenging theoretical problem.

Chapter 4

Catalytic activity of $\text{Sr}(\text{Fe}_x\text{Ti}_{1-x})\text{O}_{3-\delta}$: CH_4 and CO oxidation

After the introduction and description of the experimental details, the results of the catalytic studies of methane and carbon monoxide oxidation on $\text{Sr}(\text{Fe}_x\text{Ti}_{1-x})\text{O}_{3-\delta}$ will be given in this chapter. Emphasis will be placed on the role of point defects as redox and/or acid-base active centers in the catalytic activity of these materials. Relevant reaction mechanisms are considered at the end of the chapter.

4.1 Introduction

The definition of a catalyst

If the rate of a chemical reaction can be increased by the presence of a substance which intermediately participates in the reaction but remains unchanged after the completion of the reaction cycle, the substance is called a *catalyst*, and its impact is called *catalysis*¹. In broader terms, a catalyst is also a substance which can change selectivity of chemical reactions towards particular products when several reaction branches are present. Catalysts influence only the kinetics of chemical reactions by changing mechanisms via a modified transition state (usually with lower activation energy) while leaving the equilibrium constants unchanged.

Heterogeneous catalysis

Catalysis can be divided into homogeneous and heterogeneous catalysis. In homogeneous catalysis reactants (educts) and catalysts are in the same phase. In heterogeneous catalysis reactants and catalysts are in different phases; usually in this case, catalysts are in the solid state and reactants are either in the gaseous or liquid state. It is easy to understand that the surface (i.e., the interface) of a catalyst and its properties are most important for heterogeneous catalysis. The catalyst in heterogeneous catalysis enables a reaction path which is favorable for two reasons

¹the term ‘catalysis’ (Greek: *κατάλυσις*, meaning ‘loosening down’) was introduced by Jöns Jakob Berzelius in 1835 [105].

- (a) It increases reactant concentrations via specific adsorption/chemisorption. In heterogeneous catalysis it is understood that adsorption precedes any gas–solid reaction [105]. Medium affinities for adsorption/chemisorption of a catalyst towards educts and products are favorable for catalytic efficiency. Too strong a bonding between the adsorbed species (educt or product) and the catalyst surface *poisons* the catalyst; too weak a bonding does not provide a sufficient catalytic effect
- (b) It introduces a transition state of reactant+catalyst complex, thus lowering a kinetic barrier of the reaction path considered

It is these two key roles through which (surface) point defects present in a material could act as active catalytic centers. An extensive overview of all aspects of heterogeneous catalysis is given in Refs. [52, 105].

Catalytic activity

The catalytic activity of a catalyst is defined in the most direct way by the concept of turnover frequency or turnover number. The turnover frequency (TOF) is the number of times dn that the overall catalytic reaction in question takes place per catalytic site in a differential time interval dt for a fixed set of reaction conditions (temperature, pressure or concentration, reactant ratio, extent of reaction)

$$\text{TOF} = \frac{1}{S} \frac{dn}{dt} \quad (4.1)$$

where S is the number of active sites [105]. However, it is sometimes difficult to identify the nature of the active sites and their number. For such a case S is replaced by the total area A of the exposed catalyst, and such a TOF is called the ‘areal rate of reaction’². Having measured a reaction rate and knowing the characteristics of the catalyst, one can express the catalytic activity in terms of the TOF. For most heterogeneous catalytic reactions with small molecules in a moderate temperature (100–500 °C) and pressure range (up to few bars), TOFs are between 10^{-2} and 10^2 s^{-1} (it is interesting to mention that enzymatic reactions can have TOF up to 10^7 s^{-1} !) [105].

Activities of different catalysts are often compared in a so-called “Volcano” plot: the temperature at certain degree of conversion is indicated on the (negative) abscissa, and some enthalpic function which describes the bonding reactant–catalyst is indicated on the ordinate. Such a plot often has a “volcano” shape which supports the idea that highest activities are found for catalysts with intermediate affinities for the reactants.

4.1.1 Importance of point defects in heterogeneous catalysis

In heterogeneous catalysis the key player is a species adsorbed on the catalyst surface which ‘waits’ for its counterpart to undergo the chemical reaction. The reaction partner may come

²according to the IUPAC recommendation.

directly from the gas phase (Eley-Rideal mechanism, ER), or via surface diffusion (i.e., being previously adsorbed, Langmuir-Hinshelwood mechanism, LH), or even intermediately provided by the lattice of the catalyst (e.g. Mars-van Krevelen, MvK, mechanism [106]). In cases when adsorption is not favored, the presence of surface point defects could enhance the adsorption rate. In addition to the adsorption which facilitates the encounter of the reactants, the adsorbing site can modify the bonding within the adsorbate and thus make the reaction kinetically possible. In that way, given an appropriate model reaction, by controlling type and concentration of defects it is possible to elucidate the role of point defects in catalysis in more detail.

The chemistry of point defects in solids is of great importance for their catalytic activity, which was recognized already by Simkovich and Wagner [3]. Naturally, point defects at the surface are more responsible for catalytic activity than those in the bulk. However, the surface properties of a catalyst under reaction conditions are essentially unknown but related to the bulk properties, hence, as a first step, it is reasonable to relate the bulk properties to the catalytic behavior. The point defects represent excitations relative to the perfect lattice and are acid-base and redox centers, and should play a key role in catalysis [3, 4]. The defect chemistry of a solid and thus also its catalytic activity is determined by many factors such as

- type and concentration of active centers: redox centers and/or acid-base centers; ionic and/or electronic defects
- electronic and ionic mobility
- chemical capacitance, i.e., the ability of the oxide to release the oxygen from the lattice via stoichiometry changes

High mobility can make the other parameters less important, because the active centers required by reacting species, or the species themselves, can more easily diffuse to the place where they are needed.

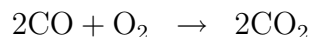
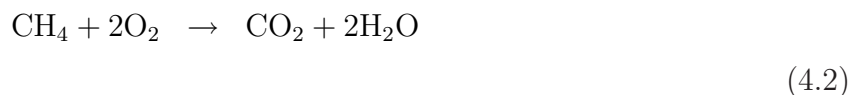
Having in mind this complexity, a well-studied model material is preferred when a clear picture of its catalytic behavior is needed. A candidate, whose defect chemistry is well-understood, is the mixed conducting perovskite $\text{Sr}(\text{Fe}_x\text{Ti}_{1-x})\text{O}_{3-\delta}$ solid solution series; the most important properties of those were presented in Chapter 2. In general, transition metals in perovskites have stable single or mixed valence states of Fe, Co, Mn, Ti, etc., or stabilized unusual valence states, which can be very important in catalysis. As a consequence of a significant oxygen vacancy concentration present in the bulk [107, 108], which is thermodynamically well-defined, acceptor doped perovskites usually have a high oxygen ion conductivity through an oxygen vacancy mechanism. However, while the bulk defect chemistry is well-settled, this is not the case for the surface. A theoretical calculation for a similar perovskite material (LaCoO_3) shows that vacancy formation at the surface is energetically more favorable than in the bulk [109]. Hence, it is reasonable to assume an enhanced concentration of oxygen vacancies on $\text{Sr}(\text{Fe}_x\text{Ti}_{1-x})\text{O}_{3-\delta}$ surface, as well.

Although perovskite-type oxides were well-studied materials they did not draw significant attention in the field of catalysis until the 1970s, when it was suggested that cobaltate perovskite may substitute noble metals in electrocatalysis [110]. The work of the Nobel laureate W. F. Libby started up the research on perovskites in automotive exhaust catalysis [49]; promising results were obtained with cobaltate and manganate perovskites in the CO oxidation and NO reduction. However, the observed *poisoning* (deactivation) of those materials by SO_2 lessened the initial optimism for their application. In catalytic combustion of methane, it was reported that $\text{La}_{0.6}\text{Sr}_{0.4}\text{MnO}_3$ has comparable catalytic activity to the Pt/Alumina catalyst at conversion levels below 80 % [51]. The perovskite-type oxides are being investigated not only in combustion catalysis, but also in other catalytic processes such as oxidative coupling, selective oxidation and dehydrogenation. Mixed conducting perovskites are also widely studied in the field of SOFC as cathode materials [46, 111]. Many general aspects of perovskite-type oxides in catalysis are well-reviewed in Refs. [112, 113, 114].

4.1.2 Two test reactions

In order to establish a closer connection between the point defects (as active centers) present in $\text{Sr}(\text{Fe}_x\text{Ti}_{1-x})\text{O}_{3-\delta}$ materials and their catalytical activity, the chosen model reaction should be as simple as possible and hence exhibit as few intermediates as possible. Since these materials are oxides in which the oxygen species are chemically active, an oxidation reaction appears especially appropriate as a test reaction. CH_4 (non-polar) and CO (slightly polar) molecules are very simple molecules and as such should be good candidates as educts to be catalytically oxidized. In these cases one could expect intermediates³ such as $\cdot\text{CH}_3$, $:\text{CH}_2$, H^+ .

Two simple test reactions were therefore investigated: total oxidation of CH_4 and total oxidation of CO



Both reactions are strongly exothermal. The overall reactions Eqs. (4.2) are basically gas phase reactions. In a heterogeneous catalytic experiment such a reaction occurs between a species from the gas phase CH_4 (or CO) and an adsorbed $\text{O}_{*,ad}^*$ species at the surface (ER mechanism), or between both adsorbed $\text{CH}_{4,ad}$ (or CO_{ad}) and adsorbed $\text{O}_{*,ad}^*$ species (LH mechanism). The oxygen species can even – as has already been mentioned – come from the lattice of the oxide (MvK mechanism). The stars in $\text{O}_{*,ad}^*$ designate that neither the state (atomic or molecular) nor the charge of the adsorbed oxygen species are *a priori* known. A short overview of possible O_{ad}^0 , O_{ad}^- , O_{ad}^{2-} , $\text{O}_{2,ad}^0$, $\text{O}_{2,ad}^-$, and $\text{O}_{2,ad}^{2-}$ atomic and molecular oxygen

³understanding their behavior could also shed light on oxidation reaction mechanisms of bigger hydrocarbon molecules, although they additionally involve stereochemical effects not seen in small molecules like CH_4 and CO.

species on various oxides is given in Ref. [115]. According to reports on LaCoO_3 reviewed in Ref. [113], and in view of Ref. [116], O_{ad}^- can be assumed to be the reactive species on the SrTiO_3 surface. In more detail, oxidation reactions of CH_4 and CO on SrTiO_3 would be described by



as the decisive steps. Due to its symmetry the CH_4 molecule is hard to activate [117]. That is the reason for the higher temperatures needed for methane oxidation compared to CO oxidation. In methane oxidation the most difficult part is the removal of the first H atom from the methane molecule, rendering Eq. (4.3) the slowest step, while the further steps finally leading to CO_2 are assumed to be much faster.

Under the reaction conditions iron in $\text{Sr}(\text{Fe}_x\text{Ti}_{1-x})\text{O}_{3-\delta}$ ions are present partially as Fe^{4+} and partially as Fe^{3+} and therefore oxygen vacancies are expected to be present. Hence, within the $\text{Sr}(\text{Fe}_x\text{Ti}_{1-x})\text{O}_{3-\delta}$ series the concentration of redox and acid-base centers including the characteristic behavior of iron can be investigated. For comparison latter, Fe_2O_3 will be also considered, as it contains only Fe^{3+} ions and a negligible oxygen vacancy concentration in the temperature range relevant for this work [118].

To separate redox and acid-base effects scandium-doped samples are studied in this work. They provide oxygen vacancies as a result of the charge compensation for Sc^{3+} ions. Since Sc^{3+} ions have empty d orbitals, a redox behavior characteristic for transition-metals is excluded. Only two different Sc-doping concentration, 1 % and 3 %, were investigated because apparently it is not possible to achieve much higher doping levels [119].

Cobalt-doped samples have the Co ions in 2+ and 3+ valence state and oxygen vacancies for the charge compensation, but on the other hand Co^{3+} ions still have 6 d -electrons which could affect the catalytic properties. These samples can show both redox and acid-base behavior. In the case of Mn-doped SrTiO_3 , which has the Mn ions in the valence state of 2+, 3+ or 4+, vacancies are present as the charge compensation for the 2+ and 3+ states. These samples could also show redox and/or acid-base behavior. However, its redox activity might be different from Fe- and Co-containing samples due to different d -electron configurations.

4.2 Chemical kinetics details

4.2.1 Adsorption isotherms

It was reported that CH_4 on RuO_2 merely undergoes a physisorption, more precisely, a weak non-dissociative adsorption [120]. This material is partly comparable to iron-rich $\text{Sr}(\text{Fe}_x\text{Ti}_{1-x})\text{O}_{3-\delta}$ due to similar electronic structure of Fe and Ru atoms, and therefore one might not expect a dissociative adsorption of methane on $\text{Sr}(\text{Fe}_x\text{Ti}_{1-x})\text{O}_{3-\delta}$ either. $\text{Sr}(\text{Fe}_x\text{Ti}_{1-x})\text{O}_{3-\delta}$ sam-

ples for low iron contents are more similar SrTiO_3 . To describe physisorption of CH_4 on $\text{Sr}(\text{Fe}_x\text{Ti}_{1-x})\text{O}_{3-\delta}$, as a first approximation, a simple Langmuir isotherm can be assumed

$$\theta_{\text{CH}_4} = \frac{K \cdot [\text{CH}_4]}{1 + K \cdot [\text{CH}_4]} \quad (4.5)$$

where $K = k_{\text{ads}}/k_{-\text{ads}}$ is the equilibrium constant comprising of the forward adsorption k_{ads} and backward desorption rate $k_{-\text{ads}}$. Eq. (4.5) can be simplified for low coverage as

$$\theta_{\text{CH}_4} \approx K \cdot [\text{CH}_4] \quad (4.6)$$

and for high coverage as

$$1 - \theta_{\text{CH}_4} \approx \frac{1}{K \cdot [\text{CH}_4]} \quad (4.7)$$

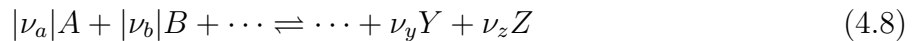
the latter being a rather improbable situation for $\text{Sr}(\text{Fe}_x\text{Ti}_{1-x})\text{O}_{3-\delta}$ materials.

A dissociative adsorption of CH_4 was observed on metals such as Ni [121], or W [122], where it dissociates into CH_3 and CH_2 groups, and into hydrogen atoms [123]. Infrared spectroscopy studies of CO adsorption on the perovskite-type oxides LaMO_3 ($M=\text{Cr}, \text{Mn}, \text{Fe}, \text{Co}$) have shown that, in contrast to simple binary oxides, at least two different carbonate species are formed on the surface upon adsorption [124]. This rules out the possibility of describing adsorption with a simple isotherm.

The situation is even more difficult in the case of the oxygen adsorption on $\text{Sr}(\text{Fe}_x\text{Ti}_{1-x})\text{O}_{3-\delta}$. The standard approach of investigation by Temperature Programmed Desorption (TDP) is inevitably connected with a change of stoichiometry of these oxides. However, it is known that adsorbed oxygen on low iron doped SrTiO_3 can have at least three different appearances: O_2^- , O_2^{2-} and O^- (well discussed in Ref. [115]); their surface concentrations are still a subject of investigation.

4.2.2 Chemical kinetics

Any chemical reaction can be expressed as



The stoichiometric coefficients ν_i are negative for educts A, B, ... and positive for products ..., Y, Z. For illustration, the following model reaction is considered



At any instant⁴ the *rate of consumption* of the educt A is defined by

$$R_A \equiv -\frac{d[A]}{dt} \quad (4.10)$$

⁴with implicit assumption of no volume change

Similarly, the *rate of formation* of Z is defined as

$$R_Z \equiv \frac{d[Z]}{dt} \quad (4.11)$$

Due to different stoichiometric coefficients the rates of consumption and formation generally differ, however, they can be equalized by dividing them by their coefficients

$$R_A = \frac{1}{3}R_B = \frac{1}{2}R_Z \quad (4.12)$$

A very useful concept in chemical kinetics and thermodynamics was introduced by T. de Donder in 1922, namely, the *extent of reaction* which is defined by any of species participating in the reaction via⁵

$$\xi \equiv \frac{n - n_0}{\nu} \quad (4.13)$$

where n_0 is the initial mole number of a species, n is the mole number at time t , and ν is the stoichiometric coefficient of the species. The extent of reaction is the same for every reactant and product, i.e., it is a characteristic of the reaction. It is an extensive variable and is proportional to the mass of the system. The *degree of reaction* or simply *conversion* is defined as

$$X \equiv \frac{\xi}{\xi_{max}} \quad (4.14)$$

where ξ_{max} is the maximum possible extent of the reaction. It is also independent of the species involved. It most directly measures at which stage is the reaction on the way towards equilibrium⁶. It is already normalized between 0 and 1, even for reversible reactions which do not have huge absolute values of equilibrium constants. In contrast to the extent of reaction, the conversion is an intensive measure of the progress of a reaction, independent of the mass involved. Reaction rates can be expressed in the form of the difference of the forward and the backward reaction rate

$$R = \vec{R} - \overset{\leftarrow}{R}. \quad (4.15)$$

The forward and the backward reaction rates are typically given by

$$\begin{aligned} \vec{R} &= \vec{k}[A]^\alpha[B]^\beta \\ \overset{\leftarrow}{R} &= \overset{\leftarrow}{k}[Z]^\gamma \end{aligned} \quad (4.16)$$

where \vec{k} and $\overset{\leftarrow}{k}$ are the *rate constants* for the forward and backward reaction, respectively; α , β and γ are called *partial reaction orders* for A, B and Z respectively; all are constants and independent of time and concentrations. The sum of all partial orders of the reactants ($\alpha + \beta$) is called the *order of the reaction*. When the system is far from equilibrium one of the partial

⁵for a reaction with time-independent stoichiometric coefficients

⁶reaction completion

rates in the righthand side of Eq. (4.15) dominates, e.g., if the forward reaction dominates, the overall reaction rate is approximately given by

$$R = \overrightarrow{R} = \overleftarrow{k}[A]^\alpha[B]^\beta = k[A]^\alpha[B]^\beta \quad (4.17)$$

In equilibrium the reaction rate vanishes, i.e., forward and backward reactions are equal

$$R = 0 \quad \text{i.e.} \quad \overrightarrow{R} = \overleftarrow{k}[A]^\alpha[B]^\beta = \overleftarrow{k}[Z]^\gamma = \overleftarrow{R} \quad (= \text{exchange rate}) \quad (4.18)$$

To get partial reaction orders of a reaction, data pairs $(R_i, [A]_i)$ ⁷ and $(R_i, [B]_i)$ are plotted in the log – log plot, and the respective partial reaction orders are obtained as the slopes in these plots

$$\log R = \alpha \log[A] + C_1 \quad \text{or} \quad \log R = \beta \log[B] + C_2 \quad (4.19)$$

Reactions in gas flow systems. Plug-flow and stirred-flow reactor

Heterogeneously catalyzed reactions are usually studied in flow systems where the reaction mixture passes through a reactor. A very common type of an experimental reactor is the tubular reactor. The core of the reactor tube is a hot zone with a catalyst bed placed in the middle of the tube. Generally two distinct flow conditions can be recognized: the first type without stirring is the so-called *plug-flow reactor*, where concentration gradients of reactants and products exist within the catalyst bed; the second type with good mixing of reactants in the catalyst bed is the *stirred-flow reactor*, where the catalyst bed has uniform concentrations of all reaction participants. The same experimental tubular reactor can behave differently, depending on temperature, conversion level, total gas flow, height of the catalyst bed, sizes and specific surface areas of catalyst particles. In extreme cases, the same reactor can act as either a plug-flow or a stirred-flow system.

If the reaction mixture flows through a plug flow reactor with catalyst volume V_0 with the volume flow rate f (in SI units $\text{m}^3 \text{ s}^{-1}$) and if the actual kinetic reaction rate is given by $v = kc^\alpha$, the general solution for the process is given by

$$- \int_{c_{ini}}^{c_{fin}} \frac{dc}{c^\alpha} = \frac{k}{f} \int_0^{V_0} dV \quad (4.20)$$

where c_{ini} is the initial concentration at the reactor inlet and c_{fin} is the final concentration after leaving the reactor. In this case the reactor operates in *integral mode*. In the case of a first order reaction ($\alpha = 1$), integration gives

$$c_{fin} = c_{ini} e^{-kV_0/f} \quad (4.21)$$

where the quantity V_0/f is usually called *contact time* or *residence time*. In the case of reaction orders α other than unity, the general solution of Eq. (4.20) is

$$\frac{1}{\alpha - 1} \left(\frac{1}{c_{fin}^{\alpha-1}} - \frac{1}{c_{ini}^{\alpha-1}} \right) = \frac{kV_0}{f}. \quad (4.22)$$

⁷pairs $(R_i, [A]_i)$ for various points i can be obtained by measuring the R_i at a $[A]_i$ while keeping a $[B]^{fix}$ constant; $(R_i, [B]_i)$ pairs are obtained analogously.

The apparent reaction rate is always given by

$$R_{app} = \frac{f(c_{ini} - c_{fin})}{V_0} \quad (4.23)$$

because it merely expresses the observed fact about the initial and final concentrations. Generally it differs from the actual kinetic reaction rate used to obtain Eq. (4.20).

In the case of an ideal stirred-flow reactor the apparent and actual reaction rates are the same, as a consequence of uniform conditions throughout the catalyst bed

$$R = R_{app} = \frac{f(c_{ini} - c_{fin})}{V_0}. \quad (4.24)$$

In this case the reactor operates in a *differential mode*, where concentrations do not vary within the catalyst bed. In tubular reactors this condition is readily fulfilled at low conversions up to 10 % of the full conversion.

Activation energy

If a reaction rate is described by Eq. (4.17), the temperature dependence is expressed through the rate constant, $k = k(T)$. At least in a limited temperature range the temperature dependence can be normally described by the *Arrhenius equation*⁸ which has the form

$$k = Ae^{-\frac{E_a}{RT}} \quad (4.25)$$

where A is the pre-exponential factor, E_a is the activation energy usually related to the energy barrier⁹ of the reaction, and R is the gas constant.

Practically, even in a limited temperature range the reactor might change its mode of operation, i.e., from differential to integral mode. It is therefore advisable to analyze the reaction in the integral mode for the whole temperature range. A limitation to moderate conversions is advisable because at a high conversion diffusion instead of chemical kinetics may become the limiting process. In the case of the reaction of first order, the conversion is then given by

$$X = \frac{c_{ini} - c_{fin}}{c_{ini}} = \frac{c_{ini} - c_{ini}e^{-kV_0/f}}{c_{ini}} = 1 - e^{-kV_0/f} \quad (4.26)$$

from which follows

$$\ln(1 - X) = -\frac{kV_0}{f} \quad (4.27)$$

and since the rate constant k is given by Eq. (4.25), the following equation is valid

$$\ln(-\ln(1 - X)) = -\frac{E_a}{RT} + Const. \quad (4.28)$$

The activation energy can be obtained from the slope of the $\ln(-\ln(1 - X))$ vs. $1/T$ plot, using data up to conversions of 0.5.

⁸in spite of the fact that other equation can better fit the data [123], they do not offer clear insight into the mechanism of the chemical process

⁹it can nevertheless also contain ΔH of preceding/succeeding steps if the reaction comprises multiple steps

Table 4.1: Masses of educts mixed to give $n_{total} = 0.05$ mol of the desired compound, and specific surface (BET) areas of the prepared compounds. $\dagger\alpha\text{-Fe}_2\text{O}_3$ was used in catalytic reactions for comparison, and it is included in the Table for consistency.

Doping level, x	Mass (g)						Stoichiometry (x in %)	BET area (m^2/g)
	SrCO ₃	TiO ₂	Fe ₂ O ₃	Sc ₂ O ₃	Co ₃ O ₄	MnO		
"pure"	7.381	3.994	*	*	*	*	SrTiO ₃	2.7
0.003	7.381	3.982	0.012	*	*	*	Sr(Fe _{0.3} Ti _{99.7})O _{3-δ}	4.9
0.01	7.381	3.954	0.040	*	*	*	Sr(Fe ₁ Ti ₉₉)O _{3-δ}	3.2
	7.381	3.954	*	0.034	*	*	Sr(Sc ₁ Ti ₉₉)O _{3-δ}	4.9
	7.381	3.954	*	*	0.040	*	Sr(Co ₁ Ti ₉₉)O _{3-δ}	2.1
0.03	7.381	3.874	0.120	*	*	*	Sr(Fe ₃ Ti ₉₇)O _{3-δ}	3.2
	7.381	3.874	*	0.103	*	*	Sr(Sc ₃ Ti ₉₇)O _{3-δ}	3.3
	7.381	3.874	*	*	0.120	*	Sr(Co ₃ Ti ₉₇)O _{3-δ}	2.7
	7.381	3.874	*	*	*	0.114	Sr(Mn ₃ Ti ₉₇)O _{3-δ}	3.0
0.10	7.381	3.595	0.399	*	*	*	Sr(Fe ₁₀ Ti ₉₀)O _{3-δ}	2.6
	7.381	3.595	*	*	0.401	*	Sr(Co ₁₀ Ti ₉₀)O _{3-δ}	1.4
0.20	7.381	3.195	0.798	*	*	*	Sr(Fe ₂₀ Ti ₈₀)O _{3-δ}	4.0
0.30	7.381	2.796	1.198	*	*	*	Sr(Fe ₃₀ Ti ₇₀)O _{3-δ}	4.1
0.50	7.381	1.997	1.996	*	*	*	Sr(Fe ₅₀ Ti ₅₀)O _{3-δ}	3.5
0.65	7.381	1.398	2.595	*	*	*	Sr(Fe ₆₅ Ti ₃₅)O _{3-δ}	4.3
*	*	*	→	*	*	*	Fe ₂ O ₃ [†]	7.8

4.3 Experimental details

4.3.1 Sample preparation

There are various approaches for the synthesis of complex oxides, e.g. the sol-gel method or the ‘ceramic method’. The perovskite samples for the catalytical investigation were prepared by the ceramic method. The basic compound is nominally pure SrTiO₃ which can be made from SrCO₃ and TiO₂. Four different dopants were used for the substitution on the B-site: Fe, Sc, Co and Mn, in the form of Fe₂O₃, Sc₂O₃, Co₃O₄ and MnO, respectively. The stoichiometry of the samples was calculated in such a way that the total B-site occupancy is 1, i.e. Sr(M_xTi_{1-x})O_{3- δ} where x denotes the dopant content. The masses of the educts were determined by the condition that the total mole number of the final product is $n_{total} = 0.05$ mol, see Table 4.1. The oxygen non-stoichiometry δ in Sr(M_xTi_{1-x})O_{3- δ} depends on the type and amount of dopant, temperature and P_{O_2} treatment. After the mixing of all educts in correct proportions in an agate mortar, the samples have been fired at 1200 °C for 2 hours in alumina crucibles, followed by ball milling (in a zirconia ball mill) for one hour. In order to assure complete reaction three more steps have been performed: firing at 1300 °C for 4 hours, ball milling for 1 hour and final firing at 1300 °C for another 4 hours.

Characterization

X-ray diffractograms of all powder samples shown in Figure 2.2 of Chapter 2 indicate a single perovskite phase. The small peak broadening points towards large crystallites. The ICP-OES¹⁰ chemical analysis of representative samples showed correct composition. High-resolution transmission electron microscopy (HRTEM¹¹) was also used to characterize selected samples. In view of Chapters 2 and 3, two samples which represent two different iron content regions were chosen: in the low x region, $x = 0.003$, and in the high x region, $x = 0.2$ sample. The HRTEM images showed in Figures 4.1-4.4 were recorded randomly and they cannot fully represent the actual situation. However, since no large accidental difference has been found on a sample, one can believe that the findings represent the sample characteristics to a good extent. The HRTEM images have confirmed that the samples are crystalline and that they have perovskite structure, before as well as after the catalysis¹². It can be also observed that the outermost surface region shows good crystallinity (as seen also from various orientations). This is a very important finding, since all the models and results presented in Chapters 2 and 3 then apply to the samples for catalysis, as much as it is possible¹³. In the upper left image of Figure 4.1, the presence of a extended linear defect (possibly a dislocation) can be observed. This is the only example of a defective structure found. Also, energy dispersive x-ray (EDX) analysis was performed. In contrast to EDX systems which accompany scanning electron microscopes (SEMs), by the EDX¹⁴ unit of the HRTEM it was possible to analyze the composition of a sample in the very small (nano) volume which directly corresponds to the recorded image. Such an analysis can detect inhomogeneities on a nano-domain level. The EDX analysis of the samples in Figures 4.1-4.4. showed that the samples have the expected composition (within experimental uncertainty) on a nano level. In the bottom right images in Figures 4.1-4.4, it can be seen that the particles of the $x = 0.2$ sample tend to have smaller sizes than that of the $x = 0.003$ sample (both before and after catalysis). This contradicts the BET results (Table 4.1), since according to them, one would expect the opposite finding. This discrepancy can have at least three origins: (i) BET experimental errors, (ii) the particle ensembles in the images do not represent correctly the real particle distribution of the samples, or (iii) the HRTEM preparative method influences differently the particle division of the two samples ($x = 0.003$ and $x = 0.2$). The most probable explanation of the difference is a synergetic influence of all the three effects.

Catalyst preparation

In order to assure uniform and reproducible gas flow conditions through powder samples during catalytic reactions, the samples were subjected to the following procedure. The powder

¹⁰Inductively Coupled Plasma Optical Emission Spectrometry

¹¹measured on a Philips CM 30ST (300 keV, LaB₆ cathode)

¹²for convenience, the images of the samples after the catalytic reaction studied in Section 4.4 will be shown here

¹³the surface always differs from the bulk, but the difference would be much larger if the surface is amorphous

¹⁴Si/Li-EDX detector (Noran, Vantage System)

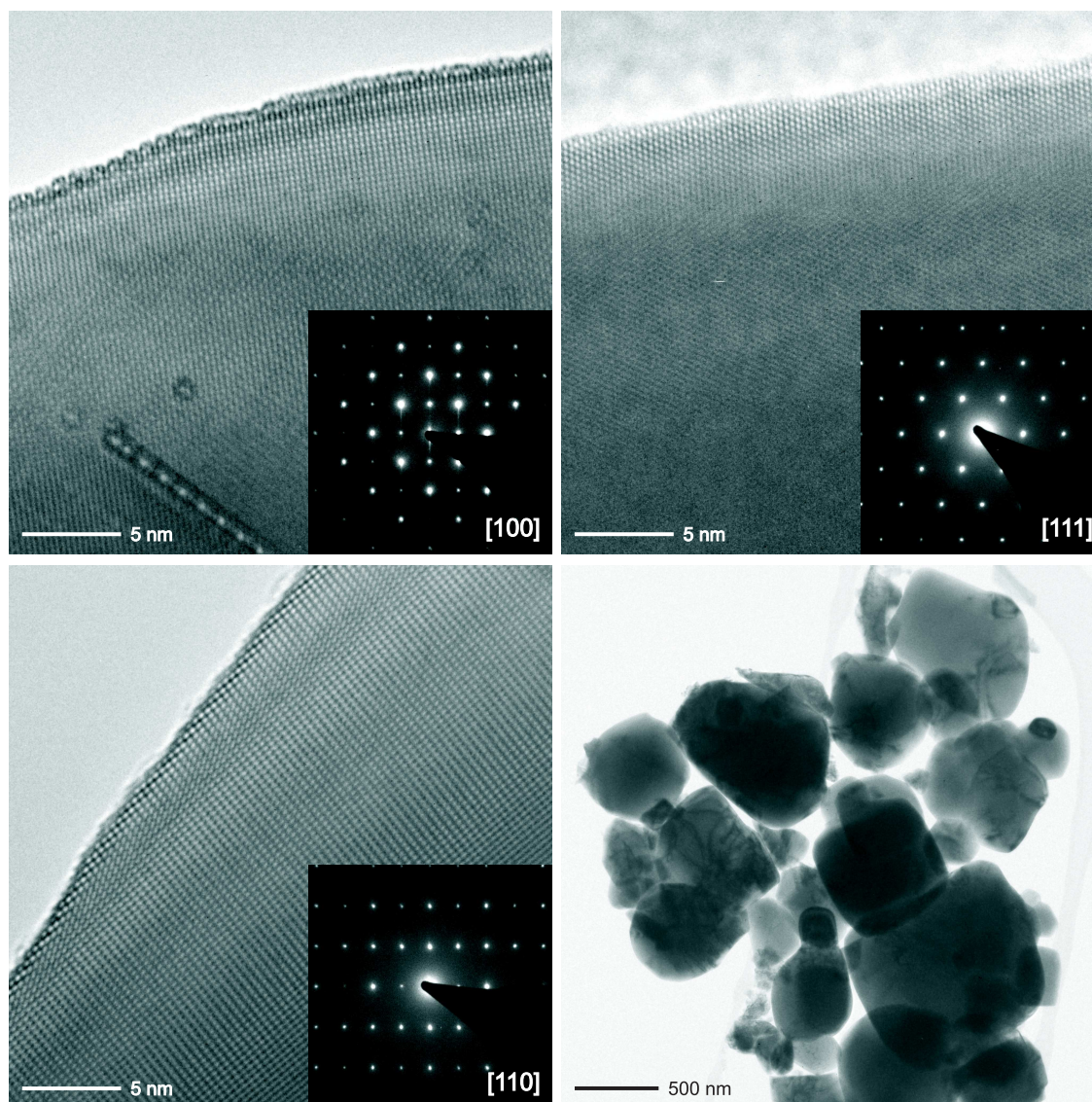


Figure 4.1: Before catalysis, $\text{Sr}(\text{Fe}_{0.003}\text{Ti}_{0.997})\text{O}_{3-\delta}$ HRTEM image. The images show good crystallinity of the sample particles, which extends to the surface of the particle.

samples have been isostatically cold pressed at about 400 MPa for 5 min and heated to ≈ 900 °C for about four hours to produce mechanically stable but still porous pellets (for Fe_2O_3 the temperature was 650 °C). The obtained pellets were carefully and repeatedly crushed in an agate mortar and sieved in fine stainless steel sieves to get particle sizes in the range between 100 μm and 250 μm . Thus all catalyst samples are regarded as the same physical medium through which the educt gas mixture will flow in the same manner during catalytic reactions.

Specific surface areas of the samples have been determined using the BET method [125] on a QUANTACHROME AUTOSORB-1 device. Before the measurements the samples were evacuated for more than 6 hours at 120 °C. Generally all samples have a relatively small specific surface area which is typical for the solid state preparation approach. The results are summarized in the rightmost column in Table 4.1.

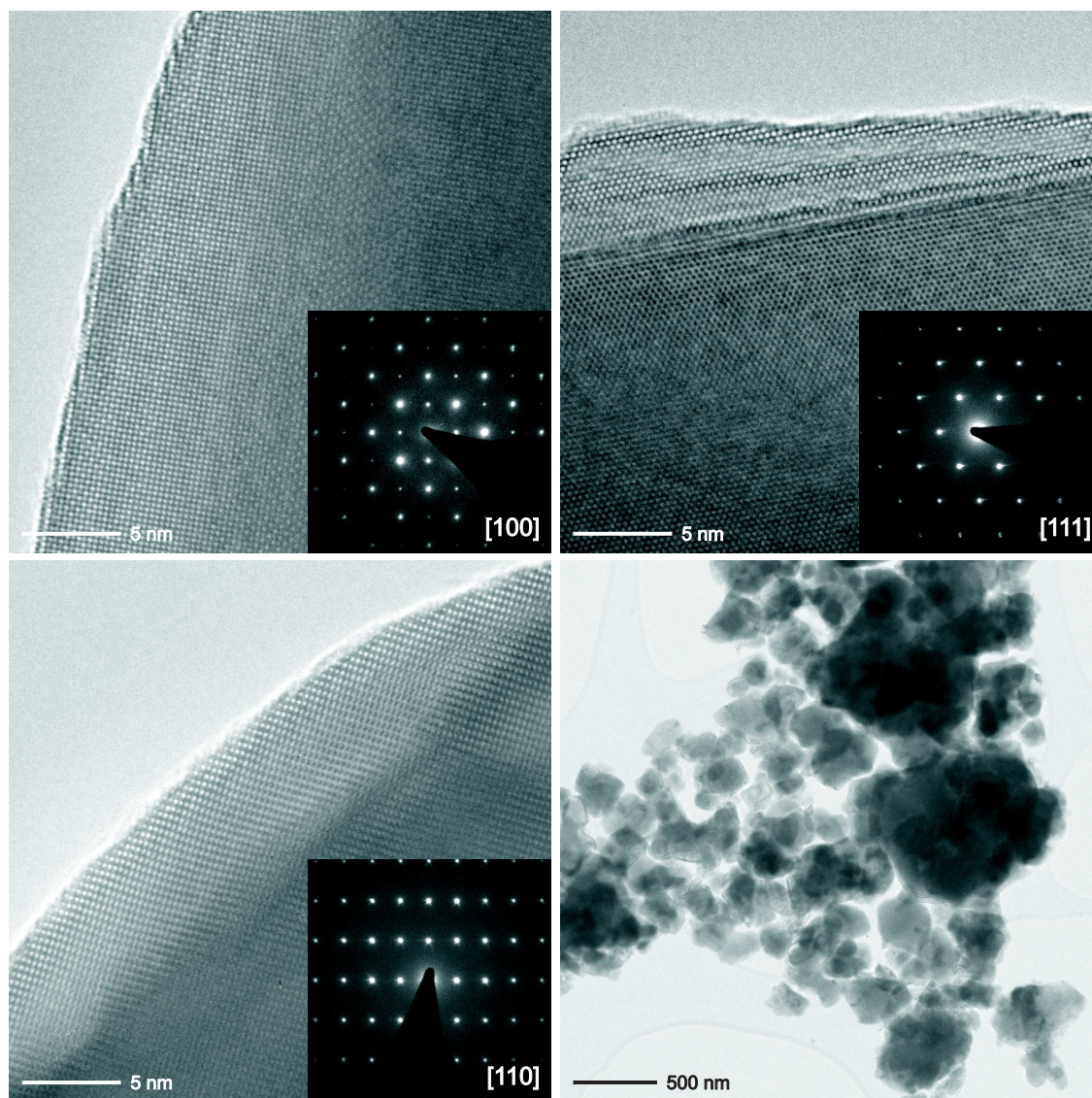


Figure 4.2: Before catalysis, $\text{Sr}(\text{Fe}_{0.2}\text{Ti}_{0.8})\text{O}_{3-\delta}$ HRTEM image. The images show good crystallinity of the sample particles, which also extends to the surface of the particle.

In heterogeneous catalysis the activity of a catalyst is proportional to its surface area. To make the catalytic measurements easily comparable between various catalysts, it is not sufficient that the reaction rates are normalized with respect to the surface area. Rather, it is necessary that the samples really have the same surface areas and therefore the conversions are of the same order of magnitude so that the detection of the products for all the catalysts occurs in a similar range of concentrations and temperatures. For practical reasons the amounts of samples have been chosen in such a way that all samples/catalysts have a surface area of $\approx 1 \text{ m}^2$. The change of the specific surface area upon catalytic cycling (five times repeated temperature program) was checked on the test sample, $\text{Sr}(\text{Fe}_{0.1}\text{Ti}_{0.9})\text{O}_{3-\delta}$, and no change was observed.

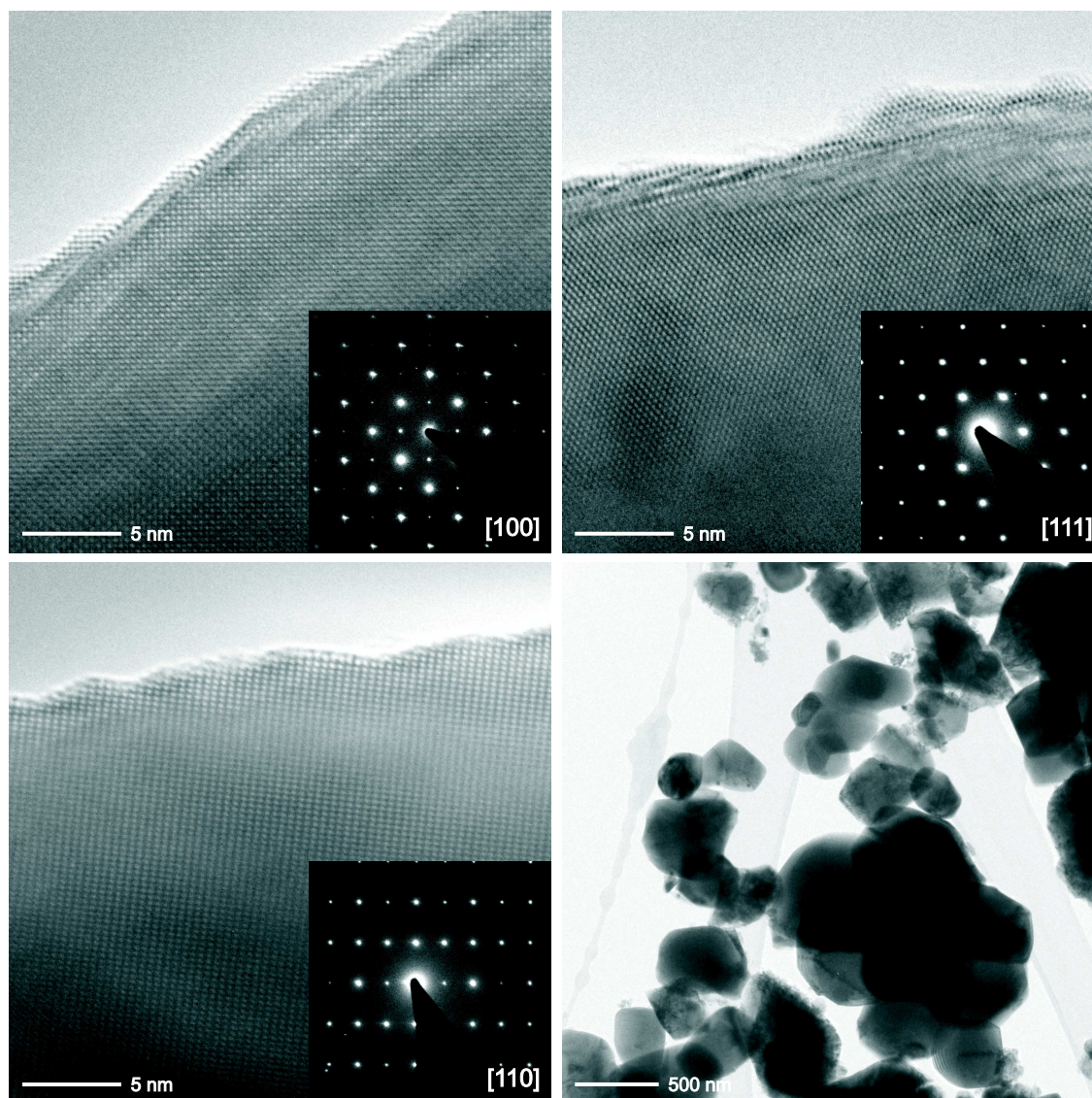


Figure 4.3: After catalysis, $\text{Sr}(\text{Fe}_{0.003}\text{Ti}_{0.997})\text{O}_{3-\delta}$ HRTEM image. A slight loss of sharpness can be observed at the surface, but the surface can still be considered as crystalline.

4.3.2 Experimental setup

Tubular (plug flow) reactor

All catalytic oxidation reactions were performed in a plug flow reactor operated at near 1 atm total pressure, schematically shown in Figure 4.5. The reactor was made of quartz glass with a total volume of about 100 cm^3 , divided into two concentric cylinders. The external cylinder at the top supplies a gas mixture into the inner cylinder and at the same time preheats the gas mixture. The catalyst samples were placed in the middle of the inner cylinder on a porous quartz frit of smaller pore size than that of the catalysts particle sizes. The diameter of the inner cylinder was of about 7.5 mm. To measure the temperature of the catalyst, a thermocouple element was placed as close as possible to the frit (from the bottom) in a

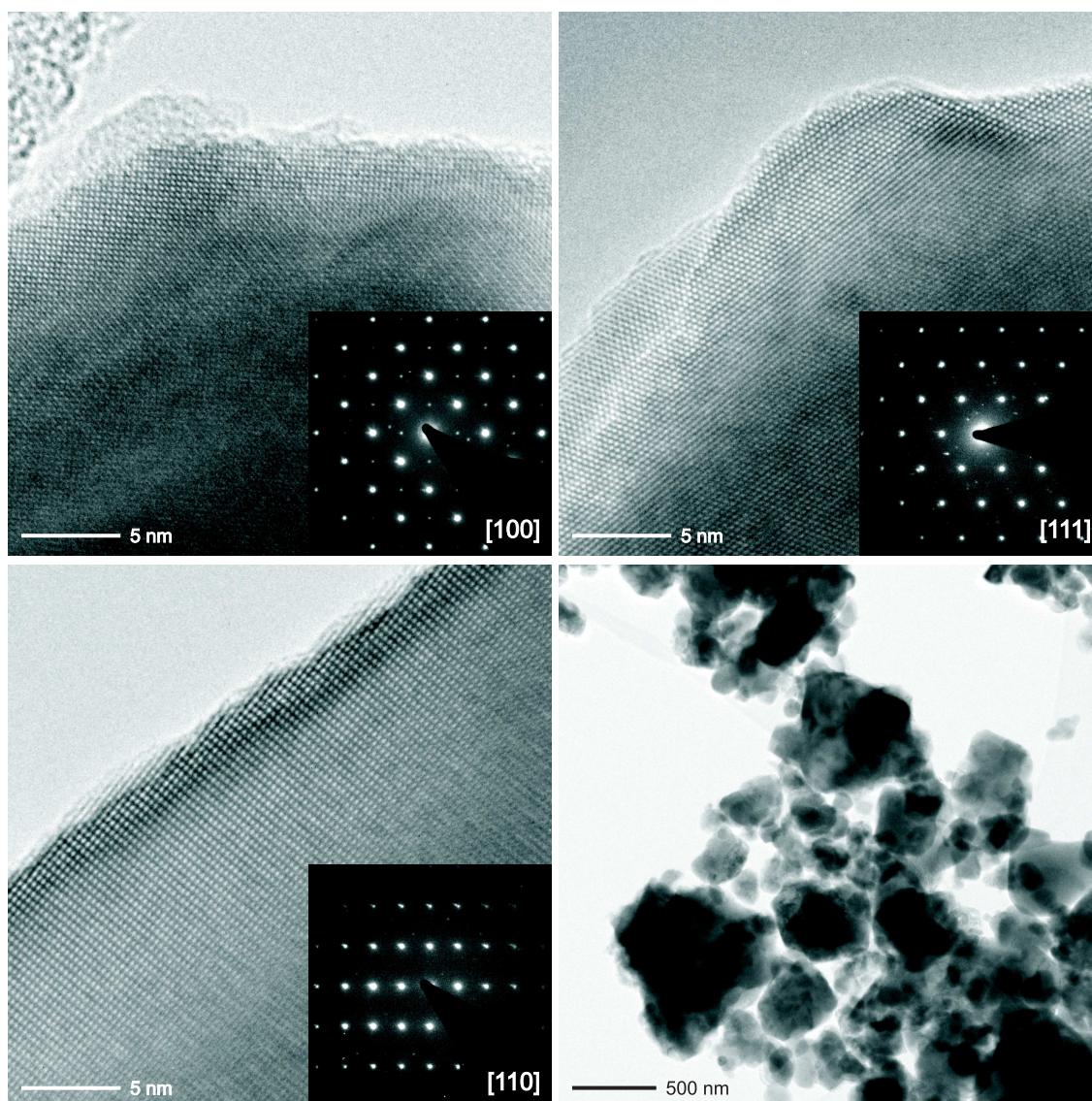


Figure 4.4: After catalysis, $\text{Sr}(\text{Fe}_{0.2}\text{Ti}_{0.8})\text{O}_{3-\delta}$ HRTEM image. Also, a slight loss of sharpness can be observed at the surface, but the surface can still be considered as crystalline.

separate quartz capillary. Due to the separation by two glass parts, the thermoelement could show a offset in the temperature value. However, this effect is of the same sign and magnitude for all measurements and therefore is of no importance for the comparison of the catalytic activity for different samples. The cylindrical part of the reactor was placed into a furnace driven by a EURO THERM 903P temperature controller. The temperature was stable within 1°C .

Gas mixing

Different gas mixtures of educts were formed using AERA and Tylan Mass Flow Controllers (MFCs) with Tylan readout boxes. Each MFC was manually calibrated for a particular gas by measuring the series of elapsed times needed by the gas to fill a test volume (at the atmospheric

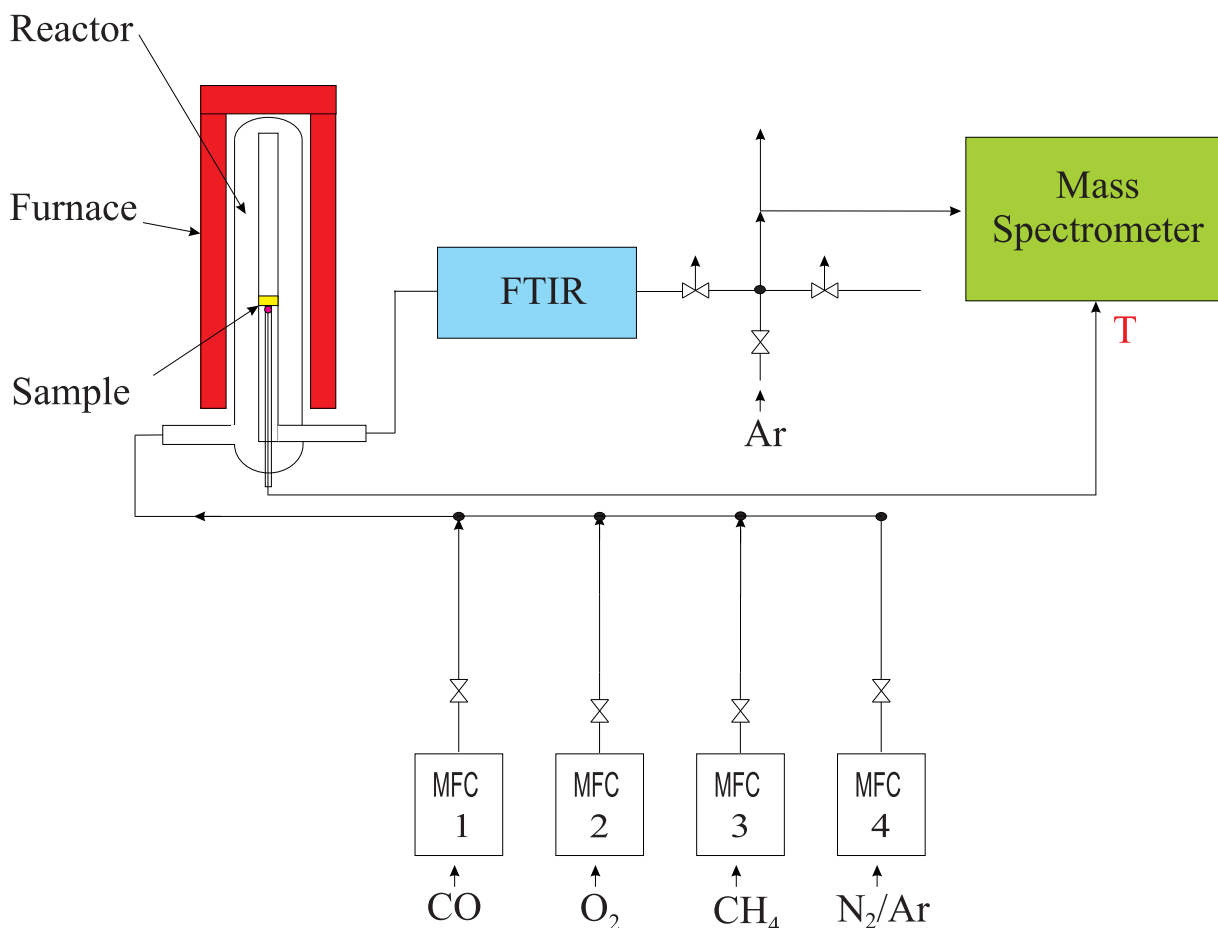


Figure 4.5: The plug flow reactor and the experimental setup.

pressure) at different flow rates. The gas tubes used before the reactor were mainly 6 mm Swagelok stainless steel pipes with the inner diameter of 4 mm; after the reactor, some of the gas tubes were made of Teflon or stainless steel pipes, both with the inner diameter of about 2 mm to minimize the dead volume between reactor and gas analysis devices. Swagelok valves were used for switching and redirecting the gas flows. Since the maximal water partial pressure under all reaction conditions was always lower than 23 mbar no water condensation was expected and therefore the gas tubes were not heated.

Gas analysis

Mass spectrometer (MS) and measurements. For the reactant/product gas analysis a BALZERS Prisma 200 quadrupole mass spectrometer (QMS) was used. Gas atoms/molecules are ionized by an electron beam in an ionizing chamber of the QMS. By such a process, ionized atoms and/or ionized molecules and their fragments are produced. The accelerated ionization products are separated with respect to their mass-to-charge ratio (m/q) in an alternating electric field and are separately collected and recorded as anodic currents. In the case of a

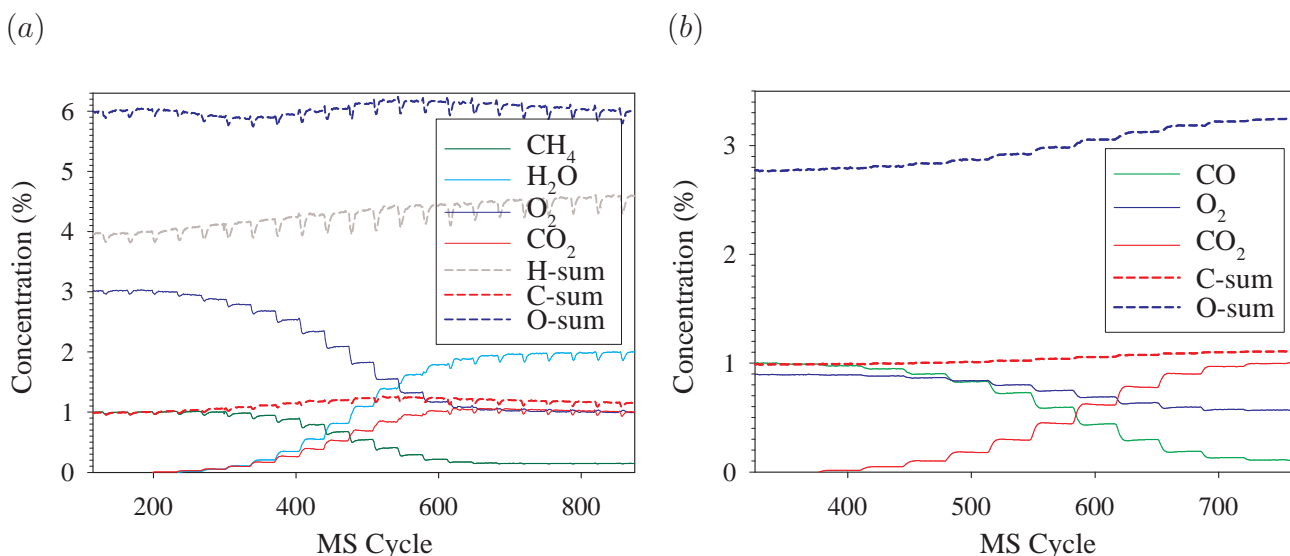


Figure 4.6: MS mass balance for the reaction on $\text{Sr}(\text{Fe}_{0.1}\text{Ti}_{0.9})\text{O}_{3-\delta}$: (a) for CH_4 and (b) for CO oxidation reactions.

pure gas, the main component is usually the singly ionized atom/molecule. The total pressure inside the MS and its stability determines the ionizing conditions in the chamber and, hence, influences levels of all measured components. Usually the longer the measurement, the bigger the drift, which could be 10 to 20 % for a 12 hour measurement, but which can be taken into account and corrected in data analysis.

The character of the QMS measurements influenced the selection of carrier gases for the reactions [Eq. (4.2)]. Since nitrogen has a main component well separated from reactant/product components it was used as the carrier gas in CH_4 oxidation. However, nitrogen is not suitable in CO oxidation for the carrier gas because it has the same m/q as the main ionization component of CO (both have $m/q = 28$). Argon was therefore used as the carrier gas in the CO oxidation.

CO_2 is the product in both reactions, Eq. (4.2). Its main component appears at $m/q = 44$ and the corresponding ionic current I_{44} was recorded (as well as currents of other components). All ionic currents are proportional to the concentrations of their atomic/molecular gas “parents” assuming no reactions of ionized particles in the ionizing chamber. In the case of CH_4 or CO oxidation, I_{44} is directly proportional to the CO_2 concentration and was used for the determination of conversions in the following manner. Before and after each reaction the reaction gas mixture was passed through the cold reactor (no reaction) long enough to get baseline currents $I_{m/q}$. The reactions were then performed as described in Section 4.4.1, and $I_{m/q}(T)$ currents were recorded. After these measurements, the I_{44} values were corrected to the baseline. The maximum value of I_{44}^{max} which corresponds to the full conversion (checked also by FTIR) was read out from the data. The whole series of $I_{44}(T)$ currents was divided by I_{44}^{max} which yielded as the result conversion vs. temperature curves.

As a test of the validity of MS measurements it was advisable to plot the C, H and O

balance of reactants and products during the course of a catalytic reaction. To do this, MS current calibration coefficients are needed. The coefficients are ratios of known concentrations and their measured $I_{m/q}$ currents. For example, the calibration coefficient for methane is

$$K_{\text{CH}_4} = \frac{[\text{CH}_4]_0}{I_{16}^0} \quad (4.29)$$

where $[\text{CH}_4]_0$ is the nominal methane concentration and I_{16}^0 its measured current (both at zero conversion). An unknown methane concentration during a measurement can be obtained as $K_{\text{CH}_4} * I_{16}$, where I_{16} is the actual measured current (after the baseline correction). The coefficients and therefore concentrations for all gas components are obtained in this way. Each gas component has a certain number of (different) atoms, and the number of each atomic species present in the mixture at any instant of a measurement must be constant (mass conservation). For methane oxidation the quantity proportional to the number of oxygen atoms present at any instant is

$$2[\text{O}_2] + 2[\text{CO}_2] + [\text{H}_2\text{O}] = \text{constant} \quad (\text{O} - \text{sum}), \quad (4.30)$$

or, for CO oxidation

$$[\text{CO}] + 2[\text{O}_2] + 2[\text{CO}_2] = \text{constant} \quad (\text{O} - \text{sum}). \quad (4.31)$$

These sums and sums for other atomic species for the measurements done on $\text{Sr}(\text{Fe}_{0.1}\text{Ti}_{0.9})\text{O}_{3-\delta}$ are shown in Figure 4.6. It can be seen in these figures that even though the concentration profiles of the gas components change in each temperature step, the overall atomic sums vary only slightly as the baseline drifts over the course of the measurement, which may last for more than six hours. The maximal change is of about 10 %. This proves that the MS operated properly and the measurements are valid.

FTIR spectrometer calibration and measurements. Additionally to QMS for the detection and monitoring of the educt/product gas concentrations a BRUKER VECTOR 22 Fourier Transform Infrared (FTIR) Spectrometer was also used. FTIR spectroscopy provides a quick insight into the gas composition by visually judging the current IR-peak intensities. This is possible because in our case the characteristic IR spectra of the educts and products are well-separated. FTIR is especially suited to show that no high-molecular byproducts (which are difficult to identify by QMS) are present in the outlet gas; gases such as O_2 , N_2 , He and Ar cannot be detected. The H_2O and CO_2 from the atmosphere contribute to a slow drift of the baseline of measured IR spectra which can be corrected.

To get quantitative information about the composition of a gas mixture, a calibration of the FTIR spectrometer is needed. The patterns of gases measured in this study do not overlap which makes the analysis easy. The spectra were measured in absorbance mode and the peak intensity (i.e. the integrated area under the peak with an appropriate baseline correction if needed) is proportional to the concentration of the respective gas component. Hence, the characteristic peaks were chosen for each gas component and their intensities were measured for different known gas concentrations. The best linear fit of these data was used as the particular gas calibration curve.

Table 4.2: Temperature program for TG

segment	from [°C]	to [°C]	rate [°C/min]	hold duration [min]
1	25	750	10	30
2	750	600	3	0
3	600	450	1.5	0
4	450	350	0.7	30
5	350	450	0.7	0
6	450	600	1.5	0
7	600	750	3	30

4.3.3 Thermogravimetry

Thermogravimetry (TG) is a thermal analysis technique whereby the weight of a substance in an environment heated or cooled at a controlled rate is recorded as a function of time or temperature. In this work a NETZSCH STA499C thermobalance coupled with a QMS was used. A typical temperature-programmed measurement was performed as follows. A sample was placed on a flat Al_2O_3 sample holder which provides a better sample–gas contact, or into a quartz crucible when the sample–gas contact was not a critical issue. The sample and its holder were placed on the thermobalance, the system was closed, and a gas of the desired composition (3 % of O_2 in N_2 , total flow of 40 ml/min) was let through the system. The temperature program was composed of the segments given in Table 4.2. The weight change of the sample was recorded during the temperature program. As a matter of fact, the recorded weight change did not come entirely from the sample, but from the sample with the sample-holder due to complicated buoyancy effects. To extract the sample weight change, an additional second measurement with the empty sample holder was performed at the very same conditions. The sample weight change as a function of temperature is then obtained by subtraction of the first and second measurement. The sample weight change can be converted into the oxygen stoichiometry change $\Delta\delta$, if the sample mole number is known. The mole number and the δ reference point necessary for the absolute oxygen nonstoichiometry calculation were obtained from the weight change after switching the gas mixture to 8 % H_2 in N_2 at 750 °C. This procedure has reduced all Fe to Fe^{3+} , and thus fixed the oxygen nonstoichiometry according to Eq. (2.4) to $\delta = x/2$. The oxygen nonstoichiometry curve for $\text{Sr}(\text{Fe}_{0.5}\text{Ti}_{0.5})\text{O}_{3-\delta}$ is given in Figure 2.4 of Chapter 2. The starting gas composition as well as evolved gases (due to a previous adsorption on the sample, sample holder, walls of the thermobalance, or from a chemical reaction occurring) were monitored by QMS. From the coincidence of the sample weights recorded in cooling and heating cycles it can be concluded that the cooling/heating rate was slow enough to allow full equilibration of the sample with the gas phase.

P_{O_2} -dependent measurements were performed in order to investigate how a sample “responses” to different oxygen partial pressures at 400 °C and 600 °C. These temperatures allows a fast sample equilibration with the surrounding gas phase. The total gas flow was 40 ml/min. Usually the P_{O_2} was switched between: 0.001, 0.0025, 0.0075, 0.03 and 0.1 bar O_2 in N_2 . As in

the case of temperature-dependent measurements, each measurement was repeated with the empty sample holder at the same conditions. The results for the $\text{Sr}(\text{Fe}_{0.5}\text{Ti}_{0.5})\text{O}_{3-\delta}$ are given in Figure 2.4 (green circles). For given oxygen deficiency δ , it is possible to calculate concentrations of Fe^{3+} and Fe^{4+} species, i.e. $[\text{Fe}^{3+}]$ and $[\text{Fe}^{4+}]$ for each pressure, respectively. From the plots $\log [\text{Fe}^{3+}] - \log P_{\text{O}_2}$ and $[\text{Fe}^{4+}] - \log P_{\text{O}_2}$, the oxygen partial pressure dependencies of $[\text{Fe}^{3+}]$ and $[\text{Fe}^{4+}]$ were obtained for the temperature range approximately from 400 °C to 600 °C

$$[\text{Fe}^{3+}] \sim P_{\text{O}_2}^{-0.07} = P_{\text{O}_2}^{-a} \quad (a = 0.07), \quad (4.32)$$

$$[\text{Fe}^{4+}] \sim P_{\text{O}_2}^{0.03 \div 0.07} = P_{\text{O}_2}^{+b} \quad (b = 0.03 \div 0.07). \quad (4.33)$$

$[\text{Fe}^{3+}]$ decreases with increasing P_{O_2} , and therefore there is a minus sign in the exponent. The exponent a stays approximately constant in the whole temperature range. This finding will be used in the discussion of kinetics models in Section 4.5. $[\text{Fe}^{4+}]$ increases with increasing P_{O_2} , however its exponent b increases approximately from 0.03 to 0.07 with increasing temperature over the studied range.

in situ TG

To investigate if the presence of CO or CH_4 , i.e. if the oxidation reaction of those molecules, influences oxygen stoichiometry of the same sample, additional *in situ* measurements under reaction conditions were performed. CO oxidation and CH_4 oxidation were performed in oxygen excess with the same temperature program but with the following gas compositions¹⁵: 0.75 % of CO and 1.5 % of O_2 in Ar for CO oxidation, and 1 % of CH_4 and 3 % O_2 in N_2 for CH_4 oxidation. The total flow for both reactions was 40 ml/min. No influence of CH_4 oxidation on the oxygen stoichiometry was observed. However, CO oxidation over the catalyst caused a significant change of the oxygen stoichiometry (which will be further discussed in Section 4.4.3).

in situ ESR

In the case of $\text{Sr}(\text{Fe}_x\text{Ti}_{1-x})\text{O}_{3-\delta}$ materials, a stoichiometry change is accompanied by a corresponding change of the iron valence state population (e.g. number of Fe^{3+} centers increases upon reduction). For a stoichiometry change of a $\text{Sr}(\text{Fe}_x\text{Ti}_{1-x})\text{O}_{3-\delta}$ sample, one therefore expects a change in ESR¹⁶ spectra of the ESR active centers (Fe^{3+} , high spin d^5) in the sample. A sample representative of low iron doped samples was chosen, specifically the $\text{Sr}(\text{Fe}_{0.003}\text{Ti}_{0.997})\text{O}_{3-\delta}$, since for low iron content the TG is not sensitive enough to detect the $[\text{Fe}^{3+}]/[\text{Fe}^{4+}]$ ratio changes (besides, conducting and magnetic materials are not well-suited for ESR measurements). CH_4 and CO oxidation reactions were performed *in situ* during high-temperature ESR measurements recorded on a BRUKER ESR Spectrometer equipped with a ER 041 XG microwave bridge (X-band). The sample was placed on the bottom of

¹⁵as close as possible to those gas compositions used in catalytic measurements, see Section 4.4.1

¹⁶Electron Spin Resonance

a quartz capillary, and a second capillary for the gas mixture supply was dipped into the sample. They were positioned in the center of the high temperature microwave cavity of the ESR spectrometer. First, ESR spectra (originating from Fe^{3+}) were recorded in 3 % O_2 in N_2 mixture. After the sample equilibration, 1 % CH_4 was also added to the mixture (in the case of CO oxidation, the concentrations were 11 % O_2 in N_2 and additional 1 % of CO). Measurements were performed at various conversions, i.e. at different temperatures in the range of 400 °C to 650 °C. The catalytic reaction at the surface of the sample, be it methane or carbon monoxide oxidation, apparently did not change the ESR spectra. Since the measurements were performed under significant limitations due to the spectrometer construction, the results may not represent the true picture.

4.4 Reactions and Results

In order to investigate the catalytic activity of various samples the same procedure was used in separate experiments for both test reactions. Before reactions with catalysts the activity of the empty reactor was tested and it was proved to yield negligible conversion in the studied temperature range. An appropriate amount of catalyst samples (having a surface area of $\approx 1 \text{ m}^2$) was placed in the plug flow reactor.

4.4.1 Reaction conditions

Temperature dependence

Temperature-dependent measurements were done in order to obtain the activities and the activation energies of the samples. All reactions were performed under the condition of oxygen excess, the ratios being $\text{CH}_4 : \text{O}_2 = 1 \% : 3 \%$ and $\text{CO} : \text{O}_2 = 1 \% : 2 \%$ in methane and carbon monoxide oxidation, respectively. The total glass flow of the gas mixture through the catalyst bed was about 83.5 ml/min. Before the first catalytic measurement each sample was annealed at 850 °C for 30 min in the reaction gas mixture. This ensures that the remaining activity is stable upon temperature cycling. The temperature program for the reactions comprised of temperature plateaus of 20 minutes duration which was long enough to obtain steady state operation. The temperature was normally raised in steps of 25 °C, or in steps of 50 °C where conversions were weak functions of temperature. For methane oxidation starting temperatures (still zero conversion) were in the range of 350 to 500 °C for most active and least active catalysts, respectively, and the end temperature was 775 °C (full conversion). For carbon monoxide oxidation starting temperatures (still zero conversion) ranged between 275 and 375 °C for most active and least active catalysts respectively, and end temperatures ranged from 500 to even 850 °C (full conversion) for most active and least active catalysts, respectively. The activation energies were obtained from the slopes of the $\ln(-\ln(1-X))$ vs. $1/T$ plots [Eq. (4.28)] using the data up to a conversion of $X = 0.5$.

From measured conversions it is possible to calculate the TOFs of catalysts. The $\frac{dn}{dt}$ factor

Table 4.3: Gas mixtures for the measurements of partial reaction orders of reactants.

	m-experiment							n-experiment						
Methane oxidation	CH ₄ reaction order							Oxygen reaction order						
Oxygen [mbar]	120							15	20	30	60	90	120	150
CH ₄ [mbar]	5	7.5	10	15	20	30	40	5						
CO oxidation	CO reaction order							Oxygen reaction order						
Oxygen [mbar]	10							10	15	25	40	70	100	
CO [mbar]	1	1.5	2.5	4	7	10		8						

from Eq. (4.1), under above described conditions, is given as the product of the reactant (CH₄ or CO) molecule flow and the conversion. Since the nominal CH₄ and CO concentration are the same, this factor is the same for both reactions, viz. $\approx 3.74 \times 10^{17} \text{s}^{-1} \times X$. The number of active centers per 1 m² of surface area can be estimated by the ratio of the dopant concentration and the square of the SrTiO₃ lattice constant, $S \approx 6.55 \times 10^{18} \text{m}^{-2} \times x$, under the assumption that each dopant ion represents an active center. The TOFs can then be estimated for any catalyst only from x and X as

$$\text{TOF} \approx 0.057 \text{s}^{-1} \times \frac{X}{x} \quad (4.34)$$

where X is conversion and x is dopant content. Note that it does not depend on the measured specific surface area since the amounts of catalyst were chosen in such a way as to have the same total surface area of 1 m².

Concentration dependence—partial reaction orders

For each sample, reaction rates dependent on CH₄ and O₂, and CO and O₂ partial pressures were measured. Thus, the partial reaction orders as defined in Eqs. (4.16) were obtained from log – log plots [Eq. (4.19)]. In all measurements the total gas flow was 83.5 ml/min, the specific partial pressures are given in Table 4.3. Temperature was kept constant in each pair of measurements, (CH₄, O₂) or (CO, O₂), but it varied for different catalysts since it was tuned such that the reaction rate did not exceed 10 % of the full conversion. Note that the experiments were performed at $P_{\text{O}_2}/P_{\text{CO}} \geq 1$ in order to prevent a potential carbon layer building at the catalyst surface.

Reaction control versus diffusion control

In flow systems, for not too fast reactions, the apparent reaction rate at lower temperatures is usually by the local reaction (reaction controlled or chemically controlled). However, upon increasing temperature the intraparticle (pore) gas diffusion and mass transfer processes tend to take control over the reaction (*diffusion* controlled), i.e. they tend to become the rate

determining processes. This is a consequence of the fact that the reaction rate is a temperature-activated process with the exponential form of $e^{-E_a/RT}$ increasing faster with T than the diffusion coefficient whose temperature dependence is proportional to \sqrt{T} . This will cause the appearance of two different activation energies in the $\ln k$ vs. $(1/T)$ plot, where in the high temperature region the intraparticle diffusion will give an apparent activation energy of one-half the actual kinetic activation energy, $E_a/2$ [105]. At even higher temperatures, mass transfer through the gas phase starts to dominate and the apparent activation energy will be less than half the slope of the chemically controlled regime. It should also be kept in mind that upon temperature increase a reactor operating in the differential mode could slide into the integral mode.

In this work, according to test measurements with varying residence time (different amounts of catalyst) on the $\text{Sr}(\text{Fe}_{0.1}\text{Ti}_{0.9})\text{O}_{3-\delta}$ sample, both methane and carbon monoxide reactions were chemically controlled and the reactor operated in the differential mode at least up to conversions of 0.1 or more.

4.4.2 Reaction results: methane oxidation

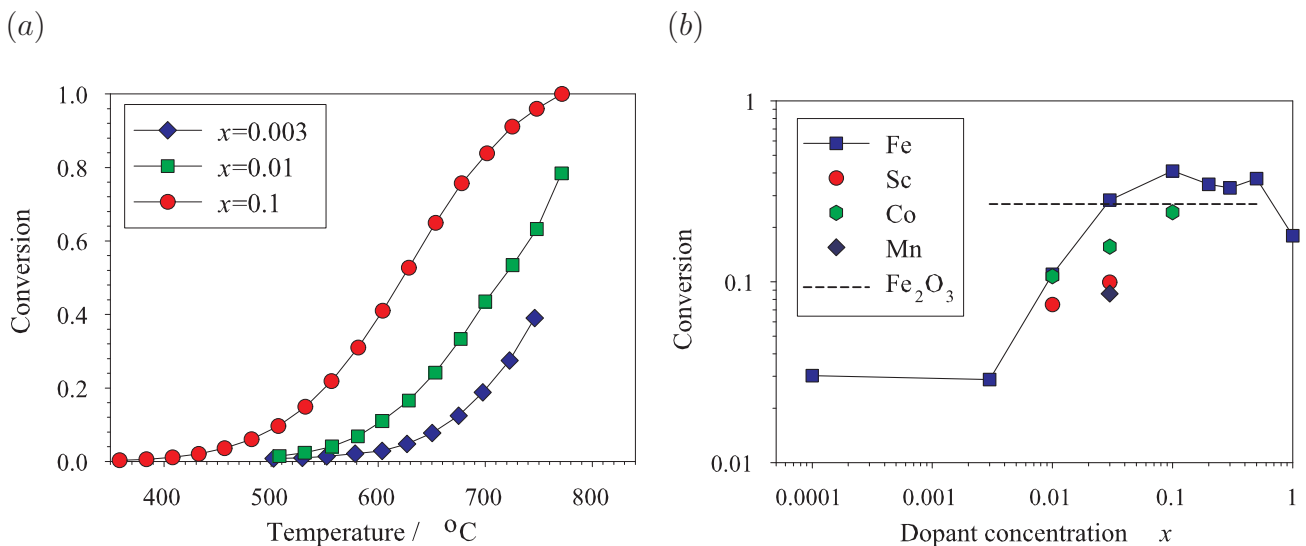


Figure 4.7: Methane oxidation, (a) Conversion as a function of temperature, (b) Comparison of activities (conversions given in logarithmic scale) at 600 °C as a function of dopant concentration.

The results of methane oxidation reactions obtained from temperature and concentration dependent measurements are given in this section.

Temperature dependence

In Figure 4.7 (a) the conversion as a function of temperature is given for representative samples. It can be seen that the least active sample is the one with the smallest iron content, $\text{Sr}(\text{Fe}_{0.003}\text{Ti}_{0.997})\text{O}_{3-\delta}$. Even at the high end temperature (≈ 750 °C) the conversion for this

sample did not exceed 0.4 (i.e. 40 % of full conversion). The $\text{Sr}(\text{Fe}_{0.01}\text{Ti}_{0.99})\text{O}_{3-\delta}$ showed already higher activity and at ≈ 750 °C its conversion was 0.6. The most active sample was $\text{Sr}(\text{Fe}_{0.1}\text{Ti}_{0.9})\text{O}_{3-\delta}$, for which conversion of 0.1 was attained at temperatures as low as ≈ 500 °C, and it reached full conversion at ≈ 750 °C. Because the results for other samples of the $\text{Sr}(\text{Fe}_x\text{Ti}_{1-x})\text{O}_{3-\delta}$ series closely follow the described trends they are omitted in Figure 4.7 (a) for clarity.

To compare the activities of catalysts, the conversions at 600 °C are given in Figure 4.7 (b) in logarithmic scale in order to emphasize relative differences between the samples. It can immediately be seen that the activity of $\text{Sr}(\text{Fe}_x\text{Ti}_{1-x})\text{O}_{3-\delta}$ strongly depends on the iron content x . Two regions are observed: one with low activity for low x , and second with high activity for $x \geq 0.1$. The iron contents where the transition between the two takes place are $0.01 \leq x \leq 0.03$. The activity of Fe_2O_3 is represented with the horizontal dotted line (the dopant concentration x has no meaning for this sample). Its activity is close to that of $\text{Sr}(\text{Fe}_x\text{Ti}_{1-x})\text{O}_{3-\delta}$ for high x . The Co-doped samples also show an increase in activity with increasing x , but slightly less pronounced. The Sc- and Mn-doped samples show a slight increase of activity in comparison to very low iron doped samples, but they are less active than the corresponding $\text{Sr}(\text{Fe}_x\text{Ti}_{1-x})\text{O}_{3-\delta}$ samples for the same x .

According to Eq. (4.34), $\text{Sr}(\text{Fe}_{0.03}\text{Ti}_{0.97})\text{O}_{3-\delta}$ has $\text{TOF} \approx 0.54 \text{ s}^{-1}$ at 600 °C [conversion of about 0.28, as seen from Figure 4.7 (b)]. Due to the factor $\frac{X}{x}$ in Eq. (4.34), TOFs are ‘enhanced’ in regions where $X \geq x$. The obtained activation energies are plotted in Figure 4.8.

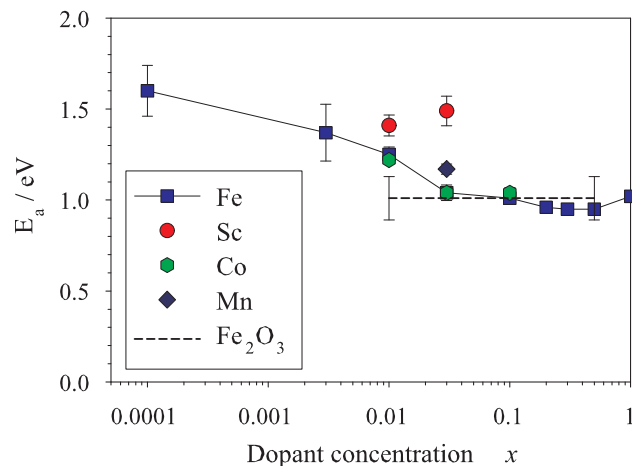


Figure 4.8: Methane oxidation. Activation energy as a function of dopant concentration. Error bars were determined from data scatter in the $\log x$ vs. $1/T$ plot for each sample.

With increasing iron content the activation energy monotonically decreases down to ≈ 1 eV (for $x \approx 0.1$), and for $x \geq 0.1$ it takes a constant value slightly less than 1 eV. This observation also supports the fact that there are two activity regions: low activity for $x \leq 0.01$, and high activity for $x > 0.01$, see Figure 4.7(b). Only Sc-doped samples have higher activation energies

in comparison with other corresponding samples, and they are comparable to low iron-doped SrTiO_3 .

In the repeatedly measured CH_4 oxidation reactions no change of the catalytic activity was observed. The temperature program was repeated five times on $\text{Sr}(\text{Fe}_{0.1}\text{Ti}_{0.9})\text{O}_{3-\delta}$ as representative test sample. In addition, the same sample showed no change of activity during 6 hours at $600\text{ }^\circ\text{C}$. The specific surface area of the sample did not change upon cycling, either. The same behavior can be reasonably well assumed for the other samples also.

Concentration dependence—Partial reaction orders

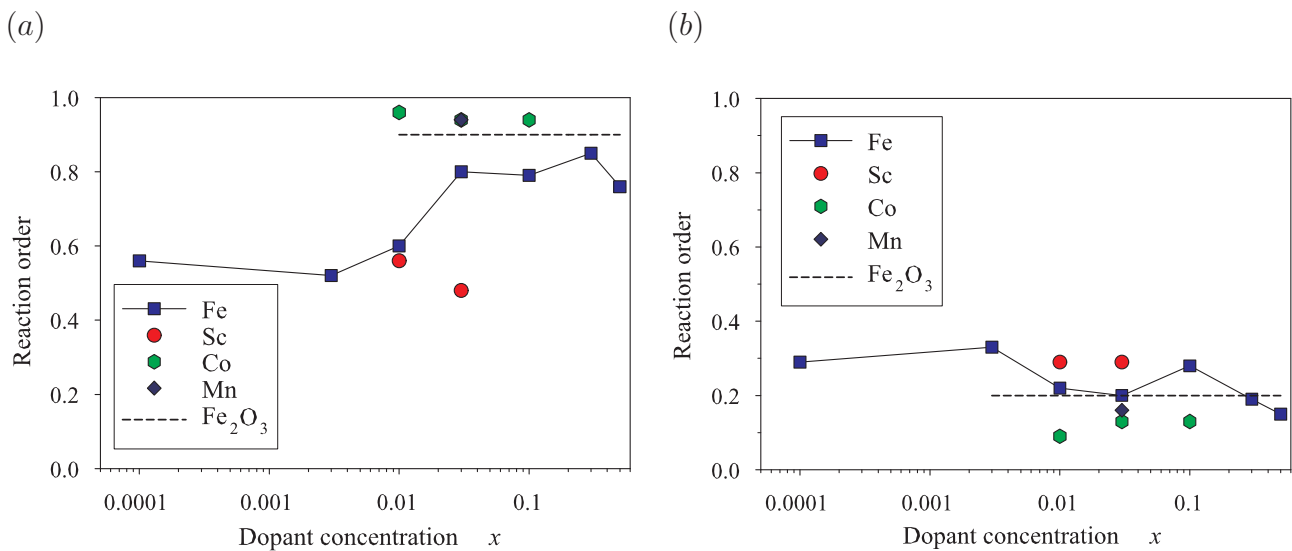


Figure 4.9: Methane oxidation, partial reaction order as function of dopant concentration, (a) m -for methane, (b) n -for oxygen. The measurements were performed at temperatures approximately between 500 and $650\text{ }^\circ\text{C}$.

The methane partial reaction order m , given in Figure 4.9 (a), significantly varies with x in $\text{Sr}(\text{Fe}_x\text{Ti}_{1-x})\text{O}_{3-\delta}$. It shows also two different regions with the change occurring in the same x range as the activity does. The Sc-doped samples show again a similar behavior as the low iron doped SrTiO_3 , while the other samples show an approximately constant partial reaction order which is slightly higher than that of the iron containing samples. In Figure 4.9 (b), the oxygen partial reaction order n has values scattering around $n=0.2$ for $x \geq 0.01$, but incidentally one sees an indication that the Sc-doped samples again level off to the values of the low iron containing samples. Although some trends can be observed, no strong conclusions should be made for the oxygen reaction order here due to the large data scatter (large relative errors).

For convenience, to compare the results for different transition metal ions present in the host material SrTiO_3 , the activation energy E_a , conversion X at $600\text{ }^\circ\text{C}$ and CH_4 partial reaction order m for $x=0.03$ are given in Figure 4.10.

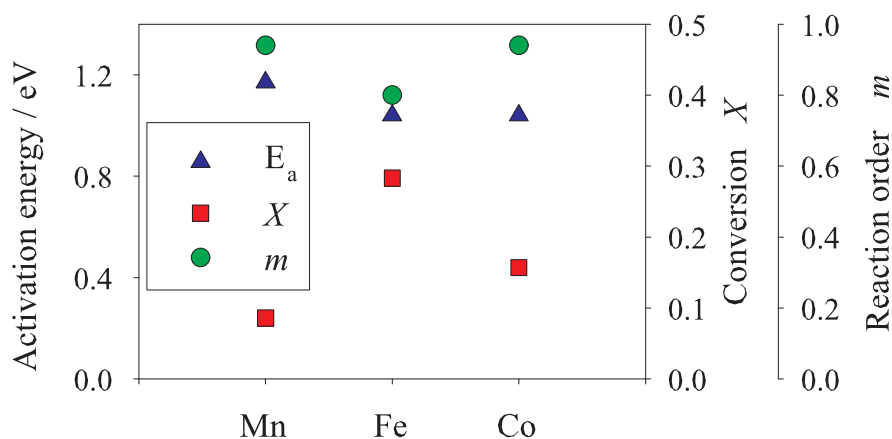


Figure 4.10: Methane oxidation, the comparison of relevant results for Mn-, Fe- and Co-SrTiO₃ samples at $x=0.03$.

in situ TG and ESR

In order to check whether the reaction at the surface (in a steady state) can induce a bulk oxygen stoichiometry change, the methane oxidation reaction was performed on a high iron content sample $[(\text{Sr}(\text{Fe}_{0.5}\text{Ti}_{0.5})\text{O}_{3-\delta})]$ *in situ* during a TG measurement with the same temperature program as explained in Section 4.3.3. According to the obtained results, the CH₄ oxidation occurring at the surface did not influence the bulk oxygen stoichiometry in the stationary state. Also, the CH₄ oxidation reaction was performed *in situ* during high-temperature ESR measurements on a low iron content sample representative, $\text{Sr}(\text{Fe}_{0.003}\text{Ti}_{0.997})\text{O}_{3-\delta}$. Measurements were performed at various conversions, i.e. at different temperatures. The catalytic reaction at the surface of the sample apparently did not change the ESR spectra. These give an indication that ongoing CH₄ oxidation does not affect the gas phase-bulk equilibrium of the samples, both in low x and high x range, at least for the investigated CH₄/O₂ composition range.

Chemical capacity

The ability of $\text{Sr}(\text{Fe}_x\text{Ti}_{1-x})\text{O}_{3-\delta}$ to supply ‘stored’ oxygen species for the reaction in the absence of oxygen in the gas phase was tested on the $\text{Sr}(\text{Fe}_{0.5}\text{Ti}_{0.5})\text{O}_{3-\delta}$ sample. The sample was allowed to reach the stationary state of the reaction with the normal reaction gas mixture at 500 °C. To check the response of the system, the CH₄ supply was switched off first. The transient curve of the dying-out concentration of CO₂ was measured. Then the stationary state of the reaction was reestablished. The supply of oxygen in the gas phase was then switched off but the CH₄ remained in the carrier N₂ gas. The decay curve for CO₂ was found to be less steep in comparison to the response of the system when the reaction stops after switching off the CH₄ supply. This proves that the sample can supply oxygen (in transients) for the reaction.

4.4.3 Reaction results: carbon monoxide oxidation

The results of carbon monoxide oxidation reactions obtained from temperature and concentration dependent measurements are given in this section.

Temperature dependence

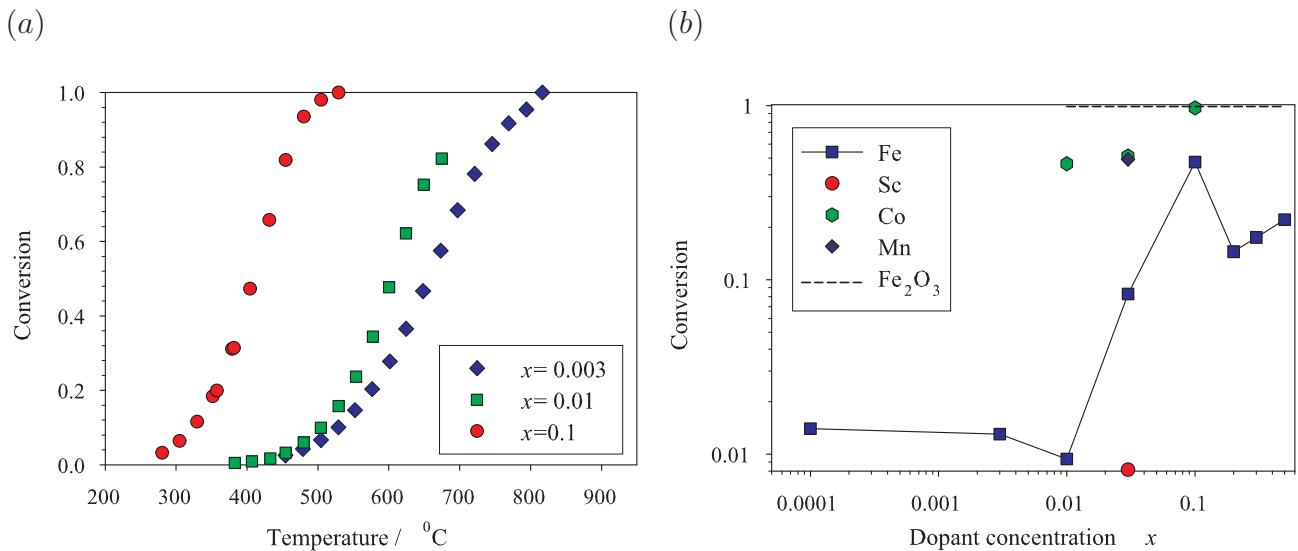


Figure 4.11: Carbon monoxide oxidation, (a) Conversion as a function of temperature, (b) Comparison of Activities (conversions given in logarithmic scale) at 400 °C as a function of dopant concentration.

In Figure 4.11 (a) the conversions are given for the same selection of samples as for methane oxidation. The reaction takes place at lower temperatures compared to methane oxidation. The samples show similar trends as for methane oxidation. The $\text{Sr}(\text{Fe}_{0.1}\text{Ti}_{0.9})\text{O}_{3-\delta}$ sample has attained a conversion of ≈ 0.1 already at ≈ 325 °C, and full conversion at ≈ 500 °C. The activity also strongly depends on dopant contents. In the activity comparison at 400 °C, Figure 4.11 (b), the two regions of low and high activities are also observed. Unlike in the methane oxidation case, Mn- and Co-doped samples show higher activities than Fe-doped samples. The Sc-doped sample stays at the level of low iron content samples.

The TOF of $\text{Sr}(\text{Fe}_{0.03}\text{Ti}_{0.97})\text{O}_{3-\delta}$ at 400 °C at ≈ 0.08 conversion is of about 0.15 s^{-1} .

The activation energies are given in Figure 4.12. The data scatter does not allow firm conclusions, no clear dependence of E_a on x can be observed. The values are almost constant and close to those found in methane oxidation.

Concentration dependence—Partial reaction orders

The results for the reaction orders are given in Figure 4.13. In contrast to methane oxidation, the carbon monoxide partial reaction order m , given in Figure 4.13 (a), does not change drastically for $\text{Sr}(\text{Fe}_x\text{Ti}_{1-x})\text{O}_{3-\delta}$ with increasing x , and two distinct regimes could not be

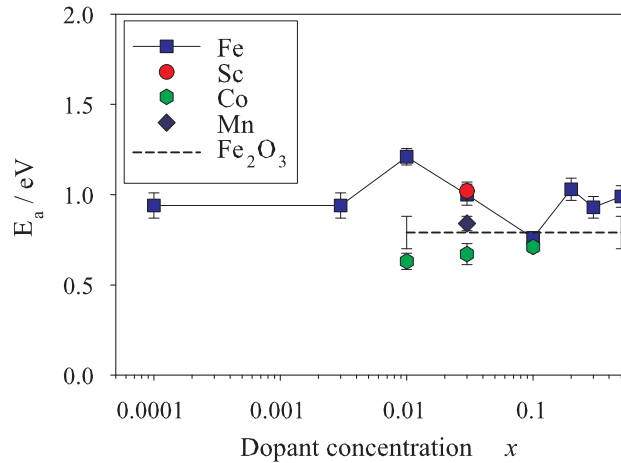


Figure 4.12: Carbon monoxide oxidation, activation energy.

observed. The large decrease of m for Co ($x = 0.1$) is not interpreted as a real change in the kinetic mechanism, but rather as an uncertainty of the measurement. Fe_2O_3 retained its high value, as in methane oxidation. For the oxygen partial reaction order n , given in Figure 4.13 (b), most data lie close to the value of 0.1, which is about half the averaged n -value in methane oxidation. For convenience, to compare results for different transition metal ions present in the host SrTiO_3 material, the activation energy E_a , conversion X at 400 °C and CO partial reaction order m for $x=0.03$ are given in Figure 4.14.

in situ TG and ESR

Similar to the CH_4 oxidation case, *in situ* CO oxidation reaction was performed on the $\text{Sr}(\text{Fe}_{0.5}\text{Ti}_{0.5})\text{O}_{3-\delta}$ during a TG measurement with the same temperature program as explained in Section 4.3.3. The result is showed in Figure 4.16. It can be observed clearly that the ongoing surface CO oxidation reduces the sample at temperatures lower than ≈ 575 °C. At 400 °C, for the $\text{CO}+\text{O}_2$ red curve, $\delta \approx 0.15$ corresponding to an effective oxygen partial pressure of about 10^{-6} bar (note that the externally set $P_{\text{O}_2} \approx 10^{-2}$ bar). The red curve, which corresponds to the *in situ* CO oxidation TG measurement, shows distinctly the influence of the reaction presence at temperatures lower than ≈ 575 °C. In the range of lower temperatures, the CO oxidation rate is faster than the rate of the bulk stoichiometry equilibration with gaseous oxygen, and in the stationary state it reduces the sample as if the sample were exposed to a lower P_{O_2} . CO oxidation reactions were likewise performed *in situ* during high-temperature ESR measurements on $\text{Sr}(\text{Fe}_{0.003}\text{Ti}_{0.997})\text{O}_{3-\delta}$. Firstly, ESR spectra (originating from Fe^{3+}) were recorded in 11 % O_2 in N_2 mixture. After the sample equilibration, 1 % of CO was added. Measurements were performed at various conversions, i.e. at different temperatures. The catalytic reaction at the surface of the sample, apparently, did not change the ESR spectra. It must be kept in mind that the samples $\text{Sr}(\text{Fe}_{0.003}\text{Ti}_{0.997})\text{O}_{3-\delta}$ and $\text{Sr}(\text{Fe}_{0.5}\text{Ti}_{0.5})\text{O}_{3-\delta}$ strongly differ, being representatives of different x doping regimes. The rate of oxygen in-

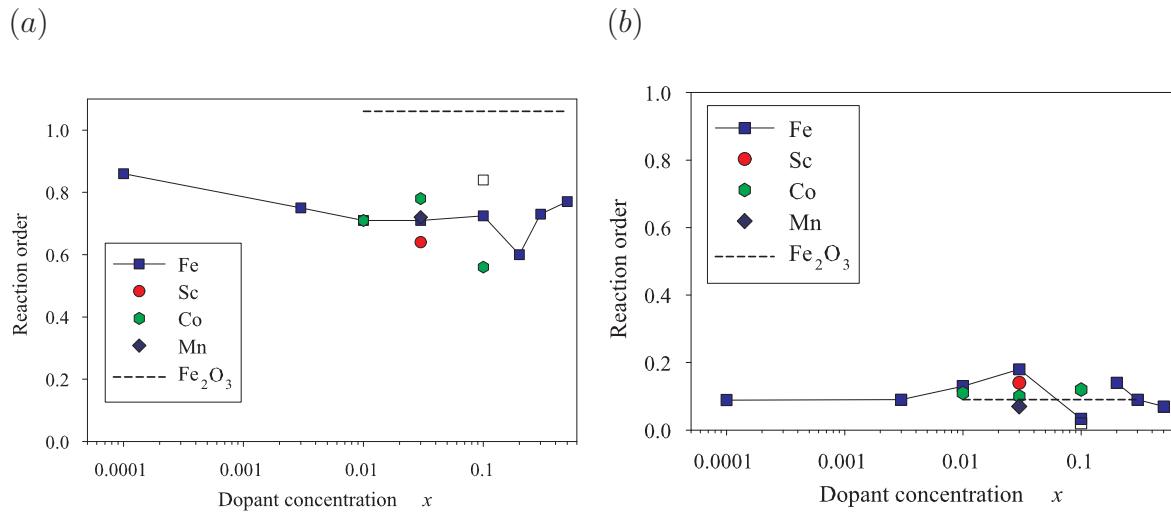


Figure 4.13: Carbon monoxide oxidation, reaction orders, (a) m for CO, (b) n for oxygen. The open square symbol represents the repeated measurement with the same iron content x . The measurements were performed at temperatures approximately between 350 and 500 °C.

incorporation into low iron doped samples, such as $\text{Sr}(\text{Fe}_{0.003}\text{Ti}_{0.997})\text{O}_{3-\delta}$, is rather sluggish in comparison to the rate for high iron doped samples. This fact and limitations of the experimental setup (e.g. poor flushing of the sample by the gas mixture in the capillary) might have caused this negative result by the ESR technique.

Chemical capacity

This experiment has not been done in the case of CO oxidation, but in a view of the *in situ* TG measurement, there is no reason to believe that this effect is absent in CO oxidation, on the contrary, it may be even more pronounced.

4.4.4 Short summary of the results

CO oxidation occurs at lower temperatures than CH_4 oxidation on all samples. This is partially due to the stability of the CH_4 molecule. It was observed that CH_4 and CO oxidation reactions on $\text{Sr}(\text{Fe}_x\text{Ti}_{1-x})\text{O}_{3-\delta}$ have qualitatively very similar behaviors (activity vs. x curve and TOFs), with the only differences in partial reaction orders m of CH_4 (from CO) and in the activation energies, both at low x . The Sc-samples were the least active, with the only exception of CH_4 oxidation at $x=0.03$ (the Mn-sample was slightly less active than the Sc-sample), and they have the highest activation energies in both reactions (for respective x). The activity of $\text{Sr}(\text{Fe}_x\text{Ti}_{1-x})\text{O}_{3-\delta}$ in both CH_4 and CO oxidation shows a division into two plateaus at $x \approx 0.03$ when plotted as a function of x . This division can also be recognized for E_a and also slightly for m in CH_4 oxidation, but is hardly visible for CO oxidation. In both reactions at $x=0.03$, E_a and m do not strongly change by switching between the Mn-, Fe- and Co-samples, Figures 4.10 and 4.14. However, the conversion changes significantly upon the interchange

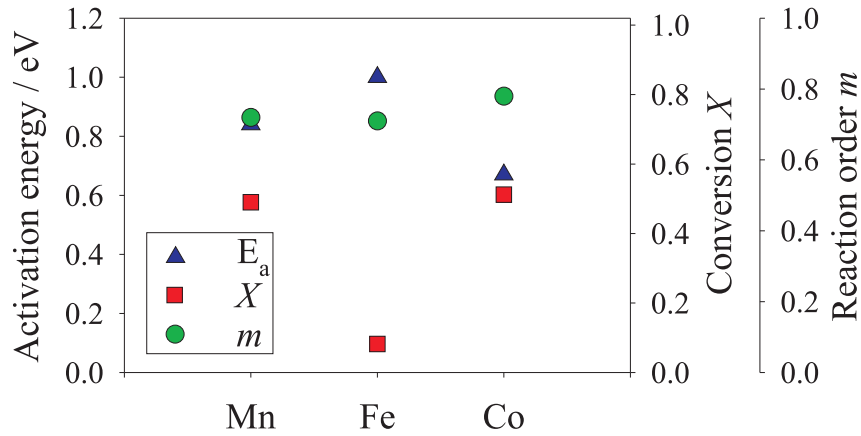


Figure 4.14: Carbon monoxide oxidation, the comparison of relevant results for Mn-, Fe- and Co-SrTiO₃ samples at $x=0.03$.

between the B site dopants (also in Figures 4.10 and 4.14). The TOFs were obtained from the activity data [Figures 4.7 (b) and 4.11 (b)] using Eq. (4.34). Note that the TOF represents the averaged activity per active center (assumed to be iron). Interestingly enough, it was found that CO is capable of reducing $\text{Sr}(\text{Fe}_x\text{Ti}_{1-x})\text{O}_{3-\delta}$ and to induce a higher oxygen deficiency, as seen in Figure 4.16, which means that the catalytic reaction can change the catalyst (i.e. shifts its point defect equilibria). This has an important implication for the kinetic modeling of catalytic reactions (see Sections 4.5.2 and 4.5.3).

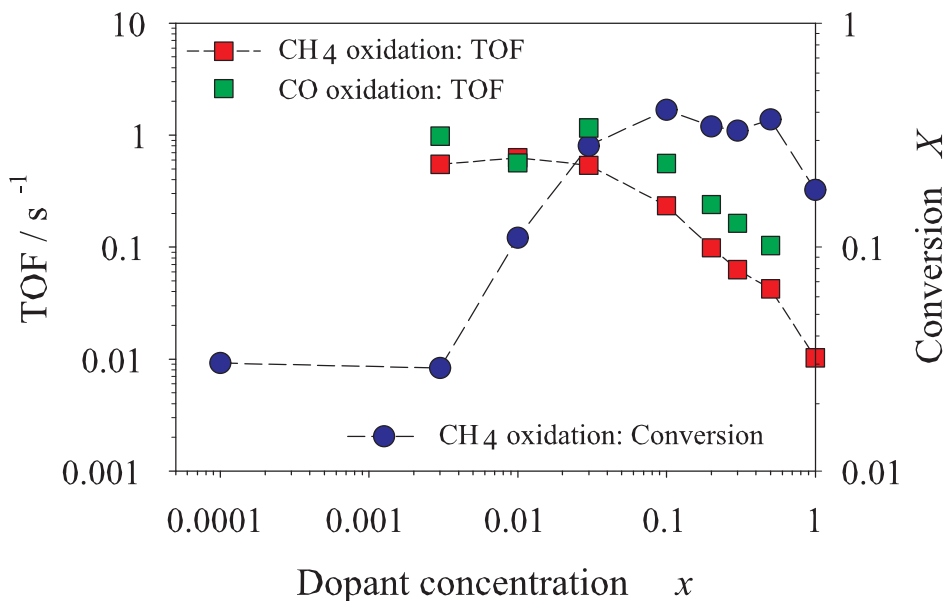


Figure 4.15: TOFs for CH_4 at $600\text{ }^\circ\text{C}$ and CO oxidation at $400\text{ }^\circ\text{C}$. The conversion for CH_4 oxidation is given to illustrate the difference from the TOFs.

4.5 Discussion

4.5.1 Literature review

To the author's best knowledge, no study has been reported which investigated the reaction kinetics of CH_4 and CO total oxidation on a complete $\text{Sr}(\text{Fe}_x\text{Ti}_{1-x})\text{O}_{3-\delta}$ solid solution series (with special emphasis on the region where it drastically changes its electronic structure). Some studies reported results for particular members of the series (mainly end members) as a comparison to other perovskite materials which were the primary focus. For example, non-substituted perovskite-type oxides containing an alkaline earth metal (ABO_3 ; $\text{A}=\text{Ca}, \text{Sr}, \text{Ba}$; $\text{B}=\text{Ti}, \text{Zr}, \text{Ce}$) were compared in oxidative coupling of CH_4 and among them SrTiO_3 showing the lowest activity [126]. A large number of perovskite type-oxides were compared to their related binary B oxides (B_mO_n), however, the test reaction was the total oxidation of propylene [127, 128]. From this comparison it can be seen that the incorporation into a perovskite structure can enhance (Fe_2O_3 vs. SrFeO_3) or reduce (TiO_2 vs. SrTiO_3) the catalytic activity for a particular reaction.

In order to correlate the solid state properties and catalytic behavior of perovskite type oxides, two different catalytic processes are to be distinguished: *suprafacial* processes (occurring between adsorbed species) and *intrafacial* processes (involving removal and replenishment of lattice oxygen [50]). Distinction between the two is usually made by the comparison of the temperature of catalytic reaction and the temperature needed to cause stoichiometry changes in the perovskite-type oxide catalyst. The distinction between the two is strongly related to the mobility of oxide ions in perovskites. The suprafacial process is understood to be influenced

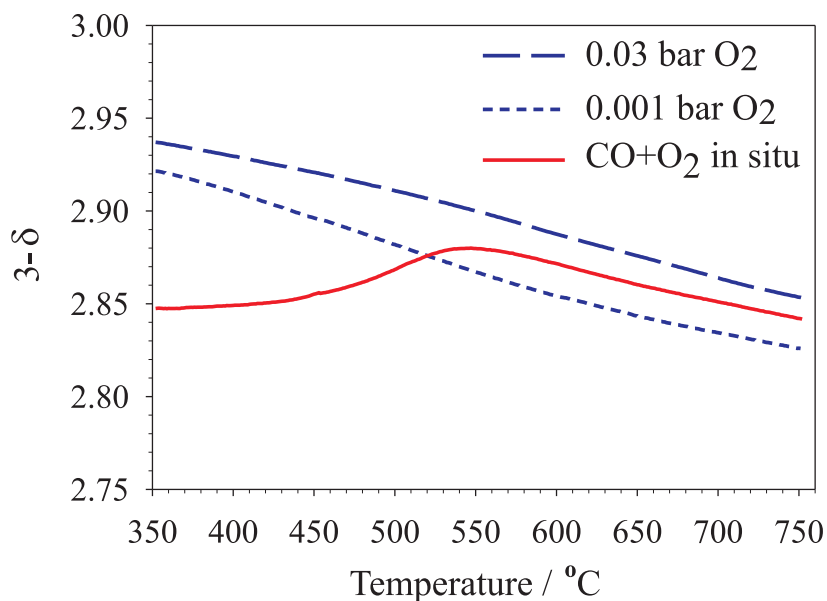


Figure 4.16: *in situ* CO oxidation on $\text{Sr}(\text{Fe}_{0.5}\text{Ti}_{0.5})\text{O}_{3-\delta}$ during a TG measurement. Nominal gas composition for the red $\text{CO}+\text{O}_2$ curve was 0.75 % of CO and 1.5 % of O_2 in Ar.

mainly by the electronic structure of the B transition metal cation. An intrafacial process is intimately connected with stoichiometry change of the oxide, and at least a few surface layers of the oxide are involved in catalysis. The low-temperature CO oxidation on BaTiO_3 [129], [130] or on cobaltates [131] belongs to the group of suprafacial catalysis. An example of an intrafacial catalysis where oxygen vacancies play the central role is the reduction of nitric oxide by CO and H_2 in the presence of a LaCoO_3 perovskite-type catalyst [132]. In close relation to supra/intrafacial processes is the finding of two qualitatively different oxygen desorption peaks in studies on $\text{La}_{1-x}\text{Sr}_x\text{CoO}_3$ [133, 127]. The broad low-temperature peak (in literature usually designated by α) was interpreted as originating from both adsorbed and “absorbed” oxygen (since the amount of desorbed oxygen exceeded a surface monolayer), whereas the sharp high-temperature peak (β) represents the released oxygen from the lattice (occurring above 800 °C).

Another kind of correlation has been also discussed, the relation of the Goldschmidt tolerance factor t (defined in Equation 2.2) and the catalytic activity in CO oxidation [134]. The tolerance factor is intimately related to the binding energy (sum of A–O and B–O parts)¹⁷ of the oxide ions. The decrease of the radius of TM ion increases t and, therefore, weakens the B–O–B interactions. As a result, surface vacancy formation may be promoted. It is plausible that this has an impact on other reactions (not only for CO oxidation). However, in a study of the $\text{Sr}(\text{Fe}_x\text{Ti}_{1-x})\text{O}_{3-\delta}$ solid solutions one should be very careful when speaking of t because different TM ion in different oxidation states (different radii) are present in the material.

In a very important work, many interesting results on catalytic methane combustion over

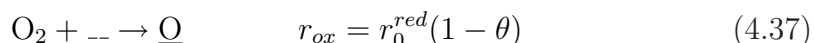
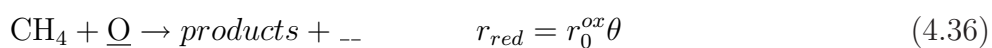
¹⁷an approach for estimating these binding energies is given in Ref. [134], originally suggested by R. J. H. Voorhoeve *et. al.*

various perovskite-type oxides were reported [51]. Partially A-cation substituted $\text{LaA}'\text{-Fe}$, $\text{LaA}'\text{-Mn}$, and $\text{LaA}'\text{-Co}$ oxide systems were examined ($\text{A}'=\text{Sr}$, Ba , Ca , Ce) and compared to a Pt/Alumina catalyst. This study showed that the A cation substitution also plays an important role in catalytic activity, in contrast to the widely accepted opinion that the nature of the B cation plays the crucial role. It was found that $\text{La}_{0.6}\text{Sr}_{0.4}\text{MnO}_3$ was the most active catalyst. For the Pt/Alumina catalyst, according to the fitted data the LH mechanism was confirmed. For perovskite-type oxides at lower temperatures, the adsorbed oxygen is believed to be more active than the lattice oxygen, and therefore the oxidation rate depends on both P_{CH_4} and P_{O_2} , and since it is unlikely that CH_4 adsorbs this would be described by the ER mechanism. However, the observed decrease in oxygen partial reaction order with increasing temperature cannot be solely explained by the ER mechanism. It was suggested that the lattice oxygen takes over the reaction control at higher temperatures, and the reaction rate is given as a sum of two parallel reactions

$$R = \frac{k_{\text{CH}_4}P_{\text{CH}_4}(k_{\text{O}_2}P_{\text{O}_2})^{1/2}}{1 + (k_{\text{O}_2}P_{\text{O}_2})^{1/2}} + k_1P_{\text{CH}_4} \quad (4.35)$$

where the first term represents the pure ER mechanism and the second term the influence of the lattice oxygen (essentially independent of P_{O_2} because of the rapid oxygen exchange with the lattice). The partial reaction orders obtained were: $m \approx 1$ and $n \approx 0.5$ at 450°C , and $m \approx 0.9$ and $n \approx 0.25$ at 650°C , for CH_4 and O_2 respectively. These results can be interpreted as follows. At low temperatures¹⁸, the intrafacial process is suppressed and thus k_1 in Eq. (4.35) is negligible. Then $n \approx 0.5$ is attainable for $1 \gg \sqrt{k_{\text{O}_2}P_{\text{O}_2}}$. At higher temperatures, the finite value of k_1 reduces n to 0.25 (this trend is reasonable, since, for very large k_1 , $n \approx 0$ would apply). Also, these results for the partial reaction orders at $T=650^\circ\text{C}$ are comparable to the results presented in Section 4.4.2 obtained on $\text{Sr}(\text{Fe}_x\text{Ti}_{1-x})\text{O}_{3-\delta}$ for high x .

In another very interesting work by Stojanović *et. al.* [135], the reaction kinetics of methane oxidation over $\text{LaCr}_{1-x}\text{Ni}_x\text{O}_3$ was investigated for $x = 0, 0.25, 0.5, 0.75$ and 1. Reactions were performed in an excess of methane. It was found that both partial reaction orders for methane and oxygen depend on nickel content x and temperature. Similar to the results presented in Section 4.4.2, they found that the partial reaction orders of methane were higher than that of oxygen. As an explanation of the results, a redox mechanism (similar to that originally proposed by Mars and van Krevelen [106]) was adopted. In this mechanism, the catalysis comprises two irreversible, alternating and unbalanced surface (multi-step) reactions



where -- and $\underline{\text{O}}$ are reduced and oxidized surface states, respectively (in notation of these authors [135]); θ is the fraction of the oxidized sites; r_0^{ox} and r_0^{red} are the maximum intrinsic

¹⁸in respect to the borderline temperature between suprafacial and intrafacial processes

rates for reduction (all sites oxidized) and oxidation (all sites reduced) reaction, respectively. The observed reaction rate is expressed by

$$\frac{1}{r_{obs}} = \frac{1}{r_0^{ox}} + \frac{1}{r_0^{red}}. \quad (4.38)$$

It is obvious that, if the two intrinsic rates greatly differ, the slowest one will determine the overall kinetics. In case of comparable magnitudes of the two, the overall rate is determined by both sets of kinetic parameters in accordance with Eq. (4.38). Further, if the two processes given by Eq. (4.36) and Eq. (4.37) have the following intrinsic partial pressure dependencies

$$r_0^{ox} = k_{red} P_{\text{CH}_4}^\alpha \quad (4.39)$$

$$r_0^{red} = k_{ox} P_{\text{O}_2}^\beta \quad (4.40)$$

then the observed effective partial reaction orders, taken around a single gas phase composition, are given by

$$m = \alpha \left[1 - \frac{r_0^{ox}}{r_0^{ox} + r_0^{red}} \right] \quad (4.41)$$

$$n = \beta \left[1 - \frac{r_0^{red}}{r_0^{ox} + r_0^{red}} \right]. \quad (4.42)$$

Under the constraint that α and β are the same for all catalyst, these authors obtained the best fit for $\alpha = \beta = 1$. According to the observed m near unity and n near zero, it can be concluded that the methane activation is the limiting process. To summarize, in Ref. [135], it was shown that the apparent partial reaction orders can differ significantly from the actual reaction orders (α and β) due to the specific MvK mechanism. The weak point of this report is the lack of knowledge of α and β which were obtained by fitting the data; and the data are potentially subject to experimental errors. The preferred approach would be to set up the full kinetic model which predicts the partial reaction orders and to compare it with the experimental results. Nevertheless, this work is a solitary example found in literature which shed more light on the mechanism under investigation.

In the group of $\text{A}(\text{BB}')\text{O}_3$ perovskite-type oxides to which $\text{Sr}(\text{Fe}_x\text{Ti}_{1-x})\text{O}_{3-\delta}$ belongs, a partial substitution of a aliovalent TM ion B' for B TM ion produces a defect structure. This has an impact on the material's catalytic activity. Additionally, a strong synergetic effect of the tandem of two neighboring B-site TM (be they identical TM ions with different oxidation states or be they different TM ions) could be expected [112, 136]. For the $\text{LaMn}_{1-x}\text{Cu}_x\text{O}_3$ system it was found that catalytic activity in CO oxidation was strongly enhanced for $x \approx 0.4$ (by a factor between 400 and 5000, compared to the end members), whereas no significant effect was observed on the same materials in propane oxidation [137]. This means that catalysis on these materials is also reaction-specific.

In investigations of catalytic activity of non-substituted LaMO_3 (M=V, Cr, Mn, Fe, Co and Ni) two maxima for Mn and Cr were found: for CO oxidation [138], and for both propene

and isobutene oxidation [139]. Such patterns are argued to stem from the two maxima in crystal field stabilization energy (CFSE) when passing from d^0 - to d^9 -electron configuration. The differences between the predictions of the CF theory and the experimental peaks were explained to be due to possible presence of surface defects. Also, it was found that the two maxima of catalytic activity coincide with those found for oxygen adsorption [139], which is an indication that the adsorbed oxygen is the determining species in these suprafacial processes.

4.5.2 Kinetic models

Although the reactions presented by Eq. (4.3) and Eq. (4.4) appear to be very simple, the system under investigation is very complicated when looked at in more detail, is involving several intermediates and reaction steps with different specific reaction rates. However, it is formally possible to roughly classify the main possible kinetic cases and to develop the respective kinetic models. A good agreement of model-predicted results with the actual data obtained in experiments could provide support for the kinetic model. However, as well-known in kinetics studies, a good agreement between experimental results and modeled ones gives no proof for the reaction mechanism, and other techniques are needed to fully elucidate the problem, which is usually a very difficult task. Nevertheless, such a comparison provides a good starting point for further investigations.

There are two main classes of reactions: class I involves reactions between CO/CH_4 and surface adsorbed oxygen species¹⁹ O_{ad}^* (i.e., without MvK mechanism²⁰), and class II involves lattice oxygen species (O_O^*) instead (i.e., with MvK mechanism). The species (O_{ad}^* or O_O^*) which is assumed to react with CO/CH_4 in a particular kinetic case will be called *reactive intermediate* species, or simply, reactive species.

A representative of the class I is given in Figure 4.17, where a convenient symbolic nomenclature is introduced for O_{ad}^* being the reactive intermediate species. In this case, it is assumed that O_{ad}^* participates in three reaction paths (branches): in the oxygen branch, gas phase oxygen is being constantly supplied to the surface of the oxide catalyst in the form of the O_{ad}^* (most probably O_{ad}^-) through a set of intermediate steps (e.g. $\text{O}_{2,ad}^-$ and $\text{O}_{2,ad}^{2-}$ as their intermediates), which further reacts with CO/CH_4 through the CO/CH_4 branch always acting as a O_{ad}^* sink, or incorporates into the oxide catalyst via the bulk branch (oxygen capacitor). It can be seen that an ER mechanism is presupposed here, because CO/CH_4 from gas phase reacts directly with O_{ad}^* . This is expected for CH_4 . However, for CO , one can imagine also CO adsorption prior to the reaction with O_{ad}^* . In this case a LH mechanism is involved and possibly a competitive adsorption of CO and O_2 . Nevertheless, for very low P_{CO} and P_{O_2} in the gas mixture (with more than 95 % of N_2 as the carrier gas), the coverage of both CO and O_2 is very low and approximately proportional to their concentrations in the gas phase [see Eq. (4.6)]. Hence, if LH mechanism were present in CO oxidation, it would not be discernible from the ER mechanism in the low coverage limit. The existence of the bulk branch is inferred

¹⁹the kind and the charge is not a priori known

²⁰used here for the purpose of distinction from the second class only

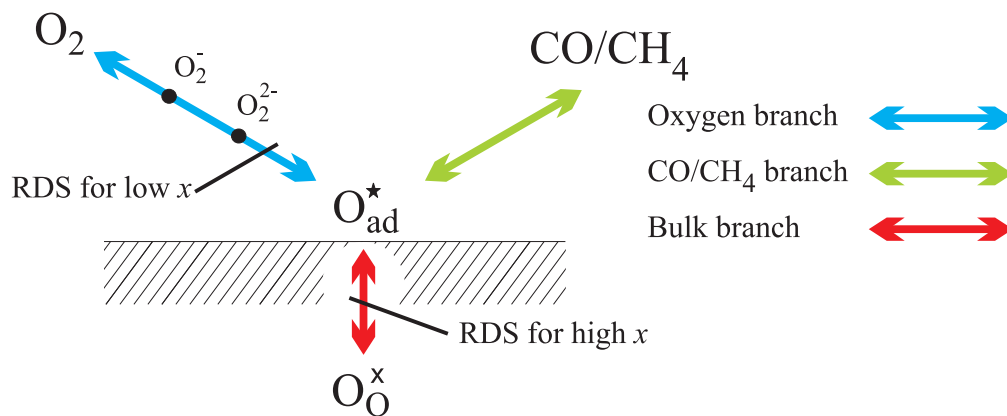


Figure 4.17: A reaction of class I, example of an O_{ad}^* intermediate which reacts with CO/CH_4 . The oxygen branch is not an elementary step, but comprises two more intermediate species $\text{O}_{2,ad}^-$ and $\text{O}_{2,ad}^{2-}$. Both the CO/CH_4 and the bulk branches are assumed to be elementary reactions. The most probable rate determining step (RDS) for the reaction sequence leading from gas phase O_2 to bulk oxide for iron-poor and iron-rich samples are also indicated.

from the oxygen chemical capacity measurement described in Section 4.4.2. The existence of the three branches requires more detailed treatment of the balance of the three reaction pathways. It is indispensable to say that since the oxygen branch is not an elementary reaction, its RDS can occur in different intermediate steps. In studies of oxygen in/ex-corporation into $\text{Sr}(\text{Fe}_x\text{Ti}_{1-x})\text{O}_{3-\delta}$ (in pure O_2 , there is no CO/CH_4 branch being present), the oxygen branch RDS is on different positions for iron-poor (low x) and iron-rich (high x) samples, as indicated in Figure 4.17 [20, 115]. It is assumed that these RDSs will remain at the same positions also in catalytic reactions in the presence of CO/CH_4 . The position of the RDS in the oxygen branch specifies the reaction mechanism and therefore influences directly kinetic results. All possible kinetic situations with the O_{ad}^* as the reactive intermediate species, omitting the details, are given in Figure 4.18. Different kinds of arrows represent different relative magnitudes of exchange rates. On account of the *in-situ* reaction TG data, the relative reaction rates of oxygen and CO/CH_4 branches generally differ. It can be inferred that there are two subgroups of the kinetic cases: the **A** group, if there is no change of oxide catalyst stoichiometry (oxygen branch is faster than CO/CH_4 branch), and the **B** group, where a stoichiometry change occurs (oxygen branch slower than CO/CH_4 branch). Based on the *in-situ* reaction TG data, CH_4 oxidation reactions belong only to the **A** group, and CO oxidation reactions can belong to both the **A** and **B** groups (depending on the temperature and the catalyst composition). Under the term *stoichiometry change* it is meant a CO -branch-driven change of the initial catalyst stoichiometry (without CO) occurring when passing into a steady state via one of the given kinetic cases. In the steady state, due to the finiteness of the catalyst bulk, the bulk branch will eventually equilibrate to the external (effective) steady state conditions dictated by the oxygen and CO branches, no matter what its relative magnitude is (with respect to the other two). It is important to emphasize that irrespective of the **A/B** cases listed above,

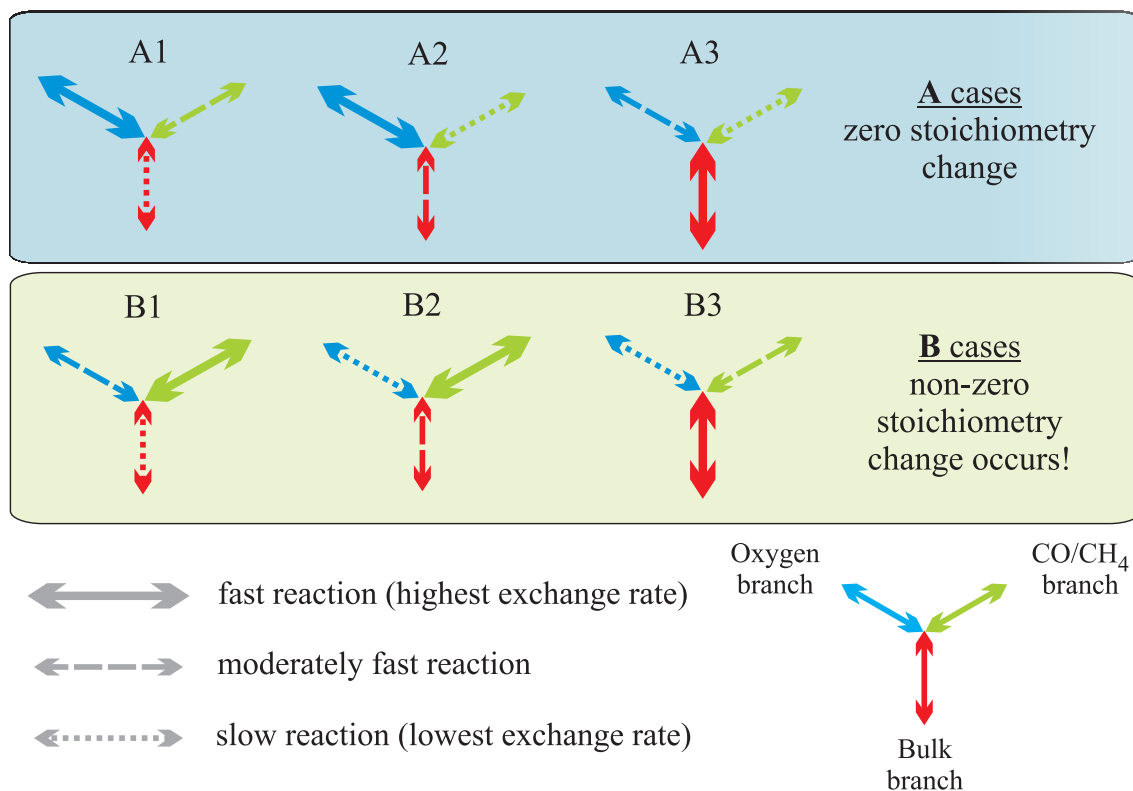


Figure 4.18: Possible kinetics cases involving O_{ad}^* where the relative magnitudes of the reaction branches are shown symbolically. Group **A**: oxygen branch is faster than CO/CH₄ branch, and no stoichiometry change is expected; group **B**: oxygen branch is slower than CO/CH₄ branch, and a stoichiometry change of the catalyst is expected.

the CO/CH₄ branch is never in equilibrium due to stationary gas flow over the catalyst which flushes off formed CO₂ molecules and moves externally the reaction away from equilibrium. The CO/CH₄ branch always acts as a O_{ad}^* sink. The different initial forms of the **A** cases for different relative branch rates A1, A2 and A3, are illustrated in Figure 4.18. Since the bulk branch does not influence the steady state, these cases cannot be distinguished from each other in the steady state, and will be considered as equivalent since transients are outside the scope of this work. The same applies for initial different of the **B** cases in the same figure.

A representative of the reaction class II, among which are the cases with a lattice O_O^* as the reactive oxygen species (with MvK mechanism), is given in Figure 4.19. In this class, the oxygen branch is the same as in the reaction class I (i.e., without MvK), but CO/CH₄ reacts directly with the O_O^* , hence reducing the system to the two branches only. Accordingly, but in contrast to the first class which has six different possible kinetic cases, in the second class there are only two possible kinetic cases which also have **A** or **B** nature: the oxygen branch is faster than the CO/CH₄ branch, or the oxygen branch is slower than the CO/CH₄ branch, respectively. Since it is assumed that the intercept of the CO/CH₄ branch with the oxygen branch at O_O^* does not change the nature of the oxygen branch, the position of its RDS remains the same as in the reaction class I.

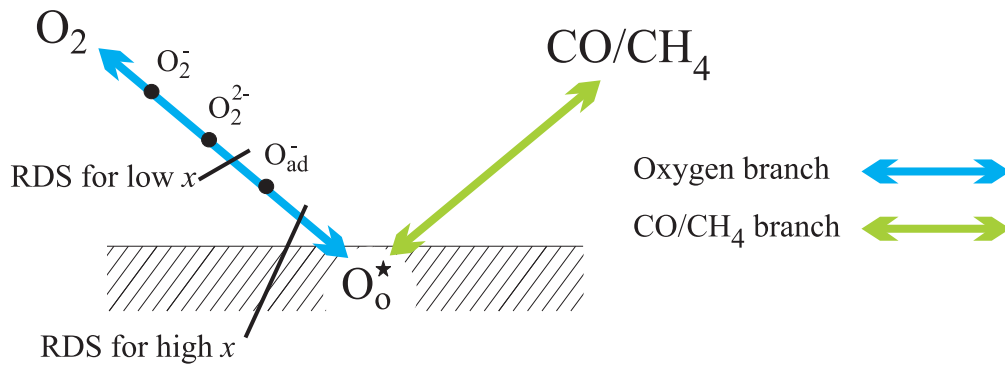


Figure 4.19: A reaction of class II. An example of an O_{O}^* intermediate which reacts with CO/CH_4 . The oxygen branch is not an elementary step reaction, but comprises two more intermediate (adsorbed) species $\text{O}_{2,ad}^-$ and $\text{O}_{2,ad}^{2-}$. The CO/CH_4 branch is assumed to be elementary reactions. The most probable RDS for iron-poor and iron-rich samples are also indicated.

Before proceeding to mathematical modeling of the kinetic cases, it is instructive to sort them out in advance. There are three criteria for sorting the kinetic cases:

- whether the catalysis is performed on iron-poor (low x) or on iron-rich (high x) samples (implying different RDS in the oxygen branch, and different defect chemistry of the catalyst bulk)
- which type of reactive intermediate is present (O_{ad}^* i.e., class I, or O_{O}^* i.e., class II)
- whether or not there is a bulk stoichiometry change present (group **B** or **A**, respectively)

The classification of the kinetic cases according to these three criteria is given in Figure 4.20, and the nomenclature from the figure will be used from now on when referring to a particular kinetic case. Each of these criteria has an influence on a kinetic model of the reactions. Upon the transition from iron-poor samples towards iron-rich samples, the RDS position in the oxygen branch changes [20, 115], as well as the abundance and mobility of electronic and ionic defects in the bulk and accordingly at the surface, as described in Chapter 2. The RDS position (indicated for different x in Figures 4.18 and 4.19) can directly control the concentration of the key intermediate species in terms of its oxygen partial pressure dependence, which leads to different partial reaction orders of the reaction. The change in the abundance of the defects reflects itself in changing the kind of catalytic active centers (e.g. from pure electronic defects such as e' and h' to Fe'_{Ti} and $\text{Fe}^{\times}_{\text{Ti}}$ redox centers). The type of the intermediate species O_{ad}^* or O_{O}^* determines the number of competing reaction branches present, as shown in Figures 4.18 and 4.19. And last but not the least, the bulk stoichiometry change (in the **B** group of reactions) induced by the presence of the fast CO branch is directly related to a different position of the bulk defect equilibria. In this case, the CO branch reduces the catalyst, which is equivalent to the statement that the sample *sees* a different (lower) effective P_{O_2} . The oxygen partial pressure dependencies of defect concentrations are given in Table 4.4. When

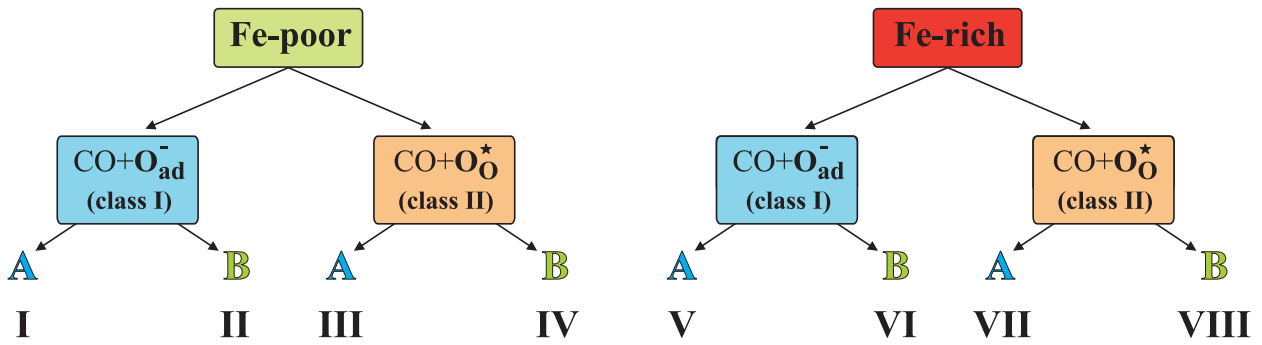


Figure 4.20: Classification of the kinetic cases. Iron-poor and iron-rich catalysts have different RDS of oxygen–bulk branch, and different defect concentration; the type of the reactive intermediate further branches the kinetic cases; and the final branching is the absence or presence of a stoichiometry change of the catalyst under steady state catalytic conditions. Cases which belong to the class I (i.e., no MvK) have three reaction branches, as shown in Figure 4.17. Cases which belong to the class II (i.e., with MvK) have two reaction branches, as shown in Figure 4.19.

Table 4.4: Partial pressure dependencies of defect concentrations in $\text{Sr}(\text{Fe}_x\text{Ti}_{1-x})\text{O}_{3-\delta}$. For low x , the data are taken from Ref. [115]; for high x , the parameters are estimated from TG measurements (see Sec. 4.3.3). Missing \times values can not be estimated due to the lack of a defect model for high x .

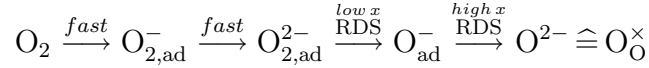
partial pressure dependence		<i>low x</i>	<i>high x</i>
$[\text{Fe}'_{\text{Ti}}]$	$\sim P_{\text{O}_2}^{-a}$	$-a$	-0.03
$[\text{Fe}^\times_{\text{Ti}}]$	$\sim P_{\text{O}_2}^{+b}$	b	0.2
$[\text{V}_{\text{O}}^\cdot]$	$\sim P_{\text{O}_2}^{-c}$	$-c$	-0.03
$[e']$	$\sim P_{\text{O}_2}^{-d}$	$-d$	-0.23
$[h^\cdot]$	$\sim P_{\text{O}_2}^{+e}$	e	0.23

considering reduced samples (due to a fast CO/CH_4 branch), P_{O_2} should be understood as an effective oxygen pressure whose value is always less than the actual P_{O_2} given in the initial gas mixture. Obviously, iron-poor samples have a more limited range of possible stoichiometry changes under reaction conditions (see Eq. (2.4)).

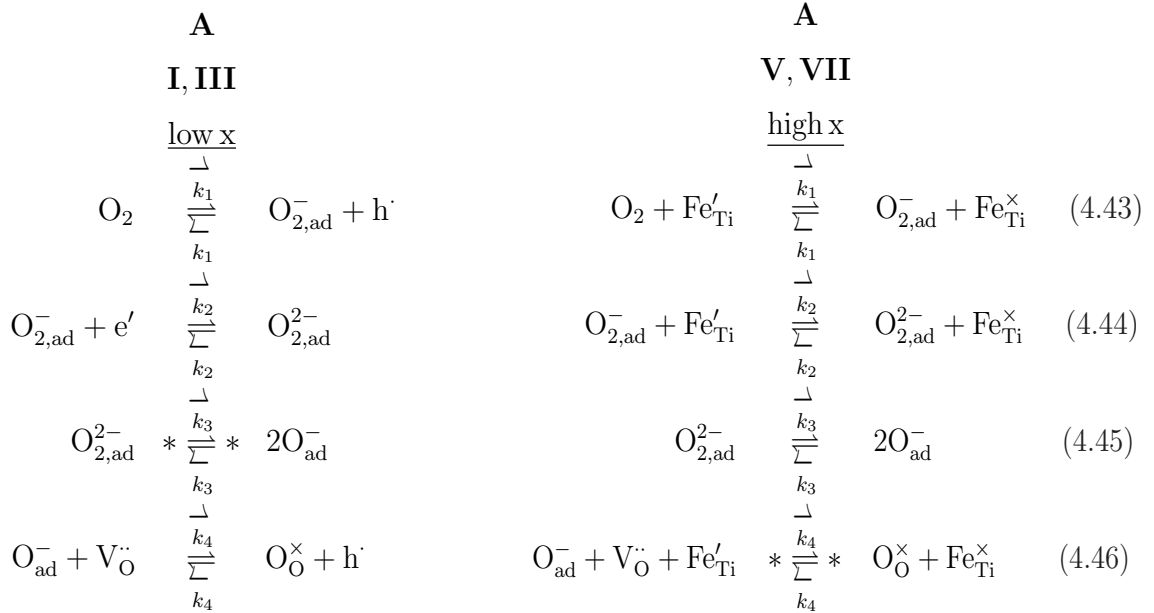
Kinetic cases A – Oxygen branch is fastest

The equations will be given for CO oxidation case notwithstanding the fact that they apply to both CH_4 and CO oxidation reactions. Before analyzing some of the given kinetic cases, it is useful to emphasize their common features. In all **A** cases, the oxygen branch is fast enough to maintain bulk equilibrium as if no CO/CH_4 branch were present. The defect equilibria and oxygen in/ex-corporation into $\text{Sr}(\text{Fe}_x\text{Ti}_{1-x})\text{O}_{3-\delta}$ for such a situation are well described in Refs. [20, 115]. According to these, the oxygen incorporation into the bulk proceeds most

probably via three intermediates



which is assumed to apply for all **A** cases. This means that the reactive species (O_{ad}^*) for the class I reactions is O_{ad}^- . As a support of this assumption, it was reported that adsorbed molecular oxygen species are not expected at temperatures above 200 °C on tin oxide gas sensors [116], and this trend is also to be expected in the case of $\text{Sr}(\text{Fe}_x\text{Ti}_{1-x})\text{O}_{3-\delta}$. Moreover, in the case of CO oxidation on LaCoO_3 , the species which actually reacts with CO is, on grounds of kinetic and spectroscopic data, also assumed to be O_{ad}^- [113]. More detailed reactions steps which describe the **A** cases with iron-poor catalysts (**I** and **III**, Figure 4.20) are given in the left column



In the right column are given those equations that describe the **A** cases with iron-rich catalysts (**V** and **VII**), whereby the position of the RDS is in the equations which have asterisks (*). On iron-poor catalysts, the reactions are most likely to proceed with the aid of delocalized electronic carriers, while on iron-rich catalysts, there are plenty of Fe'_{Ti} and $\text{Fe}_{\text{Ti}}^\times$ centers which take over the role of active centers. The exchange rate of the slowest step in the oxygen reaction chain, i.e., the RDS, is still much higher than that of the CO/CH₄ branch. Practically, the equilibrium of the reactive species O_{ad}^- (class I) and O_O^* (class II) with the gas phase is always maintained in **A** cases. For the reaction class I, the first three reactions, Eqs. (4.43-4.45), are sufficient to describe the concentration of O_{ad}^- which is given by

$$[\text{O}_{\text{ad}}^-] = \sqrt{K_1 K_2 K_3} [\text{e}']^{\frac{1}{2}} [\text{h}^\cdot]^{-\frac{1}{2}} P_{\text{O}_2}^{\frac{1}{2}} \quad \text{low } x \quad (4.47)$$

for the cases of low iron content catalysts (cases **I** and **III**²¹), and

$$[O_{ad}^-] = \sqrt{K_1 K_2 K_3} [Fe_{Ti}^\times]^{-1} [Fe'_{Ti}] P_{O_2}^{\frac{1}{2}} \quad \text{high } x \quad (4.48)$$

for the cases of high iron content catalysts (cases **V** and **VII**²²), where K_1 , K_2 and K_3 are the equilibrium constants of the three reactions Eqs.(4.43-4.45). Knowing one of the concentrations of electronic carriers, $[e']$ or $[h\cdot]$, the other can be calculated from the band gap equilibrium of the material²³, $K_{bg} = [e'][h\cdot]$.

For the cases **I** and **V**, which belong to class I, the last two equations lead readily to the final result via the reactions of CO/CH₄ with O_{ad}^-

$$\begin{aligned} \text{CO} + O_{ad}^- &\xrightarrow{\text{slow}} \text{CO}_2 + e' \quad \text{low } x \\ R_{\text{CO}_2} &= k[O_{ad}^-]P_{\text{CO}} = k\sqrt{\frac{K_1 K_2 K_3}{K_{bg}}} [e'] P_{\text{CO}} P_{O_2}^{\frac{1}{2}} \\ \text{case I : } R_{\text{CO}_2}^{\text{I}} &= k_{\text{I}} P_{\text{CO}} P_{O_2}^{\frac{1}{2}-d_{\text{I}}} \\ (m_{\text{I}} = 1 \quad ; \quad n_{\text{I}} = \frac{1}{2} - d_{\text{I}} = 0.27) & \end{aligned} \quad (4.49)$$

$$\begin{aligned} \text{CO} + O_{ad}^- + Fe_{Ti}^\times &\xrightarrow{\text{slow}} \text{CO}_2 + Fe'_{Ti} \quad \text{high } x \\ R_{\text{CO}_2} &= k[O_{ad}^-]P_{\text{CO}} = k\sqrt{K_1 K_2 K_3} [Fe'_{Ti}] P_{\text{CO}} P_{O_2}^{\frac{1}{2}} \\ \text{case V : } R_{\text{CO}_2}^{\text{V}} &= k_{\text{V}} P_{\text{CO}} P_{O_2}^{\frac{1}{2}-a_{\text{V}}} \\ (m_{\text{V}} = 1 \quad ; \quad n_{\text{V}} = \frac{1}{2} - a_{\text{V}} = 0.43) & \end{aligned} \quad (4.50)$$

In these equations k_{I} and k_{V} are constant and include the constants from the previous expressions; the partial pressure dependencies of $[e']$ and $[Fe'_{Ti}]$ are taken from Table 4.4. Although subsequent in/ex-corporation reactions of O_{ad}^- are present (Eqs. 4.46), they do not influence directly the result. In all **A** cases, the bulk of a catalyst is fully equilibrated with oxygen from the gas phase, i.e., no deviation of its oxygen stoichiometry from the one expected for the given oxygen partial pressure is present. Hence, the fourth reaction step indirectly affects the reaction kinetics of the previous steps by controlling equilibrium concentration of involved electronic and ionic carriers. (Indeed, for **B** cases where a stoichiometry change of the catalyst is present, the whole set of reactions Eqs. (4.43-4.46) also applies, but at different carrier (defect) concentration which correspond to an effective oxygen partial pressure²⁴ and not to the actual one given by the gas phase).

For the cases **III** and **VII**, which belong to the class II, the reaction of CO/CH₄ with the intermediate species occurs one step later in the oxygen branch, i.e., with the lattice oxygen species. Therefore, the required concentration of the reactive species (O_{O}^\times or $O_{\text{O}}^\bullet \equiv \{O_{\text{O}}^\times + h\cdot\}$ ²⁵)

²¹for case **III**, this is only an intermediate species towards the reactive O_{O}^* species

²²for case **VII**, this is only an intermediate species towards the reactive O_{O}^* species

²³the value of K_{bg} can be found in Ref. [28].

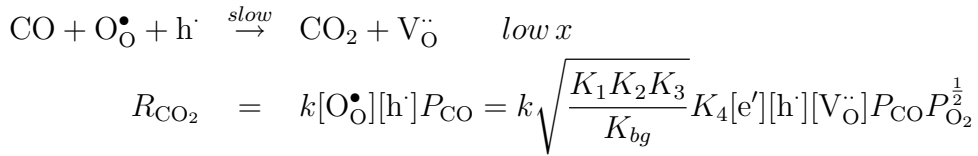
²⁴CO branch 'steals' oxygen species from the catalyst bulk, therefore the catalyst sees lower P_{O_2}

²⁵missing electron on a regular oxide ion or O_{O}^\bullet

after the fourth step can be calculated from the equilibrium conditions of the reactions Eqs.(4.43)-(4.46)

$$\begin{array}{ll}
 \text{III:} & \underline{\text{A, low } x} \\
 [\text{O}_\bullet^\circ] = [\text{O}_\times^\circ][\text{h}\cdot] & = K_4[\text{V}_\bullet^\circ][\text{O}_{\text{ad}}^-] \\
 [\text{O}_\bullet^\circ] = [\text{O}_\times^\circ][\text{h}\cdot] & = \sqrt{\frac{K_1 K_2 K_3}{K_{bg}}} K_4 [e'] [\text{V}_\bullet^\circ] P_{\text{O}_2}^{\frac{1}{2}} \\
 \text{VII:} & \underline{\text{A, high } x} \\
 [\text{O}_\times^\circ] & = K_4 [\text{O}_{\text{ad}}^-] \frac{[\text{V}_\bullet^\circ][\text{Fe}'_{\text{Ti}}]}{[\text{Fe}_\times^\circ]} \\
 [\text{O}_\times^\circ] & = \sqrt{K_1 K_2 K_3} K_4 \frac{[\text{V}_\bullet^\circ][\text{Fe}'_{\text{Ti}}]^2}{[\text{Fe}_\times^\circ]^2} P_{\text{O}_2}^{\frac{1}{2}}
 \end{array} \tag{4.51}$$

They lead to the final results for these cases via the following reactions

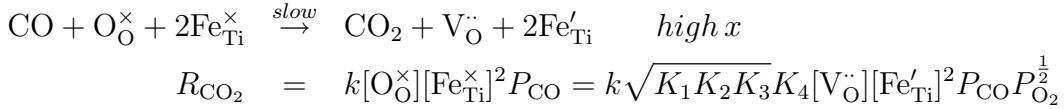


$$\text{case III :} \quad R_{\text{CO}_2}^{\text{III}} = k_{\text{III}} P_{\text{CO}} P_{\text{O}_2}^{\frac{1}{2} - d_{\text{III}} + e_{\text{III}} - c_{\text{III}}} \tag{4.52}$$

$$(m_{\text{III}} = 1 \quad ; \quad n_{\text{III}} = \frac{1}{2} - d_{\text{III}} + e_{\text{III}} - c_{\text{III}} = 0.43) \tag{4.53}$$

$$\tag{4.54}$$

For the case **III**, it is noteworthy that for the final result it makes no difference whether the reactive species is O_\times° or O_\bullet° , since they are equivalent in this respect due to the equilibrium condition of the whole oxygen branch. Final results for the case **VII** are given by



$$\text{case VII :} \quad R_{\text{CO}_2}^{\text{VII}} = k_{\text{VII}} P_{\text{CO}} P_{\text{O}_2}^{\frac{1}{2} - 2a_{\text{VII}} - c_{\text{VII}}} \tag{4.55}$$

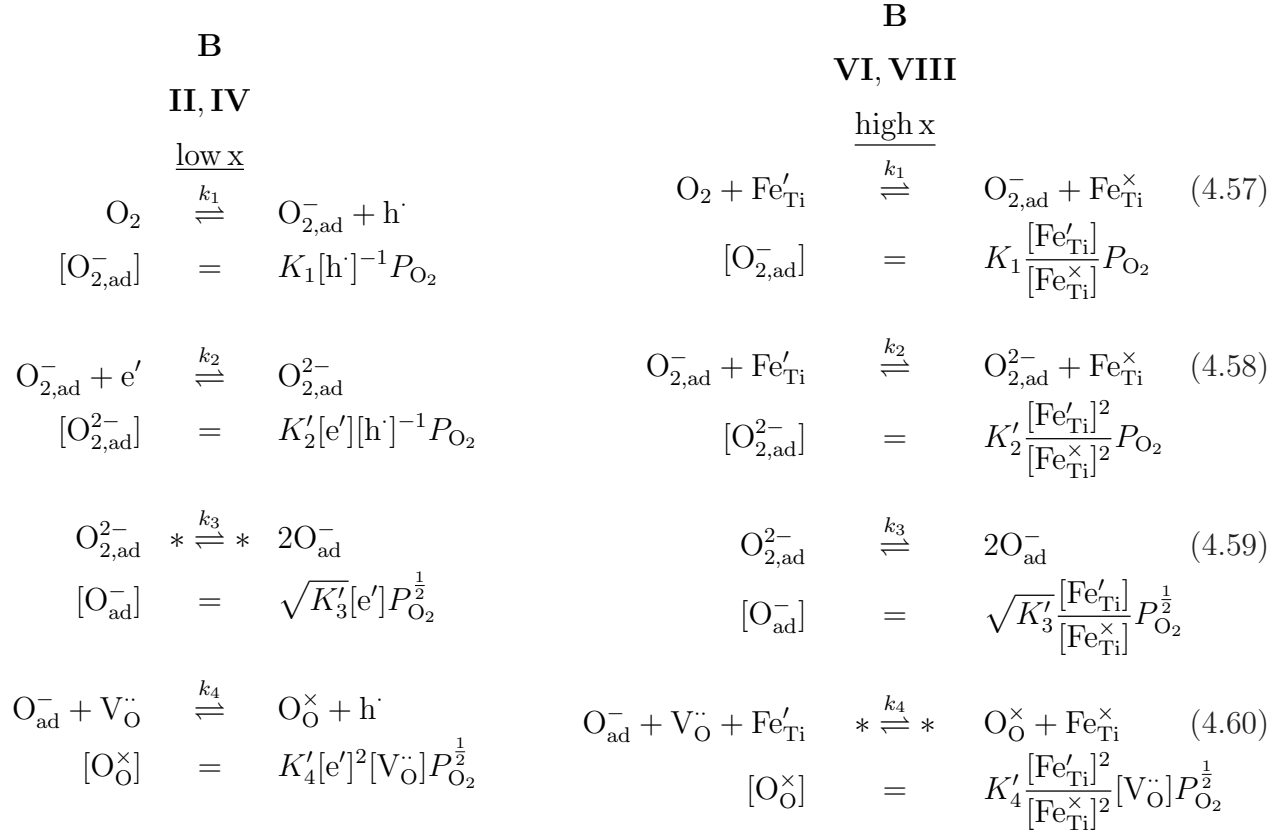
$$(m_{\text{VII}} = 1 \quad ; \quad n_{\text{VII}} = \frac{1}{2} - 2a_{\text{VII}} - c_{\text{VII}} = 0.29) \tag{4.56}$$

Kinetic cases B – CO branch is fastest

In **B** kinetic cases, the CO branch²⁶ is much faster than the oxygen branch, which means that the reactive intermediate species will be fully consumed by the CO branch. This is illustrated in Figures 4.21 and 4.22, for both reaction classes I and II, respectively. For reactive species which lie after the RDS, it is easy to see that their concentrations are close to zero: the concentration of the last (reactive) intermediate is reduced close to zero by the reaction with CO, and since the reaction steps after the RDS are faster (higher exchange rates) than the RDS, this implies that the concentration of other intermediates will be leveled off to the concentration level of the last intermediate which is being consumed by the fast CO/CH₄ branch and is close to zero.

²⁶it is highly unlikely that these cases apply for CH₄ oxidation on any sample and in any temperature range, therefore, only the CO branch will be referred to in this section.

Therefore, after the RDS, only the forward rates²⁷ will remain because there are essentially no species available for the backward reactions. The intermediates, which lie before the RDS, are equilibrated with gas phase oxygen and have higher concentrations than those which lie after the RDS, as shown on the left of RDSs in the figures. The same reaction steps of oxygen in/ex-corporation in the absence of CO are assumed, as in **A** cases



where primes on the equilibrium constants designate that they comprise all previous reaction constants, and the position of the RDS²⁸ is indicated by asterisks (*). Below each reaction, the equilibrium concentration of the end product needed for the next step is given, as if all the previous steps were in equilibrium. These equilibria will certainly be disturbed in the presence of the CO branch, and some backward rates will be zero, depending on the particular case, the arrows over the reaction rate constants are therefore omitted. However, the context can be easily recognized from Figures 4.21 and 4.22.

Firstly, the class I cases will be analyzed. From Figure 4.21 (a), it is easy to see that the

²⁷blue arrows in Figures 4.21 and 4.22

²⁸indicated also in Figures 4.21 and 4.22 by red colored letters **RDS**

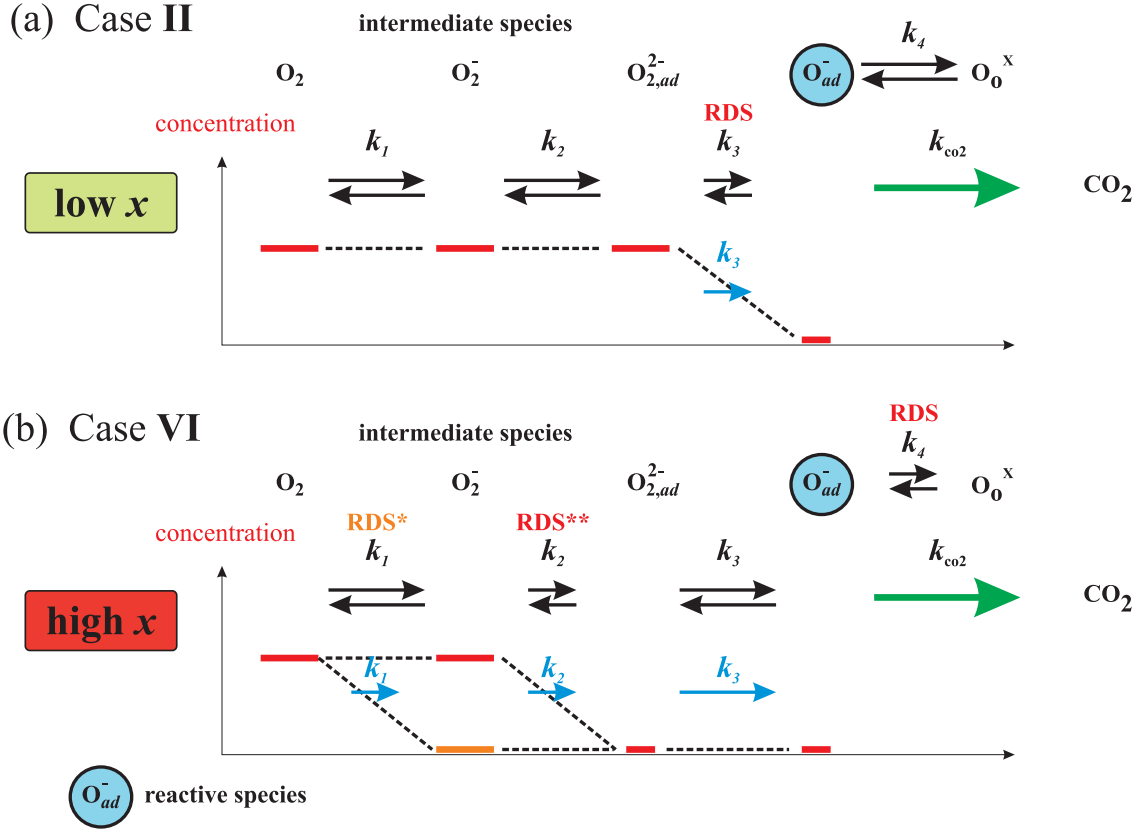


Figure 4.21: B cases, class I: reactive intermediate O_{ad}^- . Rate balances.

production rate of O_{ad}^- is given by

$$R_{\text{O}_{ad}^-} = \bar{k}_3 [\text{O}_{2,ad}^{2-}] \quad (4.61)$$

and since it has been assumed that essentially all available O_{ad}^- (which react very quickly with CO) are used up, this rate corresponds also to the rate of CO_2 production. Using the left equation of Eq. (4.58), therefore the CO_2 rate for the case **II** is

$$\begin{aligned} R_{\text{CO}_2}^{\text{II}} &= \bar{k}_3 K_2' [\widetilde{e}']^2 P_{\text{O}_2} \\ \text{case II : } R_{\text{CO}_2}^{\text{II}} &= k_{\text{II}} P_{\text{O}_2}^{1-2\widetilde{d}_{\text{II}}} \\ (m_{\text{II}} = 0 \quad ; \quad n_{\text{II}} = 1 - 2\widetilde{d}_{\text{II}}) & \end{aligned} \quad (4.62)$$

where the tilde indicates that the defect concentrations correspond to the reduced effective oxygen partial pressure ‘seen’ by the catalyst bulk, instead of the gas-phase P_{O_2} .

The kinetic case **VI**, illustrated in Figure 4.21 (b), requires a more detailed analysis. The original RDS of the oxygen-bulk branch is positioned after the reaction step $\text{O}_{ad}^- + \text{CO}$, and has no direct influence on the previous steps (only indirect, as already explained). Since the reaction with CO is very fast, one of the previous steps must take over the role of the RDS. There are two possibilities for this, either the RDS is between O_2 and $\text{O}_{2,ad}^-$ (RDS*), or between $\text{O}_{2,ad}^-$ and $\text{O}_{2,ad}^{2-}$ (RDS**). In the former case, the right reaction in Eq. (4.57) is not

in equilibrium and the forward rate is dominating, hence, the rate of $\text{O}_{2,ad}^-$ production is given by

$$R_{\text{O}_{2,ad}^-} = \overset{\downarrow}{k_1} [\text{Fe}'_{\text{Ti}}] P_{\text{O}_2} \quad (4.63)$$

Since all the following intermediates are almost fully depleted, including the reactive species at the end of the reaction chain (O_{ad}^-), the rate of newly created $\text{O}_{2,ad}^-$ will correspond directly to the rate of newly produced CO_2

$$\begin{aligned} \text{case VIa :} \quad R_{\text{CO}_2}^{\text{VIa}} &= k_{\text{VIa}} [\text{Fe}'_{\text{Ti}}] P_{\text{O}_2} \\ (m_{\text{VIa}} = 0 \quad ; \quad n_{\text{VIa}} = 1 - \widetilde{a_{\text{VIa}}}) \end{aligned} \quad (4.64)$$

In the latter case, where the RDS** is between $\text{O}_{2,ad}^-$ and O_{ad}^{2-} , and along the similar lines of reasoning the result is

$$\begin{aligned} \text{case VIb :} \quad R_{\text{CO}_2}^{\text{VIb}} &= k_{\text{VIb}} \frac{[\text{Fe}'_{\text{Ti}}]^2}{[\text{Fe}^\times_{\text{Ti}}]} P_{\text{O}_2} \\ (m_{\text{VIb}} = 0 \quad ; \quad n_{\text{VIb}} = 1 - 2\widetilde{a_{\text{VIb}}} - \widetilde{b_{\text{VIb}}}) \end{aligned} \quad (4.65)$$

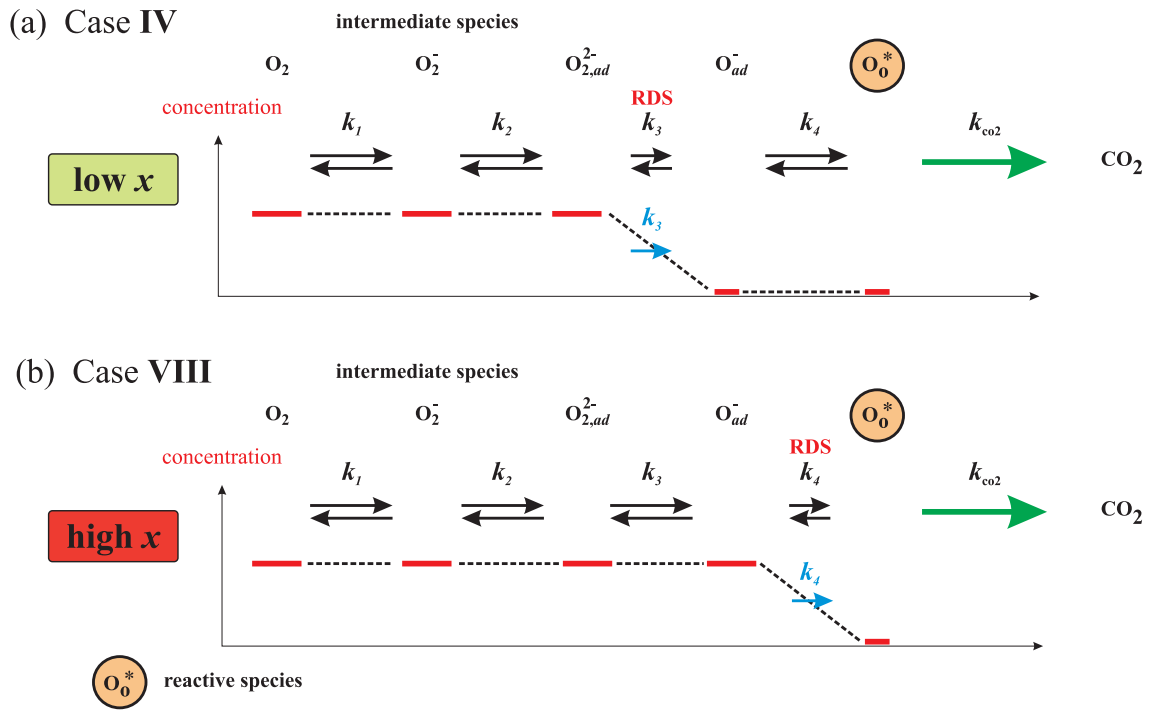


Figure 4.22: B cases, class II: reactive intermediate O_{latt} , Rate balances.

For the class II cases, given in Figure 4.22, it is important to make the following comment: since the $\text{Sr}(\text{Fe}_x\text{Ti}_{1-x})\text{O}_{3-\delta}$ compositions are oxides, it is obvious that the number of regular lattice oxygen species O_O^\times is vast, and therefore the depicted concentration profiles in Figure 4.22 (where the concentration of O_O^\times is shown to be close to zero) look at first sight rather

controversial or even wrong. However, even though a catalyst has nominally a large number of O_O^\times , due to its limited oxygen capacity, these species will be reduced by the CO branch to a certain number of $[\widetilde{\text{O}}_\text{O}^\times]$, and the further O_O^\times exorporation will be slowed down to zero due to the constraints such as electroneutrality and limited number of reducible Fe^{4+} ions (the catalyst reaches a quasi-equilibrium state dictated by the external conditions). Formally, the concentration $[\widetilde{\text{O}}_\text{O}^\times]$ is still large, but these species are not available for CO_2 synthesis. Only the excess values of these over the $[\widetilde{\text{O}}_\text{O}^\times]$ value are available for the reaction. Hence, the concentration of O_O^\times illustrated in Figure 4.22 must be understood as the excess concentration over $[\widetilde{\text{O}}_\text{O}^\times]$. For the kinetic case **IV** illustrated in Figure 4.22 (a), it is easy to write down the final result using the left equation of Eq. (4.58)

$$R_{\text{O}_{\text{ad}}^-} = \frac{1}{k_3}[\text{O}_{2,\text{ad}}^{2-}] \quad (= R_{\text{O}_\text{O}^\times}) \quad (4.66)$$

and therefore

$$\begin{aligned} \text{case IV :} \quad R_{\text{CO}_2}^{\text{IV}} &= k_{\text{IV}}[\widetilde{e}']^2 P_{\text{O}_2} \\ (m_{\text{IV}} = 0 \quad ; \quad n_{\text{IV}} = 1 - 2\widetilde{d}_{\text{IV}}) \end{aligned} \quad (4.67)$$

Analogously, for the last kinetic case **VIII**, the result according to Figure 4.22 (b) and the right equations of Eqs. (4.59) and (4.59) is equal to

$$\begin{aligned} \text{case VIII :} \quad R_{\text{CO}_2}^{\text{VIII}} &= k_{\text{VIII}} \frac{[\widetilde{\text{Fe}}_{\text{Ti}}']^2}{[\widetilde{\text{Fe}}_{\text{Ti}}^\times]} [\widetilde{\text{V}}_\text{O}] P_{\text{O}_2}^{\frac{1}{2}} \\ (m_{\text{VIII}} = 0 \quad ; \quad n_{\text{VIII}} = \frac{1}{2} - 2\widetilde{a}_{\text{VIII}} - \widetilde{b}_{\text{VIII}} - \widetilde{c}_{\text{VIII}}) \end{aligned} \quad (4.68)$$

All the results of kinetic modeling are summarized in Table 4.5. For the **B** cases, no numeric

Table 4.5: Expected partial reaction orders for different kinetic models. The partial pressure dependencies of defect concentrations designated by the tilde \sim apart from P_{O_2} , depend also on P_{CO} in CO oxidation or P_{CH_4} in CH_4 oxidation; \dagger in CO oxidation the m will differ from zero due to the f factor, as discussed in the text. \ddagger For the case **VI** there are two subcases with different n : for the first subcase **VIa** $n = 1 - \widetilde{a}_{\text{VIa}}$, and for the second subcase **VIb** the value of n is given in the table.

Reactive species	Fe poor				Fe rich			
	O_{ad}^*		O_O^*		O_{ad}^*		O_O^*	
Kinetic case:	I (A)	II (B)	III (A)	IV (B)	V (A)	VI (B)	VII (A)	VIII (B)
CO/CH₄ partial reaction order m	1	0^\dagger	1	0^\dagger	1	0^\dagger	1	0^\dagger
O₂ partial reaction order n	$\frac{1}{2} - d_{\text{I}}$ 0.27	$1 - 2\widetilde{d}_{\text{II}}$	$\frac{1}{2} - c_{\text{III}}$ 0.43	$1 - 2\widetilde{d}_{\text{IV}}$	$\frac{1}{2} - a_{\text{V}}$ 0.43	$\ddagger 1 - 2\widetilde{a}_{\text{VIb}} - \widetilde{b}_{\text{VIb}}$	$\frac{1}{2} - 2a_{\text{VII}} - c_{\text{VII}}$ 0.29	$\frac{1}{2} - 2\widetilde{a}_{\text{VIII}}$ $-\widetilde{c}_{\text{VIII}} - \widetilde{b}_{\text{VIII}}$

values of n are given in the table. This is related to the fact that in a **B** case the catalyst sees an effective $P_{\text{O}_2}^{\text{eff}}$ which can be expressed as

$$P_{\text{O}_2}^{\text{eff}} = f P_{\text{O}_2} \quad (4.69)$$

where f is the correction factor due to the reduction of the catalyst by the CO/CH_4 branch. This factor is a function of four variables: (P_{CO} or P_{CH_4}), P_{O_2} , temperature and iron content x , i.e., $f = f[(P_{\text{CO}}$ or $P_{\text{CH}_4}), P_{\text{O}_2}, T, x]$. According to the *in-situ* ESR and TG results, it can be assumed that in case of CH_4 oxidation $f(P_{\text{CH}_4}, P_{\text{O}_2}, T, x) \equiv 1$ for all measurements. According to *in situ* ESR, in CO oxidation, for low- x samples $f(P_{\text{CO}}, P_{\text{O}_2}, T, \text{low } x) \approx 1$ independently of P_{CO} (for the P_{O_2} and P_{CO} ranges in scope of this work). As shown by *in situ* TG, it can be less than unity by orders of magnitude for high- x samples at high $\frac{P_{\text{CO}}}{P_{\text{O}_2}}$ ratios. This effect has an important impact on P_{O_2} -dependencies of defect concentrations. For example, for a high- x sample, the P_{O_2} -dependence of $[\text{Fe}'_{\text{Ti}}]$ (similar applies to the other defects present in the system, see Table 4.4), is therefore given by

$$[\text{Fe}'_{\text{Ti}}] \sim (P_{\text{O}_2}^{eff})^{-a} = (f P_{\text{O}_2})^{-a} = f^{-a} P_{\text{O}_2}^{-a} \quad (4.70)$$

under the assumption that the power law in Eq. (4.32) is valid over an extended P_{O_2} range. In the *in situ* TG measurement (see Figure 4.16) on $\text{Sr}(\text{Fe}_{0.5}\text{Ti}_{0.5})\text{O}_{3-\delta}$, for example, oxygen nonstoichiometry is $\delta \approx 0.15$ at 400°C , which corresponds to an effective $P_{\text{O}_2}^{eff} \approx 10^{-6}$ bar, while the externally given P_{O_2} is 10^{-2} bar; thus in this particular point f has a value of about 10^{-4} , i.e., $f(P_{\text{CO}} = 7.5 \text{ mbar}, P_{\text{O}_2} = 15 \text{ mbar}, T = 400^\circ\text{C}, x = 0.5) \approx 10^{-4}$. This effect is illustrated in Figure 4.23. P_{CO} - and P_{O_2} -dependencies of f factors for the samples have not been quantitatively determined, but their influences can be qualitatively well understood now. Due to the appearance of the f factor in Eq. (4.70), the effective CO partial reaction order m can be different from zero even if the corresponding **B** kinetic model predicts $m = 0$, which is to be discussed in the following section.

4.5.3 Interpretation

From the experimental results it can be seen that the catalytic activity (and other kinetic parameters) of the samples strongly depends on the iron content for $\text{Sr}(\text{Fe}_x\text{Ti}_{1-x})\text{O}_{3-\delta}$, or dopant level x for samples with other dopants, as shown in Figures 4.7 (b) and 4.11(b), for CH_4 and CO oxidation respectively. Thermogravimetric measurements show that a catalyst may (in CO oxidation) or may not (in CH_4 oxidation) undergo a bulk stoichiometric change (i.e., reduction). If the stoichiometric change does occur it effects the activity of catalyst as a feedback, and effect also the corresponding kinetic model, as it will be demonstrated.

As a test of the kinetic models, their predictions for partial reaction orders summarized in Table 4.5 (m for CO/CH_4 , and n for O_2) are to be compared to the experimentally obtained data given in Figures 4.9 and 4.13. The m - and n -experiments will be therefore addressed first. As they are not subject to a direct comparison between experiment and model, the other experimental findings will be discussed afterwards. The CO oxidation will be addressed first, inasmuch it involves more subtle details. Thereafter the CH_4 oxidation will be discussed with attention paid to parallel and divergent features from the CO oxidation.

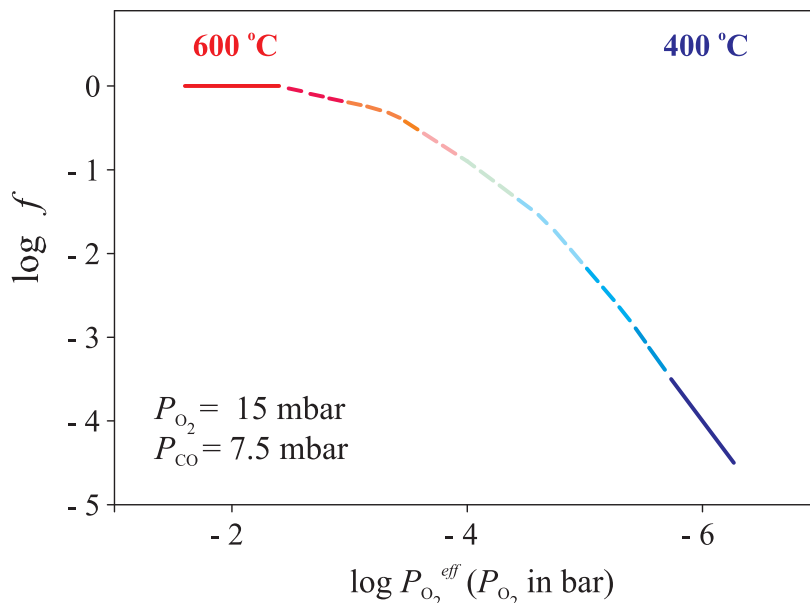


Figure 4.23: Qualitatively described temperature dependence of the f factor of the $x = 0.5$ sample. According to the *in situ* TG measurement it can be inferred that (i) an effective $P_{\text{O}_2}^{eff}$ appears due to the presence of CO oxidation, (ii) $f = P_{\text{O}_2}^{eff}/P_{\text{O}_2}$ is a function of temperature $f = f(T)$ when the other variables are fixed (note that $P_{\text{O}_2}/P_{\text{CO}} = 2$), and that f can significantly change upon a temperature change as illustrated by the shown curve which comprises three parts: 1. the red solid line describes a situation where no reduction of the catalyst occurs (600 °C), i.e., $P_{\text{O}_2}^{eff} = P_{\text{O}_2}$; 2. the dashed line is an arbitrary one since the quantitative dependence is unknown; and 3. the blue solid line illustrates a region where severe reduction of the catalyst does occur (at 400 °C), i.e., $P_{\text{O}_2}^{eff} = 10^{-6}$.

CO oxidation: CO partial reaction order (m -experiment)

For low- x samples, it is reasonable to assume that reduction of the catalyst does not occur at all (as shown by *in-situ* ESR). A good agreement between the measured m_{exp} and n_{exp} [see Figures 4.13 (a) and (b)] and $m_{\mathbf{A}}$ and $n_{\mathbf{A}}$ values (see Table 4.5) predicted by the \mathbf{A} kinetic models is attained. On the other hand, in view of *in-situ* TG for CO oxidation, one certainly expects that CO oxidation reaction should belong to the \mathbf{B} group for high- x samples. However, the \mathbf{B} kinetic models predict values $m_{\mathbf{B}} = 0$, which significantly differ from the experimentally found $m_{exp} \approx 0.8$. Obviously, a more elaborate analysis of the apparent contradiction is needed. The standard experimental technique for measuring the partial reaction order m_Z of a reactant Z (m_Z -experiment) is to fix the concentration of all other reactants and to measure the reaction rate R_Z (of a presupposed form $R_Z = kP_Z^{m_Z}$) upon a reactant Z concentration variation: the m_Z is thus obtained from a $\log R_Z = m_Z \log P_Z$ plot. This is an acceptable approach when the system, comprising the reactant Z, the catalyst and the other reactants, is decoupled, i.e., a change in P_Z does not effect does the prefactor k . Now it will be demonstrated that this coupling exist in case of CO oxidation, and that the prediction of \mathbf{B} models must be revised.

For example, the Eq. (4.68) for the case **VIII** (**B** group, class II) reads

$$R_{CO_2}^{VIII} = k \frac{[\widetilde{Fe'_{Ti}}]^2}{[\widetilde{Fe^x_{Ti}}]} [\widetilde{V_O}] P_{O_2}^{\frac{1}{2}} \quad (4.71)$$

It is understood that since the catalyst sees an effective $P_{O_2}^{eff}$, the P_{O_2} -dependencies of $[Fe'_{Ti}]$ and $[Fe^x_{Ti}]$ (for high x , given in Table 4.4) must be corrected by the f factor using Eq. (4.70), the last equation thus becomes

$$R_{CO_2}^{VIII} = k f^{-2a-b-c} P_{O_2}^{-2a-b-c} P_{O_2}^{\frac{1}{2}} = k f^{-2a-b-c} P_{O_2}^{\frac{1}{2}-2a-b-c} \quad (4.72)$$

Taking a logarithm of both sides gives

$$\log R_{CO_2}^{VIII} = \log k - (2a + b + c) \log f + \left(\frac{1}{2} - 2a - b - c\right) \log P_{O_2} \quad (4.73)$$

In an m -experiment, P_{O_2} is kept constant and therefore the last equation can be written as

$$\log R_{CO_2}^{VIII} = \log k' - (2a + b + c) \log f \quad (4.74)$$

The P_{CO} -dependence of f is generally unknown, but it is not difficult to show that in a first order Taylor approximation, the previous equation can be written as

$$\log R_{CO_2}^{VIII} = \log k'' - (2a + b + c) \left(\frac{d \log f}{d \log P_{CO}} \right)_{P_{CO}=P_{CO}^0} \log P_{CO} \quad (4.75)$$

in the vicinity of a $P_{CO} = P_{CO}^0$ point. From discussion in the previous section and from Figure 4.23, it can be argued that the f does decrease with increasing P_{CO} (or put differently, on decreasing P_{O_2}/P_{CO}), and that $f \leq 1$. The prefactor therefore satisfies the relation

$$F^{CO} \stackrel{def}{=} \left(\frac{d \log f}{d \log P_{CO}} \right)_{P_{CO}=P_{CO}^0} \leq 0 \quad (4.76)$$

Since $(2a + b + c) > 0$, Eq. (4.75) with the help of inequality Eq. (4.76) leads to the conclusion that the m -experiment will therefore result in

$$m^{VIII} = -(2a + b + c) F^{CO} \geq 0. \quad (4.77)$$

The value of F factor is the slope of the $\log f$ vs. $\log P_{CO}$ plot in a point $P_{CO}=P_{CO}^0$ which is externally set (but remains unknown) by the experimental conditions. For illustration, F can be deduced for the $x = 0.5$ sample: $m \approx 0.8$ is experimentally obtained, and with the value²⁹ $(2a + b + c) \approx 0.28$, the value of F^{CO} (in case **VIII**) can be estimated to be $F_{VIII}^{CO} \approx 3$. For the case **VIb**, it turns out that the factor $(2a + b) \approx 0.21$ appears instead of $(2a + b + c)$, which leads to $F_{VIb}^{CO} \approx 4$. With these deduced F values, **B** kinetic models could explain the experimentally obtained nonzero partial reaction orders for CO oxidation. However, these F values remain unknown and need to be investigated experimentally in more detail. Nevertheless, there are

²⁹according to Table 4.4, taking the upper limit of the b value for high x

two indications that this interpretation may be the correct one. First, the data points for high- x samples (expected $f \leq 1$) in a $\log R$ vs. $\log P_{\text{CO}}$ plot showed a slight deviation from the straight line [in contrast to low- x samples (expected $f = 1$)], which according to Eq. (4.75) is expected³⁰ when an extended P_{CO} range is covered. It is not clear whether these findings come from experimental errors or are real features of the system, since the covered P_{CO} range used in the experiment was only one order of magnitude (see Table 4.3). Experiments with a broadened P_{CO} range and lower temperatures are needed for the final confirmation of these findings. Second, in Figure 4.23, it is realistic to assume that the slope $F^{T=400^\circ\text{C}}$ at the point $(\log f = -4, \log P_{\text{O}_2}^{eff} = -6)$ must be between 1 and 10, since the curve must end up with $F^{T=600^\circ\text{C}} = 1$. This shows that F is quite sensitive to a temperature change. (Incidentally, the m -experiment for the $x = 0.5$ was performed at $T \approx 390^\circ\text{C}$). It is therefore not too unrealistic to expect a high sensitivity of the F^{CO} to a P_{CO} change, as well, and a value $F^{\text{CO}} \sim 5$ could be realistic in the used P_{CO} range.

CO oxidation: O_2 partial reaction order (n -experiment)

For n -experiments, all **A** kinetic models and the model **VIII (B)** predict values lower than $\frac{1}{2}$ which are more close to the experimental results [see Figure 4.13 (b)] than the values predicted by the remaining **B** models. Again, the theoretical and experimental values of n are in good agreement for the low- x $\text{Sr}(\text{Fe}_x\text{Ti}_{1-x})\text{O}_{3-\delta}$, which is an indication that in low- x region **A** kinetic models apply.

For high- x catalysts, prediction of the **VIII (B)** model is already close to the experimentally found $n_{exp} \approx 0.1$, but in view of Eq. (4.73) it needs to be corrected, too, since the f factor also depends on P_{O_2} . For an n -experiment, from Eq. (4.73) follows an equation similar to Eq. (4.75)

$$\log R_{\text{CO}_2}^{\text{VIII}} = \log k''' - (2a + b + c) \left(\frac{d \log f}{d \log P_{\text{O}_2}} \right)_{P_{\text{O}_2}=P_{\text{O}_2}^0} \log P_{\text{O}_2} + \left(\frac{1}{2} - 2a - b - c \right) \log P_{\text{O}_2} \quad (4.78)$$

and the corrected n is therefore given by

$$n = \frac{1}{2} - (2a + b + c) \left[1 + \left(\frac{d \log f}{d \log P_{\text{O}_2}} \right)_{P_{\text{O}_2}=P_{\text{O}_2}^0} \right] = \frac{1}{2} - (2a + b + c) (1 + F^{\text{O}_2}). \quad (4.79)$$

Since f increases with increasing P_{O_2} it follows that $F^{\text{O}_2} \geq 0$, and thus it has been shown that the corrected n can further approach the experimentally found $n_{exp} \approx 0.1$. For illustration, deduced values of F^{O_2} which bring to accord experimental and predicted values are $F_{\text{VIII}}^{\text{O}_2} \approx 0.4$ and $F_{\text{VIb}}^{\text{O}_2} \approx 3.3$, for **VIII** and **VIb** cases, respectively. This shows that for case **VIII**, a weaker P_{O_2} -dependence of the f factor could fully describe the experimental findings.

To summarize conclusions for CO oxidation, in the region of low x , the $\text{Sr}(\text{Fe}_x\text{Ti}_{1-x})\text{O}_{3-\delta}$ samples are less active with respect to the oxygen in/ex-corporation and are less subject to an

³⁰since the 1st order Taylor approximation fails in an extended P_{CO} range: the more the $P_{\text{CO}}^{\text{max}}$ (maximal P_{CO}) deviates from the P_{CO}^0 (middle point of the swept P_{CO} range) in the measurement

influence of the CO presence, which favors an **A** kinetic model without lattice oxygen O_O^* as the reactive species, and which leads to the conclusions that the kinetic case **I** is the most suitable one. Note that CO oxidation occurs at much lower temperatures ($T \approx 400$ °C) which is not in favor for an involvement of O_O^* in a reaction mechanism on low- x $\text{Sr}(\text{Fe}_x\text{Ti}_{1-x})\text{O}_{3-\delta}$. High- x catalysts are more sensitive to the CO presence and they readily change their stoichiometry, which favors a **B** kinetic model, i.e., **VI** or **VIII**. According to the previous discussion, the model **VIII** predicts the lowest n , which is the closest to the experimentally observed fact. Hence, it is believed that the mechanism with involvement of lattice oxygen as the reactive species *viz.* the **VIII** case, is the operational one in CO oxidation over high- x $\text{Sr}(\text{Fe}_x\text{Ti}_{1-x})\text{O}_{3-\delta}$ in steady state.

Although neither *in-situ* ESR nor TG measurement during CO oxidation on Mn- and Co-doped SrTiO_3 were performed, it can be assumed that they do undergo Notwithstanding the fact that they apply to both CH_4 and CO oxidation reactions, reduction as well. As Mn and Co ions have more possible oxidation states available than an Fe ion in SrTiO_3 , much richer defect chemistry is therefore expected in these catalysts. According to the discussion above, their m and n values are just apparent notions and they point to no kinetic model directly.

CH_4 oxidation: m - and n -experiment

According to *in situ* ESR and TG results no reduction of catalysts occur, **A** kinetic models are therefore favored in CH_4 oxidation over $\text{Sr}(\text{Fe}_x\text{Ti}_{1-x})\text{O}_{3-\delta}$ for all $0 \leq x \leq 1$. [Note that even CO oxidation (according to *in situ* TG) could not reduce the catalyst at 600 °C, which represents temperatures for CH_4 oxidation m experiments on low- x samples]. In contrast to CO oxidation, measured m and n in CH_4 oxidation are the true partial reaction orders ($f_{\text{CH}_4} \equiv 1$ in all measurements). For low- x samples, although **B** kinetics models predict m values closer to the experimentally found $m \approx 0.5$ and are tempting to be taken as the correct ones, they have to be excluded on account of *in-situ* ESR and TG results. Both **A** kinetic models predict reasonably well the n value, but they fail to explain the experimentally found lower value of $m \approx 0.6$. This remains an open problem. For high x , the partial reaction orders are well described by both the **V** and **VII** cases of class **A**, where the **VII** predicts lower n closer to the experimental findings. Although no final proof for the involvement of the lattice oxygen species O_O^* in the reaction mechanism can be given, the slightly closer prediction for n of the **VII** kinetic model and the higher temperature involved in CH_4 oxidation, makes it plausible to conclude that this model applies in this case and that the lattice oxygen species is involved in the reaction mechanism (*viz.* Mars-van Krevelen).

4.6 Conclusions

It is instructive to emphasize two points here. First, it has been demonstrated that a heterogeneous reaction (CO oxidation) over a complex perovskite oxide system [$\text{Sr}(\text{Fe}_x\text{Ti}_{1-x})\text{O}_{3-\delta}$] can greatly impact the defect chemistry of the catalyst, and that there is a subtle relation

between defect chemistry, kinetic models and experimental findings. To the best knowledge of the author, in published reports on oxidation reactions over similar perovskite-oxide systems this fact is not appreciated at all. If such a perovskite oxide is susceptible to stoichiometric changes (direct indication of a vivid defect chemistry) under reaction conditions, a direct fitting of experimental data to kinetic models is not acceptable, since the experimental data in such a case provide only apparent kinetic parameters which greatly overlook subtleties imposed by the defect chemistry. Second, according to the developed kinetic models (as seen in Table 4.5; note the similar predictions of m and n for both O_{ad}^- and O_O^\times), an experimentally found value of $m \approx 1$ accompanied by a low n is by no means proof for the direct involvement of lattice oxygen as the reactive species, as it is usually regarded to be in literature. For example, such a conclusion was made in the report mentioned in Section 4.5.1 although the investigated perovskite systems involved Mn or Co, for which a very complicated defect chemistry can be anticipated. To discern whether adsorbed or lattice oxygen acts as the reactive species other techniques are necessary (e.g. tracer experiments with isotope labeled oxygen).

An enhanced oxygen vacancy concentration alone seems not to be of importance for CO and CH_4 oxidation. This is best seen in Sc-doped samples which do have enhanced $[\text{V}_O^\bullet]$ but mostly behave as the low- x $\text{Sr}(\text{Fe}_x\text{Ti}_{1-x})\text{O}_{3-\delta}$ catalysts. Since V_O^\bullet are seen as acid-base active centers, it can be concluded that acid-base catalysis does not play an essential role in the reactions considered here [it may have a slight effect in CH_4 oxidation, see Figure 4.7 (b)]. This also suggests that variation of redox activity is of greater relevance for CO and CH_4 oxidations.

Apparently, Fe_2O_3 is the most active sample for the CO oxidation, which has iron ions in the form of Fe^{3+} , meaning that those are important for the catalytic activity. In Fe_2O_3 the oxygen in/ex-corporation into/from the bulk does not take place, and this material is inert in this respect. $\text{Sr}(\text{Fe}_x\text{Ti}_{1-x})\text{O}_{3-\delta}$ become more active with increasing x . Both Fe_2O_3 and high- x $\text{Sr}(\text{Fe}_x\text{Ti}_{1-x})\text{O}_{3-\delta}$ have Fe^{3+} ions and cannot give away bulk oxygen³¹. Naturally, Fe_2O_3 has more Fe^{3+} ions available for catalysis than the $\text{Sr}(\text{Fe}_x\text{Ti}_{1-x})\text{O}_{3-\delta}$ catalyst for any x , which means that its highest catalytic activity does not necessarily include the highest TOFs. It is possible that TOFs of $\text{Sr}(\text{Fe}_x\text{Ti}_{1-x})\text{O}_{3-\delta}$ for $x \approx 0.03$ are comparable or even higher than that of Fe_2O_3 , but in the overall catalytic activity the active centers in the $\text{Sr}(\text{Fe}_x\text{Ti}_{1-x})\text{O}_{3-\delta}$ are just outnumbered by those in Fe_2O_3 . This means that active centers of Mn-, Fe-, and Co-doped catalyst are more active than those of Fe_2O_3 .

When the activity of catalysts with different TM dopants is compared, a so-called twin-peak in the conversion X is found for the series of Mn-, Fe- and Co-doped catalyst (see Figure 4.14). The Mn- and Co-doped samples are more active than the Fe-doped sample in-between located. This is in agreement with the findings of Voorhoeve *et. al.* [50], Figure 4.24, which indicates a possible importance of the electronic d -orbital configuration of the active centers (in CO oxidation more than in CH_4 oxidation), owing to the specific electronic structure of the CO molecule. CO could bind to the transition metal ion as a carbonyl (similar to the adsorption

³¹a reduced $\text{Sr}(\text{Fe}_x\text{Ti}_{1-x})\text{O}_{3-x/2}$ cannot give any more away bulk oxygen in the relevant P_{O_2} range.

on metals [140]). This involves the donation of the carbon electron lone pair into an empty d_z^2 orbital of the metal (which forms a σ bond), and a back donation of t_{2g} electrons into the CO π^* bond. To be more effective in this respect, the transition metal ion should have empty e_g levels and full t_{2g} levels, as in the case of Mn and Co, while iron doped $\text{Sr}(\text{Fe}_x\text{Ti}_{1-x})\text{O}_{3-\delta}$ are less effective due to the $t_{2g}^3 e_g^2$ configuration of Fe'_{Ti} (Fe^{3+}), keeping in mind that they are reduced in CO oxidation ($[\text{Fe}'_{\text{Ti}}] \gg [\text{Fe}^{\times}_{\text{Ti}}]$). Similar results for such a comparison were also found in literature, Refs. [134, 136].

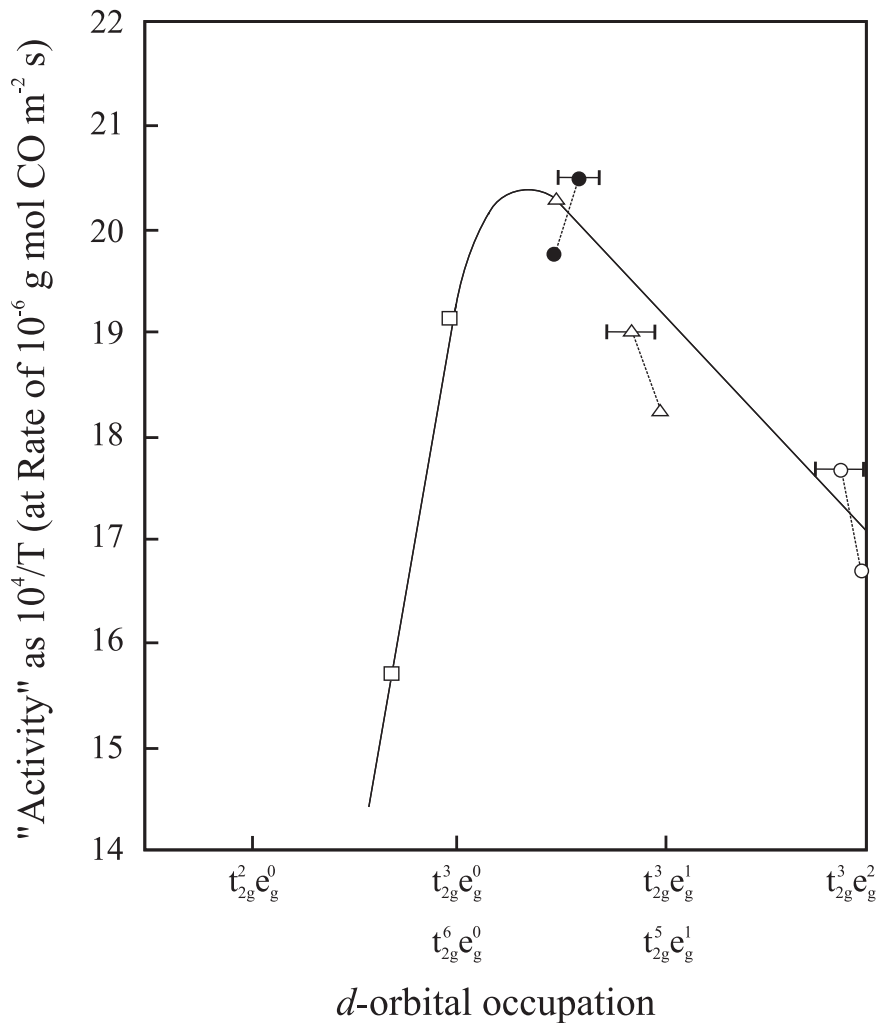


Figure 4.24: Activity of perovskites for the oxidation of CO versus the electronic configuration of the B ion: (□) chromates; (△) manganates; (○) ferrates; (●) cobaltates. Maximum activity occurs when the occupation of e_g levels is low, but t_{2g} levels need to be occupied. Activity is expressed as $10^4/T$, where T is the temperature at which the rate of oxidation is 10^{-6} gm mol m^{-2} sec, in a 2:1 mixture of CO and O_2 at atmospheric pressure. (Data taken from Voorhoeve *et al.* [50])

The change of the $\text{Sr}(\text{Fe}_x\text{Ti}_{1-x})\text{O}_{3-\delta}$ electronic structure with increasing x , as discussed in Chapters 2 and 3, leads to an increased catalytic activity [see Figures 4.7 (b) and 4.11 (b)]. In CH_4 oxidation, a more pronounced increase of the activity of $\text{Sr}(\text{Fe}_x\text{Ti}_{1-x})\text{O}_{3-\delta}$ when passing from low- x to high- x region is observed [Figure 4.7 (b)] where for high- x , the activity becomes

the highest in comparison to all other samples (even higher than Fe_2O_3). Also, a significant reduction in the activation energy with increasing x is observed (see Figure 4.8). These results indicate that the change of the electronic structure of $\text{Sr}(\text{Fe}_x\text{Ti}_{1-x})\text{O}_{3-\delta}$ with x , discussed in Chapter 3, has a more pronounced impact on the catalytic activity in CH_4 oxidation than in CO oxidation.

Approximately similar activation energies ($E_a \approx 1$ eV) for all catalysts in CO oxidation, indicates that the dominant activation process is independent of the catalyst nature, and suggests that it is closely related to the activation process of the CO molecules themselves. The CO molecule is certainly more active than the CH_4 molecule, and it is to be expected that the CO oxidation reaction will show less pronounced features of the catalysts, as in the case of E_a which is similar for all the catalysts.

Chapter 5

Electrocatalytic ammonia synthesis using Lithium nitride solid electrolyte

In this chapter, the work done on the anticipated possibility of electrocatalytic ammonia synthesis using lithium nitride (Li_3N) will be described. Li_3N is in many respects a unique material¹, and one of these unique features is that the presence of the highly polarizable N^{3-} ion [141] in this ionic compound is leading to an excellent lithium-ion conductivity. This combined with the rather low thermodynamic decomposition voltage, led to the idea of using it to deliver reactive nitrogen at the anode in a process of Li_3N electrolysis. Nitrogen *in statu nascendi* should be reactive enough to react with H_2 molecules supplied as a reactant at the anode to form NH_3 molecules possibly even at atmospheric pressure and comparatively low temperatures. At the cathode side, the transferred and reduced lithium ions are expected to react with N_2 and therefore build a new Li_3N layer. This electrochemical approach is sketched in Figure 5.1. The half-cell reaction at the anode is described by

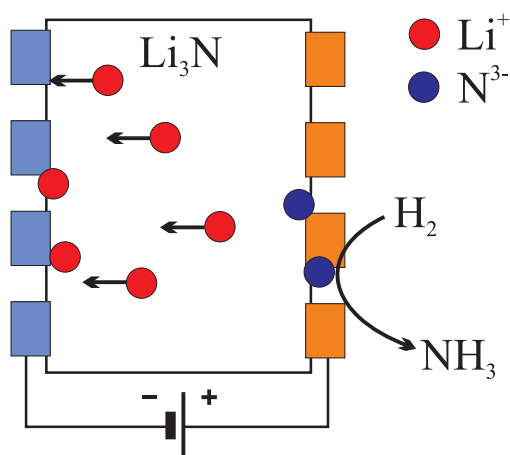
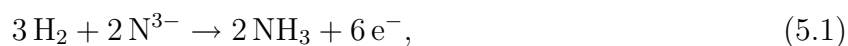


Figure 5.1: The sketch of electrochemical ammonia synthesis using Li_3N .

¹in seventies and eighties of the last century, a great deal of work on characterization of Li_3N has been done at Max Planck Institute for Solid State Research in Stuttgart by A. Rabenau, E. Schönherr, H. Schulz, K. Schwarz, H. Brendecke, U. van Alpen, and others.



and the second reaction at the cathode is



By changing the polarity of the electrolysis cell in proper time intervals the loss of electrode/electrolyte contact should be prevented and thus a steady state of ammonia production ought to be achieved. This picture is rather simplified. In an attempt to carry out such an experiment, one encounters numerous practical problems which will also be described in this chapter. In this work, various measurement techniques were used to investigate Li_3N samples. Measurements involving Li_3N surfaces/interfaces, such as impedance spectroscopy, dc current and voltage measurements, or surface analysis by photo-electron spectroscopy, proved usually not to be well-reproducible, which made drawing of firm conclusions very difficult. The origin of the irreproducibility is most likely to be found in the high chemical reactivity of Li_3N which led to an almost instantaneous contamination of its surface if exposed even to traces of oxygen or moisture. Another reason for the irreproducibility of electric measurements are structural changes of samples under current flow and voltage cycling.

5.1 Introduction

Lithium nitride is the only stable alkali-metal nitride, which spontaneously forms in the reaction of elemental lithium and nitrogen gas even at room temperature. Li_3N is an ionic compound and belongs to the group of fast lithium-ion conductors. Lithium conductors are especially interesting for energy storage applications. Low weight of lithium metal and its strong electropositive character enable high-energy storage capacity per weight in a lithium-based battery. In seventies and eighties of the last century, Li_3N arose a lot of interest mainly as a potential electrolyte for lithium battery applications. For such an application it is necessary that the electrolyte is stable in contact with elemental Li, and that it has a high lithium-ion conductivity. Li_3N fulfills both requirements. As a solid, it has a rather high ionic conductivity at room temperature which is comparable to those of liquid electrolytes, while its electronic conductivity is minor, and it was therefore initially considered as an excellent electrolyte candidate. However, Li_3N has three major drawbacks: (i) it has a very narrow thermodynamic stability window which limits the maximum cell voltage to the value of about 0.44 V; (ii) it is an extremely reactive material which is very difficult to handle, which is even ignitable in form of a fine powder; and (iii) it is a brittle solid with bad contact to solid electrodes. It has therefore not experienced a larger scale of usage in battery applications. Apart from the research for battery applications, extensive theoretical and experimental work on the material's properties such as electronic band structure [142, 143, 144], transport mechanism [145, 146], optical properties [147], and lattice dynamics [148, 149] has been performed. A good review article which summarized the work done on Li_3N until 1982 has been written by

the late A. Rabenau [150]. Recently, Li_3N is considered as a potential material for reversible hydrogen-storage applications [151, 152, 153].

5.1.1 Properties of lithium nitride

Li_3N is an anisotropic ionic solid of a dark ruby-red color. Li_3N crystals of high quality are transparent. It has a mass density of about 1.29 g/cm^3 and a melting point at $813 \text{ }^\circ\text{C}$. It is a very reactive material and must be handled very carefully. Li_3N powder can explode if it comes in contact with (even cold) water. Owing to reaction with moisture Li_3N powder has a strong ammonia odor.

Preparation methods

Due to high reactivity of both elemental lithium and lithium nitride, it is very hard to prepare high purity samples. Several methods have been reported. For preparation of single crystal and polycrystalline samples, Schönherr *et. al.* have used the Czochralski method [154], for which tungsten was found to be a suitable crucible material². Raw poly-crystalline Li_3N was obtained by the reaction of 99.9 % lithium metal with purified nitrogen, and was further melted in a crystal growth chamber. The authors had managed to grow ingots up to 3 cm in diameter and 5 cm in length. Good samples were of a ruby-red color and they were transparent when sliced to 1 to 2 mm. Traces of Al, Mg, and Cu were found in the pulled crystals, whereas Ca was also present in the solidified residual melts.

Preparation of Li_3N single crystals by the floating-zone (FZ) technique has been reported by Nishida *et. al.* [155]. The authors started with a rod (diameter about 9 mm) of 99 % metallic lithium which was reacted for two days without heating with 5N nitrogen gas. The reaction proceeds until all Li is used up. This is possible because the newly formed Li_3N is porous and N_2 gas can always reach unreacted Li by diffusion. The rod was afterwards introduced into an infrared imaging furnace where the crystal was grown in a stream of 5N nitrogen gas. During the growth, due to substantial temperature gradients (from the surface to the center of the melted zone), decomposition of Li_3N occurred with release of N_2 which was followed by lithium evaporation. The overall extent of evaporated Li_3N was estimated to 15-30 %. The process of crystal growth was therefore very difficult to control, which makes this technique rather inconvenient. In contrast to the Czochralski growth, samples contained also oxygen and hydrogen impurities apart from other metals traces.

When crystallinity is not a critical issue, Li_3N can be prepared as described by Barker *et. al.* [156]. They have added pure lithium into an excess of molten sodium in a stainless steel crucible (at $250 \text{ }^\circ\text{C}$), which after cooling was sealed inside a distillation vessel. The vessel was evacuated, filled with nitrogen (*ca.* 2 atm), and heated to $650 \text{ }^\circ\text{C}$. The excess of Na was removed by vacuum distillation for 12h. The advantage of this method is that sodium will

²this was a critical issue since molten Li_3N was severely attacking chemically all other tested material

react with contaminants faster than lithium, thus purifying the system during the synthesis process.

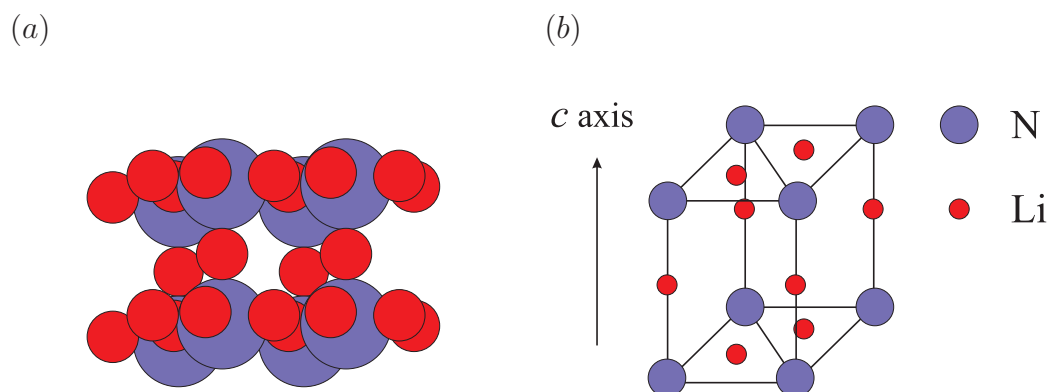


Figure 5.2: (a) Layered structure of Li_3N . (b) Li_3N unit cell. The cell parameters are $a \approx 3.65 \text{ \AA}$ and $c \approx 3.88 \text{ \AA}$

Crystal structure

Based on crystal-chemical considerations, Zintl and Brauer (1939) concluded that Li_3N is composed of Li^+ and N^{3-} ions, and proposed a layered hexagonal crystal structure for Li_3N , composed of alternating Li_2N and sparsely populated Li layers, in which the nitrogen ions are coordinated by 8 lithium ions, where lithium ions are surrounded by 2 or 3 nitrogen ions [157]. This contributes to the stabilization of the N^{3-} ion in this material. Similar stabilization effects by the Madelung potential are shown for O^{2-} and S^{2-} ions. Li_3N crystals are ruby-red rather than colorless, which along with the fact that the structure shows strongly directed bonds arose a debate of the nature of the bonding in Li_3N , as described in Ref. [158]. The structure predicted by Zintl and Brauer was later re-evaluated by Rabenau and Schulz, and the space group was specified to be $\text{P6}/\text{mmm}$ [159]. Low-temperature investigations have shown that the bonding in Li_3N is predominately ionic, and that the N^{3-} ion exists in this material (unprecedented in solid ionic compounds) [158]. An additional confirmation came from nuclear magnetic resonance (NMR) studies of crystal electric field gradients in Li_3N [160]. The structure of Li_3N is shown in Figure 5.2, Li_3N is formed from Li_2N layers with graphite-like structure (Li ions within the layers are labeled as Li(2) for convenience) bridged by Li ions (labeled as Li(1)) between N ions. The c axis is perpendicular to the Li_2N layers. According to the depicted structure, it can immediately be expected that Li_3N shows anisotropic properties in respect of in-layer (normal to c axis) or layer-perpendicular (parallel to c axis) properties.

Band structure

Doubts about the ionic binding in Li_3N emerged mainly from its optical properties, e.g. from its ruby-red color that is rather unexpected for an ionic compound. The optical absorption edge of Li_3N resembles an edge found in indirect semiconductors [147], and, for example, differs from the one found in typical ionic alkali-halide compounds, which have a direct band gap and narrow and strongly absorbing exciton peaks. As expected, optical properties of Li_3N are strongly anisotropic, e.g. the optical absorption edge features, as well as transmission magnitudes for the $E \parallel c$ or $E \perp c$ (E is the polarization vector of the electric field)³. For $E \parallel c$, the measured band gap energy E_g has a value of about 2 eV at room temperature, which increases slightly with decreasing temperature [147]. For $E \perp c$, optical absorption studies corroborated by photoluminescence studies [161] nevertheless confirmed a similar value of E_g for this polarization.

A first self-consistent electronic structure calculation of Li_3N based on first-principle pseudopotentials, obtained from *ab initio* atomic calculations for lithium and nitrogen, was reported by Kerker [142]. This work confirmed the ionic nature of bonding in Li_3N , where a negative charge (stabilized within a Watson sphere with a radius of 1.4 Å) of about 2.8 elementary charge was ascribed to each nitrogen ion. The calculation yielded an indirect band gap of 1 eV between the N 2*p* and Li 2*s* states. This value is too small compared to the experimentally found 2.2 eV (close to 0 K). The short Li–Li interatomic distances (reduced as compared to metallic lithium) might be the reason for a broadening of the Li 2*s* band, which explains therefore why the optical absorption occurs in the visible region (at ≈ 2.2 eV). It is likely that this broadening is overestimated in these calculations (such a discrepancy is also known in band-structure calculations of semiconductors [162]). However, the obtained ground-state charge densities and electron momentum densities (via the autocorrelation function) reproduce to a high degree the experimentally found Compton profiles [163]. A similar underestimated result of the band gap was reproduced as a first step of *ab initio* molecular-dynamics (MD) study of diffusion processes in Li_3N by Sarnthein *et. al.*, who used a very accurate full potential linearized augmented plane wave method [164].

Ionic conductivity

First measurements of lithium ion conductivity in polycrystalline Li_3N were reported by Galais and Masdupuy [169, 170]; the obtained values were rather low. However, since these measurements were done on loosely compacted powder Li_3N samples, these results were subjected to serious doubt by Boukamp and Huggins [171]. After optimizing the preparation and thermal treatment of sintered samples, these authors reported much higher conductivities [165]. By means of impedance spectroscopy (IS), they have managed to separate the overall conductivity into the ‘transgranular’ (i.e., bulk) and ‘intergranular’ (i.e., grain-boundary (gb)) conductiv-

³distinction of optical properties in an experiment on Li_3N for the two orientations is not trivial (if not impossible), since frozen-in strains present in Li_3N crystals lead to a gradual change of the orientation even in an one domain single crystal [147]

Table 5.1: Ionic conductivity of Li_3N . E_a is the thermal activation enthalpy. The last two lithium-ion conducting materials were added for comparison.

Material	E_a [eV]	$\sigma_{300\text{K}}$ [$(\Omega \text{ cm})^{-1}$]	$\sigma_{400\text{K}}$ [$(\Omega \text{ cm})^{-1}$]	$\sigma_{500\text{K}}$ [$(\Omega \text{ cm})^{-1}$]	Ref.
Li_3N sinter, bulk†	0.25	6.6×10^{-4}	2.3×10^{-3}	8×10^{-3}	[165]
Li_3N sinter, gb†	0.71	$*(0.3 - 9.1) \times 10^{-5}$	$*(0.2 - 5.7) \times 10^{-2}$		[165]
Li_3N single crystal ($\perp c$)‡	0.29	1.2×10^{-3}	8×10^{-3}	4×10^{-2}	[166]
Li_3N single crystal ($\parallel c$)‡	0.49	1×10^{-5}	6×10^{-4}	8×10^{-3}	[166]
Li- β -alumina		1.3×10^{-4}			[167]
Li, Na- β -alumina		5×10^{-3}			[168]

† Boukamp and Huggins (1978)

‡ v. Alpen *et. al.* (1977)

* these values depend on the sample thermal history

ities, and obtained the respective activation enthalpies, given in Table 5.1. Different thermal activations lead to a dominance (magnitudes) of one of the two conductivities in temperature regions below and above a ‘transition’ temperature. From the intercept of the two conductivity curves in a $\log \sigma T$ vs. $10^3/T$ plot, the transition temperature can be estimated. Above 200 °C, the grain-boundary conductivity dominates, whereas below circa 70 °C the bulk conductivity is dominant (see Figure 5.12). It is noteworthy to say that they offered an explanation for the observed decrease of the grain-boundary conductivity upon temperature cycling between ambient temperature and 200 °C. The initial conductivity can be restored by annealing at 750 °C for half an hour. The explanation is that due to strongly anisotropic properties of Li_3N , the contact areas between the grains change a lot upon temperature cycling, effecting therefore the conductivities. This effect caused the transition temperature between the regions of dominant bulk or grain-boundary conductivity to shift between approximately 70 to 150 °C depending on the sample thermal history. Conductivity of single crystal Li_3N was first reported by v. Alpen *et. al.* [166]. Their results for both directions ($\perp c$ and $\parallel c$) are also indicated in Table 5.1.

Due to practical problems, the transference number of lithium-ion conduction in Li_3N remained unknown [150]. In an attempt of its measurement, using an Mo|Li| Li_3N |Li|Mo configuration, the current was measured with sufficient precision, but the amount of the transferred Li could not be determined exactly since it was not possible to separate neatly the Mo and Li electrodes and the Li_3N sample. Nevertheless, lithium-ion transport was clearly observed in these measurements.

The ionic conduction in Li_3N is explained by a vacancy mechanism, which occurs predominantly in the Li_2N layers (i.e., in the Li(2) sublattice) [172] and which is responsible for the conduction in a direction $\perp c$. Li(1) ions are less mobile, and diffusion processes involving both Li(1) and Li(2) ions therefore require a higher activation energy. It is argued that the Li(2) sublattice is intrinsically underoccupied by about 2 % [173], and the reason for this is the

presence of hydrogen as impurity, which results in $(\text{NH})^{2-}$ ion formation on N^{3-} sites [174]. A theoretical study predicted the activation energy E_a^\perp for diffusion in a direction $\perp c$, to be ≈ 0.3 eV [164], which agrees with experimental findings. However, the study showed that the main contribution to E_a^\perp originates from the defect formation enthalpy $[\text{nil} \rightleftharpoons \text{V}'_{\text{Li}(2)} + \text{Li}(1)_i]$, and not from the potential barrier between the sites involved in diffusion, as it was initially expected.

Applications

Apart from its use as a starting material in synthesis of binary and ternary nitrides, and as Li^+ -conductor in electrochemistry, a work reported by Chen *et. al.* [151] set off a research for Li_3N potential use for reversible hydrogen storage (see e.g. Refs. [152, 153, 175, 176]). Conversions of Li_3N powder samples into Li_2NH and LiNH_2 in presence of H_2 under various temperature and pressure (cycling) conditions and their thermodynamic aspects were investigated in these reports.

5.1.2 Ammonia synthesis

In a modern conventional Bosch-Haber process, ammonia synthesis is achieved using Al_2O_3 , K_2O and CaO promoted iron-based catalysts [105, 52]. To achieve conversion of 10–20 %, the synthesis must take place at high temperatures (450 – 500 °C) and high pressures (up to 300 bar). The reaction kinetics is very slow at lower temperatures, but the chemical equilibrium is shifted towards reactants at higher temperatures, as seen in Table 5.2, therefore, higher pressures are needed to shift the equilibrium toward the product and to increase efficiency.

Table 5.2: Approximate Gibbs free energies of formation and equilibrium constants for ammonia formation in relevant temperature range and ambient pressure, from Ref. [177].

T [°C]	T [K]	ΔG_f [kJ/mols]	K_f
25	298	-16.41	750
127	400	-5.98	6.04
*182	456	0	1.00
227	500	4.76	0.318

* interpolated value

Since its discovery, ammonia synthesis played the role of a benchmark reaction, and numerous approaches and methods have been reported in literature. Two examples from literature, which to some extent might be related to this work, will be briefly noted. Marnellos *et. al.* reported ammonia synthesis at ambient pressure using solid electrolytes [178, 179]. They used proton-conducting Yb-doped strontium cerate, $\text{SrCe}_{0.95}\text{Yb}_{0.05}\text{O}_3$, with porous Pd electrodes as electrochemical hydrogen pump. They tested double-chamber cell and single-chamber cell (where N_2 and H_2 are mixed in the chamber) configurations. They obtained conversions of

more than 75 % of the electrochemically transported hydrogen into ammonia at 570 °C in the double-chamber configuration, which is above the thermodynamical limit of the conventional ammonia synthesis. In the single-chamber configuration, the authors observed a weak non-Faradaic electrochemical modification of catalytic activity (NEMCA) effect in ammonia synthesis, first time for a thermodynamically limited reaction.

Another interesting approach of electrolytic ammonia synthesis from water and nitrogen gas in a molten salt at atmospheric pressure involving Li_3N has been reported by Murakami *et. al.* [180]. The authors used a molten salt eutectic (LiCl-KCl-CsCl) at 573 K. Li_3N was added to the melt in an amount of 0.5 mol %, which served as an N^{3-} ion source. Gaseous H_2O in Ar was added to the melt, and it reacted with nitride ions to NH_3 , which was afterwards bubbled out by pure Ar gas and quantified. Gaseous N_2 was introduced to the melt at the porous Ni cathode and reduced to N^{3-} . At the carbon anode, O^{2-} was converted to CO_2 as byproduct. The process is not continuous, but a sequence of alternating ammonia synthesis by water insertion and reduction of N_2 to new N^{3-} at the cathode. The estimated efficiency was about 23 % in terms of the total transferred charge through the cell. The process at the anode was recently improved by using a non-consumable anode, which resulted in O_2 as the only byproduct [181]. This method exploits two facts, (i) the tendency of Li_3N to react with water into NH_3 , and (ii) an LiCl-KCl-CsCl eutectic is used as a ‘solvent’ for Li_3N and thus allows nitrogen to form fresh Li_3N which can be re-used for ammonia synthesis. In contrast to the principal idea described at the beginning of the chapter, this complex catalytic system involves very many chemical components (in particular water⁴) which obscure the underlying mechanism.

5.2 Experimental details

For a realization of the idea of electrochemical ammonia synthesis described at the beginning of the chapter, it is most important to have good Li_3N samples, preferably single crystals, which should provide smooth and reversible lithium-ion transport conditions. Second important point is a good three-phase contact of the electrolyte, the gas phase, and the electrode. Unlike for standard conductivity measurements, here, a maximal possible area of a solid contact between the electrolyte and the electrode must be sacrificed in order to provide an access for the gas phase to the electrolyte (N_2 and H_2 to get into contact, and NH_3 to leave the three-phase boundary region). Porous electrodes are therefore intentionally used in electrocatalytic experiments in forms of net or pasted electrodes. Since at the cathode and anode two different reactions occur, the highest efficiency for ammonia synthesis would be achieved if the electrolyte at the same time plays the role of a membrane which separates cathode and anode gases, i.e. N_2 and H_2 respectively.

⁴which can in a spontaneous reaction with Li_3N for NH_3

Li_3N samples

In this work three kinds of samples were used

‘old’ single crystals: old single/poly-crystalline samples, which were ‘leftovers’ from the work done between 1975-1985 at this institute (prepared by the Czochralski method, as described in the introduction and Ref. [154]). Most of the samples originated from the solidified melt, and only one ingot of a moderate quality remained available for this work. These samples were sealed in Schlenk flasks with Ar or N_2 for more than thirty years. These samples will be referred to as ‘old-single crystals’ (OSC) although they were seldom one-domain single crystals;

‘new’ single crystals: newly prepared Li_3N crystals in the crystal growth service group of this institute (C. T. Lin) according to the described floating-zone procedure [155]; they are hereafter called the ‘new single crystals’ (NSC). One sample prepared by this technique, the NSC No. 3, is shown in Figure 5.4. As can be seen, the crystal rod is not perfect cylinder. Along such an Li_3N rod, the diameter varies approximately between 6 and 11 mm. Three such rod were prepared.

sintered Li_3N : sintered samples, which will be termed sintered poly-crystalline samples (SPC); their preparation will be described in the following subsection.

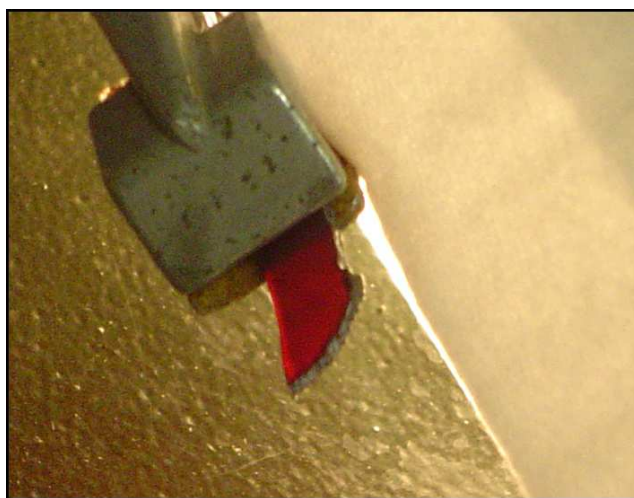


Figure 5.3: A slice of an old ‘single’ crystal. Although on the photograph it appears uniform, the crystal is composed of many crystal domains. This was the best OSC sample. On the edge area, white residues from methanol etching can be observed. Note the irregular shape of the slice, this imposes a constriction for electrocatalytic reactor design (see Section 5.2.7).

Preparation by sintering

For sintering, dark red-brown Li_3N powder (Alfa Aesar) of 99.5 % purity was used. Powders were handled in a glove box under Ar protective atmosphere with oxygen levels less than

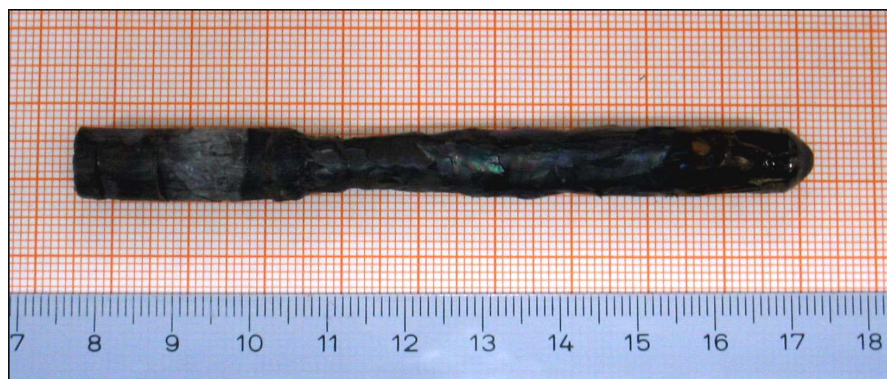


Figure 5.4: The third sample prepared by floating zone technique, by the crystal growth service group at MPI-FKF Stuttgart. The dominant orientations in the growth directions were (100) in central, and (110) in the outermost region of the rod in terms of the radial coordinate, see Section 5.3.2.

0.5 ppm and water levels less than 0.1 ppm. For pressing, stainless steel dies (8 mm inner diameter) were used. A force about 20 kN was applied for 5 min. The pressed samples were regularly-shaped and mechanically very stable. The sample in a tungsten boat was introduced into a quartz cylinder, and sintered under N_2 for 6 hours at 650 °C. (The first attempt to perform the sintering in a duran glass cylinder with an alumina boat resulted in destruction of the cylinder, whilst the alumina heavily reacted with the Li_3N sample as well). After sintering, the samples were almost black (very dark gray), and remained mechanically very stable, but not as brittle as samples made by other two techniques.

5.2.1 Sample preparation

Sample preparation for impedance spectroscopy (IS) and electrocatalytic measurements was performed in a glove-box filled with nitrogen protective atmosphere. The levels of oxygen and water partial pressures in the glove box were kept as low as possible [unfortunately, due to the out of date glove-box equipment (which was the only available during this work) no precise records of those levels were available]. As a quick test of ‘atmosphere’ quality, freshly-cut sodium pieces were exposed to it, which were then visually checked from time to time. Work was performed only when not more than a minimal change on the surface of a freshly-cut sodium pieces was observed (as estimate of the atmosphere quality). (However, the problem of a good working atmosphere might remained a critical issue). The preparation comprised usually of crystal cutting (apart from sintered samples) and surface polishing procedures. Some samples were crushed for powder diffraction measurements in an agate mortar into fine powders. Quartz capillaries were filled with them and sealed. In all sample characterization measurements described in Section 5.2.2, all possible measures to protect samples from air contact or moisture were taken, however, for some procedures, a short contact with air was unavoidable.

Sample cutting

Crystal cutting was performed on a BUEHLER Isomet low speed saw, equipped with a diamond cutting wheel and a wheel-cooling bowl with BUEHLER IsoCut-Fluid as a coolant. The coolant did apparently not react with the samples and was wiped off by a paper towel after cutting. However, the composition of the coolant is unknown and it could be the origin of some impurities found by XPS surface analysis (see in Section 5.2.2). With a low angular rate and a small weight load used to press the crystal against the cutting wheel, cutting of an Li_3N crystalline sample of a diameter about 2–3 cm could take more than 10 hours. Higher angular rates and heavier weight loads provided a higher cutting speed, but usually led to sample fracture. Especially in the second cut, detaching the slice from the bulk, samples were very susceptible to fractures along domain borders. Even when the cutting procedure had been successfully finished, sample slices would sometimes break apart during the polishing procedure or in further stages of the work performed with them.

OSC samples were always of irregular shape, it was not possible to obtain well-shaped disks or even parallelepiped-shaped pieces from those crystals. As the NSC samples were prepared as rods (see Figure 5.4), it was easier to cut them compared to OSC samples. Although less frequent than in the case of OSC samples, similar problems of sample cracking were also present. A perfectly cylindrical pellet was not achievable since the rods were not close to a perfect cylinder. For illustration, one piece of NSC No. 1 is shown in Figure 5.5. The sample is rather dark, and inhomogeneities over the rod profile can be seen.

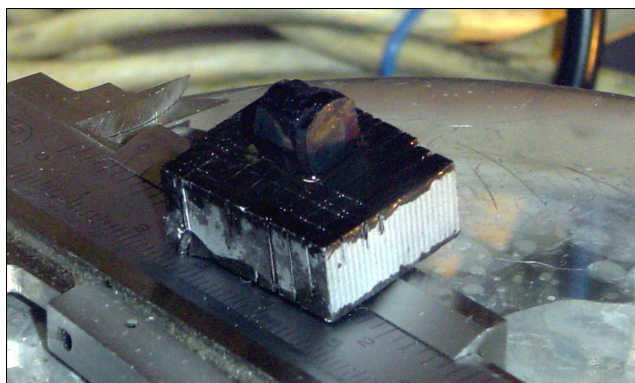


Figure 5.5: A piece of NSC No.1 between two cutting procedures. The sample is glued to a suitable sample support.

Sample polishing

Before mounting a sample into the reactor and applying the electrodes, the sample surface was polished with a silicon carbide emery paper (2400 and 4000 #) and sometimes additionally with a 1 μm - diamond dispersion (Mant, Germany) on a paper which apparently did not react with samples. Occasionally, samples were etched in dry methanol for some seconds, and the produced methanolate surface layer was wiped off by a paper towel.

5.2.2 Sample characterization

XRD characterization

Single crystal diffractograms were recorded using a STOE IPDS II diffractometer ($\text{Mo K}\alpha_1$, $\lambda_1=0.71073$ Å; $\text{Mo K}\alpha_2$ was also present) in ω -scans measuring mode at room temperature. In determining the lattice parameters only reflections which obeyed the relation $I > 20\sigma$ (where σ is an experimentally determined standard deviation of peak intensities) over a range from $10\text{-}13^\circ$ to 69° were included. Cell dimensions were corrected by an Si single crystal.

Powder diffractograms were recorded on a BRUKER AXS D8 Advance diffractometer ($\text{Cu K}\alpha_1$, $\lambda = 1.5406$ Å; equipped with a Ge (111) primary beam monochromator and a VANTEC detector) in the Debye-Scherrer geometry, in a 2θ range from 5 to 65° with a 0.17° step. Samples were sealed in glass capillaries of 0.5 mm diameter. A quantitative phase analysis was performed by the Rietveld refinement method, implemented in the TOPAS 3.0 software.

X-ray photoelectron spectroscopy (XPS)

XPS was used for surface analysis. XP spectra were recorded with the help of an electron spectrometer (AXIS ULTRA, Kratos, UK) using monochromatized $\text{Al K}\alpha_1$ radiation (1486.58 eV). The vacuum during the measurements was kept below 10^{-9} Torr. From the glove box, samples were transferred to the XP spectrometer in a stainless steel vacuum-tight vessel. The sample surfaces were sputtered with high purity Ar^+ ions using a 4 kV argon gun with a current density of ≈ 1.5 $\mu\text{A}/\text{mm}^2$. Prior to the first measurement, the sample was sputtered shortly (typically for 5 min). Surface analysis was performed by series of alternating spectra recording and sputtering steps. Spectra were recorded in normal mode or in survey mode (for a quicker measurements with less resolution). The ubiquitous carbon peak was used as an internal standard because Li_3N is not metallic, and Fermi levels of the Li_3N samples and the analyzer are therefore not equal. According to the difference of the known and the measured position of the carbon peak, all Li_3N XPS spectra were corrected by -1.4 eV. The sensitivity of this technique is determined by the so-called electron escape depth, which depends on the material under investigation, and it is usually limited to several nm. The sputtering rate, apart from the ion-beam energy and intensity, depends strongly on the material⁵. For Li_3N , the actual sputtering rate was not known, and therefore only sputtering times are noted. As a rough estimate, a sputtering rate higher than 1 nm/min is expected for Li_3N .

Chemical check

The content of Li_2CO_3 was checked on a selected sample by dissolving 0.33 g of Li_3N in boiling distilled water under N_2 atmosphere. No visible precipitate was observed, and no significant amount of Li_2CO_3 is therefore expected to be present in the sample. This result was confirmed also in XRD measurements.

⁵for example, the sputtering rate for wet thermally grown SiO_2 under the described conditions is 1.5 nm/min

5.2.3 Electrodes for IS and electrocatalysis

For electric contacts several possibilities were tested. For electrochemical ammonia synthesis is important to have a great length of so-called three phase boundaries, where Li_3N , electrode and gas phase meet. Only porous electrodes are thus used for this purpose. As net electrodes, three kinds of Pt-nets were used: coarse, one with 1024 mesh/cm² (wire \emptyset 0.06 mm), and the finest with 3600 mesh/cm² (wire \emptyset 0.04 mm). They provide a very good gas contact, but a poorer electric contact than Pt-paste or Pt-sputtered electrodes.

Pt paste (Heraeus CLII-5100 Capacitor metallization) was used for electrodes occasionally both in IS and electrocatalytic experiments. The paste was applied on the polished surface of a sample in the form of very thin layer, and the sample was let to dry until the organic solvent had evaporated. Afterwards, the sample was placed in a small tungsten boat and calcinated under N_2 in a quartz cylinder at ≈ 600 °C for an hour. In this last step, the sample experienced ambient atmosphere for a couple of seconds. Pt-paste electrodes after such a calcination are known to be porous.

A few samples were prepared with sputtered Co/Au or Pt electrodes for comparison. The sputtering device used had no sample-transfer vessel. Initially polished sample surfaces were probably contaminated by an oxide or hydroxide layer formed during the sample mounting, in spite of the Ar glove bag used for sample protection. Samples with sputtered electrodes were used for IS only.

It must be emphasized that all applied electrodes belong to the group of non-reversible electrodes since they were not made of metallic lithium.

5.2.4 Impedance spectroscopy

Impedance spectra were recorded with a Solatron SI 1260 impedance analyzer, in a frequency range from 10^7 to 10^1 Hz. IS spectra were analyzed and fitted to equivalent circuits by ZView 2.80 program.

For IS measurements and electrocatalysis it is important to know the c -axis direction of an Li_3N sample. Many attempts of sample orientations were made using a Buerger precession camera. However, this has not been achieved since Li_3N crystals used were never of one single-crystal domain (these domains were much smaller than the required pellet size). No matter which sample was used, Laue photographs contained more reflections than expected for one single-crystal domain. From IS measurement it was therefore not possible to obtain separated conductivities for directions $\perp c$ and $\parallel c$.

5.2.5 Cyclic voltammetry

For cyclic voltammetry measurements an electrochemical interface Solatron SI 1287, together with a Solatron 1255 HF frequency response analyzer was used. Various measurement regimes were tested on one OSC (No 3, slice 3th) using two reversible lithium electrodes (reference and counter) and one blocking electrode (Pt paste).

5.2.6 Scanning electron microscopy and optical micrographs

Sample morphologies before and after electrocatalytic reactions were investigated by a Leica STEREOSCAN 420 scanning electron microscope. Optic micrographs were taken in air with a Mitutoyo optic microscope equipped with a Panasonic convertible camera AE-E300. During the optical investigation, OSC samples appeared to be stable in air.

5.2.7 Experimental setup

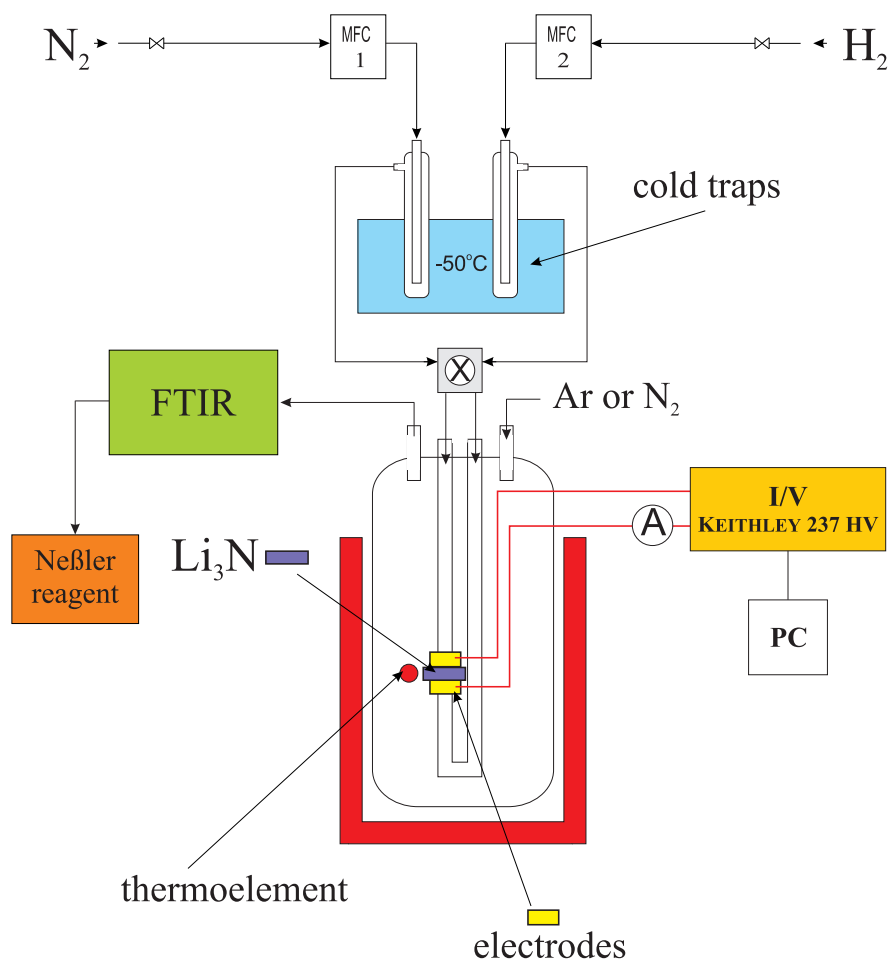


Figure 5.6: The experiment setup with the quasi-double chamber reactor.

An experimental setup for the electrochemical ammonia synthesis has to fulfill many requirements. Due to the high reactivity of Li_3N , all gas connections must be (vacuum) tight, and besides, the reactant gases (H_2 and N_2) must be dried before getting into the reactor which is the IS and electrolytic cell at the same time. If different gas compositions are used at both sides, a possibility of interchanging of the supplied gases (H_2 or N_2) at both electrodes must be provided. Good mechanical stability and good electric contact of a sample between the electrodes are also required. Also, control of reactor-operation temperature must be achieved,

and temperature must be measured as close as possible to the sample. The scheme of the used experimental setup is shown in Figure 5.6.

Due to the above mentioned difficulty to obtain well-shaped Li_3N samples, it was not possible to design a reactor with fully gas-separated electrodes. One approximate solution of such a design was tested, namely, the quasi-double chamber reactor.

Single-chamber reactor

First IS and electrocatalysis measurements were performed on a single chamber (SC) reactor without gas-separated electrodes, as shown in Figure 5.7. In this case, the same gas compo-

(a)



(b)



Figure 5.7: (a) The quartz ‘fork’ is the sample holder used for a single chamber reactor, which can supply a single gas mixture at both sides of the sample. (b) The single chamber reactor which serves simultaneously as IS-measurement and electrolysis cell. All glass parts are made of quartz. An Li_3N sample, sandwiched with two platinum nets electrodes, is mounted between the two quartz branches which can supply a single gas composition. In operation, the gases were supplied from the left-hand side and were leaving the reactor through an outlet (not seen completely in the photograph) to the FTIR.

sition is supplied to both electrodes through quartz capillaries. The capillaries also serve as sample holder. The sample is placed between the two quartz frits, which are embedded into

the capillary ends [see the left-hand side of the quartz ‘fork’ in Figure 5.7 (a)]. These frits press the sample (together with the electrodes) by elastic forces due to the particular capillary shape. The sample thickness was always slightly greater than the distance between the frits of the relaxed quartz fork. The three straight horizontal capillaries serve to fix/guide a thermoelement and electrode wires. The reactant gas mixture is supplied through the capillaries to the electrodes, and flushes them. This prevents, or at least reduces, a backward gas diffusion of products to the electrodes. The experiment-ready reactor, with sample, Pt-net electrodes, wiring and thermoelement, is shown Figure in 5.7 (b). The reactor can be flushed by N_2 or Ar through an additional gas inlet (not visible in the figure) when needed. The gases leave the reactor through an outlet at the right-hand side of the cylinder. One shortcoming of this particular reactor is the large ‘dead’ volume in the cylinder, which dilutes produced ammonia and flattens the gas detector (FTIR) response. Another shortcoming is that the sample is not uniformly pressed (not ideally parallel frits). Also, the capillaries are very fragile and broke several times during sample mounting.

Quasi-double chamber reactor

The reactor design is improved in a quasi-double chamber (QDC) reactor shown in Figure 5.8. In this reactor, a different gas can be supplied at each electrode. The force which keeps the sample between the frits and electrodes is produced by a stainless steel spring-like gas connector [shown at the left-hand side of Figure 5.8 (a)]. A close-up of the sample position is shown in Figure 5.8 (b). The lateral view in Figure 5.8 (c) shows the reduced lateral and, therefore, the reduced total volume of the reactor, as compared to the SC reactor. In this reactor the mechanical force acts uniformly over the whole sample-electrode area.

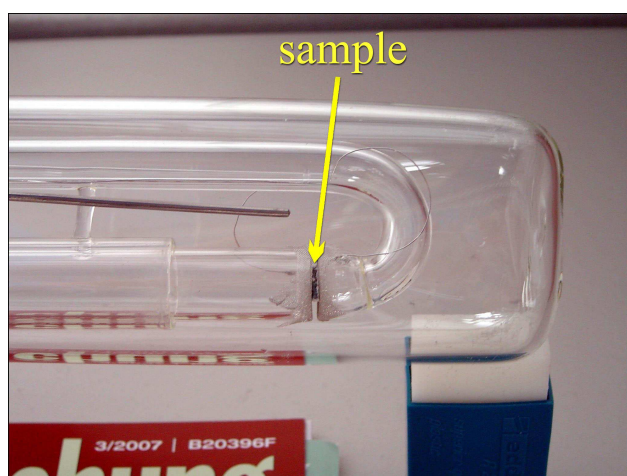
5.2.8 Detection of ammonia

For ammonia detection the FTIR spectroscopy, that was already described in Chapter 4, was used. Prior to measurements, the FTIR spectrometer was calibrated for NH_3 . For some measurements (mainly in the preliminary experiments), an additional qualitative check has been performed to assure the detection if the ammonia concentration is under the detection limit of the FTIR. The presence of NH_3 in the exhaust gas leaving the FTIR spectrometer was checked by means of two gas bubblers in series, each containing a small amount of the Neßler’s reagent ($\text{K}_2[\text{HgI}_4]$). The second bottle was used for a test whether or not the first bubbler was efficient enough to collect all the ammonia from the gas passed through. The Neßler reagent reacts very sensitively to ammonia and changes its color depending on the amount of ammonia with which it has reacted. The fresh (unused) Neßler reagent has a pale yellow color, whereas an ammonia saturated Neßler reagent has a dark yellow-brown color. Also, for the visual ‘calibration’, four different solutions with known ammonia content were made, which gradually changed in the described color range.

(a)



(b)



(c)

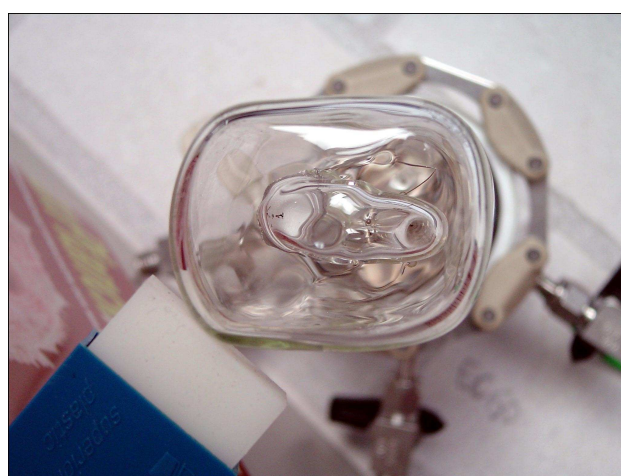


Figure 5.8: The quasi-double chamber reactor (i.e. simultaneously IS-measurement and electrolysis cell). All glass parts are made of quartz. An Li_3N sample, sandwiched with two platinum nets electrodes, is mounted between the two quartz branches which can supply different gases at electrodes. (c) A side view which shows the reduced reactor volume compared to the single chamber reactor.

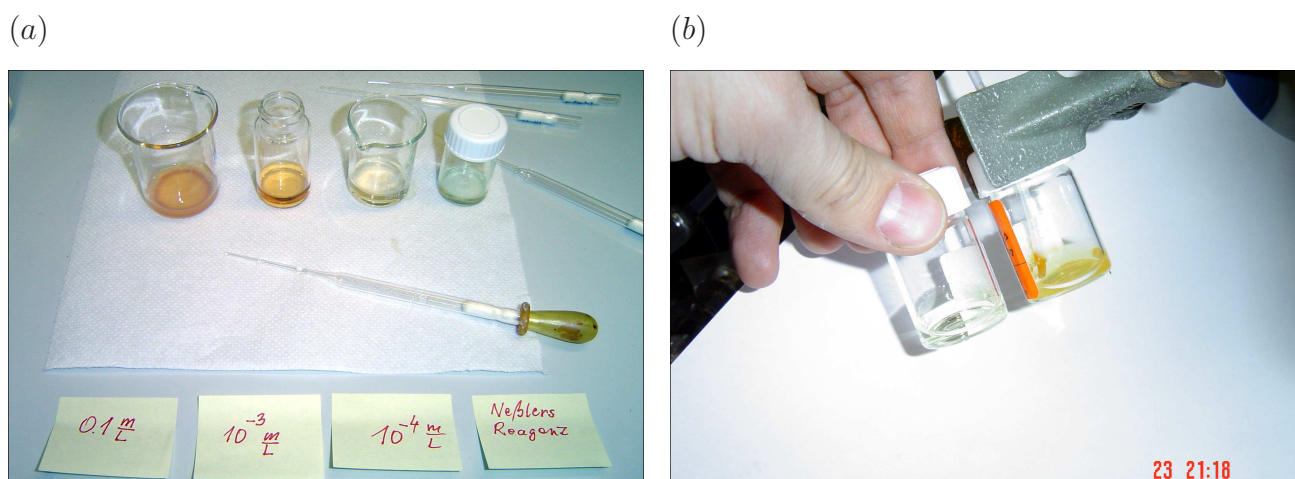


Figure 5.9: (a) Neßler's reagent 'calibration' with ammonia solutions of different concentrations. (b) An example of detected ammonia in the gas after a reaction.

5.2.9 Reaction conditions

In the ideal case, the desired operational temperature for ammonia synthesis would be ambient temperature. At these temperatures, NH_3 formation is exergonic at ambient pressure. The high pressure used in technical ammonia synthesis is necessary as the critical kinetics demand elevated temperatures. However, electrocatalytic test measurements have shown that ammonia synthesis at ambient temperature is not feasible. The main reason is probably the high resistance of the sample-electrode system and/or too slow electrode kinetics at low temperature. Since in many measurements the contact between a sample and the Pt-net electrodes was just mechanical, higher temperatures provided better IS spectra. However, high operational temperature is limited by two factors: (i) temperature dependence of the equilibrium constant of ammonia synthesis, for 1 bar pressure the temperature is limited to ≈ 150 °C, where the Gibbs free energy of ammonia formation becomes zero (higher temperatures would make this reaction thermodynamically not favorable); (ii) a transition temperature for sintered samples between bulk and gb conductivity (as discussed in Section 5.1.1) happens to be approximately in a range of 70 to 150 °C and temperature should be kept as low as possible⁶. Hence, experiments were performed between room temperature and 145 °C, however, most of the reactions were therefore performed between 130 and 140 °C.

The applied gases were the following. For reactions performed in the SC reactor, a gas mixture of 8 % H_2 in N_2 was supplied to the both of electrodes. In a very important experiment a gas mixture of 5 % H_2 in Ar was also used. Total flows were usually $F_{total} \approx 3.3$ to 5 ml/min. Occasional flushing of the reactor with N_2 or Ar was achieved on demand by an extra gas connection. For IS measurements, pure N_2 or Ar were used. For reactions performed in the

⁶at higher temperatures gb conductivity dominates, which makes the sample less susceptible to electrolysis (see Section 5.3); for 'single' crystal samples this a less critical point, taken that they have negligible amount of grain boundaries.

Table 5.3: XPS relative surface concentrations of selected samples. Surface composition is determined by the species found, and which are indicated in atomic percent. For each sample, the composition is given for two sputtering times.

species	SPC Li_3N		NSC Li_3N		OSC Li_3N	
	5 min	90 min	5 min	210 min	5 min	150 min
O	14.1	9.4	11.1	10.4	6.2	1.8
N	16.6	17.9	18.4	20.1	22.9	25.3
Li	65.1	70.6	69.6	68.2	69.6	72.6
C	4.2	2.1	1.0	1.2	1.3	0.2

QDC reactor, where a different gas composition is possible at each electrode, a gas mixture of 5 % H_2 in Ar was used at the anode side, and pure N_2 at the cathode side. In both reactors, the total flow was kept as low as possible ($F_{total} \approx 3.3$ ml/min) in order to minimize dilution of produced ammonia and to assure its detection by FTIR. Prior to entering the reactor, the gases were dried by passing through a cold trap (glass vessels immersed in Dewar vessels with dry ice and ethanol mixtures) at ≈ -50 °C. An extra gas connection with N_2 or Ar was also used for reactor flushing.

A KEITHLEY 237 High Voltage source unit, controlled by a PC, was used as a voltage/current source and as a measurement unit. Various regimes of operation in electrocatalytic measurements were tested, e.g. unipolar and bipolar voltage pulses of various amplitudes, intervals and frequencies. The data storage capacity of the device was 1000 data points, with maximum sampling rate of 10 kHz. This imposed a constriction such that very fast and very slow transition processes cannot be investigated at the same time with this device. The charge transferred during an electric pulse can be obtained by an automatic integration procedure, but it was subject to large errors due to very noisy current measurements (poor electric contact). Applied voltages spanned from 0 up to 300 V. Remarkably, all Li_3N samples appeared to be stable even at such high voltages, as compared to the thermodynamic decomposition voltage which is ≈ 0.44 eV. This stability is probably due two reasons: generally poor electric contact between the electrodes and the electrolyte; and presence of thin but highly resistive Li_2O or LiH surface layers.

5.3 Results and Discussion

5.3.1 XPS results

Results of the surface analysis on selected samples by XPS are given in Table 5.3. Although the numerical values appear to be very accurate, they must not be taken as exact values, but rather as an indication of the observed trends. It can be seen that in deeper regions the samples have higher purity as compared to the surface. Surprisingly, a high level of oxygen was found also in deeper regions of NSC. Such a finding is not so surprising for the sintered sample, since the starting material was a powder, whose contamination is difficult to avoid.

Table 5.4: Results of single crystal XRD of an NSC sample. Two measurements were performed in the central region of the original Li_3N slice. The indicated growth directions are approximate.

sample region	a [Å]	c [Å]	growth direction
central 1	3.6447(52)	3.8700(51)	1 0 0
central 2	3.6446(97)	3.8619(108)	1 0 0
edge	3.6463(42)	3.8768(46)	1 1 0

OSC samples appeared to be of the highest quality, although they originate from the leftover melts, and are more than thirty years old. Traces of elements such as C, Si and F, were also found in XPS spectra. Apart from its omnipresence in the environment as dust, Si traces are probably coming from the polishing procedure done on an SiC emery paper. Carbon traces are probably coming from the emery paper as well, or they are traces of organic solvents used in the glove box. Fluorine traces could have come from the saw coolant which remained of unknown composition.

5.3.2 XRD analysis of single crystals

A piece of a coin-like NSC slice, similar to those used in electrocatalytic measurement, was investigated under a polarizing microscope prior to an XRD measurement. The sample had a transparent edge region (of ruby-red color) which corresponded to the surface region of the original Li_3N rod, i.e. the slice had a transparent outer ring-like region of a radial thickness about 1 mm, which will be called *edge* region. The region which corresponded to the central part of the original Li_3N rod was dark and not transparent, and will be called *central* region. This indicates that the crystal growth of NSC by FZ technique was therefore not well-optimized. It seems that the best crystal growth conditions were in a region of the melted zone with the highest tangential velocity (i.e at the surface of the rod), which suggests that higher angular velocities are needed to obtain good crystallinity over the whole radius range of the rod. Single crystal XRD was performed both on the edge and central region of the sample at room temperature. The obtained diffractograms corresponded to a hexagonal primitive crystal system. The obtained lattice parameters are given in Table 5.4. For qualitative illustration, the diffraction patterns for the two different regions are shown in Figure 5.10. In the central region of the sample, Figure 5.10 (a), ring-like reflection can be observed which are characteristic for poly-crystalline or powder samples; this indicates that the central region of the sample has many micro-domains. In the edge region of the sample, Figure 5.10 (b), ring-patterns are less pronounced which indicates larger single-crystal domains. The dominant orientation in the growth direction is given in the Table 5.4. However, another set of measurements on a different NSC sample, with a dark and intransparent edge region, could not reproduce the results which would indicate better crystallinity of the sample-edge region.

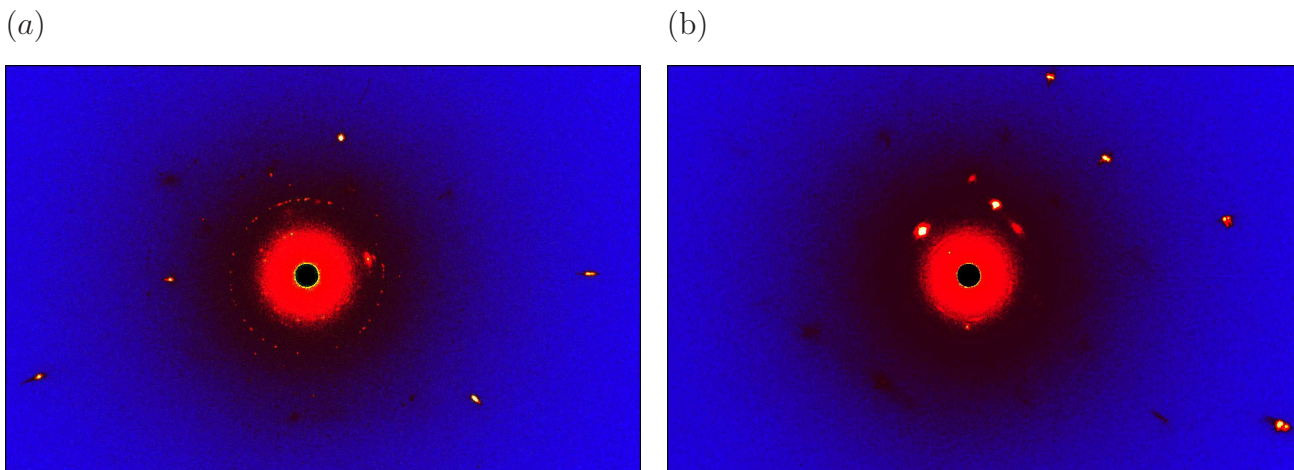


Figure 5.10: Screenshots from the analysis of XRD measurements performed on an NSC sample. The lower quality of the central region of the sample slice is seen in appearance of ring-like reflection patterns, as compared to the edge region which contains less ring-like patterns. The reflection points are in fact doublets due to Mo $K\alpha_1$ and $K\alpha_2$ lines.

5.3.3 Impedance spectroscopy

One example of an impedance spectrum, together with the equivalent circuit used for the data fitting, is shown in Figure 5.11. The NSC sample (third growth, 4th slice) was equipped with Pt-paste electrodes, which means that the electric contact to the electrolyte was pretty good. Pt-mesh electrodes as often used for electrocatalytic measurements, typically, gave much more noisy impedance spectra. This could be due to two reasons: a Pt-paste electrode (*i*) has a larger effective contact area (i.e. behaves as a very fine mesh), and (*ii*) the Li_3N surface beneath it seems to be better protected against contamination compared to Pt-mesh electrodes. In Figure 5.11, it can be seen that the high-frequency semicircle is not ideally shaped, which means that there are parameter distributions within the sample. The low frequency tail belongs to electrode processes (usually fitted by Warburg elements). The temperature dependencies of the bulk and gb conductivities of this sample are shown in Figure 5.12. They were obtained by fitting the equivalent circuit parameters to measured data for each temperature point. This is possible since bulk and grain boundaries in this material have different conductances and effective capacitances (i.e. different ϵ_r), which makes their time constants different from each other, and thus separable in the frequency domain. The bulk capacitance of the sample is $C_{bulk} \approx 1.6 \times 10^{-12}$ F (assuming $\epsilon_r^\infty \approx 10$), while the gb capacitance obtained from the fit is $C_{gb} \approx 8 \times 10^{-10}$ F. Absolute values of conductivity of analyzed samples were usually lower than those reported in literature. Only one sample of OSC and one of NCS had conductivities similar to those of Boukamp and comparable to those of v. Alpen, see Figure 5.12. Bulk activation energies of all analyzed samples have values of about 0.25 eV, which agrees with experimental (see Table 5.1) and theoretical findings [164]. Determined activation energies for grain boundaries were approximately around 0.8 eV, which is close to the values reported by Boukamp (see Table 5.1). Data for one sintered sample are also shown in Figure

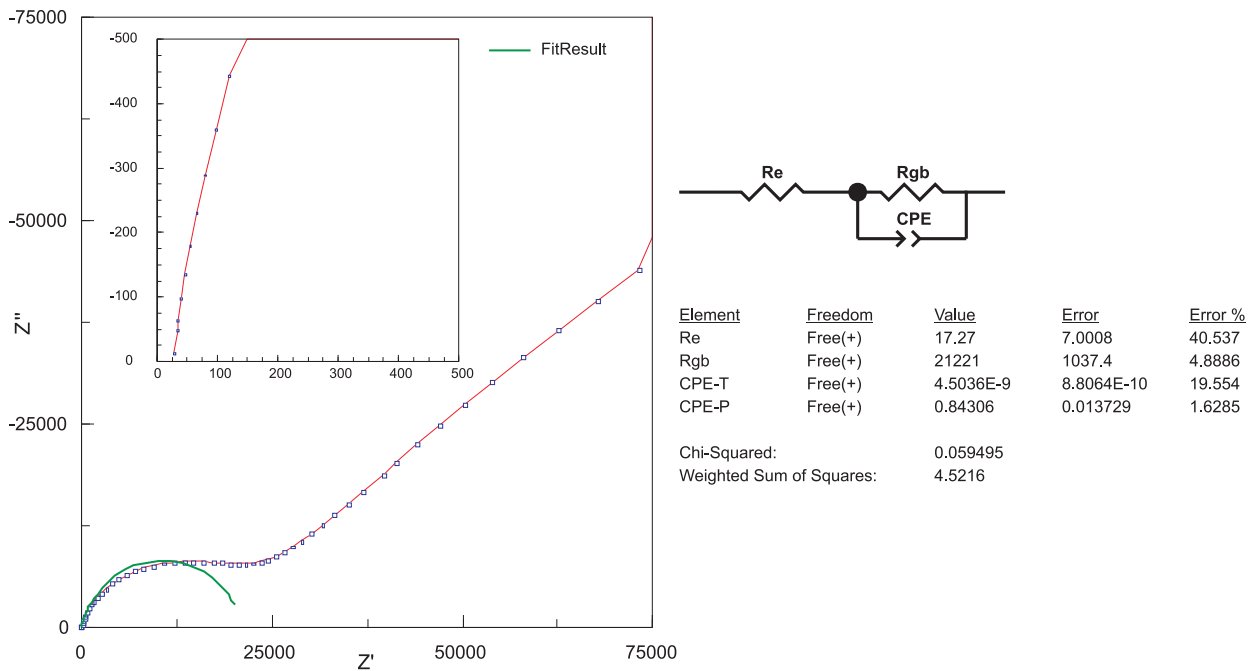


Figure 5.11: The impedance spectrum of an NSC sample (third growth, 4th slice) measured with Pt-paste electrodes at $T \approx 140^\circ\text{C}$. High frequency region was fitted to the given equivalent circuit in order to obtain conductivities for bulk and grain boundaries. CPE is a constant phase element.

5.12. The bulk conductivities agree with those of Boukamp, however, an additional small gb semicircle was obtained from the data fitting. In case of Li_3N sinters, grain boundaries might contain more impurities than bulk. The high σ_{gb} value could be explained by contamination or/and an increased electronic contribution to the conductivity. This is in accord with the absence of mass transport in electrocatalytic measurements on sinters.

Cyclic voltammetry

To look at electrode processes into more detail, cyclic-voltammetry (CV) was applied. However, the measurements were very noisy and highly irreproducible, and no meaningful conclusions were therefore drawn. Still, this is an indication that a good electric contact, a smooth current flow, and reversibility of the whole process is very hard to achieve in case of solid Li_3N electrolyte, in agreement with the general picture given in Ref. [182].

5.3.4 Electrocatalytic reactions in the SC and QDC reactors

Most of the electrocatalytic measurements in the SC, as well as in the QDC reactor were performed at about 140°C , since for lower temperatures the impedance spectra were very noisy (high resistivity and/or indication of poor electric contacts), and total conductivities were much lower. Higher temperatures were not used because of the discussed thermodynamic reasons.

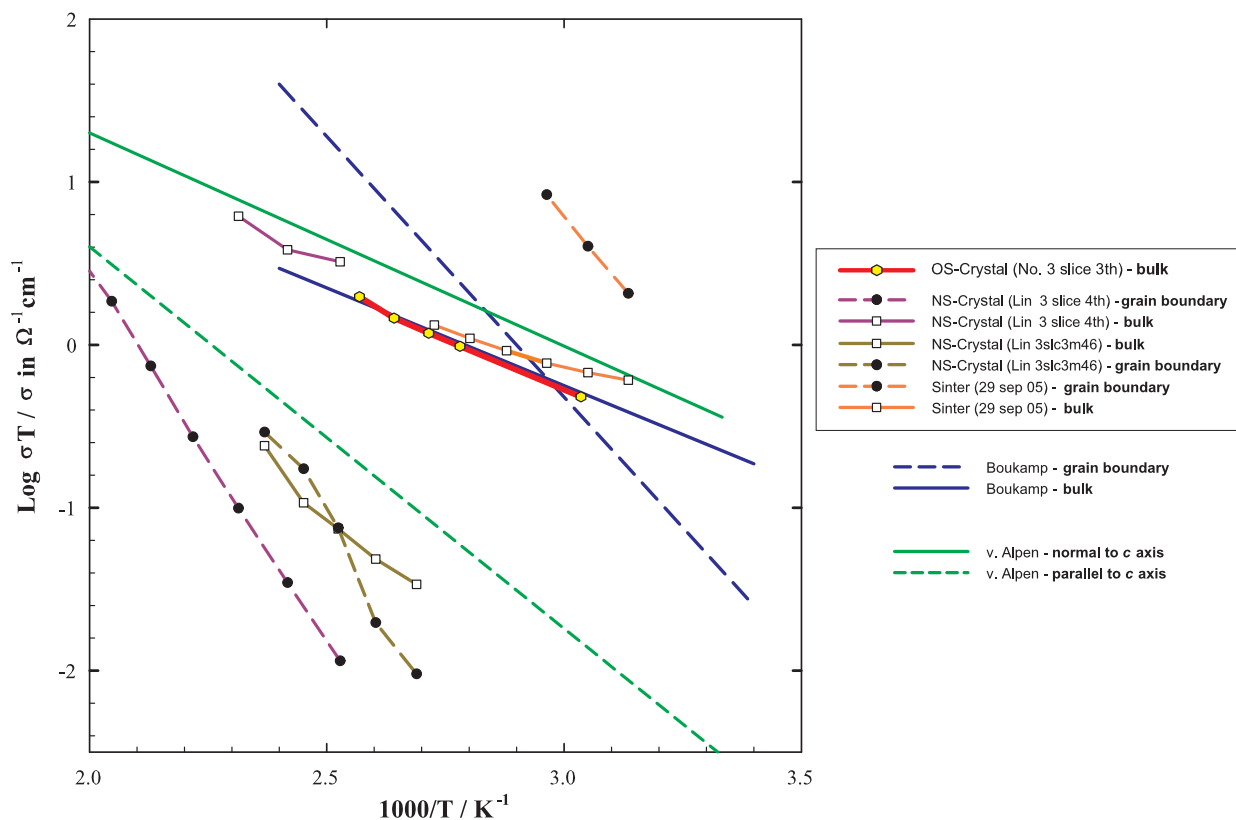


Figure 5.12: Conductivity comparison. Conductivities from literature, for sintered Li_3N (Boukamp *et. al* [165]) and for single crystal (v. Alpen *et. al.* [166]), are given for comparison.

Promising results were obtained with Pt-net electrodes and full attention was focused on them. Pt-paste electrodes usually gave better impedance spectra, but according to preliminary experiments, did not lead to ammonia synthesis. An optimal electrode contacting procedure has not been found.

As a rule, before performing an electrocatalytic experiment, electric contacts were tested by a couple of IS measurements. One or two bipolar pulses with amplitudes up to 50 V and a pulse interval between 10 and 30 s were necessary to obtain meaningful impedance spectra. This procedure was performed in N_2 or Ar, thereby parasitic isolating surface layers (Li_2O , LiH or LiOH) were probably punched-through, improving the electric contact to the Li_3N . However, this might not have helped to improve the gas access to the $\text{Li}_3\text{N}/\text{Pt}$ three phase boundary. It must be emphasized that each tested sample responded differently, as seen in impedance spectra and dc current-time curves, hence, no standard procedure was found.

Before applying any electric stimulus to the electrolyte in an electrocatalytic experiment, the reaction gas flows were established, and the gas analysis was started on the FTIR spectrometer. No traces of ammonia were found in FTIR spectra in the absence of electric stimuli. However, the much more sensitive Neßler's reagent indicated traces of ammonia present in an overnight 'blind' measurement.

In an electrocatalytical experiment, low-voltage pulses (e.g. 1 to 5 V) were tested first.

Bipolar pulses were preferentially used in order to keep both $\text{Li}_3\text{N}/\text{Pt}$ electrode contacts as close as possible in the same condition (in respect of current-cycling history). If no ammonia was observed after the estimated time interval needed for the FTIR spectrometer to respond, the voltage was increased. This was performed up to voltages as high as 200 to 300 V. The sample was visually checked after the experiment. If the sample was not damaged, the polishing procedure was repeated on demand, and new electrodes were made. A new experiment was started afterwards, for example, with different stimulus pulses. Several electrocatalytic experiments with ac voltages were also performed, but no ammonia production was observed.



Figure 5.13: The OSC No. 3 sample before the first electrocatalytic experiment in the SC reactor. The Pt-net electrodes were well-separated and made no short circuit.

Electrochemically synthesized ammonia in the SC reactor

The results of two particular and subsequent experiments performed in the SC reactor with the OSC No. 3 sample (see Figures 5.7 (b) and 5.13) are shown in Figure 5.14. As indicated in the figure, lower voltages were tested first, but only a unipolar pulse of 200 V for a longer time period (≈ 1 hour) resulted in ammonia synthesis, which was clearly detected in the time interval corresponding to the electric stimulus, as shown by the blue curve. The maximum NH_3 concentration was about 0.01 % (blue curve). The total gas flow of the 8 % H_2 in N_2 gas mixture was 3.3 ml/min, and the maximum concentration therefore corresponds to an ammonia molar flow of $\dot{n}_{\text{NH}_3}^{\text{exp}} \approx 2.5 \times 10^{-10}$ mol/s. The shape of the ammonia concentration profiles will be now briefly discussed. The estimated dead volumes of the reactor and the measurement chamber in the FTIR spectrometer (connected by a capillary) were 125 and 240 cm^3 , respectively. Such a gas-vessel system behaves like a low-pass filter, if the ammonia concentration is taken as the signal (measured in the FTIR) with its source being the electrochemical reaction in the reactor. The time constant of such a system is higher than 1 h for the magnitude of the total gas flow used, and is similar to the duration of the applied voltage pulses⁷. As the result, a

⁷this shows also why a small dead volume in the reactor is preferred. A higher total gas flow would speed up the system response, but, on the other hand, it would dilute the ammonia concentration too much.

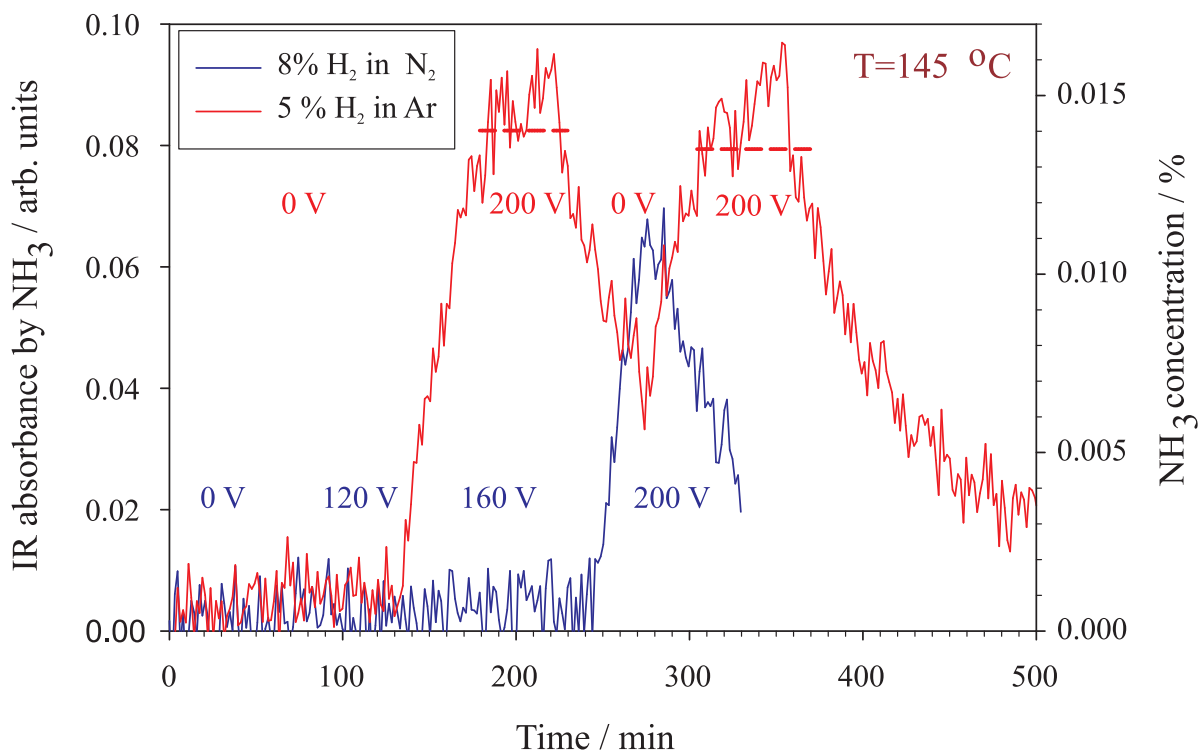


Figure 5.14: Ammonia was detected in two electrocatalytic experiments on the OSC sample (No. 3) monitored by FTIR spectrometer. The blue curve corresponds to the first experiment with H_2/N_2 mixture, and the red curve to the second experiment in H_2 without N_2 . Dashed lines represent the average absorbance in the time intervals where 200 V was applied, they correspond to an ammonia concentration of $\approx 0.014\%$.

pulse of ammonia with a constant production rate in the reactor will be detected in the FTIR spectrometer as a delayed bell-shaped curve. The maximum of this curve is less or equal to the pulse amplitude, and is delayed in time in respect to the middle of the pulse. Two important conclusions can be drawn from this: (i) the maximum of the measured ammonia concentration corresponds to a value which is not an overestimation of the actual ammonia production rate in the reactor; (ii) if the current decays during the pulse, the current values at the beginning of the pulse will correspond more to the time-delayed measured maximum of ammonia concentration.

Since this was one of the first experiments, the experimental setup had not yet been equipped for automatic current recording, but the current was manually read out several times during the pulse. The current at the beginning of the 200 V pulse was fluctuating around a value of $I^{exp} \approx 1$ mA. According to Eqs. (5.1-5.2), three Li^+ need to be transferred in order to produce one NH_3 molecule, hence, in the ideal case, I^{exp} would correspond to an ammonia production rate of

$$\dot{n}_{\text{NH}_3}^{ideal} = \frac{I^{exp}}{3F} \approx 3.5 \times 10^{-9} \frac{\text{mol}}{\text{s}} \quad (5.3)$$

where F is the Faraday constant. The ratio between this value and the measured ammonia

molar flow defines the efficiency of the synthesis process

$$\eta = \frac{\dot{n}_{\text{NH}_3}^{\text{exp}}}{\dot{n}_{\text{NH}_3}^{\text{ideal}}} = 0.07 \quad (5.4)$$

The reason of this low value of the efficiency could be twofold. First, if the lithium-ion transference number of Li_3N is lower than unity, it would result in a decreased number of released N^{3-} ions. Second, if not all released N^{3-} ions participate in NH_3 formation, i.e. some of them form N_2 , a lower efficiency is also expected.

However, during this experiment, an acoustic noise generated in the reactor synchronously to the electric stimulus disclosed an electrical breakdown of the gas (due to tiny gaps between Pt and Li_3N) and a possible ammonia synthesis by a plasma process [183, 184]. In order to confirm that the nitrogen which forms NH_3 molecules originates from the Li_3N sample and not from the gas (via. the plasma process), a second experiment was performed. The experimental conditions were the same as in the first experiment, with the following exceptions: the used gas was 5 % H_2 in Ar without N_2 , and bipolar 200 V pulses were applied (each polarization for ≈ 1 h) instead of the unipolar. After the first bipolar pulse, no stimulus was applied for about 1 h, the second pulse was applied afterwards. The acoustic noise was also present during these pulses. The observed NH_3 production is given by the red curve in Figure 5.14. The peak concentrations were about 0.014 %, which corresponds to an ammonia production rate $\dot{n}_{\text{NH}_3}^{\text{exp}} \approx 3.4 \times 10^{-10}$ mol/s. The current at the beginning of the pulse (i.e. at the beginning of each $+/-$ half period of the pulse) was fluctuating around $I^{\text{exp}} \approx 7$ mA, whereas at the pulse end, it was about 2.5 mA. If the maximal current is taken for the efficiency consideration, the estimation will show the lower limit of the efficiency. According to Eq. (5.3), the current corresponds to $\dot{n}_{\text{NH}_3}^{\text{ideal}} \approx 2.4 \times 10^{-8}$ mol/s, and thus the lower limit of the efficiency of the second experiment is

$$\eta = 0.014 \quad (5.5)$$

The two possible reasons for a low efficiency were already discussed: as the first reason, the transference number might have further decreased as compared to the first experiment (note higher current values); and the second reason might have here a higher contribution due to the lower H_2 concentration offered to the sample. The second experiment confirmed that the nitrogen present in NH_3 must have originated from the Li_3N sample. Unfortunately, an indirect plasma ammonia synthesis cannot be completely excluded: the released N^{3-} ions could have formed N_2 first, and then through plasma activation reacted with H_2 to NH_3 . In this case one also expects a lower efficiency of the whole process.

Observation of lithium ion transport

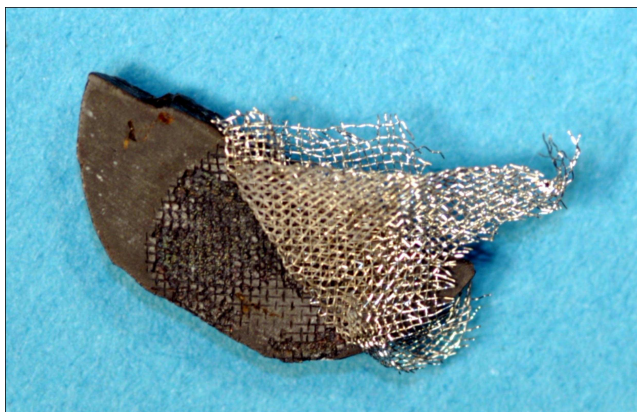
The sample immediately after these two experiments, still between the electrodes but slightly pulled out, is shown in Figure 5.15. Both sides of the sample are shown in Figure 5.16. As can be seen in Figure 5.16 (a), the Pt-net has penetrated into the sample and has made an imprint on this side of the sample. This clearly shows that some amount of Li_3N underwent



Figure 5.15: The OSC No. 3 sample after the second electrocatalytic experiment in the SC reactor.

electrolysis, i.e. Li^+ was transferred to the other side of the sample, while N^{3-} released at the three-phase boundary reacted with H_2 or formed N_2 . As can be seen in Figure 5.16 (b),

(a)



(b)



Figure 5.16: Observed lithium-ion mass transport in the OSC No. 3: (a) the anode side, the electrode imprint clearly shows that electrolysis occurred; (b) the cathode side, where the newly formed material can be seen.

some new material has grown on the other side of the sample, and has captured the second Pt-net electrode. This is to be expected to occur in an experiment with a unipolar pulse such as the first performed experiment. This asymmetric morphology was probably created in the first experiment, and remained during the second experiment. In the first experiment, in the ideal case, the Li deposited on the Pt-electrode should react with N_2 to Li_3N . However, some amount of LiH can be also expected (see the following subsection), or even LiOH, if traces of water were present in spite of the cold traps. Three kinds of deposits with different colors can be seen (white, ruby-red, and black). Attempts to analyze their nature by means of single-crystal XRD failed, since the samples appeared to be amorphous.

It would be feasible to estimate the amount of the electrolyzed Li_3N (i.e. transported

mass) by examination of the imprint profile⁸. However, this information alone is not sufficient to estimate the lithium-ion transference number of the sample. The total charge transferred through the sample, which is the second information needed to calculate the transference number, remained unknown due to the uncertain current measurements. The estimation of mass transport was therefore not done. The exact origin of the low efficiency in the two experiments cannot therefore be specified in more detail.

Similar experiments performed afterwards on different samples in this configuration did not deliver better results or new features. The Neßler's reagent probe shown in Figure 5.9 (b) corresponds to one of these experiments.

Reactions in the QDC reactor

The second reactor (QDC) was designed in order to avoid N_2 and H_2 mixing in the gas phase around the electrodes, i.e. to rule out the possibility of ammonia synthesis in plasma. Additionally, the mechanical contact between the electrodes and the sample was improved by uniform and higher mechanical pressure; and the dead volume of the reactor was decreased which yielded smaller detection time constant than in the case of the SC reactor. An additional chemical experiment confirmed the need for gas separation at the electrodes as well. The experiment was meant to show whether or not a new layer of Li_3N can be formed at the cathode side from the electrically transferred lithium in the presence of an H_2/N_2 mixture. A freshly cut piece of Li metal was heated up to 200 °C in a stream of the 8 % H_2 in N_2 mixture in a quartz vessel, and kept at this temperature for about 8 hours. The Li did not transform into Li_3N . The same procedure, but in pure N_2 , yielded Li_3N . This means that H_2 can passivate Li conversion into Li_3N , probably via formation of an LiH protective layer. Gas separation is therefore needed for the reversible electrocatalysis.

In the QDC reactor shown in Figure 5.8, a volumetric gas flow of ≈ 2 ml/min of H_2 was supplied to the anode, and ≈ 3 ml/min of N_2 was supplied to the cathode. All other procedures were the same as described for the SC reactor. The quality of the gas separation depends on the sample size, e.g. the sample shown in Figure 5.8 (b) does not fully fill the gap between the electrodes, and some gas mixing can therefore occur.

In parallel, the current measurement was improved by a possibility to record automatically the current values, with a sampling frequency which was unfortunately coupled with the voltage pulse duration. As illustration of a current measurement and its problems, two output figures of the automatized data evaluation are given in Figure 5.17. In an electrocatalytic experiment, the measured currents in different half periods of a bipolar voltage pulse (cycle) are indicated by different colors (blue and red). Values of the applied voltage, integrated (transferred) charge in the cycle, and total transferred charge (sum of all previous cycles) are also indicated in the figures. It can be clearly seen that the electric contact was decaying with the voltage cycling, the current was less noisy (a) after 200 cycles than (b) after 450 cycles. A

⁸this is just the opposite situation from the one described in the introduction [150]. The authors measured precisely the current, but could not determine the transported mass (reversible Li electrodes were used.)

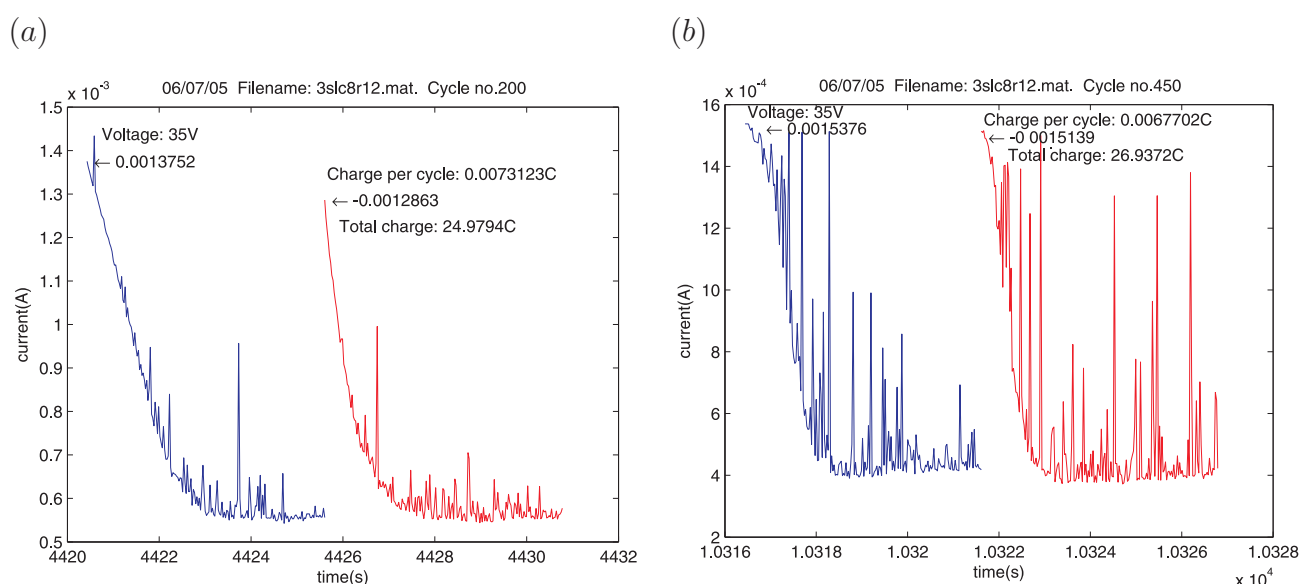


Figure 5.17: An example of contact degradation in an experiment with alternating pulses on an NSC sample in the QDC reactor. The figures were produced by MATLAB using the developed code for automatic data evaluation. A cycling program comprised from bipolar 35 V square pulses, 5 s each with a pause of 1 s for data transfer: (a) after 200 cycles, and (b) after 450 cycles.

moderate decrease in the current amplitude can be also observed upon cycling, i.e. the overall resistance increases. The problem of the electrolyte–electrode contact degradation seems to be very pronounced in the case of Li_3N .

In the case of the sintered Li_3N samples, it was reported that the anodic dissolution of lithium from a lithium metal electrode is not reversible although reversible Li electrodes were used [182]: the resistance at the interface increased significantly upon voltage cycling if the cycling was started with the anodic dissolution first. The process of contact degradation could be slowed down by an initial cathodic pre-deposition of Li at the interface. However, for the electrocatalytic ammonia synthesis reversible Li electrodes can not be used, and in the case of the initially porous Pt-net/paste electrodes, the contact degradation is expected therefore to be even more pronounced. The contact degradation is observed in all electrocatalytic experiments, which also made the current measurements inaccurate.

In electrocatalytic experiments performed in the QDC reactor no ammonia has been detected under the same conditions as applied in the SC reactor. However, it must be emphasized that the samples used in these reactions (mainly NSC) could not match the quality of the OSC No. 3, which could explain the failure of these experiments. Also, the acoustic noise, usually present in the SC reactor, has not been detected in the QDC reactor. The absence of the noise, or its reduction below the detection limit, was probably due to the improved mechanical contact (constant pressure at electrodes imposed by the spring). Because of the poorer sample quality it can not be proved nor disproved that the absence of the acoustic noise is directly related to the absence of ammonia synthesis. The absence of ammonia synthesis is

corroborated by a less pronounced lithium transport in these samples, as illustrated in Figure 5.18. Although a much higher mechanical pressure was present at the electrodes during

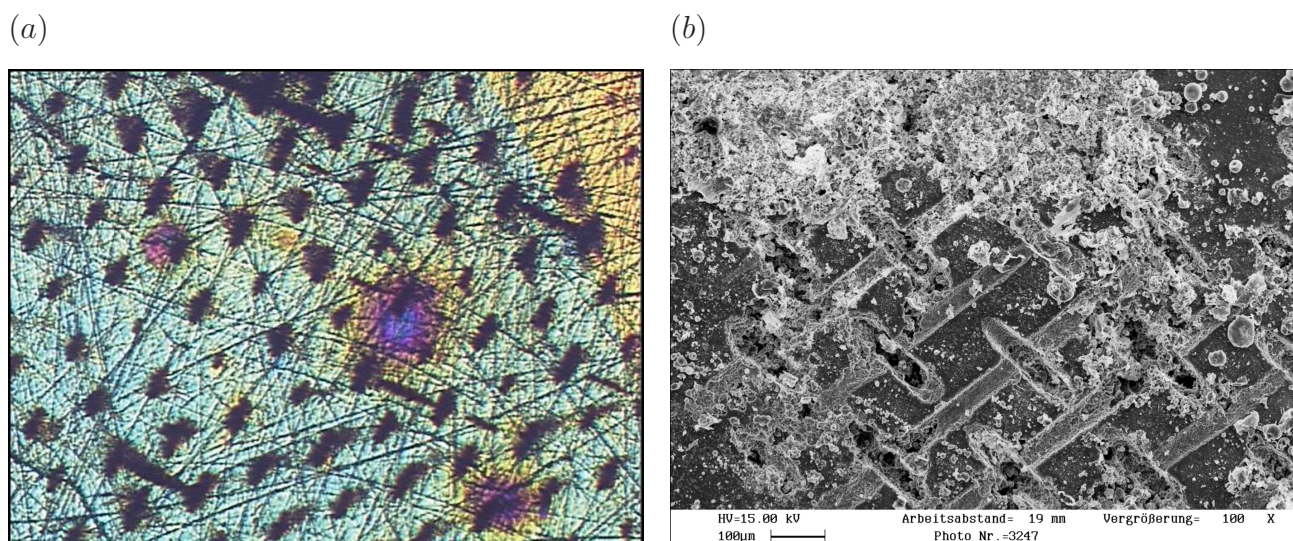


Figure 5.18: Lithium-ion mass transport is observed in experiments performed in the QDC reactor on an NSC. (a) a photograph of the anode side (which was exposed to H_2) made with the optical microscope; (b) an SEM image of the anode side.

an experiment, just very moderate electrode imprints can be observed. In Figure 5.18 (a), the scratches originate from the polishing procedure; the region with a golden color (in the top right corner) belongs to the edge region, which according to single-crystal XRD exhibits better crystallinity (obviously it behaves chemically different as well). Although not visible in this figure, lithium mass transport was more pronounced in the edge region. In the SEM image, Figure 5.18 (b), porous-like structures can be observed in the electrode imprints, which indicate that the initially imperfect single-crystal sample has further deteriorated under the voltage/current cycling. As in the case of spontaneous chemical reaction between metallic Li and N_2 , it seems that the newly formed Li_3N (formed under the electrode from the electrically transferred Li) has a tendency to be porous. The transference number could not be estimated due to large uncertainties in charge/current measurements (noisy data). For example, if the total charge, indicated in Figures 5.17 (a) and (b), is taken as a rough estimate of the total amount of the transported lithium, its value overestimates the depth of the observed electrode imprints. This indicates that the transference number is less than one in the case of SPC and NSC samples⁹. A possible explanation for a low transference number lies in the following facts. Crystal imperfections such as dislocations, grain boundaries, or pores, can have intrinsically (or due to impurities) enhanced electronic conductivity. Even if not, it is possible that small local deviations in the chemical potential of the lithium ions in the vicinity of such imperfections, upon current cycling, will lead to an evolution of metallic lithium within the sample, which would certainly increase the electronic contribution to the total conductivity

⁹mainly used in reactions performed in the QDC reactor.

and prevent further sample decomposition [185]. Related to this, it was reported that an electric breakdown due to Li-dendrite formation occurs in Li_3N single crystals¹⁰ after transfer of some coulombs [186]. All these observations suggest that pure and perfect Li_3N single crystal samples are necessary for the electrocatalytic ammonia synthesis.

5.3.5 XRD analysis after reactions

Powder XRD measurements were performed on selected samples after electrocatalytic reactions. The XRD patterns, fitted curves, and results of the quantitative phase analysis are given in Figure 5.19. Figures 5.19 (a) and (b) correspond to the pulverized parts of the first slice of the NSC No. 3. This sample with Pt-paste electrodes was used in electrocatalytic measurements, i.e. the sample had experienced high voltages, current flows, and long exposures to N_2 and H_2 . In Figure 5.19 (a), the results for a pulverized piece of the sample whose surface was shortly polished are shown, i.e. the Pt-paste and white layers formed on the surface during reactions were intentionally not removed completely. High fractions of LiOH (about 30 %) and Li_2O (about 7 %) were found¹¹. This indicates that in spite of all precautions taken to operate in a dry atmosphere, minimal traces of moisture were reacting with the sample surface and building cumulatively the layers during extended experiments. One unknown peak centered at $2\theta \approx 40.5^\circ$ is observed. As expected, due to the Pt paste used for electrodes, platinum traces were also found. For comparison, Figure 5.19 (b) shows the results for a different piece of the same sample which was thoroughly polished and represents deeper regions of the samples. The unknown peak does not appear in the pattern, which means that the unknown compound was present only at the surface. The results still show presence of lower fractions of LiOH (about 3 %) and Li_2O (about 7 %) in the sample. These findings indicate that there is space for improvement in sample handling procedures and electrocatalytic experiments in order to avoid sample contamination. A very important result from these measurements is that no significant fractions of Li_2NH and LiNH_2 are found, although these compounds could have formed under reaction conditions. This shows that under reaction conditions, at least for poly-crystalline and well-compacted Li_3N sinters, no significant transformation of Li_3N into these compounds occurs. The absence of LiH excludes the thermodynamically possible reactions (at about 150°C) of Li_3N and H_2 to NH_3 , which could represent a hidden and misleading ammonia source during the electrocatalytic experiments. A possible reaction path could be: (i) the multi-step reaction



where according to thermodynamic considerations each of these intermediate steps has a lower reaction Gibbs free energy than the overall reaction, which makes the last step thermodynamically

¹⁰although the samples used in Ref. [186] contained high concentrations of grain boundaries, they were denoted as single crystals.

¹¹note that sample grinding, filling and sealing of the XRD capillaries were performed in a glove box.

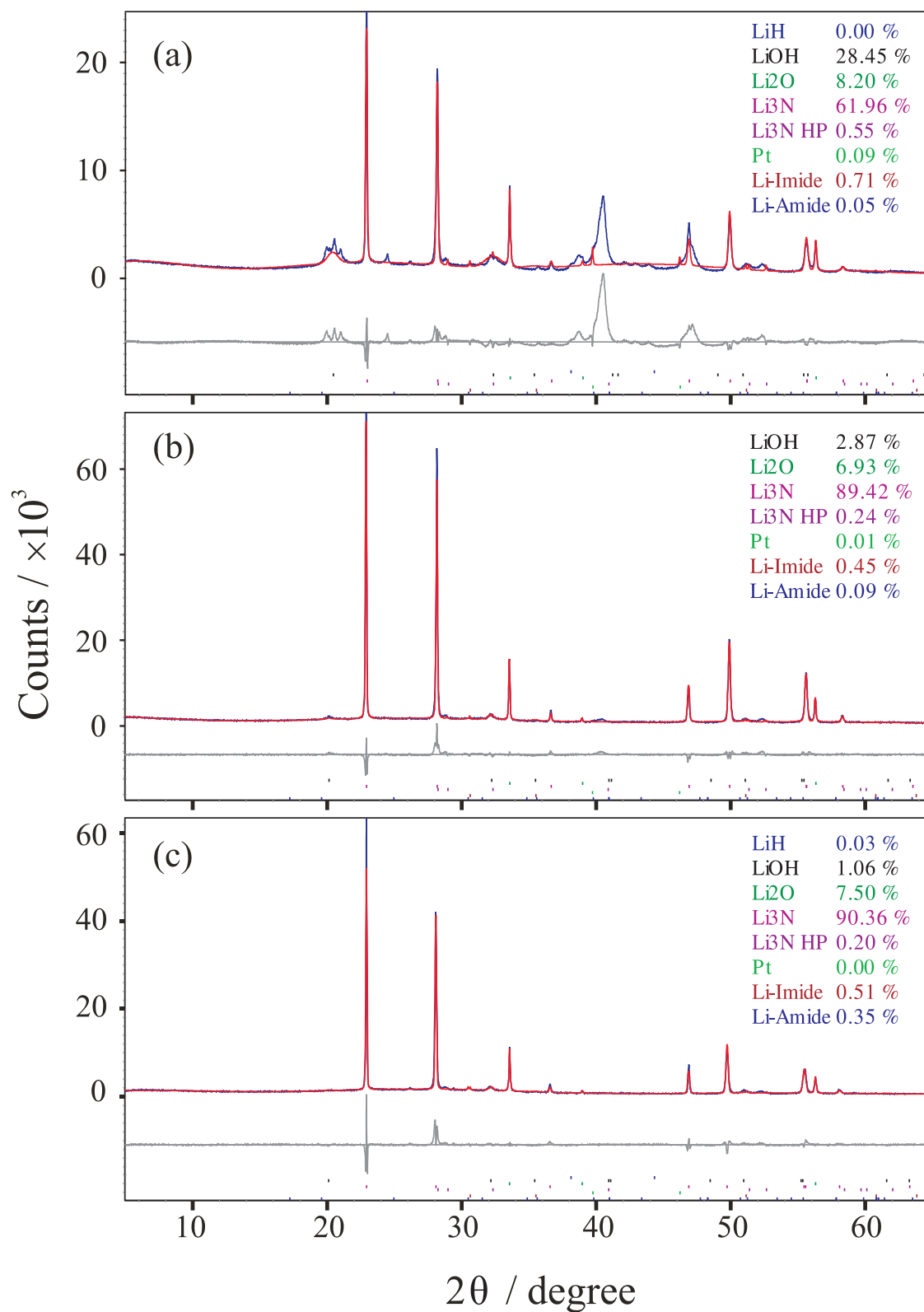


Figure 5.19: Powder XRD phase analysis: NSC No. 3 (a) briefly polished, (b) thoroughly polished; (c) sintered Li_3N .

ically not favorable; or (ii) the direct reaction



As already said, even though thermodynamically possible, these intermediate products were found only in traces, whereas LiH, if present as the final product, was below the detection limit. Small fractions of the observed high-pressure Li_3N phase probably originate from the grinding procedure which was performed in order to obtain powder samples.

5.4 Conclusions

The presented results show that, although strongly hindered by many practical problems, the electrocatalytic ammonia synthesis using Li_3N is possible at moderate temperatures and ambient pressure. In order to exclude that this occurs solely through a plasma (i.e. gas discharge) process, further research is necessary. To achieve higher efficiency of the ammonia synthesis, high quality Li_3N samples are needed. More specifically, the sample should be a very pure one-domain single crystal, which would be characterized by a high lithium-ion conductivity, a transference number close to unity, the absence of grain boundaries, and improved reversibility. However, a long term reversibility/reproducibility might not be achieved in a cycling operation mode due to the anisotropy of Li_3N and the tendency of the newly re-formed Li_3N to be porous. In search for a stationary electrocatalytic ammonia synthesis, each step/element of the described processes must be improved, e.g., different electrode materials (including composites) should also be tested. In practice, if the optimized electrocatalytic cell for ammonia synthesis can be achieved, it could find its application as an NH_3 micro/nano pump. Such a device could deliver a desired amount of NH_3 in an electronically controlled way.

Bibliography

- [1] C. Wagner and K. Hauffe. The stationary state of catalysts in heterogeneous reactions. I. *Z. Elektrochem.*, 44:172, 1938.
- [2] J. Maier. Acid-base centers and acid-base scales in ionic solids. *Chem. Eur. J.*, 7:4763, 2001.
- [3] G. Simkovich and C. Wagner. The role of ionic point defects in the catalytic activity of ionic crystals. *J. Catal.*, 1:521, 1962.
- [4] J. Maier and P. Murugaraj. The effect of heterogeneous doping on heterogeneous catalysis: dehydrohalogenation of tertiary butyl chloride. *Solid State Ionics*, 40/41:1017, 1990.
- [5] C. Wagner. Adsorbed atomic species as intermediates in heterogeneous catalysis. *Adv. Catal.*, 21:323, 1970.
- [6] C. G. Vayenas and I. V. Yentekakis. “*Electrochemical modification of catalytic activity*”, p. 1310, in *Handbook of Heterogeneous Catalysis*. Wiley-VCH, Weinheim, 1997.
- [7] V. M. Goldschmidt. Geochemische Verteilungsgesetze der Elemente VII, VIII. *Skrif. Nor. Vidensk. Akad. Oslo. I*, 8:7, 1927.
- [8] R. D. Shannon. Revised effective ionic radii and systematic studies of interatomic distances in halides and chalcogenides. *Acta Cryst. A*, 32:751, 1976.
- [9] H. Gränicher. *Helv. Phys. Acta*, 29:210, 1956.
- [10] K. A. Müller. *Helv. Phys. Acta*, 31:173, 1958.
- [11] H. Sakudo and T. Sakudo. Electron spin resonance of Fe^{3+} in SrTiO_3 with special reference to the 100°CK phase transition. *J. Phys. Soc. Jpn.*, 23:546, 1967.
- [12] F. A. Kröger. *The Chemistry of Imperfect Crystals*. North-Holland Publishing Company, Amsterdam, 1964.
- [13] P. Adler and S. Eriksson. Structural properties, Mössbauer spectra, and magnetism of perovskite-type oxides $\text{SrFe}_{1-x}\text{Ti}_x\text{O}_{3-y}$. *Z. Anorg. Allg. Chem.*, 626:118, 2000.

- [14] M. Schmidt and S. J. Campbell. *J. Solid State Chem.*, 156:292, 2001.
- [15] J. Mizusaki, M. Okayasu, S. Yamauchi, and K. Fueki. Nonstoichiometry and phase relationship of the SrFeO_{2.5}-SrFeO₃ system at high temperature. *J. Solid State Chem.*, 99:166, 1992.
- [16] C. W. Burnham. *LCLSQ Version 8.4, Least-Squares Refinement of Crystallographic Lattice Parameters. Dept. of Earth and Planetary Sciences, Harvard University*, 1991.
- [17] A. Boulfif and D. Louer. *J. Appl. Crystallogr.*, 24:987, 1991.
- [18] P. W. Tasker. The stability of ionic crystal surfaces. *J. Phys. C: Solid State Phys.*, 12:4977, 1977.
- [19] E. Heifets, W. A. Goddard III, E. A. Kotomin, R. I. Eglitis, and G. Borstel. *Ab initio* calculations of the SrTiO₃ (110) polar surface. *Phys. Rev. B*, 69:035408, 2004.
- [20] R. Merkle and J. Maier. *submitted to Solid State Ionics*, 2006.
- [21] M. Vračar, R. Merkle, A. Kuzmin, J. Purans, E. A. Kotomin, J. Maier, and O. Mathon. Jahn-Teller distortion around Fe⁴⁺ in Sr(Fe_xTi_{1-x})O_{3-δ} from x-ray absorption spectroscopy, x-ray diffraction, and vibrational spectroscopy. *Phys. Rev. B*, 76:174107, 2007.
- [22] R. Merkle. *unpublished data*, 2005.
- [23] A. H. Kahn and A. J. Leyendecker. Electronic energy bands in strontium titanate. *Phys. Rev.*, 135:A1321, 1964.
- [24] G. Cappellini, S. Bouette-Russo, B. Amadon, C. Noguera, and F. Finocchi. Structural properties and quasiparticle energies of cubic SrO, MgO and SrTiO₃. *J. Phys.: Condens. Matter*, 12:3671, 2000.
- [25] T. Bieger. *Optische und elektrochemische Untersuchungen zur Sauerstoffaustauschkinetik von SrTiO₃*. PhD thesis, Fakultät für Chemie und Pharmazie der Eberhard-Karls-Universität Tübingen, 1993.
- [26] F. M. Michel-Calendini and K. A. Müller. Interpretation of charge transfer bands in Fe doped SrTiO₃ crystals. *Solid State Commun.*, 40:255, 1981.
- [27] T. Bieger, J. Maier, and T. Waser. An optical in-Situ method to study Redox-kinetics in Ionic Crystals. *Ber. Bunsen-Ges. Phys. Chem.*, 97:1098, 1993.
- [28] I. Denk, W. Münch, and J. Maier. Partial conductivities in SrTiO₃: Bulk polarization experiments, oxygen concentration cell measurements, and defect-chemical modeling. *J. Am. Ceram. Soc.*, 78:3265, 1995.

- [29] P. A. Cox. *Transition Metal Oxides: an introduction to their electronic structure and properties*. Clarendon Press, 1992.
- [30] W. L. Bond. Measurement of the refractive indices of several crystals. *J. Appl. Phys.*, 36:1674, 1965.
- [31] S. Ohta, T. Nomura, H. Ohta, and K. Koumoto. High-temperature carrier transport and thermoelectric properties of heavily La- or Nb-doped SrTiO₃ single crystals. *J. Appl. Phys.*, 97:034106, 2005.
- [32] G. M. Choi and H. L. Tuller. Defect structure and electrical properties of single-crystal Ba_{0.03}Sr_{0.97}TiO₃. *J. Am. Ceram. Soc.*, 71:201, 1988.
- [33] A. Rothschild, W. Menesklou, H. L. Tuller, and E. Ivers-Tiffée. Electronic structure, defect chemistry, and transport properties of SrTi_{1-x}Fe_xO_{3-y} solid solutions. *Chem. Mater.*, 18:3651, 2006.
- [34] R. Merkle. *unpublished data*, 2006.
- [35] S. Steinsvik, R. Bugge, J. Gjønnes, J. Taftö, and T. Norby. The defect structure of SrTi_{1-x}Fe_xO_{3-y} (x=0-0.8) investigated by electrical conductivity measurements and electron energy loss spectroscopy (EELS). *J. Phys. Chem. Solids*, 58:969, 1997.
- [36] M. Fleischer, H. Meixner, and C. Tragut. Hole mobility in acceptor-doped, monocrystalline SrTiO₃. *J. Am. Ceram. Soc.*, 75:1666, 1992.
- [37] H. D. Zhou and J. B. Goodenough. *J. Solid State Chem.*, 177:1952, 2004.
- [38] J. Blanc and D. L. Staebler. Electrocoloration in SrTiO₃: Vacancy drift and Oxidation-Reduction of Transition Metals. *Phys. Rev. B*, 4:3548, 1971.
- [39] R. Waser. Bulk conductivity and defect chemistry of acceptor-doped strontium titanate in the quenched state. *J. Am. Ceram. Soc.*, 74:1934, 1991.
- [40] J. Maier. *Physical Chemistry of Ionic Materials*. Wiley, 2004.
- [41] J. Maier. Mass transport in the presence of internal defect reactions-concept of conservative ensembles: III, trapping effect of dopants on chemical diffusion. *J. Am. Ceram. Soc.*, 76:1223, 1993.
- [42] J. Maier. The role of effective rate constants in interfacial kinetics. *Mater. Res. Soc. Symp. Proc.*, 548:415, 1999.
- [43] T. Ishigaki, K. Yamauchi, S. Kishio, J. Mizusaki, and K. Fueki. Diffusion of oxide ion vacancies in perovskite-type oxides. *J. Solid State Chem.*, 73:179, 1988.

- [44] R. Moos, W. Menesklou, H.-J. Schreiner, and K. H. Härdtl. Materials for temperature independent resistive oxygen sensors for combustion exhaust gas control. *Sens. Actuators B*, 67:178, 2000.
- [45] P. Meuffels. Propane sensing with high-density $\text{SrTi}_{0.6}\text{Fe}_{0.4}\text{O}_{3-\delta}$. *J. Eur. Ceram. Soc.*, 27:285, 2007.
- [46] L. J. Gauckler, D. Beckel, B. E. Buegler, E. Jud, U. P. Muecke, M. Prestat, J. L. M. Rupp, and J. Richter. Solid Oxide Fuel Cells: Systems and Materials. *Chimia*, 58:837, 2004.
- [47] T. Kawada and H. Yokokawa. Material and Characterization of Solid State Fuel Cell. *Key Eng. Mat.*, 125:187, 1997.
- [48] Z. P. Shao, H. Dong, G. X. Xiong, Y. Gong, and W. S. Yang. Performance of a mixed-conducting ceramic membrane reactor with high oxygen permeability for methane conversion. *J. Membr. Sci.*, 183:181, 2001.
- [49] W. F. Libby. Promising Catalyst for Auto Exhaust. *Science*, 171:499, 1971.
- [50] R. J. H. Voorhoeve. in: *Advanced Materials in Catalysis*, eds. J. J. Burton and R. L. Garten, chapter 5. Perovskite-Related Oxides as Oxidation-Reduction Catalysts, pages 129–180. Academic Press, 1977.
- [51] H. Arai, T. Yamada, K. Eguchi, and T. Seiyama. Catalytic combustion of methane over various perovskite-type oxides. *Applied Catalysis*, 26:265, 1986.
- [52] G. Ertl, H. Knözinger, and J. Weitkamp, editors. *Handbook of Heterogeneous Catalysis*. Wiley-VCH, Weinheim, 1997.
- [53] J. B. MacChesney, R. C. Sherwood, and J. F. Potter. Electric and magnetic properties of strontium ferrates. *J. Chem. Phys.*, 43:1907, 1965.
- [54] R. A. Evarestov, S. Piskunov, E. A. Kotomin, and G. Borstel. *Phys. Rev. B*, 67:064101, 2003.
- [55] H. A. Jahn and E. Teller. Stability of polyatomic molecules in degenerate electronic states. i. orbital degeneracy. *Proc. R. Soc. London A*, 161:220, 1937.
- [56] I. B. Bersuker. *The Jahn-Teller Effect*. Cambridge University Press, 2006.
- [57] R. Englman. *The Jahn-Teller effect in Molecules and Crystals*. Wiley-Interscience, 1972.
- [58] J. Als-Nielsen and D. McMorrow. *Elements of modern x-ray physics*. Wiley, 2001.
- [59] B. K. Teo. *EXAFS: Basic Principles and Data Analysis*. Springer-Verlag, Berlin, 1986.

- [60] J. J. Rehr and R. C. Albers. Theoretical approaches to x-ray absorption fine structure. *Rev. Mod. Phys.*, 72:612, 2000.
- [61] A. Filipponi, M. Borowski, D. T. Bowron, S. Ansell, S. De Panfilis, A. Di Cicco, and J.-P. Itie. *Rev. Sci. Instrum.*, 71:2422, 2000.
- [62] A. Kuzmin. *Physica B*, 208/209:175, 1995.
- [63] M. Newville, B. Ravel, D. Haskel, J. J. Rehr, E. A. Stern, and Y. Yacoby. Analysis of multiple-scattering XAFS data using theoretical standards. *Physica B*, 208&209:154, 1995.
- [64] A. L. Ankudinov, B. Ravel, J. J. Rehr, and S. D. Conradson. *Phys. Rev. B*, 58:7565, 1998.
- [65] J. J. Rehr and R. C. Albers. *Rev. Mod. Phys.*, 72:621, 2000.
- [66] A. Filipponi, A. Di Cicco, and C. R. Natoli. *Phys. Rev. B*, 52:15122, 1995.
- [67] N. Binsted and S. S. Hasnain. *J. Synchrotron Rad.*, 3:185, 1996.
- [68] A. Kuzmin, J. Purans, M. Benfatto, and C. R. Natoli. *Phys. Rev. B*, 47:2480, 1993.
- [69] A. Kuzmin, J. Purans, G. Dalba, P. Fornasini, and F. Rocca. *J. Phys.: Condens. Matter*, 8:9083, 1996.
- [70] M. G. Kim, H. S. Cho, and C. H. Yo. *J. Phys. Chem. Solids*, 59:1369, 1998.
- [71] M. Abbate, G. Zampieri, J. Okamoto, A. Fujimori, S. Kawasaki, and M. Takano. *Phys. Rev. B*, 65:165120, 2004.
- [72] A. E. Bocquet, A. Fujimori, T. Mizokawa, T. Saitoh, H. Namatame, S. Suga, N. Kimizuka, Y. Takeda, and M. Takano. *Phys. Rev. B*, 45:1561, 1992.
- [73] A. Kuzmin and J. Purans. *J. Phys.: Condens. Matter*, 5:267, 1993.
- [74] A. Kuzmin and J. Purans. *J. Phys.: Condens. Matter*, 5:9423, 1993.
- [75] B. Houser and R. Ingalls. *Phys. Rev. B*, 61:6515, 2000.
- [76] R. Merkle and J. Maier. Defect association in acceptor-doped SrTiO₃: case study for Fe'_{Ti}V_O and Mn''_{Ti}V_O. *Phys. Chem. Chem. Phys.*, 5:2297, 2003.
- [77] J. Rodriguez, J. A. Pereda, M. Vallet, J. G. Calbet, and J. Tejada. Mössbauer study of vacancy ordering in the system SrTi_{1-x}Fe_xO_{3-y} (0.50 ≤ x ≤ 0.70). *Mat. Res. Bull.*, 21:255, 1986.

- [78] C. Greaves and R. A. Buker. The defect structure of $\text{Sr}_2\text{FeTiO}_{6-x}$. *Mat. Res. Bull.*, 21:823, 1986.
- [79] J. Xu, A. P. Wilkinson, and S. Pattanaik. *Chem. Mater.*, 12:3321, 2000.
- [80] S. C. Tarantino, P. Ghina, C. McCammon, R. Amantea, and M. A. Carpenter. *Acta Cryst. B*, 61:250, 2005.
- [81] E. Sevillano, H. Meuth, and J. J. Rehr. *Phys. Rev. B*, 20:4908, 1979.
- [82] G. Beni and P. M. Platzman. *Phys. Rev. B*, 14:1514, 1976.
- [83] T. Trautmann and C. Falter. *J. Phys.: Condens. Matter*, 16:5955, 2004.
- [84] A. Yoshiasa, K. Nakajima, K. Murai, and M. Okube. *J. Synchrotron Rad.*, 8:940, 2001.
- [85] P. A. Fleury and J. M. Worlock. *Phys. Rev.*, 174:613, 1968.
- [86] W. G. Nilsen and J. G. Skinner. *J. Chem. Phys.*, 48:2240, 1968.
- [87] H. Vogt and G. Neumann. *Phys. Status Solidi B*, 92:57, 1979.
- [88] P. Ranson, R. Ouillon, J.-P. Pinan-Lucarre, Ph. Pruzan, S. K. Mishra, R. Ranjan, and D. Pandey. *J. Raman Spectrosc.*, 36:898, 2005.
- [89] A. A. Sirenko, I. A. Akimov, J. R. Fox, A. M. Clark, H.-C. Li, Weidong Si, and X. X. Xi. Observation of the first-order raman scattering in SrTiO_3 thin films. *Phys. Rev. Lett.*, 82:4500, 1999.
- [90] A. Tkach, P. M. Vilarinho, A. L. Kholkin, P. Pashkin, P. Samoukhina, J. Pokorny, S. Veljko, and J. Petzelt. *J. Appl. Phys.*, 97:044104, 2005.
- [91] H. Zheng, I. M. Reaney, G. D. C. Csete de Györgyfalva, R. Ubic, J. Yarwood, M. P. Seabra, and V. M. Ferreira. *J. Mater. Res.*, 19:488, 2004.
- [92] J. B. Goodenough and J. S. Zhou. *Structure and Bonding*, 98:17, 2001.
- [93] R. V. Vedrinskii, V. L. Kraizman, A. A. Novakovich, Ph. V. Demekhin, and S. V. Urazhdin. *J. Phys.: Condens. Matter*, 10:9561, 1998.
- [94] Y. Joly, D. Cabaret, H. Renevier, and C. R. Natoli. Electron population analysis by full-potential x-ray absorption simulation. *Phys. Rev. Lett.*, 82:2398, 1999.
- [95] T. E. Westre, P. Kennepohl, J. G. DeWitt, B. Hedman, K. O. Hodgson, and E. I. Solomon. *J. Am. Chem. Soc.*, 119:6297, 1997.
- [96] F. Farges, Y. Lefrère, S. Rossano, A. Berthereau, G. Calas, and G. E. Brown Jr. *J. Non-Cryst. Solids*, 344:176, 2004.

- [97] H. Meštrić, R. A. Eichel, T. Kloss, K. P. Dinse, So. Laubach, St. Laubach, P. C. Schmidt, K. A. Schönau, M. Knapp, and H. Ehrenberg. *Phys. Rev. B*, 71:134109, 2005.
- [98] M. N. Iliev and M. V. Abrashev. *J. Raman Spectrosc.*, 32:805, 2001.
- [99] V. S. Vikhnin and L. S. Sochava. Noncentral Jahn-Teller ion: coupled polar and tetragonal strains. *Sov. Phys. Solid State*, 21:1193, 1979.
- [100] V. S. Vikhnin, L. S. Sochava, and Yu. N. Tolparov. Noncentral Jahn-Teller ion: localization in an energy minimum of C_1 symmetry. *Sov. Phys. Solid State*, 21:1023, 1979.
- [101] C. H. Booth, F. Bridges, G. H. Kwei, J. M. Lawrence, A. L. Cornelius, and J. J. Neumeier. *Phys. Rev. Lett.*, 80:853, 1998.
- [102] C. H. Booth, F. Bridges, G. H. Kwei, J. M. Lawrence, A. L. Cornelius, and J. J. Neumeier. *Phys. Rev. B*, 57:10440, 1998.
- [103] B. Buffat, M. H. Tuilier, H. Dexpert, G. Demazeau, and P. Hagenmuller. X-ray absorption investigation of some high oxidation states of six-co-ordinated iron in oxides of perovskite or K_2NiF_4 -type structures. *J. Phys. Chem. Solids*, 47:491, 1986.
- [104] B. Buffat and M. H. Tuilier. X-ray absorption edges of iron and cobalt with six-fold coordination in oxides. *Solid State Commun.*, 64:401, 1987.
- [105] J. M. Thomas and W. J. Thomas. *Principles and practice of Heterogeneous Catalysis*. VCH Weinheim, 1997.
- [106] P. Mars and D. W. van Krevelen. Oxidation carried out by means of vanadium oxide catalyst. *Special Supplement to Chemical Engineering Science*, 3:41, 1954.
- [107] H. Iwahara, T. Esaka, and Y. Miyawaki. Oxide ion conduction in highly electronic conductors based on $SrMnO_{3-\delta}$. *Solid State Ionics*, 44:257, 1991.
- [108] J. Mizusaki. Nonstoichiometry, diffusion, and electrical properties of perovskite-type oxide electrode materials. *Solid State Ionics*, 52:79, 1992.
- [109] S. Khan, R. J. Oldman, F. Corà, C. R. A. Catlow, S. A. French, and S. A. Axon. A computational modelling study of oxygen vacancies at $LaCoO_3$ perovskite surfaces. *Phys. Chem. Chem. Phys.*, 8:5207, 2006.
- [110] D. B. Meadowcroft. Low-cost Oxygen Electrode Material. *Nature*, 226:847, 1970.
- [111] F. S. Baumann. *Oxygen reduction kinetics on mixed conducting SOFC model cathodes*. PhD thesis, Max-Planck-Institut für Festkörperforschung, Stuttgart, 2006.
- [112] L. G. Tejuca, J. L. G Fierro, and J. M. D. Tascón. Structure and reactivity of perovskite-type oxides. *Advances in Catalysis*, 36:237–328, 1989.

- [113] M. A. Peña and J. L. G. Fierro. Chemical structures and performance of perovskite oxides. *Chem. Rev.*, 101:1981, 2001.
- [114] A. Cimino and F. S. Stone. Oxide solid solutions as catalysts. *Advances in Catalysis*, 47:141, 2002.
- [115] R. Merkle and J. Maier. Oxygen incorporation into Fe-doped SrTiO₃: Mechanistic interpretation of the surface reaction. *Phys. Chem. Chem. Phys.*, 4:4140, 2002.
- [116] N. Barsan and U. Weimar. Conduction model of metal oxide gas sensors. *J. Electroceramics*, 7:143, 2002.
- [117] R. H. Crabtree. Aspects of methane chemistry. *Chem. Rev.*, 95:987, 1995.
- [118] R. Dieckmann. Point defects and transport in haematite (Fe₂O_{3-ε}). *Philos. Mag. A*, 68:725, 1993.
- [119] K. D. Kreuer, St. Adams, W. Münch, A. Fuchs, U. Klock, and J. Maier. Proton conducting alkaline earth zirconates and titanates for high drain electrochemical applications. *Solid State Ionics*, 145:295, 2001.
- [120] U. Erlekam, U. A. Paulus, Y. Wang, H. P. Bonzela, K. Jacobi, and G. Ertl. Adsorption of Methane and Ethane on RuO₂ (110) surfaces. *Z. Phys. Chem.*, 219:819, 2005.
- [121] M. B. Lee, Q. Y. Yang, and S. T. Ceyer. Dynamics of the activated dissociative chemisorption of CH₄ and implication for the pressure gap in catalysis: A molecular beam-high resolution electron energy loss study. *J. Chem. Phys.*, 85:2724, 1987.
- [122] C. T. Rettner, H. E. Pfnür, and D. J. Auerbach. Dissociative chemisorption of CH₄ on W(110): Dramatic activation by initial kinetic energy. *Phys. Rev. Lett.*, 54:2716, 1985.
- [123] K. J. Laidler. *Chemical Kinetics*. Harper & Row, Publishers, Inc., 1987.
- [124] L. G. Tejuca, C. H. Rochester, J. L. G. Fierro, and J. M. D. Tascón. Infrared spectroscopic study of the adsorption of Pyridine, Carbon monoxide and Carbon dioxide on the Perovskite-type Oxides LaMO₃. *J. Chem. Soc., Faraday Trans.*, 80:1089, 1984.
- [125] S. Brunauer, P. H. Emmett, and E. Teller. Adsorption of gases in multimolecular layers. *J. Am. Chem. Soc.*, 60:309, 1938.
- [126] H. Nagamoto, K. Amanuma, H. Nobutomo, and H. Inoue. Methane oxidation over perovskite-type oxide containing alkaline-earth metal. *Chem. Lett.*, page 237, 1988.
- [127] T. Seiyama, N. Yamazoe, and K. Eguchi. Characterization and activity of some mixed metal oxide catalysts. *Ind. Eng. Chem. Prod. Res. Dev.*, 24:19, 1985.

- [128] T. Seiyama. Total oxidation of hydrocarbons on perovskite oxides. *Catal. Rev.-Sci. Eng.*, 34(4):281, 1992.
- [129] T. Kawai, K. Kunimori, T. Kondow, T. Onishi, and K. Tamaru. *Z. Phys. Chem. Frankfurt*, 86:268, 1973.
- [130] T. Shimizu and H. Hara. Oxidation of CO on La₂O₃-doped BaTiO₃. *J. Am. Ceram. Soc.*, 55:533, 1972.
- [131] G. W. Berkstresser. PhD thesis, University of South California, 1973.
- [132] R. J. H. Voorhoeve, J. P. Remeika, and L. E. Trimble. *Ann. N.Y. Acad. Sci.*, 272:3, 1976.
- [133] N. Yamazoe, Y. Teraoka, and T. Seiyama. TPD and XPS study on thermal behavior of absorbed oxygen in La_{1-x}Sr_xCoO₃. *Chem. Lett.*, page 1767, 1981.
- [134] T. Shimizu. Effect of electronic structure and tolerance factor on CO oxidation activity of perovskite oxides. *Chem. Lett.*, page 1, 1980.
- [135] M. Stojanović, C. A. Mims, H. Moudallal, Y. L. Yang, and A. J. Jacobson. Reaction kinetics of methane oxidation over LaCr_{1-x}Ni_xO₃. *J. Catal.*, 166:324, 1997.
- [136] N. Yamazoe and Y. Teraoka. Oxidation catalysis of perovskites – Relationships to bulk structure and composition (valency, defect, etc.). *Catal. Today*, 8:175, 1990.
- [137] N. Mizuno, Y. Fujiwara, and M. Misono. Pronounced synergetic effect in the catalytic properties of LaMn_{1-x}Cu_xO₃. *J. Chem. Soc. Chem. Commun.*, page 316, 1989.
- [138] J. M. D. Tascón and L. G. Tejuca. Catalytic activity of perovskite-type oxides LaMO₃. *React. Kinet. Catal. Lett.*, 15:185, 1980.
- [139] G. Kremenić, J. M. L. Nieto, J. M. D. Tascón, and L. G. Tejuca. Chemisorption and catalysis on LaMO₃. *J. Chem. Soc., Faraday Trans. 1*, 81:939, 1985.
- [140] G. Blyholder. Molecular orbital view of chemisorbed carbon monoxide. *J. Phys. Chem.*, 68:2772, 1964.
- [141] P. W. Fowler, P. Tole, R. W. Munn, and M. Hurst. Polarizability of the nitride ion in the lithium nitride crystal. *Mol. Phys.*, 67:141, 1989.
- [142] G. Kerker. Electronic structure of Li₃N. *Phys. Rev. B*, 23:6312, 1981.
- [143] R. Dovesi, C. Pisani, F. Ricca, C. Roetti, and V. R. Saunders. Hartree-Fock study of crystalline lithium nitride. *Phys. Rev. B*, 30:972, 1984.

- [144] M. Causá, R. Dovesi, C. Pisani, and C. Roetti. *Ab initio* study of the autocorrelation function for lithium nitride. *Phys. Rev. B*, 32:1196, 1985.
- [145] J. R. Walker and C. R. A. Catlow. Defect structure and conductivity in Li_3N . *Phil. Mag. A*, 43:265, 1981.
- [146] M. L. Wolf, Walker J. R., and C. R. A. Catlow. A molecular dynamics simulation study of the superionic conductor lithium nitride: I and ii. *J. Phys. C: Solid St. Phys.*, 17:6623, 1984.
- [147] H. Brendecke and W. Bludau. Optical absorption of lithium nitride. *J. Appl. Phys.*, 50:4743, 1979.
- [148] H. R. Chandrasekhar, G. Bhattacharya, R. Migoni, and H. Bilz. Infrared and raman spectra and lattice dynamics of the superionic conductor Li_3N . *Phys. Rev. B*, 17:884, 1978.
- [149] W. Kress, H. Grimm, W. Press, and J. Lefebvre. Lattice vibrations in lithium nitride, Li_3N . *Phys. Rev. B*, 22:4620, 1980.
- [150] A. Rabenau. Lithium nitride and related materials: Case study of the use of modern solid state research techniques. *Solid State Ionics*, 6:277, 1982.
- [151] P. Chen, Z. Xiong, J. Luo, J. Lin, and K. L. Tan. Interaction of hydrogen with metal nitrides and imides. *Nature*, 420:302, 2002.
- [152] Y. H. Hu and E. Ruckenstein. H_2 storage in Li_3N . Temperature-programmed hydrogenation and dehydrogenation. *Ind. Eng. Chem. Res.*, 42:5135, 2003.
- [153] T. Ichikawa, N. Hanada, S. Isobe, H. Leng, and H. Fujii. Mechanism of novel reaction from LiNH_2 and LiH to Li_2NH and H_2 as a promising hydrogen storage system. *J. Phys. Chem. B*, 108:7887, 2004.
- [154] E. Schönherr, G. Müller, and E. Winckler. Czochralski growth of Li_3N crystals. *J. Cryst. Growth*, 43:469, 1978.
- [155] K. Nishida, K. Kitahama, and S. Kawai. Preparation of Li_3N single crystal by floating zone technique. *J. Cryst. Growth*, 62:475, 1983.
- [156] M. G. Barker, A. J. Blake, P. P. Edwards, D. H. Gregory, T. A. Hamor, D. J. Siddons, and S. E. Smith. Novel layered lithium nitridonickelates; effect of Li vacancy concentration on N co-ordination geometry and Ni oxidation state. *Chem. Commun.*, 1999:1187.
- [157] E. Zintl and G. Brauer. Constitution of lithium nitride. *Z. Elektrochem.*, 41:102, 1935.
- [158] H. Schulz and K. Schwarz. Is there an N^{3-} ion in the crystal structure of the ionic conductor lithium nitride (Li_3N)? *Acta Cryst. A*, 34:999, 1978.

- [159] A. Rabenau and H. Schulz. Re-evaluation of the lithium nitride structure. *J. Less-Common Metals*, 50:155, 1976.
- [160] K. Differt and R. Messer. NMR spectra of Li and N in single crystals of Li_3N : discussion of ionic nature. *J. Phys. C: Solid St. Phys.*, 13:717, 1980.
- [161] H. Brendecke and W. Bludau. Photoluminescence properties of lithium nitride. *Phys. Rev. B*, 21(2):805, 1980.
- [162] D. R. Hamann. Semiconductor charge densities with hard-core and soft-core pseudopotentials. *Phys. Rev. Lett.*, 42:662, 1979.
- [163] P. Pattison and J. R. Schneider. An investigation of the electron density in Li_3N using Compton scattering. *Acta Cryst. A*, 36:390, 1980.
- [164] J. Sarnthein, K. Schwarz, and P. E. Blöchl. Ab initio molecular-dynamics study of diffusion and defects in solid Li_3N . *Phys. Rev. B*, 53:9084, 1996.
- [165] B. A. Boukamp and R. A. Huggins. Fast ionic conductivity in lithium nitride. *Mat. Res. Bull.*, 13:23, 1978.
- [166] U. v. Alpen, A. Rabenau, and G. H. Talat. Ionic conductivity in Li_3N single crystals. *Appl. Phys. Lett.*, 30(12):621, 1977.
- [167] M. S. Whittingham and R. A. Huggins. in "Solid State Chemistry", ed. by R. S. Roth and S. J. Schneider, *Nat. Bur. Standards Special Pub.* 364:139 1972.
- [168] W. L. Roth and G. C. Farrington. Lithium-sodium beta alumina: First of a family of Co-ionic conductors? *Science*, 196:1339, 1977.
- [169] F. Gallais and E. Masdupuy. Sur la constitution du nitrure de lithium et l'existence de l'ion N^{3-} . *Compt. Rendus*, 227:635, 1948.
- [170] E. Masdupuy. Contribution of the study of nitrides, acetylides, and silicides. evidence for the N^{3-} ion. investigations of the existence of a carbon ion. *Ann. Chim. (Paris)*, 13-2:527, 1957.
- [171] B. A. Boukamp and R. A. Huggins. Lithium ion conductivity in lithium nitride. *Phys. Lett. A*, 58:231, 1976.
- [172] R. Messer, H. Birli, and K. Differt. NMR study of diffusion in Li_3N . *J. Phys. C*, 14:2731, 1981.
- [173] H. Schulz and K. H. Thiemann. Defect structure of the ionic conductor lithium nitride (Li_3N). *Acta Cryst. A*, 35:309, 1979.

- [174] J. Wahl. Ionic conductivity of lithium nitride doped with hydrogen. *Solid State Commun.*, 29:485, 1979.
- [175] Y. H. Hu, N. Y. Yu, and E. Ruckenstein. Effect of the heat pretreatment of Li_3N on its H_2 storage performance. *Ind. Eng. Chem. Res.*, 43:4174, 2004.
- [176] Y. Nakamori, G. Kitahara, K. Miwa, S. Towata, and S. Orimo. Reversible hydrogen-storage functions for mixtures of Li_3N and Mg_3N_2 . *Appl. Phys. A*, 80:1, 2005.
- [177] I. Barin and O. Knacke. *Thermochemical Data of Pure Substances*. VCH Verlagsgesellschaft, Weinheim, 1989.
- [178] G. Marnellos and M. Stoukides. Ammonia synthesis at atmospheric pressure. *Science*, 282:98, 1998.
- [179] G. Marnellos, S. Zisekas, and M. Stoukides. Synthesis of ammonia at atmospheric pressure with the use of solid state proton conductors. *J. Catal.*, 193:80, 2000.
- [180] T. Murakami, T. Nohira, T. Goto, Y. H. Ogata, and Y. Ito. Electrolytic ammonia synthesis from water and nitrogen gas in molten salt under atmospheric pressure. *Electrochim. Acta*, 50:5423, 2005.
- [181] T. Murakami, T. Nohira, Y. Araki, T. Goto, R. Hagiwara, and Y. H. Ogata. Electrolytic ammonia synthesis from water and nitrogen under atmospheric pressure using a boron-doped diamond electrode as a nonconsumable anode. *Electrochemical and Solid State Letter*, 10:E4, 2007.
- [182] M. Meyer, H. Rickert, and U. Schwaitzer. Investigations on the kinetics of the anodic dissolution of lithium at the interface $\text{Li}/\text{Li}_3\text{N}$. *Solid State Ionics*, 9&10:689, 1983.
- [183] T. Mizushima, K. Matsumoto, J. Sugoh, H. Ohkita, and N. Kakuta. Tubular membrane-like catalyst for reactor with dielectric-barrier-discharge plasma and its performance in ammonia synthesis. *Applied Catal., A*, 265:53, 2004.
- [184] B. Mingdong, B. Xiyao, Z. Zhitao, and B. Mindi. Synthesis of ammonia in a strong electric field discharge at ambient pressure. *Plasma Chem. Plasma Process.*, 20:511, 2000.
- [185] O. V. Zheltonozhko, V. P. Obrosof, and N. N. Batalov. Electrochemical behaviour of Li_3N solid electrolyte during current flow. *Soviet Electrochemistry*, 28:183, 1992.
- [186] U. v. Alpen. Li_3N : A promising Li ionic conductor. *J. Solid State Chem.*, 29:379, 1979.

Acknowledgments

I would like to thank Prof. Dr. Joachim Maier for introducing me to the world of solid state chemistry and for giving me the opportunity to work and benefit from the excellent research conditions in his group at the Max Planck Institute for Solid State Research. I am most grateful to Prof. Maier for the understanding shown in the most difficult period of my private life.

I am grateful to Prof. Dr. Helmut Bertagnolli, Prof. Dr. Friz Aldinger, and Prof. Dr. Thomas Schleid for kindly accepting to accept to participate in the examination committee.

I cannot possibly emphasize enough how grateful I am to my supervisor and office mate Dr. Rotraut Merkle for her extraordinary readiness to help with daily scientific work, for numerous discussions, for her patience, and for sharing her in-depth chemistry knowledge with me. This proved to be essential for the electrical engineer in the world of chemistry. Not to mention her kindness for providing me ‘real-time’ German lessons.

I would like to thank cordially our secretary Sofia Weiglein for her great help in official matters, for explaining to me peculiarities of both the German and English languages, and above all, I thank her for her kindness which made me feel welcome since the very day I joined the group. With an apology to those whom I unintentionally failed to mention, I will name the colleagues and friends who deserve my gratitude for the help, support and time shared with me during the years spent at MPI-FKF. I cordially thank Dr. Hans-Georg Libuda for everything he has done for me since the day we have met at MPIs in Stuttgart. I thank my former colleague Dr. Frank Allmendinger for his initial help in the lab and my predecessor Dr. Bernhard ‘Bernie’ Kamp for giving me important tips about problems which appear during a doctoral work. I thank Peter Senk and Udo Klock for their substantial technical help in the labs, for their Swabian lessons, and for always being in good spirits. I thank Uwe Traub for providing me with IT-help in the office as well as in the labs. I thank Gabi Götz for recording many powder diffractograms for me. I thank our former technician Will Kussmaul for his help. I thank Annette Fuchs, Barbara Reichert and Renee Stotz for their readiness to help and kindness. I thank Mr. Kammerlander and Mr. Preininger from the glass-workshop for the wonderful work done in making the glass parts for the experiments. I thank Dr. Chengtian Lin for the preparation of the Li_3N samples by FZ. I am grateful to Dr. Mitsuharu Konuma

for the XPS measurements and for teaching me some Japanese words and expressions. I thank my friend Dr. Hiroki (Oku) Okudera (currently at Kanazawa University) for his help in performing XRD single crystal measurements on Li_3N and for discussing the results. I thank Dr. Constantin Hoch for his readiness to help with the XRD issues after Oku's leaving for Japan. I am grateful to Prof. Dr. Robert Dinnebier for his readiness to help me learn how to perform powder XRD and for his help in the analysis of the data. I thank Mr. Jan Čurda for his help in operating Buerger cameras. I thank Mr. Wolfgang König for IR measurements, Dr. Clemens Ulrich, Mohammed Bakr and Armin Schulz for Raman measurements. I thank Christoph Kalfass for his help to export XRD data from the TOPAS software package (which proved to be a formidable/impossible task for a novice under time pressure). I would like to thank Prof. Dr. Heinz Dieter Carstanjen and Michel Bechtel for the beamtime and for helping me to perform exciting ion-beam irradiation experiments on the Pelletron Accelerator at MPI-MF (this project was not included in this thesis). I am very grateful to Dr. Alexei Kuzmin, Dr. Eugene A. Kotomin, and Dr. Juris Purans for encouraging me to take part in the EXAFS project; special thanks go to Alexei for introducing me to the field of EXAFS and his hospitality during my one-month stay in Riga. I thank Dr. Heinz Barentzen for explaining to me the basics of the crystal field theory (splitting). I thank Prof. Dr. Ilan Riess for his interest in my work and for the discussions. I thank Dr. Klaus-Dieter Kreuer for his most friendly attitude and for numerous discussions. Last but not least I thank all my colleagues from the department Maier for the friendly atmosphere.

I am indebted to my colleagues Dr. Philip Brydon and Dr. David Mebane for their help with the English language and corrections. However, I am responsible for any remaining mistakes. I thank my dear and numerous friends, whom I have met during these years, for their unfailing friendship: Dr. Hiroki 'Oku' Okudera for infecting me with the 'Mac virus' and for the help with Japanese, Dr. Alexandra (Schröder) Wilde, Branislava Biba Pavlović, Dr. Jan Honolka, Marina Vogt, Vladimir Damljanović, Dr. Frank Baumann, Sanela and Dr. Jörn Goeres, many thanks to Dr. Maël Guennou for teaching me some German grammar and for discussions about Japanese and other languages, Anika Vavić, Violetta Sessi, Dr. Ioannis Zegkinoglou, Dr. Akihiro Noda, Kayoko and Dr. Hirotoshi Yamada, Maki and Dr. Hiroyuki Yamase, Dr. Kei Noda, Dr. Ville Saarinen, little Lucia and Marina and Milan Struhar, Tamara (Basta) and Olivier Le Berre, little Adrian and Ivana (Buntić) and Pascal Ogor, family Kumrić, Dr. Mark Lynass and Eleonora Storace, Dr. Sabine Andergassen, Dr. Marijana Kirćan and Dr. Martin Indergand, Francesco Giannici, Dr. Philip Brydon, Dr. Philippe Leininger, Marko Stojčić, Dr. Vladimir Hinkov, Dr. Lilia Boeri, Martin Hetzel, Dr. Camilla Coletti, many thanks to Dr. Petra Stegmaier, and last but not least, many thanks to my Carina.

I would like to thank and mention my friends, from the period prior to the MPI, who influenced my life and made it interesting and beautiful: Zoltan 'Zolika' Bikadi, Duška Subotić, Ivan Milutinov, Vladimir Sajdl, Jelena and Darko Almažan, family Vavra, Dragan Milić, Milena Milićević, Nadja Ročkomanović, Ivan Canić, Dr. Nenad Kartalović, Nikola Stojanović, Igor Bogićević, Ivan Rajković, Milče Smiljanić, Masaharu Kitajima (Sokol-san), and Mirjana.

In the end, I would like thank my mother, father and brother Marko for their constant love and unwavering support throughout my whole life. I cannot express my sorrow that my mother, to whom I am grateful for being who I am and who was supporting me until her last breath, is not among us anymore and whose untimely death prevented her from sharing the joy of this moment with me.

As an apology for not being present at his 1st-birthday party, because I was writing the thesis, I also dedicate it to my little nephew Miloš 'Jr.', hoping that he will forgive me this when he grows up.

Curriculum Vitae

Name: Miloš Vračar
Date of Birth: May 9th 1972
Place of Birth: Belgrade (Serbia)
Nationality: Serbian

Education

- September 2002-April 2008 Doctoral degree at the Max Planck Institute for Solid State Research in the Department of Prof. Maier and at the University of Stuttgart
- October 1991-June 2002 Diploma in Electrical Engineering (10 semesters), Department of Physical Electronics at the Faculty of Electrical Engineering, University of Belgrade
- October 1995-October 1997 Four semesters at the Faculty of Physics, University of Belgrade
- September 1987-June 1991 Secondary School of Science and Mathematics (Gymnasium) in Bela Crkva, Province of Vojvodina, Serbia

Publications

1. M. Vračar, A. Kuzmin, R. Merkle, J. Purans, E. A. Kotomin, J. Maier, and O. Mathon, "Structural studies of $\text{Sr}(\text{Fe}_x\text{Ti}_{1-x})\text{O}_{3-\delta}$ solid solutions by XAS, XRD and vibrational spectroscopy", *Phys. Rev. B* **76** 174107 (2007).
2. M. Vračar, A. Kuzmin, R. Merkle, J. Purans, E. A. Kotomin, J. Maier, and O. Mathon, "Structural studies of $\text{Sr}(\text{Fe}_x\text{Ti}_{1-x})\text{O}_{3-\delta}$ solid solutions by XAS and Raman spectroscopy", *Highlights 2007 of European Synchrotron Radiation Facility*, p.94.

3. V.E. Alexandrov, R.A. Evarestov, E.A. Kotomin, A. Kuzmin, J. Purans, M. Vračar, R. Merkle, J. Maier, “Theoretical and experimental studies of charge ordering in CaFeO_3 and SrFeO_3 ”, submitted to *Acta Materialia*.
4. M. Vračar, R. Merkle and J. Maier, “Catalytic activity of $\text{Sr}(\text{Fe}_x\text{Ti}_{1-x})\text{O}_{3-\delta}$ and kinetic models for CO and CH_4 total oxidation reactions”, (in preparation).
5. A. Kuzmin, M. Vračar, R. Merkle, J. Purans, E. A. Kotomin, J. Maier, and O. Mathon, “Structural studies of SrFeO_3 and CaFeO_3 by XAS, XRD and vibrational spectroscopy” (in preparation).
6. M. Vračar, R. Merkle, J. Maier, “Electrocatalytic Ammonia synthesis using Li_3N ” (in preparation).